



University of Kentucky
UKnowledge

Theses and Dissertations--Pharmacy

College of Pharmacy

2019

PHASE BEHAVIOR OF AMORPHOUS SOLID DISPERSIONS: MISCIBILITY AND MOLECULAR INTERACTIONS

Kanika Sarpal

University of Kentucky, kanika.krishna@gmail.com

Digital Object Identifier: <https://doi.org/10.13023/etd.2019.152>

[Right click to open a feedback form in a new tab to let us know how this document benefits you.](#)

Recommended Citation

Sarpal, Kanika, "PHASE BEHAVIOR OF AMORPHOUS SOLID DISPERSIONS: MISCIBILITY AND MOLECULAR INTERACTIONS" (2019). *Theses and Dissertations--Pharmacy*. 98.

https://uknowledge.uky.edu/pharmacy_etds/98

This Doctoral Dissertation is brought to you for free and open access by the College of Pharmacy at UKnowledge. It has been accepted for inclusion in Theses and Dissertations--Pharmacy by an authorized administrator of UKnowledge. For more information, please contact UKnowledge@lsv.uky.edu.

STUDENT AGREEMENT:

I represent that my thesis or dissertation and abstract are my original work. Proper attribution has been given to all outside sources. I understand that I am solely responsible for obtaining any needed copyright permissions. I have obtained needed written permission statement(s) from the owner(s) of each third-party copyrighted matter to be included in my work, allowing electronic distribution (if such use is not permitted by the fair use doctrine) which will be submitted to UKnowledge as Additional File.

I hereby grant to The University of Kentucky and its agents the irrevocable, non-exclusive, and royalty-free license to archive and make accessible my work in whole or in part in all forms of media, now or hereafter known. I agree that the document mentioned above may be made available immediately for worldwide access unless an embargo applies.

I retain all other ownership rights to the copyright of my work. I also retain the right to use in future works (such as articles or books) all or part of my work. I understand that I am free to register the copyright to my work.

REVIEW, APPROVAL AND ACCEPTANCE

The document mentioned above has been reviewed and accepted by the student's advisor, on behalf of the advisory committee, and by the Director of Graduate Studies (DGS), on behalf of the program; we verify that this is the final, approved version of the student's thesis including all changes required by the advisory committee. The undersigned agree to abide by the statements above.

Kanika Sarpal, Student

Dr. Eric J. Munson, Major Professor

Dr. David J. Feola, Director of Graduate Studies

PHASE BEHAVIOR OF AMORPHOUS SOLID DISPERSIONS: MISCIBILITY AND
MOLECULAR INTERACTIONS

DISSERTATION

A dissertation submitted in partial fulfillment of the
requirements for the degree of Doctor of Philosophy in the
College of Pharmacy at the University of Kentucky

By

Kanika Sarpal

Lexington, Kentucky

Co-Directors: Dr. Eric J. Munson, Professor of Pharmaceutical Sciences
and Dr. Thomas Dziubla, Professor of Chemical Engineering

Lexington, Kentucky

2019

Copyright © Kanika Sarpal 2019

ABSTRACT OF DISSERTATION

PHASE BEHAVIOR OF AMORPHOUS SOLID DISPERSIONS: MISCIBILITY AND MOLECULAR INTERACTIONS

Over the past few decades, amorphous solid dispersions (ASDs) have been of great interest to pharmaceutical scientists to address bioavailability issues associated with poorly water-soluble drugs. ASDs consist of an active pharmaceutical ingredient (API) that is typically dispersed in an inert polymeric matrix. Despite promising advantages, a major concern that has resulted in limited marketed formulations is the physical instability of these complex formulations. Physical instability is often manifested as phase heterogeneity, where the drug and carrier migrate and generate distinct phases, which can be a prelude to recrystallization. One important factor that dictates the physical stability of ASDs is the spatial distribution of API in the polymeric matrix. It is generally agreed that intimate mixing of the drug and polymer is necessary to achieve maximum stabilization, and thus understanding the factors controlling phase mixing and nano-domain structure of ASDs is crucial to rational formulation design. The focus of this thesis work is to better understand the factors involved in phase mixing on the nanometric level and get insights on the role of excipients on overall stabilization of these systems. The central hypothesis of this research is that an intimately mixed ASD will have better physical stability as compared to a partially homogeneous or a non-homogeneous system. Our approach is to probe and correlate phase homogeneity and intermolecular drug-excipient interactions to better understand the physical stability of ASDs primarily using solid-state nuclear magnetic resonance (SSNMR) spectroscopy and other solid-state characterization tools. A detailed investigation was carried out to understand the role of hydrogen bonding on compositional homogeneity on different model systems. A comprehensive characterization of ternary ASDs in terms of molecular interactions and physical stability was studied. Finally, long-term physical stability studies were conducted in order to understand the impact of different grades of a cellulosic polymer on phase homogeneity for two sets of samples prepared via different methods. Overall, through this research an attempt has been made to address some relevant questions pertaining to nano-phase heterogeneity in ASDs and provide a molecular level understanding of these complex systems to enable rational formulation design.

KEYWORDS: Amorphous solid dispersions, Solid-state nuclear magnetic resonance spectroscopy, Drug-polymer miscibility, Hydrogen bonding, Physical stability

Kanika Sarpal

(Name of Student)

04/26/2019

Date

PHASE BEHAVIOR OF AMORPHOUS SOLID DISPERSIONS: MISCIBILITY AND
MOLECULAR INTERACTIONS

By
Kanika Sarpal

Eric J. Munson, Ph.D.

Co-Director of Dissertation

Thomas Dziubla, Ph.D.

Co-Director of Dissertation

David J. Feola, Ph.D.

Director of Graduate Studies

04/26/2019

Date

DEDICATION

To Mummy and Papa

“Dwell in Possibility”- Emily Dickinson

ACKNOWLEDGEMENTS

“ The journey of a thousand miles begins with one step.” – Lao Tzu

I take this opportunity to thank all those who made this journey a memorable one. It is because of their support and encouragement that I could get to this stage in my life. First and foremost, I would express my heart felt gratitude to my advisor, Professor Eric Munson for his continued guidance and support throughout the duration of my stay in his laboratory. He has been a great mentor throughout and I could not thank him enough for his technical expertise and valuable suggestions. I am indebted to him for teaching me how to approach technical problems and work independently.

I would like to express my sincere thanks to my dissertation committee members – Dr. Dzuibla, Dr. Pack, Dr. Marsac and Dr. Bae for their time and valuable suggestions. I would also like to acknowledge Dr. Miller for agreeing to serve on my committee in between and for her insightful comments. Special thanks to Dr. Bae for being accomodating and accepting my last minute request to serve on my committee.

I would also like to thank Dr. Anderson for his valuable coursework and lectures. I would like to express my whole hearted thanks to Dr. Zhang for his guidance and advise whenever needed. I extend my thanks to Dr. Polli at University of Maryland for giving me an opportunity to work on a collaboartive project.

To the past and present members of the Munson group – Dr. Sean Delaney, Dr. Matt Nethercott, Dr. Xiaoda Yuan, Julie Calahan, Ashley Lay, Travis Jarrells. Special thanks to Julie for being a wonderful colleague. I am grateful to Cole Tower, who was an incredible summer undergraduate in the lab, for all his help. I would also like to thanks the Marsac group members – Matt Defrese, Freddy Arce and Dr. Nico Setiwan.

I owe much gratitude to the Department of Pharmaceutical Sciences at College of Pharmacy for providing an amazing environment and infrastructure for completion of this degree. I would like to express my sincere thanks to Catina Rossoll and Tonya Vance for their help and support throughout. Catina has been extremely helpful in managing the requirements of the college and making sure that each job gets finished on time. All the help from Tonya related to travel arrangements and lab orders is much appreciated. Special vote of thanks to Todd Sizemore and Kristi Moore for making sure that the lab runs efficiently. I would like to thank all the funding sources for the financial support to complete this work.

Last but not least, I am forever indebted to my wonderful family for their support and encouragement. It would not have been possible without their sacrifices. To my mom and dad, I am extremely grateful for their teachings and unconditional love. Though thousand miles apart, they always made sure that I was doing fine. I thank my brother and his family for their support and affection. Special thanks to my two beautiful nieces, Devishi and Mishika, for being so cute and loving. I thank my in-laws with open heart for being understanding and supportive throughout this phase. Lastly, I thank my loving husband, Nimish Gera, for his encouragement, love and unflinching support. Thank you for being patient with me always and helping me become a better person.

TABLE OF CONTENTS

ACKNOWLEDGEMENTS	iii
LIST OF TABLES	viii
LIST OF FIGURES.....	ix
CHAPTER 1. Introduction: Fundamentals of Amorphous Solid Dispersions.....	1
1.1 Introduction.....	1
1.2 The Amorphous State	3
1.3 Amorphous Solid Dispersions	4
1.3.1 Classification of Solid Dispersions	6
1.3.2 Preparation Methods	8
1.3.2.1 Fusion Based Technologies.....	8
1.3.2.2 Solvent Based Technologies	9
1.3.3 Characterization of Amorphous Solid Dispersions.....	11
1.3.3.1 Differential Scanning Calorimetry	12
1.3.3.2 Thermogravimetric Analysis.....	15
1.3.3.3 Powder X-ray Diffraction.....	16
1.3.3.4 Vibrational Spectroscopy	18
1.3.4 Physical Stability of Amorphous Solid Dispersions	19
1.3.4.1 Theory of Crystallization	20
1.3.4.2 Role of Polymers in Physical Stabilization	24
1.3.4.3 Glass Transition Temperature	25
1.3.4.4 Specific Interactions.....	28
1.3.4.5 Drug-Polymer Miscibility	30
1.4 Thesis Overview	33
1.4.1 Chapter 2.....	33
1.4.2 Chapter 3.....	34
1.4.3 Chapter 4.....	34
1.4.4 Chapter 5.....	34
1.4.5 Chapter 6.....	35
CHAPTER 2. Solid-state NMR of Pharmaceuticals: An Overview.....	36
2.1 Introduction.....	36
2.2 NMR-General Introduction.....	37
2.2.1 NMR Theory.....	37
2.2.2 The Chemical Shift	39
2.3 SSNMR Principles and Techniques.....	41
2.3.1 Dipolar Coupling and High-Power Proton Decoupling	41
2.3.2 Chemical Shift Anisotropy and Magic Angle Spinning.....	42
2.3.3 Cross Polarization.....	44
2.3.4 Relaxation	45
2.4 Applications - Amorphous solid dispersions	47
2.4.1 Proton Relaxation Times and Spin Diffusion	47

2.4.2	Molecular Interactions	52
2.4.3	Detection and Quantitation of Amorphous Phases	53
2.5	Conclusions.....	56
CHAPTER 3. Phase Behavior of Amorphous Solid Dispersions of Felodipine: Homogeneity and Drug-Polymer Interactions		
3.1	Introduction.....	57
3.2	Experimental Section.....	61
3.2.1	Materials	61
3.2.2	Preparation of Amorphous Materials.....	61
3.2.3	Differential Scanning Calorimetry (DSC)	62
3.2.4	Solid-State NMR Spectroscopy	63
3.2.5	Theoretical Calculations	65
3.3	Results and Discussion	66
3.3.1	DSC Results.....	66
3.3.1.1	DSC Heating Cycles	66
3.3.1.2	Fitting DSC Data to Gordon-Taylor Equation	71
3.3.1.3	Drug Crystallization-First Heating Scan	72
3.3.1.4	Summary – DSC Results.....	74
3.3.2	¹³ C CP/MAS Solid-State NMR Results – Miscibility.....	76
3.3.2.1	SSNMR Spectra and Interpretation.....	76
3.3.2.2	SSNMR Relaxation Times - Investigation of Phase Behavior.....	80
3.3.2.3	SSNMR Relaxation Times - Determination of Domain Sizes	85
3.3.3	¹³ C CP/MAS Solid-State NMR Results – Molecular Interactions	89
3.3.4	NMR Chemical Shift Calculations for Proposed Species.....	97
3.4	Conclusions.....	99
CHAPTER 4. Understanding Drug-Polymer Miscibility in Two Structurally Similar Molecules.....		
4.1	Introduction.....	101
4.2	Experimental.....	105
4.2.1	Materials	105
4.2.2	Solubility Parameter Calculation	106
4.2.3	Preparation of Amorphous Materials.....	107
4.2.4	Thermal Analysis.....	108
4.2.5	¹³ C Solid-state NMR Spectroscopy.....	109
4.3	Results and Discussion	111
4.3.1	Baseline Characterization	111
4.3.2	Solubility Parameters.....	111
4.3.3	Differential Scanning Calorimetry.....	113
4.3.3.1	Estimation of Drug-Polymer Miscibility.....	113
4.3.3.2	Glass Transition Temperature (T _g).....	118
4.3.4	FTIR Spectroscopy	121
4.3.5	Solid-state NMR Spectroscopy.....	122
4.4	Conclusions.....	132
CHAPTER 5. Molecular Interactions and Phase Behavior of Binary and Ternary Amorphous Solid Dispersions of Ketoconazole		
		134

5.1	Introduction.....	134
5.2	Experimental.....	136
5.2.1	Materials.....	136
5.2.2	Preparation of Amorphous Materials.....	136
5.2.3	Differential Scanning Calorimetry.....	137
5.2.4	Fourier Transform Infrared Spectroscopy.....	138
5.2.5	Solid-state Nuclear Magnetic Resonance Spectroscopy.....	139
5.2.6	Powder X-ray Diffraction.....	140
5.2.7	Physical Stability.....	140
5.3	Results and Discussion.....	141
5.3.1	Chemical Structures.....	141
5.3.2	DSC Results.....	141
5.3.3	FTIR Spectroscopy.....	147
5.3.4	Solid-state NMR spectroscopy.....	153
5.3.4.1	¹³ C CP/MAS Experimental Results.....	153
5.3.4.2	¹⁵ N CP/MAS Spectra Analysis.....	166
5.3.4.3	Investigation of Phase Homogeneity by SSNMR.....	167
5.3.5	Physical Stability.....	170
5.4	Conclusions.....	173
CHAPTER 6. Impact of HPMCAS Grade on Phase Behavior of Itraconazole Solid Dispersions: Effect of Preparation Method.....		174
6.1	Introduction.....	174
6.2	Experimental.....	176
6.2.1	Preparation Method.....	176
6.2.2	Solid-State NMR Spectroscopy.....	177
6.2.3	Powder X-ray Diffraction.....	178
6.2.4	Vapor Sorption.....	178
6.3	Results and Discussion.....	179
6.3.1	¹³ C CP/MAS Solid-state NMR Spectra.....	179
6.3.2	Phase Homogeneity Using Proton Relaxation Measurements.....	186
6.3.3	Determination of Domain Sizes.....	188
6.3.4	Physical Stability.....	191
6.4	Conclusions.....	193
CHAPTER 7. Summary and Future Directions.....		200
7.1	Summary.....	200
7.2	Future Directions.....	203
REFERENCES.....		206
VITA.....		220

LIST OF TABLES

Table 1.1. Classification of solid dispersions.	8
Table 1.2. Commonly used characterization techniques for ASDs.	15
Table 1.3. Physicochemical properties of the polymers commonly used in ASDs.	27
Table 1.4. List of pharmaceutical solid dispersions available in the market.	32
Table 1.5. Relative strength of drug-polymer interactions. Adapted from reference. ⁷⁰	33
Table 2.1. NMR frequency listing for a few common nuclei found in the pharmaceutical samples.	43
Table 2.2. List of pulse sequences used for measuring relaxation times.	49
Table 3.1. Chemical Structures showing H-bond donors (in blue) and acceptors (in red) of model compounds along with their physicochemical properties.	65
Table 3.2. ¹ H T ₁ and T _{1ρ} values along with the standard errors associated with the fit for FEL (as-received and amorphous) and Polymers measured via ¹³ C resonances.	81
Table 3.3. Domain Sizes in amorphous solid dispersions for FEL:Polymer systems as estimated by SSNMR and DSC. Composition represents felodipine to polymer ratio.	90
Table 3.4. ¹³ C chemical shifts (ppm) of carbonyl carbon of polymer in FEL:Polymer dispersions.	91
Table 4.1. Physicochemical properties of raw materials.	106
Table 4.2. Calculation showing solubility parameters of felodipine and nifedipine based on the Hoftyzer-Van Krevelen group contribution method.	112
Table 4.3. F-H interaction constants A and B as obtained from melting point depression data.	115
Table 4.4. Domain sizes (nm) as calculated from SSNMR analysis.	132
Table 5.1. Proton relaxation times of as received and amorphous KET along with polymers PAA and HPMC.	169
Table 6.1. Composition of different grades of HPMCAS (wt %).	181
Table 6.2. ¹ H T ₁ and T _{1ρ} values along with the standard errors associated with fit for ITZ (as-received and amorphous) and HPMCAS grades measured via ¹³ C resonances.	188
Table 6.3. Comparison of percent crystallinity for different time periods for 30% ITZ film stability sample (40 °C/75 %RH) as measured by SSNMR.	196

LIST OF FIGURES

Figure 1.1. Biopharmaceutics classification system (BCS) and formulation approaches applicable for different classes. Adapted from reference. ¹²	5
Figure 1.2. Schematic representation of thermodynamic relationship of amorphous and crystalline states. The green curve represents T_g curve of a solid dispersion. T_K : Kauzmann temperature, T_g : glass transition, T_m : melting temperature. Modified from the reference. ¹⁷	6
Figure 1.3. Classification of solid dispersions and their properties. Adapted from references. ^{19,27}	7
Figure 1.4. Commonly used methods in preparation of ASDs.....	11
Figure 1.5. Schematic representation of spray-drying equipment. Taken from source. ⁸²	11
Figure 1.6. A typical mDSC plot showing the three signals corresponding to total heat flow (top), non reversible heat flow (middle), and reversible heat flow (bottom). The glass transition (T_g) is apparent in the reversible heat flow, whereas the crystallization exotherm is apparent both in reversible and non reversible heat flow. Melting is apparent in all three signals.	14
Figure 1.7. A typical TGA plot showing weight % as a function of temperature for a spray dried dispersion sample.	16
Figure 1.8. PXRD patterns for crystalline (as-received) and amorphous celecoxib (CEL). Amorphous celecoxib is devoid of characteristic Bragg peaks as seen in as received celecoxib.....	18
Figure 1.9. Illustration of “spring and parachute” mechanism. Adapted from reference. ³⁰	20
Figure 1.10. Schematic representation of free energy ΔG as a function of nucleus radius r . Adapted from the reference. ⁶⁰	23
Figure 1.11. Schematic representation of nucleation rate and crystal growth rate as a function of temperature for undercooled melts. Adapted from reference. ⁶⁰	24
Figure 1.12. Deviations from the Gordon-Taylor equation; D represents drug and P represents polymer. Adapted from reference. ¹³	29
Figure 2.1. Schematic depicting the response of nuclear spins in the presence of the external magnetic field. The splitting of nuclear spin states is also shown.....	40
Figure 2.2. Illustration of the magnetic shielding of a nucleus by surrounding electrons and the effective magnetic field experienced by the nucleus.....	40
Figure 2.3. A schematic of magic-angle spinning.....	43
Figure 2.4. A scheme of cross polarization pulses sequence. The rectangles represent rf pulses, while the oscillating curve represents the FID.....	45
Figure 2.5. A scheme of pulse sequence for 1H T_1 using saturation recovery.....	49
Figure 2.6. A scheme for pulse sequence for measuring 1H $T_{1\rho}$	50
Figure 2.7. A comparison of ^{13}C CP/MAS spectra of crystalline and amorphous itraconazole (ITZ).	54
Figure 2.8. ^{13}C cross polarization dynamic curves for various forms of neotame, taken from reference. ³² ..	55

Figure 3.1. DSC thermograms from first heating scan for FEL:Polymer dispersions A) FEL:PVP B) FEL:PVP/VA and C) FEL:PVAc. The values reported here are the mean glass transition temperatures.	69
Figure 3.2. DSC thermograms from second heating scan for FEL:Polymer dispersions A) FEL:PVP B) FEL:PVP/VA and C) FEL:PVAc. The values reported here are the mean glass transition temperatures.	70
Figure 3.3. T_g -composition relationship for FEL:Polymer dispersions. Mean experimental T_g values are denoted by symbols (red circle for FEL:PVP, green square for FEL:PVP/VA, and FEL:PVAc). The respective Gordon-Taylor curves are shown in colored broken lines.....	72
Figure 3.4. DSC thermograms showing non reversing heat flow versus temperature as a function of polymer loading: A) 10% polymer B) 20% polymer.	74
Figure 3.5. X-ray powder diffraction patterns of FEL:Polymer dispersions for A) FEL:PVP, B) FEL:PVP/VA and C) FEL:PVAc.....	76
Figure 3.6. Stacked plot of ^{13}C CP/MAS spectra for (A) Felodipine (as received) (B) amorphous felodipine (C) PVP (D) PVP/VA and (E) PVAc. The ^{13}C resonances relate to the numbering scheme presented in Table 3.1.....	78
Figure 3.7. ^{13}C CP/MAS spectra of (A) FEL:PVP dispersions (B) FEL:PVP/VA and (C) FEL:PVAc. In each stacked plot the spectra from top to bottom include amorphous FEL, FEL:Polymer dispersions with 50-90% drug load and neat polymer. The central aromatic peaks at 146 ppm, 128 ppm and 104 ppm (indicated by the red box; plot A-C) were attributed to FEL specific resonances while the peaks at 175 ppm (indicated by blue box; plot A), 68 ppm (indicated by blue box; plots B and C) were identified as non-overlapping regions for PVP, PVP/VA and PVAc respectively.	79
Figure 3.8. $^1\text{HT}_{1p}$ differential between FEL and polymer in dispersions for A) FEL:PVP, B) FEL:PVP/VA and C) FEL:PVAc as a function of weight fraction of polymer. The error bar signifies 95% confidence interval associated with the fit. The dashed line represents the zero.	83
Figure 3.9. $^1\text{HT}_{1p}$ differential between FEL and polymer in dispersions for A) FEL-PVP, B) FEL:PVP/VA and C) FEL:PVAc as a function of weight fraction of polymer. The error bar signifies 95% confidence interval associated with the fit. The dashed line represents the zero.	87
Figure 3.10. $^1\text{HT}_{1p}$ differential for 90:10 FEL:PVP ratio as the function of PVP grade. The error bar signifies 95% confidence interval associated with the fit. The dashed line represents the zero.	88
Figure 3.11. $^1\text{HT}_{1p}$ differential for 90:10 FEL:PVP before and after heating <i>in situ</i> in NMR rotor. The error bar signifies 95% confidence interval associated with the fit. The dashed line represents the zero.	88
Figure 3.12. Deconvolution of carbonyl region of amorphous FEL. The experimental spectrum is shown in brown; the simulated spectrum is shown in magenta while the residual spectrum is depicted in red. The blue lines represent the fitted individual species used in deconvolution.	91
Figure 3.13. ^{13}C SSNMR sub spectra of FEL:Polymer dispersions in the carbonyl region for A) FEL:PVP, B) FEL:PVP/VA and C) FEL:PVAc. The experimental spectrum is shown in brown; the simulated spectrum is shown magenta while the residual spectrum is depicted in red. The blue lines represent the fitted individual species used in deconvolution.....	95

Figure 3.14. The fraction of dimer and free FEL carbonyl carbon for FEL:Polymer dispersions with A) PVP, B) PVP/VA and C) PVAc as a function of polymer weight fraction.	96
Figure 3.15. The comparison of dimer and free fractions for 50:50 FEL:Polymer samples.	97
Figure 4.1. Melting temperatures (T_m) of NIF (black circles) and FEL (red diamonds) as a function of drug weight percent. The data points represent the average of two separate runs and errors bars represent the standard deviation.	116
Figure 4.2. Plot used to calculate the Flory-Huggins interaction parameter for NIF:SOL (green circles) and FEL:SOL (blue circles). The slope would represent the value of the Flory-Huggins interaction parameter. The respective values of slope were obtained using linear regression.	116
Figure 4.3. A plot of $\Delta G_{mix}/RT$ as a function of volume fraction of drug (ϕ_{drug}) for (A) FEL:SOL and (B) NIF-SOL.	117
Figure 4.4. Binary phase diagram for (A) FEL:SOL and (B) NIF:SOL.	119
Figure 4.5. A plot showing experimental and predicted T_g as a function of Soluplus weight fraction. The red and green circles represent mean experimental T_g values from DSC second heating cycle for NIF:SOL and FEL:SOL respectively. The error bars denote the standard deviation. The broken lines represent the predicted T_g values from the Gordon-Taylor equation.	120
Figure 4.6. FTIR spectra for FEL:SOL (plots A, C) and NIF:SOL (plots B, D) samples. The NH stretching region ($3150-3450\text{ cm}^{-1}$) and the carbonyl stretching region ($1550-1800\text{ cm}^{-1}$) are shown in plots (A, B) and (C, D) respectively.	124
Figure 4.7. Stacked plot for ^{13}C CP/MAS Spectra of as received felodipine (top), as received nifedipine (middle) and Soluplus (bottom). Resonance assignments are done in reference to the numbering scheme used in Table 4.1.	125
Figure 4.8. Stacked ^{13}C CP/MAS spectra for dispersions samples (A) FEL-SOL system and (B) NIF-SOL system.	125
Figure 4.9. Bar graphs depicting the differences in “free” and “dimer” fractions for NIF:SOL system (green bars) and FEL:SOL system (pink bars).	129
Figure 4.10. $^1\text{HT}_1$ (black squares) and $^1\text{HT}_{1p}$ (red circles) plots for FEL:SOL system as a function of Soluplus weight percent.	130
Figure 4.11. $^1\text{HT}_1$ (black squares) and $^1\text{HT}_{1p}$ (red circles) plots for NIF:SOL system as a function of Soluplus weight percent.	130
Figure 5.1. Chemical structures of (A) ketoconazole (KET) (B) PAA and (C) HPMC.	142
Figure 5.2. DSC thermograms from first heating cycle for (A) KET:PAA binary system (B) KET:HPMC binary system and (C) KET:PAA:HPMC ternary system. The composition of the samples is indicated by drug:polymer ratio on a weight basis: black for KET, gold for PAA and blue for HPMC.	143
Figure 5.3. DSC thermograms from second heating cycle for (A) KET:PAA binary system (B) KET:HPMC binary system and (C) KET:PAA:HPMC ternary system. The composition of the samples is indicated by drug:polymer ratio on a weight basis: black for KET, gold for PAA and blue for HPMC.	146

Figure 5.4. Mean experimental and theoretical T_g plotted as a function of weight fraction of KET for KET:PAA dispersions (red color), KET:HPMC dispersions (blue color) and KET:PAA:HPMC dispersions (green color). The dotted lines represent theoretical T_g values obtained from the Gordon-Taylor equation.	147
Figure 5.5. FTIR spectra of pure KET, pure PAA and dispersions showing the carbonyl stretching region and the single bond region for KET:PAA binary system (plots A and B), KET:HPMC binary system (plots C and D) and KET:PAA:HPMC ternary system (plots E and F).	151
Figure 5.6. FTIR spectrum of PAA and its sodium salt. The peaks $\sim 1549\text{ cm}^{-1}$ and 1399 cm^{-1} found in sodium salt of PAA are attributed to asymmetric and symmetric stretching vibration of the carboxylate group respectively.	152
Figure 5.7. Comparison of FTIR spectra of PAA, HPMC and their spray dried blends. In presence of HPMC, the intensity of dimer peak ($\sim 1695\text{ cm}^{-1}$) decreases and moves to higher wavenumbers as the weight fraction of HPMC increases. Spectrum of 50:50 physical mixture of PAA and HPMC is shown as a reference.	152
Figure 5.8. Comparison of ^{13}C CP/MAS spectra of (A) crystalline KET (B) amorphous KET (C) PAA and (D) HPMC.	159
Figure 5.9. Donor to acceptor molar ratio calculated for binary KET:PAA and ternary KET:PAA:HPMC as a function of weight percent of KET. The cross point on the curve represent the theoretical 1:1 molar ratio in each case.	160
Figure 5.10. Comparison of ^{13}C CP/MAS spectra of (A) crystalline KET (B) amorphous KET (C) PAA and (D) HPMC.	160
Figure 5.11. ^{13}C CP/MAS sub spectra in the carbonyl region (160-190 ppm) for (A) KET:PAA binary dispersions and (B) KET:PAA:HPMC ternary dispersions. The shaded box shows how peak around 172 ppm shifts upfield with increase in drug loading.	161
Figure 5.12. ^{13}C CP/MAS SSNMR spectra of PAA and sodium salt of PAA. The main peak in the carbonyl region of sodium salt resonated around $\sim 186\text{ ppm}$	161
Figure 5.13. ^{13}C CP/MAS spectra of 50:50 KET:PAA binary dispersion (red) and 50:50 KET:PAA physical mixture (purple). The shoulder peak around 172 ppm is visible in dispersion sample but absent in physical mixture. Spectra of PAA and amorphous KET is included as a reference.	162
Figure 5.14. ^{13}C CP/MAS spectra of spray dried blends of PAA and HPMC at various ratios.	163
Figure 5.15. Deconvolution of the carbonyl region of (A) binary KET:PAA samples and (B) ternary KET:PAA:HPMC samples. The fitted peaks are shown in blue; the sum of the fit is shown in yellow; the residual is shown in red.	163
Figure 5.16. Plots of % peak area for various species as a function of KET weight % obtained from deconvolution of the carbonyl region from SSNMR spectra for (A) KET:PAA binary system and (B) KET:PAA:HPMC ternary system. The black and gold curves belong to KET and PAA species respectively.	164

Figure 5.17. Plots depicting comparison of various species in binary and ternary systems calculated for total (A) PAA carbonyl fraction and (B) KET carbonyl fraction as a function of KET weight%.....	165
Figure 5.18. ¹⁵ N CPMAS SSNMR spectra of (A) amorphous KET, (B) 80:20 KET:PAA binary dispersion and (C) 80:10:10 KET:PAA:HPMC ternary dispersion.	168
Figure 5.19. Comparison of ¹ HT ₁ (plots A, C, E) and ¹ HT _{1p} (plots B, D and F) for drug and polymer(s) components. The relaxation times for KET, PAA, HPMC are shown in black, orange and blue bars respectively. Plots A, C and E belong to ¹ HT ₁ relaxation times for binary KET:PAA system, binary KET:HPMC system and ternary KET:PAA:HPMC system respectively. Plots B, D and F belong to ¹ HT _{1p} relaxation times for binary KET:PAA system, binary KET:HPMC system and ternary KET:PAA:HPMC system respectively.	169
Figure 5.20. PXRD patterns of stability binary and ternary dispersions for (A) KET:PAA (B) KET:HPMC and (C) KET:PAA:HPMC stored at RT/94% RH. The plots of stability samples stored at 40 °C/75% RH are shown in (D) KET:PAA (E) KET:HPMC and (F) KET:PAA:HPMC. Crystalline KET is included as a reference.	172
Figure 6.1. Chemical structures of itraconazole (left) and HPMCAS (right).	182
Figure 6.2. SSNMR spectra from bottom to top include crystalline ITZ, amorphous ITZ and HPMCAS grades-H, L and M.	182
Figure 6.3. Deconvolution of the carbonyl region (160-180 ppm) in SSNMR spectra for HPMCAS grades. The fitting of succinate and acetate peaks is shown in black and blue respectively; the sum of the species is shown in magenta; the residual difference between the experimental and fitted peaks is shown in orange.	183
Figure 6.4. Stacked ¹³ C CP/MAS spectra for ITZ film samples formulated with (A) HPMCAS H grade, (B) HPMCAS L grade and (C) HPMCAS M grade. Green and pink shaded boxes represent HPMCAS and ITZ specific regions respectively.	184
Figure 6.5. Stacked ¹³ C CP/MAS spectra for ITZ spray dried dispersion samples formulated with (A) HPMCAS H grade, (B) HPMCAS L grade and (C) HPMCAS M grade. Green and pink shaded boxes represent HPMCAS and ITZ specific regions respectively.	185
Figure 6.6. Absolute difference in ¹ H T ₁ values between ITZ and HPMCAS grades for A) film and B) spray dried samples as a function of ITZ weight percent. The error bars represent the 95% confidence interval associated with the fit. The dashed line signifies the zero difference line. The green, red and blue diamond symbols represent HPMCAS H, L and M grades respectively.....	189
Figure 6.7. Absolute difference in ¹ H T _{1p} values between ITZ and HPMCAS grades for A) film and B) spray dried samples as a function of ITZ weight percent. The error bars represent the 95% confidence interval associated with the fit. The dashed line signifies the zero difference line. The green, red and blue diamond symbols represent HPMCAS H, L and M grades respectively.	190
Figure 6.8. PXRD patterns of stability spray dried samples at 40 °C/75% RH for (A) H Grade (B) L Grade and (C) M Grade.	194

Figure 6.9. Stacked plots for SSNMR spectra of crystalline ITZ, amorphous ITZ and spray dried stability samples at 40 °C/75 % RH for (A) H grade (B) L grade and (C) M grade.	195
Figure 6.10. Absolute difference in ^1H T_1 (plots (A-C); green bars) and ^1H $T_{1\rho}$ (plots (D-E); blue bars) values between ITZ and HPMCAS spray dried stability samples (40 °C/75 % RH) for a period of 6 months. The error bars represent the 95% confidence interval associated with the fit.	196
Figure 6.11. PXRD patterns of stability film samples at 40 °C/75% RH for (A) H Grade (B) L Grade and (C) M Grade.	197
Figure 6.12. Stacked plots for SSNMR spectra of crystalline ITZ, amorphous ITZ and film samples at 40 °C/75 % RH for (A) H grade (B) L grade and (C) M grade.	198
Figure 6.13. Absolute difference in ^1H T_1 (plots (A-C); green bars) and ^1H $T_{1\rho}$ (plots (D-E); blue bars) values between ITZ and HPMCAS film stability samples (40 °C/75 % RH) for a period of 6 months. The error bars represent the 95% confidence interval associated with the fit.	199
Figure 6.14. Moisture sorption isotherms of ITZ, amorphous ITZ and HPMCAS grades.	199

CHAPTER 1. INTRODUCTION: FUNDAMENTALS OF AMORPHOUS SOLID DISPERSIONS

1.1 Introduction

Oral route for drug delivery is considered the most preferred for its ease of administration, high patient compliance, cost effectiveness and flexible dosage design.¹ After oral ingestion of the solid dosage form, the drug is released in gastrointestinal (GI) tract, dissolved in GI fluids, then absorbed across the intestinal mucosa and passed through the liver to systemic circulation to reach its site of action.² For the drug to dissolve in GI medium, appreciable aqueous solubility is required for adequate absorption and oral bioavailability. Thus, the two key properties of drug candidates that govern their extent of oral bioavailability are aqueous solubility and intestinal permeability. Based on these two properties, Amidon et al., proposed the biopharmaceutics classification system (BCS) in the year 1995.³ According to BCS, drug substances are classified into four classes based on their aqueous solubility and intestinal permeability (Figure 1.1). These four categories include drugs with high solubility/high permeability (class I), low solubility/high permeability (class II), high solubility/low permeability (class III), and low solubility/low permeability (class IV). A drug substance is considered “highly soluble” when the highest dosage strength is soluble in 250 mL or less in aqueous media (pH 1-7.5) whereas the drug is considered “highly permeable” when $\geq 90\%$ of the administered dose is absorbed across GI barrier.⁴

Combinatorial chemistry and high-throughput screening employed in drug discovery have significantly increased the number of poorly water soluble drug candidates.^{5,6} Poor aqueous solubility is responsible for a large number of attritions with the majority of new chemical entities (NCEs) with challenging physicochemical

properties. This has emerged as a major obstacle in drug discovery and development.⁷ It is estimated that approximately over 75 % of drug candidates, 60 % of NCEs, and 90 % of marketed drugs belong to either BCS class II or class IV.⁷⁻¹⁰ Thus, there is an increased interest in developing efficient formulation strategies for such drug candidates. This has resulted in progress of BCS class II compounds further along the drug development stages and several have become successful marketed drugs.^{2,5}

Some approaches that have been utilized successfully to address low drug solubility include salt formation, crystal modification, pH modification, cyclodextrin complexation, particle size reduction, lipid based systems, and amorphization.^{11,12} Among the approaches stated above, amorphization is a prominent solubilization strategy. Amorphous solids are characterized by short range order and high internal energy.¹³ Generally, amorphous drugs have higher solubility than the corresponding crystalline form since the need of overcoming the lattice energy for the solubilization process is waived off.¹⁴ Studies point out that an amorphous form of a drug can generate 1.1 to 1000 fold increase in solubility of the same drug compared to its crystalline form.^{15,16} These benefits come with a cost and the enhanced thermodynamic properties also accounts for higher chemical reactivity and crystallization tendency that can occur during manufacturing, storage or dissolution.¹⁷ Hence, an amorphous form of drug is seldom used alone.

An important strategy for stabilizing an amorphous drug against crystallization is to disperse it into a polymer matrix, forming a solid dispersion.^{18,19} A solid dispersion can potentially enhance the physical stability by reducing the molecular mobility of a drug and increasing the diffusion length for the assembly of drug molecules into a drug

rich phase or recrystallization.^{20,21} In spite of the benefits offered by this formulation technology, developing a robust solid dispersion formulation still remains a daunting task for pharmaceutical scientists. Therefore, a significant part of pharmaceutical academic and industrial research is directed towards understanding the critical factors for physical stabilization of amorphous drugs. In this chapter, we will discuss the characteristics of amorphous state and factors affecting the physical stability and physicochemical properties of amorphous solid dispersion. In addition, preparation methods and the characterization techniques are also reviewed. Last but not least, a comprehensive overview of available literature on amorphous solid dispersions (ASDs) is presented here.

1.2 The Amorphous State

A convenient way to visualize the energetics of the amorphous state can be achieved through drawing the schematic representation of enthalpy (or volume) variations as a function of temperature (Figure 1.2). If we consider a situation where molten drug is cooled to the melting point (T_m) of the crystalline phase, which is a first-order transition and leads to a decrease in free volume and enthalpy. However, if crystallization is not allowed to occur then the material enters the “supercooled” liquid state without depicting any discontinuity in H and V . The “supercooled” liquid state is often called a rubbery state due to the high viscosity of the material. Further cooling will result in substantial increase in viscosity and produce a glass at the glass transition state (T_g), accompanied by a change of slope. It should be noted that the “glassy state” is a non-equilibrium state and T_g can fluctuate with processing conditions and as a function of the history of the sample, which implies that T_g is a thermal event affected by kinetic

factors.¹³ At temperatures below T_g , the material becomes brittle and extremely viscous ($>10^{12}$ Pa s).²² Moreover at temperatures below T_g , the real glass relaxes to reach asymptotically the equilibrium state and when the material is re-heated to the T_g , the lost enthalpy is recovered again.¹⁷ If the supercooled liquid curve is traced below T_g , there comes a point where it meets the crystal curve at temperature known as the Kauzmann temperature (T_K). At T_K , the configurational entropy of the system reaches zero and is believed to be a temperature with zero mobility ensuring sufficient physical stability for the sample.¹³

The amorphous state is characterized by the absence of long-range three dimensional order and has enhanced thermodynamic properties in comparison to their crystalline counterparts as a result possess higher apparent solubility. Since the amorphous state is thermodynamically unstable, there is a tendency to approach a lower energy level through a process of relaxation.²³ In theory, three types of relaxations are observed (α , β and γ relaxations). The slower, primary and universal motions involving T_g belong to α relaxations while β relaxations represent faster, secondary local motions of specific chemical groups or sequences and are dominant below the T_g . It is suggested that α relaxations are the key kinetic factor for crystallization, whereas β relaxations are responsible for crystallization below T_g for many systems.²⁴ Besides these two relaxation processes, γ relaxations are closely related to β relaxations but occur at lower temperatures.²³

1.3 Amorphous Solid Dispersions

Historically the term “solid dispersion” was first used by Chiou and Riegelmann in 1971 who defined it as “a dispersion of one or more active ingredients in an inert

carrier at the solid state, prepared either by the melting, the solvent or the combined melting solvent methods".²⁵ However, the concept was first used earlier where the drug was delivered with a carrier as a eutectic mixture but it was Chiou and Riegelmann who first proposed a classification system for solid dispersions.^{25,26} Since then, this technology has been used as a viable formulation strategy to overcome the low oral-bioavailability of BCS class II compounds. Before we discuss the other topics related to this important platform technology, it is relevant to study briefly its classification system.

BCS Class	Formulation Approaches
Class I (High Permeability and High Solubility) <input type="checkbox"/> Verapamil hydrochloride, Warfarin sodium	<input checked="" type="checkbox"/> Immediate release (IR) solid dosage forms
Class II (High Permeability and Low Solubility) <input type="checkbox"/> Diazepam, Nifedipine, Felodipine, Ketoconazole, Ritonavir, Itraconazole	<input checked="" type="checkbox"/> Crystal modifications <input type="checkbox"/> Metastable polymorphs <input type="checkbox"/> Salt formation <input type="checkbox"/> Co-crystal formation <input checked="" type="checkbox"/> IR solid oral dosage forms with surfactant <input checked="" type="checkbox"/> Particle size reduction <input type="checkbox"/> Micronization <input type="checkbox"/> Nanocrystals <input checked="" type="checkbox"/> Cyclodextrin complexation <input checked="" type="checkbox"/> Amorphous dosage forms <input checked="" type="checkbox"/> Lipid formations <input type="checkbox"/> Self-emulsifying systems <input checked="" type="checkbox"/> pH modification
Class III (Low Permeability and High Solubility) <input type="checkbox"/> Cimetidine, Captopril, Chloramphenicol	<input checked="" type="checkbox"/> IR solid dosage forms with absorption enhancer
Class IV (Low Permeability and Low Solubility) <input type="checkbox"/> Dapsone, Docycline, Theophylline	<input checked="" type="checkbox"/> Combination of approaches for BCS class II and absorption enhancer

Figure 1.1. Biopharmaceutics classification system (BCS) and formulation approaches applicable for different classes. Adapted from reference.¹²

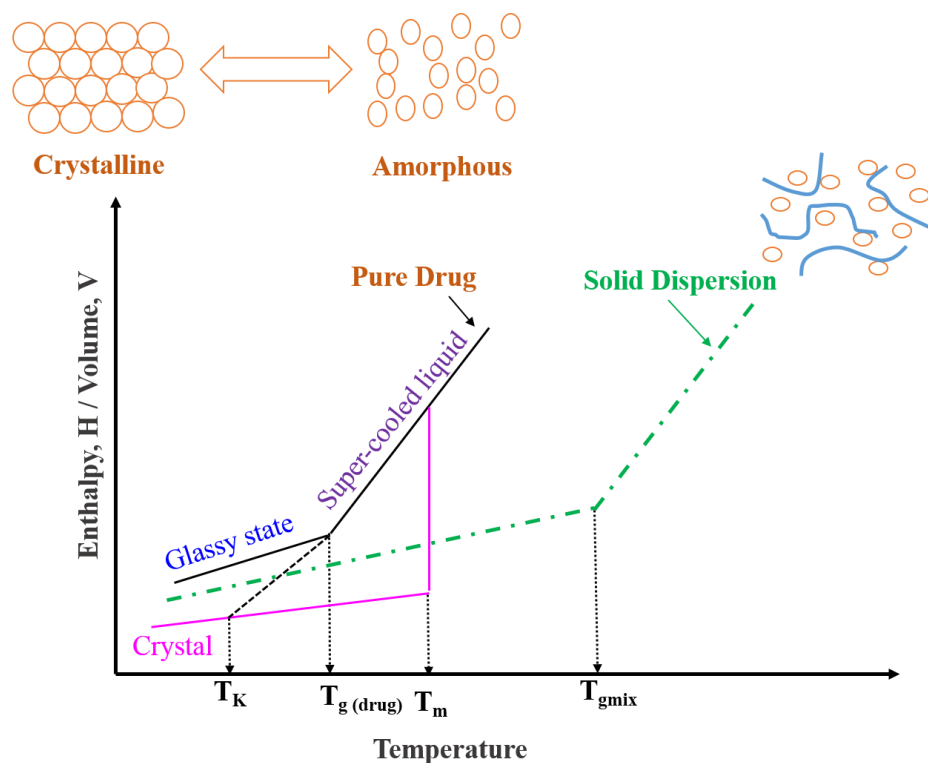


Figure 1.2. Schematic representation of thermodynamic relationship of amorphous and crystalline states. The green curve represents T_g curve of a solid dispersion. T_K : Kauzmann temperature, T_g : glass transition, T_m : melting temperature. Modified from the reference.¹⁷

1.3.1 Classification of Solid Dispersions

Depending on the molecular structure of active pharmaceutical ingredient (API) in the carrier, the solid dispersions can be divided into crystalline solid dispersion and amorphous solid dispersion (ASD). Furthermore, within crystalline solid dispersion two classes exist: solid solution and eutectic mixture. Likewise, ASD group can be further divided into two sub-groups: glass solutions and glass suspensions. Here, we restrict ourselves to the ASD group, consisting of amorphous API and the carrier. The classification system for solid dispersions is shown in Table 1.1.

In the case of glass solutions, the carrier is amorphous while the drug molecules are molecularly dispersed in the amorphous matrix forming a homogenous single-phase system. These days polymers such as synthetic poly(vinylpyrrolidone) (PVP), semisynthetic hydroxypropyl methyl cellulose (HPMC) are employed as amorphous carriers.²⁷ An intimate mixing between the drug and polymer ensures a physically stable system provided solubility of the drug in the polymer does not exceed. However, if drug is present at supersaturated concentration, recrystallization may occur. For a system to classify as a glass suspension, the drug is no longer dispersed molecularly within the amorphous polymer and multiple phases exist. In such system, the drug usually exists as a separate drug rich amorphous phase and may have higher tendency to recrystallize.

More recently a different system of classification has been proposed based on the complexity of solid dispersions and their evolution over the time.¹⁹ Based on this classification system, solid dispersions can be categorized into four generations (Figure 1.3). The generations highlight the advancement of knowledge and their composition.

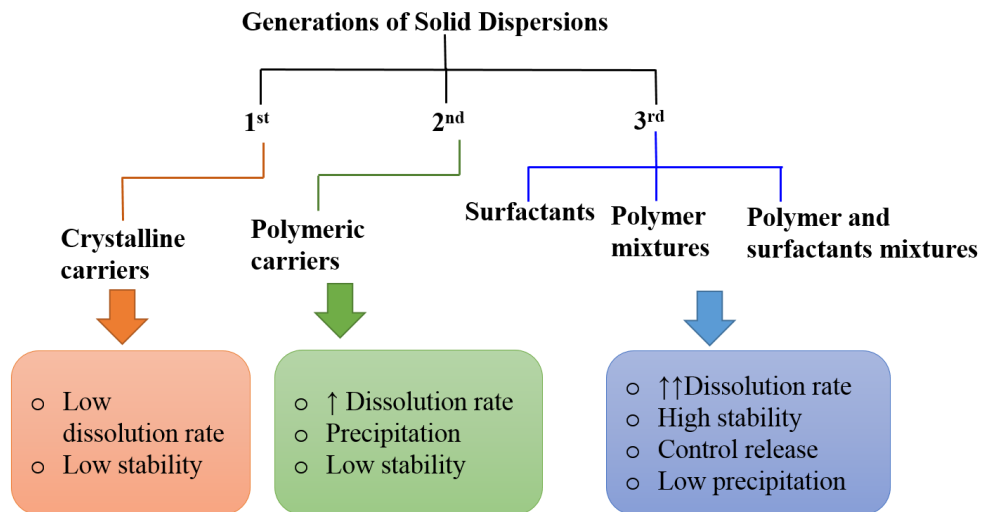


Figure 1.3. Classification of solid dispersions and their properties. Adapted from references.^{19,27}

Table 1.1. Classification of solid dispersions.

<i>State of API</i>	<i>Number of Phases</i>	
	1	2
Crystalline	Solid solution	Eutectic mixture
Amorphous	Glass solution	Glass suspension

1.3.2 Preparation Methods

Broadly, the preparation methods for ASDs can be classified into two major groups: solvent based or fusion based.²⁷ Each group encompasses many technologies under it and the same is shown as a schematic in Figure 1.4.

1.3.2.1 Fusion Based Technologies

In general, fusion based approach involves heating the drug and carrier mixture above their melting point or T_g and then cooling the mixture to kinetically trap the amorphous form of the drug. The resultant solid sample is then crushed, pulverized and sieved to reduce the particle size. Even though this approach is solvent-free and frequently used, this method has some limitations such as thermolability of the drug and carrier at high temperatures.²⁷ In addition, the drug and carrier need be to miscible at high temperatures as any immiscibility can potentially lead to phase separation from inhomogeneous distribution of drug in the matrix.

Hot-melt extrusion (HME) is a popular fusion based technique that has been used for manufacturing ASDs on an industrial scale. The technique has its origin in plastic industry and known for its high scalability and applicability. In this method, the drug and carrier are mixed together and pumped through a heated barrel by one or two screws

under pressure and then discharging the extrudate through a die to get product in a specific shape such as a rod, pellet or tablet.²⁸ The intense mixing and agitation forced by rotating screws ensure homogenous mixing and also make the process continuous.²⁹ In order to lower the processing temperature or reduce the melt viscosity, low molecular weight additives such as plasticizers are added.²³ This technique offers many advantages like solvent free method, efficient process, easy scale up and continuous manufacturing. Moreover, another important advantage of HME in comparison with other fusion based methods is the low residence time of the drug-polymer melt at higher temperature which diminishes the risk of degradation in the case of thermolabile drug. This technology has been successfully used for manufacturing marketed products like Kaletra, Onmel, Rezuin, Norvir, and Zoladex.³⁰

Other fusion based technologies that have been developed for ASDs include KinetiSol[®]. KinetiSol[®] is a new upcoming technology that is specifically suitable for thermolabile compounds as it uses shorter residence time than a regular HME process.³⁰ It can work better with viscous melts and thus the use of plasticizers can be avoided.³¹ This technology is being developed for industrial manufacturing and there are no marketed products yet being manufactured via this process.

1.3.2.2 Solvent Based Technologies

The solvent based technologies include spray drying, freeze drying, rotary evaporation, supercritical fluid technology, fluid bed granulation, coprecipitation, spray freeze drying and electrospinning.²⁷ With solvent based technologies, the common steps involve preparation of drug carrier solution in a common solvent followed by evaporation of the solvent to produce a solid sample. This approach is devoid of any

melting at elevated temperature and hence most suited for thermolabile APIs. An important requirement for this approach is the sufficient solubility of API and the carrier in a common solvent, which can be challenging at times. Solvent like methanol, ethanol, methylene chloride, acetone, water or their mixtures have been employed and sometimes surfactants are also incorporated to aid in solubilization. The main disadvantage of this method is the issue of residual solvent, which is nearly impossible to remove completely and may pose toxicity based on solvent(s) used.³⁰ Also, the residual solvent can act like a plasticizer and promote potential phase separation.³² Other challenges that are associated with this approach are high production cost, extra infrastructure for solvent removal, environmental concerns and potential explosion hazards.

Spray drying is the most industrially applicable technique based on solvent based approach to be employed for ASDs manufacturing. It has been used in the field of pharmaceuticals since 1970s and is known for its efficient processing.³³ This unit operation consists of drug-carrier solution or suspension that is atomized into fine droplets and evaporating the droplets rapidly using a drying hot gas inside the drying chamber followed by collection of solid particles in a cyclone. This technique has proven to be effective method for preparation of ASDs and offers better process control with desired particle properties.³⁴ Compared to traditional solvent based methods like rotary evaporation, this approach ensure better mixing and hence molecularly dispersed ASDs are produced. It has been shown that phase separation in the final product can be controlled through processing conditions.³⁵ A typical schematic of spray drying process is presented in Figure 1.5. Several marketed products prepared by this technology include InCivek, Kalydeco, Intelence and Torcetrapib.³⁰

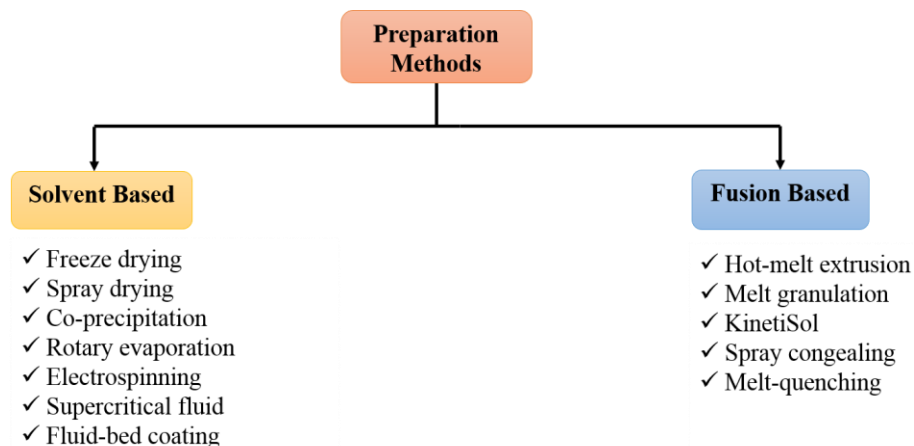


Figure 1.4. Commonly used methods in preparation of ASDs.

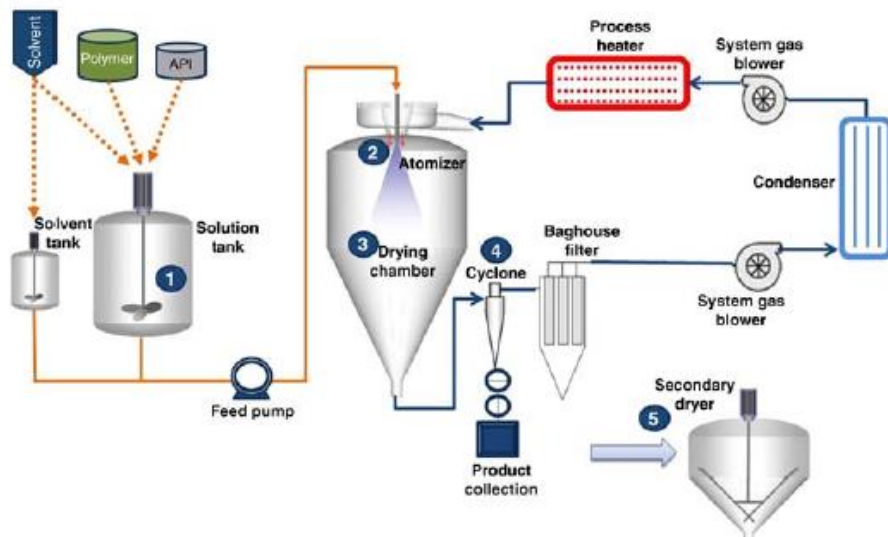


Figure 1.5. Schematic representation of spray-drying equipment. Taken from source.⁸²

1.3.3 Characterization of Amorphous Solid Dispersions

The characterization of ASDs is very crucial in order to study their phase behavior and require in-depth comprehensive characterization. A variety of characterization tools are available and multiple analytical techniques are used in conjunction to provide qualitative and quantitative information on crystallinity, phase

mixing, molecular mobility, intermolecular interactions, residual moisture/solvent content etc. In this section, the focus is given to techniques that are most widely applied such as differential scanning calorimetry (DSC), powder X-ray diffraction (PXRD), thermogravimetric analysis (TGA) and fourier transform infrared spectroscopy (FTIR). A comparative analysis of commonly employed technique is presented in Table 1.2. For this thesis work, special focus is given to solid-state nuclear magnetic resonance (SSNMR) spectroscopy, which is covered in-depth in Chapter 2.

1.3.3.1 Differential Scanning Calorimetry

DSC has been used as a very important technique for examining the thermal properties of ASDs like melting point, T_g event, enthalpy recovery, crystallinity, polymorphic transitions etc.³⁶ The operating principle involves heating the sample and the empty reference pan inside the furnace and measuring the temperature difference between them. The total heat flow can be described by:

$$\frac{dQ}{dt} = C_p \cdot \frac{dT}{dt} + f(t, T) \quad (1.1)$$

where dQ/dt is the total heat flow, C_p is the heat capacity of the sample, dT/dt is the heating rate and $f(t, T)$ is the kinetic heat flow. It can be seen from the equation 1.1 that total heat flow contains two components: a specific heat component (non kinetic) and a kinetic component, which is a function of time and temperature.³⁷ In a standard DSC setup, it is not possible to resolve these two components and hence modulated DSC (mDSC) is used. In mDSC experiments, a nonlinear waveform is superimposed on the linear heating rate. Thus, it possible to deconvolute the total heat flow into the reversing (C_p related) and non reversing (kinetic) contributions, where non reversing heat flow

signal is the difference between the total and reversing heat flow as shown in equation 1.2.³⁸

$$Q_{total} = Q_{reversing} + Q_{nonreversing} \quad (1.2)$$

mDSC improves the sensitivity and permits the investigation of important signals like T_g separately, which is usually depicted as a step change in heat capacity with a baseline shift in the thermogram. Reversing heat flow includes transitions like heat capacity, T_g , and melting, while non reversing heat flow includes transitions like enthalpic relaxation, cold crystallization, thermal decomposition, evaporation, etc.³⁹ Since T_g is a kinetic phenomenon, it is strongly dependent on scanning rate and the thermal history of the sample.³⁶ In practice, T_g is normally measured as the mid-point temperature at the half height of the step change. A typical mDSC thermogram is depicted in Figure 1.6.

Another important piece of information that can be obtained from mDSC measurements is the phase homogeneity in ASDs. In multicomponent systems such as ASDs, it is important to assess phase mixing, which can be confirmed from the number of T_g events observed in a thermogram. In general, the presence of a single T_g is indicative of a homogenous sample, whereas multiple T_g events are consistent with possible phase separation.³⁶ In addition, detecting phase mixing with mDSC requires individual T_g 's to be 10 °C apart and domains larger than 30 nm.^{23,40} Theoretical T_g values can also be compared with the predicted T_g values based on number empirical mathematical models available. Among them, Gordon-Taylor relationship has been widely used and any deviation from the predicted T_g behavior is suggestive of the presence of specific interactions between components.⁴¹

In recent years, the field of DSC has seen new advancements especially when fast heating or cooling rates are performed. Fast DSC, hyper DSC or flash DSC is helpful for cases where heating or cooling rate faster than the time scale of the event in interest is required.⁴² Thus, fast cooling rates and fast heating rates can be useful for *in situ* amorphization of rapidly crystallizing drugs and thermally unstable materials, respectively. Moreover, hyper DSC measurements permit better assessment of miscibility in ASDs, as fast heating rates do not affect the miscibility of the drug and polymer in the sample.

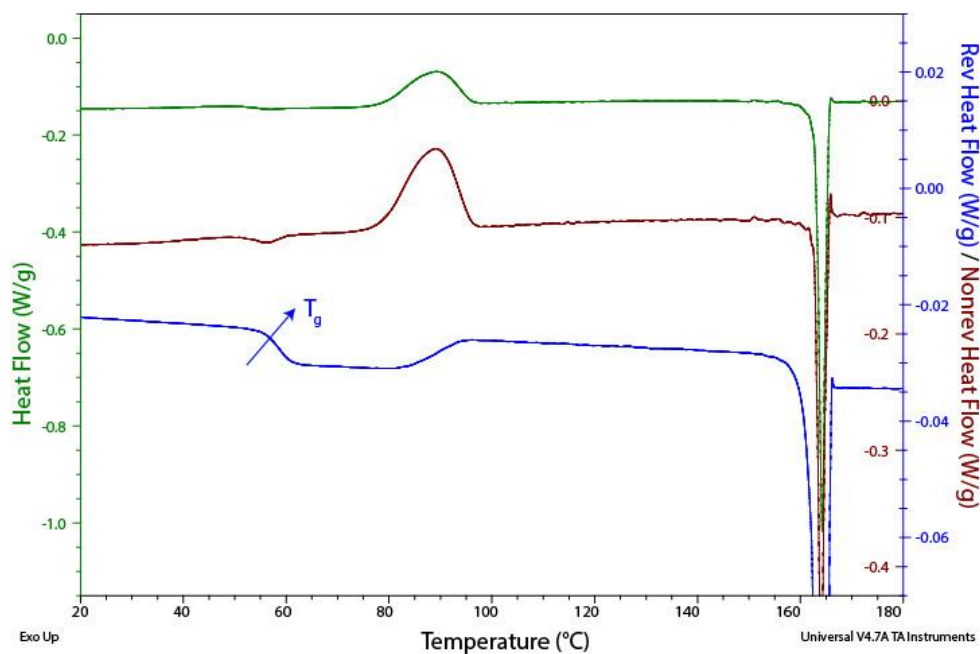


Figure 1.6. A typical mDSC plot showing the three signals corresponding to total heat flow (top), non reversible heat flow (middle), and reversible heat flow (bottom). The glass transition (T_g) is apparent in the reversible heat flow, whereas the crystallization exotherm is apparent both in reversible and non reversible heat flow. Melting is apparent in all three signals.

Table 1.2. Commonly used characterization techniques for ASDs.

Properties	DSC	TGA	FTIR/Raman	PXRD	SSNMR
Glass Transition (T_g) temperature	☑	☒	☒	☒	☒
Crystallinity	☑	☒	☑	☑	☑
Mobility	☑	☒	☒	☒	☑
Drug-polymer interactions	☒	☒	☑	☒	☑
Moisture/ Residual content	☒	☑	☒	☒	☒
Number of phases	☑	☒	☒	☒	☑
Hydration/ Dehydration	☒	☑	☒	☒	☒
Sample destructiveness	☑	☑	☒	☒	☒
Abbreviations					
DSC	Differential scanning calorimetry				
TGA	Thermogravimetric analysis				
PXRD	Powder X-ray diffraction				
FTIR/Raman	Fourier transform infrared spectroscopy and Raman spectroscopy				
SSNMR	Solid state nuclear magnetic resonance spectroscopy				

1.3.3.2 Thermogravimetric Analysis

In TGA analysis, the change in sample weight is measured as a function of time and temperature. It is useful for studying the thermal stability of a material, total volatile content, kinetics of drying or desolvation, as well as dehydration.⁴³ As with DSC, this method is sensitive to sample condition and experimental variables like heating rate. A typical TGA plot is illustrated in Figure 1.7. For spray dried ASDs, TGA is used

routinely to evaluate the residual solvent content in the samples.²⁷ Another useful application is found for stability dispersions samples, where the moisture uptake can be measured easily following equilibration of the sample at a particular condition.

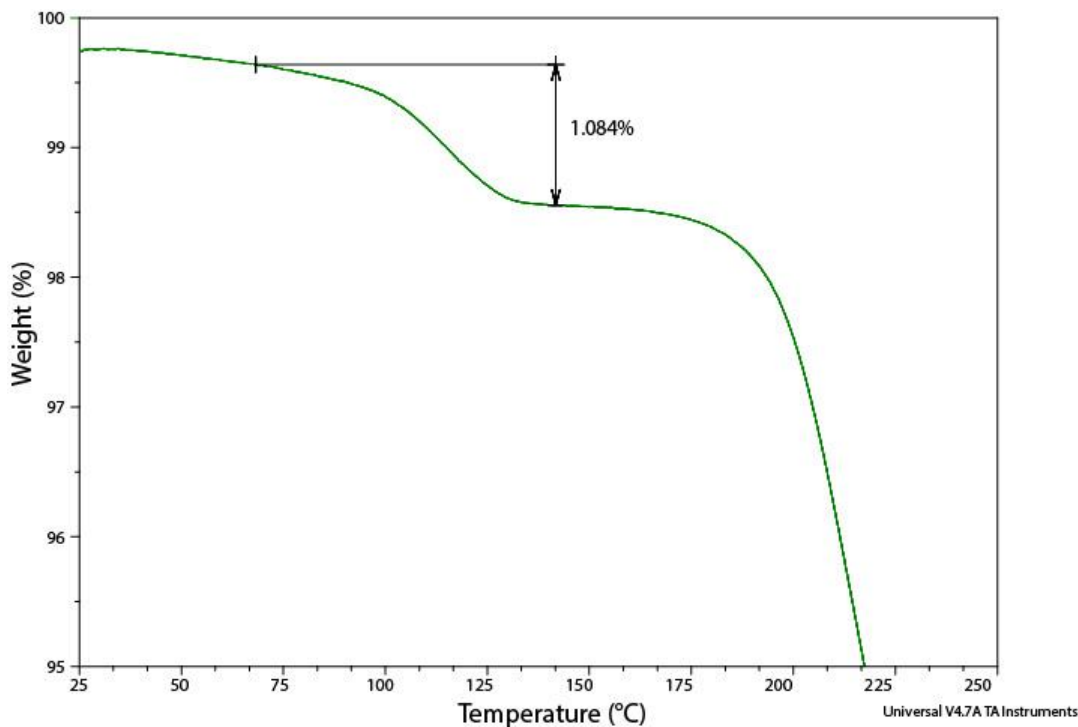


Figure 1.7. A typical TGA plot showing weight % as a function of temperature for a spray dried dispersion sample.

1.3.3.3 Powder X-ray Diffraction

PXRD is the most common technique for detecting crystallinity in ASDs and confirms the amorphous nature of dispersion samples, since it is relatively simple to operate, non-destructive and can provide both qualitative and quantitative information.²³ Its principle is based on Bragg's law, which can be described by the equation:

$$n\lambda = 2d \sin\theta \quad (1.3)$$

where n , λ , d and θ are an integer, the incident x-ray wavelength, the spacing between a set of lattice planes and the angle between the diffraction planes respectively. The common laboratory X-ray instruments use a monochromatic X-ray source (Cu or Mo) and measures a diffraction pattern by continuously increasing θ till the entire coverage of d satisfying Bragg's condition for each plane. Furthermore, the measurements are conducted in either reflection mode (Bragg-Brentano geometry) or transmission mode (Debye-Scherrer geometry). In a typical powder diffractogram, diffraction intensity is plotted against 2θ . For crystalline powder samples, Bragg peaks related to particular space groups are observed and this pattern of peaks would typically correspond to a unique signature of the material. In contrast, analysis of amorphous powder samples gives broad, diffuse scattering signals without distinct Bragg peaks (Figure 1.8). Amorphous materials are characterized by lack of long-range order and exhibit short-range periodicity (translational, orientational and/or conformational).⁴⁴ Thus, amorphous samples including ASDs portray a continuous "halo" pattern, which is the mean response of the average local order of an ensemble of short-range orders. In characterizing ASDs samples, PXRD analysis is useful for determining the residual crystallinity in samples after manufacturing or during stability studies. It should be noted here that typical detection limit for crystalline content is 5-10 % (w/w).²³ In addition, in recent years PXRD has been explored to characterize miscibility and phase structure in ASD using atomic pair distribution function (PDF).⁴⁵ Another recent advancement permit measurements to be performed under non ambient conditions with the introduction of variable temperature (VT) or humidity control set up to assess structural changes associated with recrystallization under stressed conditions.⁴⁶

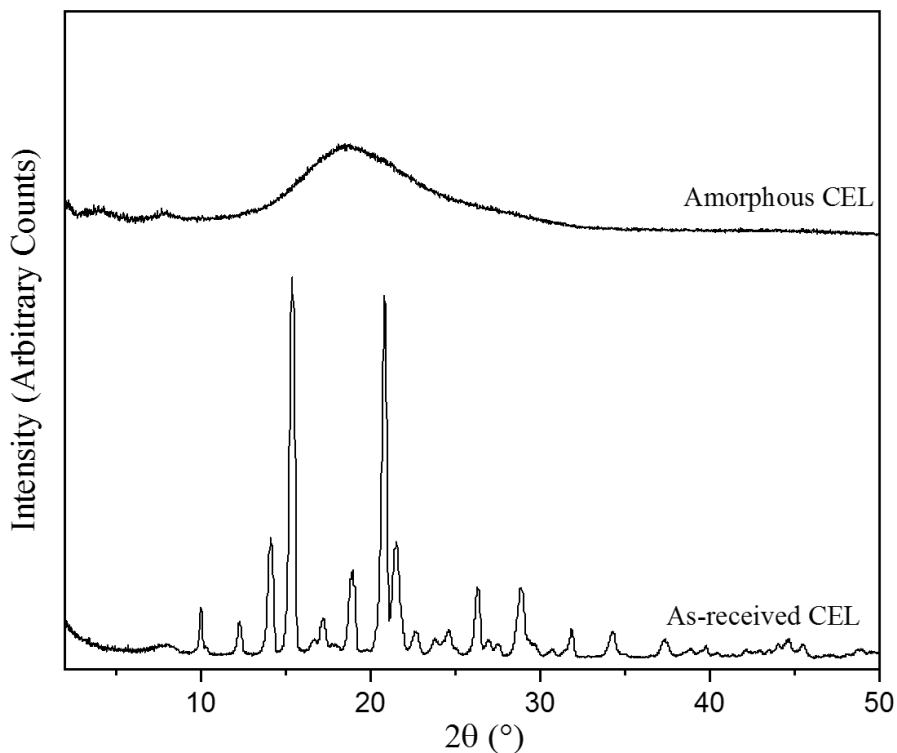


Figure 1.8. PXRD patterns for crystalline (as-received) and amorphous celecoxib (CEL). Amorphous celecoxib is devoid of characteristic Bragg peaks as seen in as received celecoxib.

1.3.3.4 Vibrational Spectroscopy

FTIR and Raman spectroscopy are two well-established techniques for probing molecular vibrations in pharmaceutical samples. These two techniques are complementary and have been used extensively for evaluating intermolecular interactions, phase transitions, polymorph identification, crystallinity and phase separation. The signal is seen as a result of change in polarizability of molecules in Raman spectrum, whereas in IR spectrum it originates from the change in the dipole moment of the molecules.²³ The IR spectrum consists of three regions: the near-IR (NIR) region between 0.78-2.5 μm , the mid-IR region between 2.5-50 μm and the far-IR region between 50-1000 μm . With the arrival of attenuated total reflectance (ATR) sampling

mode, it is possible to study bulk samples for routine analysis.⁴⁷ The mid-IR region has been employed to probe drug-polymer specific interactions via variations in peak shape and or position that are involved in molecular interactions especially through the analysis of O-H, N-H and C=O stretching frequencies. For instance, the presence of hydrogen bonding between the donor and acceptor groups can be inferred from the shift to lower wavenumbers and or peak broadening.⁴⁸ A number of publications highlight the applications of FTIR spectroscopy in the area of ASDs.^{49,50} Apart from the mid-IR region, NIR region has been found to be applicable especially for evaluating powder samples without saturation.⁵¹ In addition, NIR spectroscopy has been routinely used as a process analytical tool (PAT) for real time monitoring as well as for quantification of crystalline or amorphous content in a multi component system.⁵²

Raman spectroscopy is a powerful light scattering technique, which sometimes offers advantages in sampling and specificity when compared to IR spectroscopy.⁵¹ With shorter wavelengths of light being used it can be combined with microscopy. Confocal Raman microscopy has enabled detailed spatial analysis of pharmaceutical materials.^{53,54} For this thesis work, focus is given to FTIR spectroscopy for its more convenient experimental setup and data collection.

1.3.4 Physical Stability of Amorphous Solid Dispersions

For a robust ASD formulation, it is desired that the dosage form remains stable during the manufacturing and the shelf life. Moreover, stability is preferred in solution phase as well when the formulation dissolves upon expose to the biological fluids. In solution phase, ASDs provide a “spring + parachute” effect, thereby sustaining the supersaturation achieved for longer times to elicit its action (Figure 1.9).⁵⁵ If the “spring

+ parachute” effect fails, it is clear that the solubility advantage from ASDs will not be realized. Hence, it is of utmost importance to understand the factors affecting the physical stability of these enabling dosage forms. Before we list the factors affecting the physical stability, it is equally important to review the crystallization theory.

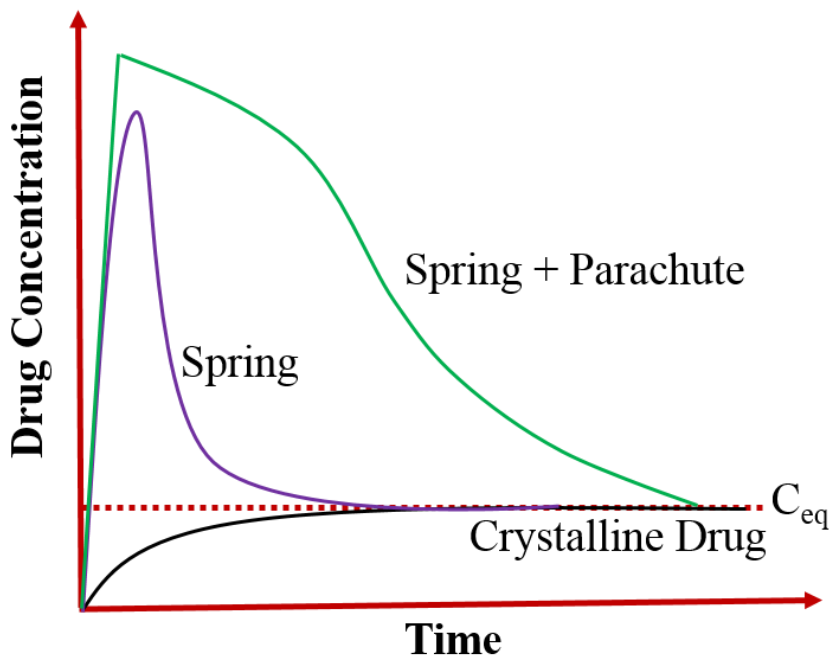


Figure 1.9. Illustration of “spring and parachute” mechanism. Adapted from reference.³⁰

1.3.4.1 Theory of Crystallization

Crystallization is a two-stage process: (1) nucleation and (2) crystal growth. During the nucleation stage, small number of molecules come together to form a nucleus. At the start of the nucleation process, the growth of the assembly is unfavorable. However, once the critical size is reached the process continues irreversibly.⁵⁶ As per the classical nucleation theory, the Gibbs free energy of nucleation consists of two terms given by the equation:

$$\Delta G(r) = \Delta G_v + \Delta G_s \quad (1.4)$$

where ΔG_v is the bulk free energy difference between the crystalline and amorphous phase and ΔG_s is the energy required to make a new interface. Here, ΔG_v is negative (favorable to nucleation) and ΔG_s is positive (unfavorable to nucleation).^{56,57} For a spherical nucleus, equation 1.4 can be written as:

$$\Delta G(r) = -\frac{4}{3}\pi r^3 \Delta G_v + 4\pi r^2 \gamma \quad (1.5)$$

where r is the radius of nucleus and γ is the interfacial tension between the nucleus and the supercooled liquid. It is clear from equation 1.5 that ΔG_v and ΔG_s are proportional to r^3 and r^2 respectively. The relationship of ΔG versus r is illustrated in Figure 1.10. The maximum of $\Delta G(r)$ corresponds to the critical nucleus size r^* , and defines the energy barrier for nucleation ΔG^* .

$$\Delta G^* = \frac{16\pi\gamma^3}{3\Delta G_v^2} \quad (1.6)$$

$$r^* = \frac{2\gamma}{\Delta G_v} \quad (1.7)$$

It is apparent from the above discussion that once the size of assembly reaches the critical radius the process becomes thermodynamically favorable and continues. In addition, ΔG_v can be estimated from enthalpy of fusion (ΔH_{fus}) and the melting temperature of the crystal (T_m).⁵⁸

$$\Delta G_v = \frac{\Delta H_{fus}(T_m - T)T}{T_m^2} \quad (1.8)$$

$$I = I_0 \exp\left[-\frac{\Delta G^*}{k_B T}\right] \quad (1.9)$$

It can be inferred from equation 1.9 that several variables influence the nucleation rate. Most importantly, the degree of undercooling ($T_m - T$) should increase the nucleation rate indefinitely. However, experimentally it is seen that the rate of nucleation increases with the degree of undercooling, reaches a maximum and then decreases (Figure 1.11). This behavior can be explained by the increase in the viscosity as the temperature decreases and thereby decreasing the molecular mobility.⁶⁰ To account for this behavior, an additional kinetic term (ΔG_a) is included in the equation 1.9, which defines the molecular mobility of crystallizing species.

$$I = I_0 \exp\left[-\frac{\Delta G^* + \Delta G_a}{k_B T}\right] \quad (1.10)$$

In practice, homogenous nucleation is seldom encountered and therefore presence of foreign bodies, impurities and surfaces may also influence the observed nucleation.⁶⁰

The second stage is the crystal growth, where the critical size nucleus increases in size resulting in the development of the crystalline phase. There are several ways molecules can join to the growing crystal surface. In the case of smooth crystal interfaces, models like screw-dislocation and two dimensional or surface nucleation growth have been employed. For pharmaceutical systems, the crystal growth rate U is given by⁶¹:

$$U = \frac{6aD}{\lambda^2} \exp\left(-\frac{\Delta S}{k}\right) \left[1 - \exp\left(-\frac{\Delta G_c}{k_B T}\right)\right] \quad (1.11)$$

where a is the molecular diameter, D is the diffusion coefficient, λ is the diffusion jump distance, f is the fraction of interface sites that are active growth sites, ΔS is the entropy difference between the two phases, k is the Boltzmann's constant, ΔG_c is the thermodynamic driving force for crystal growth and T is the absolute temperature. The observed nucleation rate and crystal growth rate is dependent on factors such thermodynamic, kinetic and intermolecular. Additionally, the external conditions like humidity, method of preparation, stress may also impact the overall crystallization tendency of amorphous dosage forms.⁶⁰

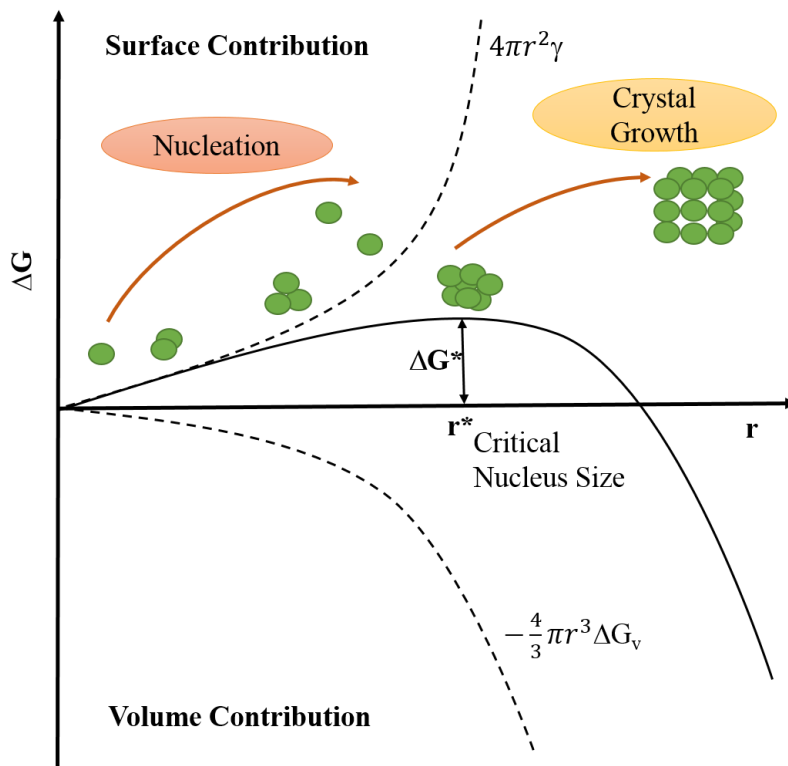


Figure 1.10. Schematic representation of free energy ΔG as a function of nucleus radius r . Adapted from the reference.⁶⁰

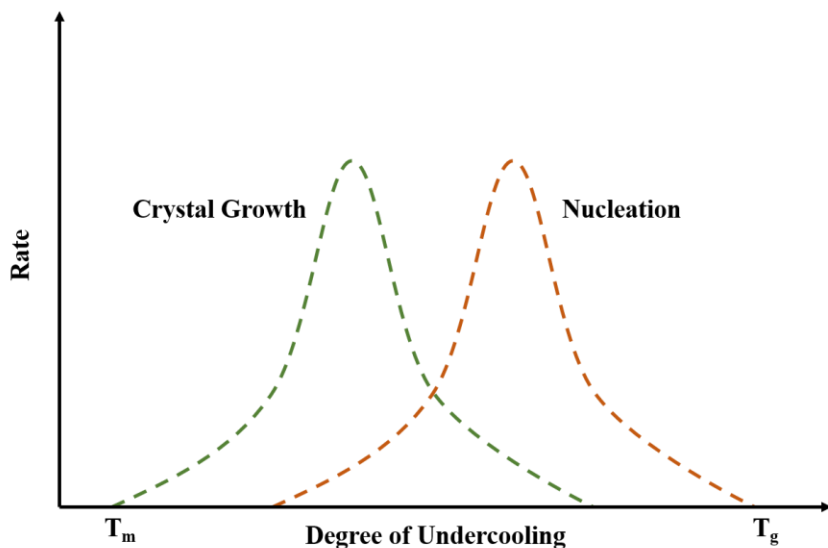


Figure 1.11. Schematic representation of nucleation rate and crystal growth rate as a function of temperature for undercooled melts. Adapted from reference.⁶⁰

1.3.4.2 Role of Polymers in Physical Stabilization

There are wide varieties of polymers that are employed in formulation of ASDs. Chemically, polymers consist of structural units known as “monomers” which are combined together to form a chain-like structural backbone. They can be classified on the basis of their charge into: (a) nonionic or non pH dependent and (b) ionic or pH dependent. Additionally, nonionic polymers can further be categorized into polyvinyl lactam polymers and cellulosic ethers. The ionic polymers are further subdivided into two sub groups: anionic and cationic polymers.⁶² A summary of common polymers with their important properties is listed in Table 1.3. Polymers can impact physical stability to a large extent and control factors like overall T_g of the system, mobility etc. Moreover, intermolecular interactions between the drug and polymer also play a crucial role in physical stabilization of ASDs.^{63,64} Thus, important performance

factors of polymers like T_g , thermal stability, solubility in solvents, drug-polymer miscibility should be considered in the polymer selection process. The list of commercially available solid dispersion products along with the polymer used is given in Table 1.4.

1.3.4.3 Glass Transition Temperature

ASDs are often characterized by their T_g , which is an important parameter dictating their physical stability.³⁶ In general, high T_g for the system is desired as it guarantees better stability at room temperature and under typical storage conditions. For drug-polymer mixtures, it is possible to predict the T_g of the blend through many models, which have been widely studied for ASDs. One popular quantitative model for the prediction of T_g of a multicomponent system is the Gordon-Taylor relationship. It uses the T_g values of the individual components and predicts the T_g of the dispersion intermediate in value of T_g 's of each component. It is based on the assumption that the free volumes of both components are additive and that the system lacks any specific interactions.⁶⁵ Based on these assumptions, the resultant T_g of the mix can be calculated by:

$$T_{gmix} = \frac{w_1 T_{g1} + k w_2 T_{g2}}{w_1 + k w_2} \quad (1.12)$$

where w_1 , w_2 are weight fractions of each component, T_{g1} and T_{g2} are their glass transition temperatures. The constant k is related to density and expansion coefficient and may be approximated using Simha-Boyer rule.⁶⁶

$$k = \frac{\rho_1 \Delta \alpha_1}{\rho_2 \Delta \alpha_2} \approx \frac{\rho_1 T_{g1}}{\rho_2 T_{g2}} \quad (1.13)$$

The Gordon-Taylor equation can be modified with a different value of k to define Couchman-Karaz relationship with the value k being defined by heat capacity change at T_g .⁶⁷

$$k = \frac{\Delta C_{p1}}{\Delta C_{p2}} \quad (1.14)$$

$$\frac{1}{T_{gmix}} = \frac{w_1}{T_{g1}} + \frac{w_2}{T_{g2}} \quad (1.15)$$

The component with the lower T_g is called a plasticizer whereas the component with the higher T_g is called an antiplasticizer. Polymers generally have higher T_g values than the drug and therefore act as antiplasticizers and increase the overall T_g of the system. The presence of moisture in the system can reduce the T_g to a significant extent. Water is a great plasticizer ($T_g \sim -140$ °C) and can lead to physical and chemical instability of product.⁶⁹

In practice, deviations from ideality have been reported.^{13,36} This signifies that mixing of components is non ideal and are classified as: positive and negative deviations (Figure 1.12). In the case of positive deviations where experimental T_g values are greater than the predicted T_g values result from lower net excess free volume upon mixing or the drug-polymer interactions (D-P) are stronger than the drug-drug (D-D) and the polymer-polymer (P-P) interactions. The negative deviations result from higher net excess free volume upon mixing or the drug-polymer interactions (D-P) are weaker than the drug-drug (D-D) and the polymer-polymer (P-P) interactions, which leads to experimental T_g values being lower than the predicted T_g values.

Table 1.3. Physicochemical properties of the polymers commonly used in ASDs.

Polymers	Classification	T_g (°C)	Solubility	Molecular weight (g/mol)	Hygroscopicity
Cellulosic Derivatives					
Hypromellose (HPMC)	Nonionic	170-180	Water Soluble	85,000-150,000	High
Hypromellose acetate succinate (HPMCAS)	Anionic	~125	> pH 5.0	~50,000	Low
Hypromellose phthalate (HPMCP)	Anionic	133-137	> pH 5.0	80,000-130,000	Medium
Cellulose acetate phthalate (CAP)	Anionic	~160-170	> pH 6.0	~2534	Medium
Polyvinyl lactam (co)polymers					
Polyvinyl pyrrolidone (PVP)	Nonionic	150-180	Water Soluble	30,000-100,000	High
Copovidone (Kollidon [®] VA64)	Nonionic	105-110	Water Soluble	45,000-70,000	High
Soluplus [®]	Nonionic	~70	Water Soluble	118,000	Medium
Methacrylate (co)polymers					
Eudragit [®] EPO	Cationic	~48	< pH 5.0	~47,000	Low
Eudragit [®] L100	Anionic	> 150	> pH 6.0	~125,000	Low
Eudragit [®] L100-55	Anionic	~110	> pH 5.5	~320,000	Low
Eudragit [®] S100	Anionic	> 130	> pH 7.0	~123,000	Low

Comments	
Soluplus [®]	Polyvinyl caprolactam-polyvinyl acetate-polyethylene copolymer
Eudragit [®] EPO	Poly(butylmethacrylate-co-(2-dimethylaminoethyl)methacrylate-co-methyl methacrylate) 1:2:1
Eudragit [®] L100-55	Poly(methacrylic acid-co-ethylacrylate) 1:1
Hypromellose	Hydroxypropyl methyl cellulose
Copovidone	Poly(vinyl pyrrolidone-co-vinyl acetate)

Furthermore, T_g is an important parameter for molecular mobility under typical storage conditions (15-30 °C). As a rule to predict the stability of ASDs under long term conditions, it has been suggested to store at 50 °C below T_g (T_g -50 rule).¹³ This rule suggests that a T_g of at least 75-80 °C is preferred for storing ASD products at ambient storage conditions.

1.3.4.4 Specific Interactions

Intermolecular drug-polymer interactions play a significant role in making the matrix stable. Additionally, drug-polymer interactions prevent drug precipitation upon *in vivo* dissolution by maintaining supersaturation. The drug-polymer interactions can exist as ionic interactions, hydrogen bonding, dipole-dipole interactions and van der Waals interactions. These interactions differ in their relative strength with ionic and van der Waal interactions being the strongest and weakest respectively (Table 1.5).⁷⁰ Many pharmaceutically grade polymers have hydrogen bond donors or acceptors in their structures, whereas many APIs also have chemical groups to form a hydrogen bond. Therefore, hydrogen bonding is one of the most common drug-polymer interactions observed in pharmaceutical systems.⁷¹⁻⁷³ For instance, Matsumoto and Zografi

demonstrated the role of polymers like PVP in disruption of indomethacin dimers for enhanced stability.⁷⁴ In a different study by Song et al., the role of polystyrene sulfonic acid was highlighted to stabilize two APIs, lapatinib and gefitinib, through ionic interactions.⁷⁵ The stronger drug-polymer interactions will result in better miscibility and favor a single phase ASD. Moreover, it has been reported that specific interactions like hydrogen bonding can inhibit nucleation process, thereby rendering the system more stable.⁷⁶

Moisture uptake by hydrophilic polymers can interfere with physical stability by promoting demixing of the drug and polymer by weakening the existing interactions. In a study published by Rumondor et al., it was postulated that the physical stability of dispersions is based on the interplay of two factors, the strength of drug-polymer interactions and hygroscopicity.⁷⁷ Additionally, water also reduces the T_g of the system and increase the mobility, which can further pose stability challenges.⁶⁹

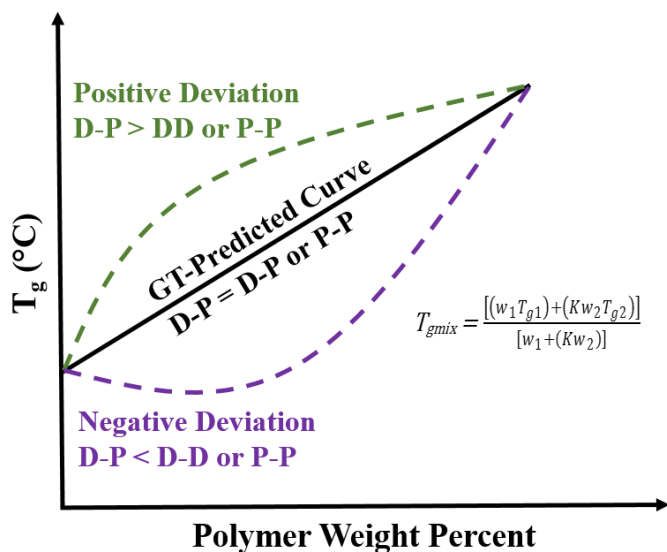


Figure 1.12. Deviations from the Gordon-Taylor equation; D represents drug and P represents polymer. Adapted from reference.¹³

1.3.4.5 Drug-Polymer Miscibility

The drug-polymer miscibility is one of the key factors that may impact the physical stability and performance of ASDs.³⁶ Amorphous miscibility can be defined in terms of the level of mixing which results in a single-phase system. It must be kept in mind that even a miscible single-phase system can undergo crystallization, as the system is still metastable relative to its crystalline form. Consequently, it is important to review some key aspects related to miscibility. Here, we shall address some thermodynamics principles for binary amorphous systems. The Gibbs free energy of mixing, ΔG_{mix} , at temperature T is given by:

$$\Delta G_{mix} = \Delta H_{mix} - T\Delta S_{mix} \quad (1.16)$$

where ΔH_{mix} and ΔS_{mix} are the enthalpy and entropy of mixing respectively. In general, mixing increases the disorder of the system, which makes the entropic term positive. Hence, the sign of ΔH_{mix} will dictate whether the mixing is favorable or unfavorable. Stronger drug-polymer interactions will result in loss of enthalpy, while stronger drug-drug and polymer-polymer interactions will lead to an increase in enthalpy. Therefore, exothermic mixing is attained when adhesive interactions are stronger and/or more numerous than cohesive interactions. Athermal mixing results when adhesive interactions are similar and/or extent to the cohesive interactions.⁷⁸ Thus, it is important to determine the nature of intermolecular interactions between the drug and polymer. Furthermore, it is desirable to predict the drug polymer miscibility based on predictive models such as the Flory-Huggins theory, which is a lattice based solution model

originally developed for polymers.⁷⁹ Based on this model, the free energy of mixing, ΔG_{mix} , can be described as:

$$\frac{\Delta G_{mix}}{RT} = n_d \ln \phi_d + n_p \ln \phi_p + \chi_{dp} n_d \phi_p \quad (1.17)$$

where R is the gas constant, T is the absolute temperature, $n_{d,p}$ are the number of moles the drug and the polymer respectively, $\phi_{d,p}$ are the volume fractions of the drug and the polymer, and χ_{dp} is the Flory-Huggins interaction parameter. The first two terms on the right side describe the entropic contribution (combinatorial entropy) and the last term signifies the enthalpic contribution to the total free energy of mixing of the binary system.⁸⁰ The enthalpic contribution will dictate the sign of the ΔG_{mix} and thus, the sign of χ_{dp} is the determining factor. It is therefore considered an indicator for drug-polymer miscibility. The smaller or more negative the Flory-Huggins interaction parameter, the stronger the intermolecular interaction between the drug and polymer. The value of χ_{dp} can be determined by the melting point depression approach and the solubility parameter approach.⁸¹ The details on how to obtain the value of χ_{dp} are discussed in Chapter 4. The drawbacks of the Flory-Huggins theory are that it does not account for the specific interactions and the energy for breaking the crystal lattice so that makes it only applicable for amorphous polymers.

Table 1.4. List of pharmaceutical solid dispersions available in the market.

<i>Product</i>	<i>API</i>	<i>Preparation Method</i>	<i>Company</i>	<i>Year of Approval</i>	<i>Carrier</i>
Cesamet®	Nabilone	Solvent Evaporation	Meda Pharmaceuticals	1985	PVP
Sporanox®	Itraconazole	Fluid Bed Bead Layering	Janssen Pharmaceuticals	1992	HPMC
Prograf®	Tacrolimus	Spray Drying	Astellas Pharma	1994	HPMC
Kaletra®	Lopinavir, Ritonavir	Melt Extrusion	AbbVie Inc.	2007	PVP/VA
Intelence®	Etravirine	Spray Drying	Janssen Pharmaceuticals	2008	HPMC
Zortress®	Everolimus	Spray Drying	Novartis Pharmaceuticals	2010	HPMC
Norvir®	Ritonavir	Melt Extrusion	AbbVie	2010	PVP/VA
Onmel®	Itraconazole	Melt Extrusion	Merz Pharma	2010	HPMC
Incivek®	Telaprevir	Spray Drying	Vertex Pharmaceuticals	2011	HPMCAS
Zelboraf®	Vemurafenib	Co-precipitation	Roche	2011	HPMCAS
Kalydeco®	Ivacaftor	Spray Drying	Vertex Pharmaceuticals	2012	HPMCAS
Orkambi®	Lumacaftor, Ivacaftor	Spray Drying	Vertex Pharmaceuticals	2015	HPMCAS /SLS

Table 1.5. Relative strength of drug-polymer interactions. Adapted from reference.⁷⁰

<i>Type of Interaction</i>	<i>Bond Energy (kJ/mol)</i>	<i>Approximate Relative Strength</i>
Ionic Interactions	850-1700	1000
Hydrogen Bonding	50-170	100
Dipole-dipole Interactions	2-8	10
van der Waals Interactions	~1	1

1.4 Thesis Overview

Chapter 1 deals with the introduction to the amorphous state, the importance of ASDs in drug development, the preparation methods, a brief outline of common analytical tools used for characterization of amorphous solids, and the factors affecting physical stability of ASDs. The central objective of my thesis research is to gain fundamental insights into the role of drug-polymer phase homogeneity and the factors impacting (specifically drug-polymer interactions) phase homogeneity and the physical stability of ASDs.

1.4.1 Chapter 2

In Chapter 2, the fundamentals and key features of SSNMR are introduced. It highlights the underlying principles of SSNMR, its advantages and limitations, and the applications pertaining to the field of ASDs. In addition, special focus has been given to the proton relaxation measurements and their importance in evaluating phase homogeneity in ASDs.

1.4.2 Chapter 3

Chapter 3 presents a case study involving felodipine (FEL) as a model drug with three polymers, poly(vinylpyrrolidone), or PVP, poly(vinylpyrrolidone-co-vinylacetate), or PVP/VA, and polyvinylacetate or PVAc. In this investigation, the role of drug-polymer hydrogen bonding and its impact on phase homogeneity is studied in-depth. A detailed comparative evaluation using DSC and SSNMR is presented on the model systems to investigate the phase homogeneity and hydrogen bonding interactions.

1.4.3 Chapter 4

Previously in Chapter 3, we studied the role of hydrogen bonding on phase homogeneity using felodipine as a model drug. Chapter 4 focuses on two structurally similar APIs nifedipine and felodipine, and their miscibility with Soluplus. In this chapter, both the aspects of miscibility: thermodynamic and kinetic are dealt with. Furthermore, differences in the hydrogen bonding patterns of two APIs will be discussed.

1.4.4 Chapter 5

So far through Chapters 3-4, we focused on the investigation of binary ASDs. In Chapter 5, we provide an in-depth comparative assessment of binary and ternary ASDs involving ketoconazole and two polymers, polyacrylic acid (PAA) and hydroxypropylmethyl cellulose (HPMC). The underlying molecular interactions are revealed in both the systems, which involved the identification and quantification of various species present. In addition, long-term physical stability is assessed for the samples at two different conditions.

1.4.5 Chapter 6

Chapter 6 describes the impact of different grades of hydroxypropylmethyl cellulose acetate succinate (HPMCAS) on the phase behavior of itraconazole dispersions. The dispersions are prepared using two approaches and the role of preparation method is evaluated at various drug loadings. The samples are subjected to accelerated physical stability to investigate the influence of temperature and moisture on the dispersions.

CHAPTER 2. SOLID-STATE NMR OF PHARMACEUTICALS: AN OVERVIEW

2.1 Introduction

Nuclear magnetic resonance (NMR) spectroscopy has been used in pharmaceutical analysis typically for (a) structure elucidation¹, (b) chirality analysis of drug substances², (c) protein studies³, and (d) determination of cellular metabolism⁴. In most of these applications, solution NMR spectroscopy has been employed. However, since approximately 80-90% of pharmaceutical products on the market exist in the solid form,² solid-state NMR spectroscopy has the potential to play a large role in the characterization of pharmaceutical solids, and recent developments in the field of SSNMR spectroscopy have made it amenable for a routine analysis for Pharm. Res. and development.

In the area of solid-state characterization of pharmaceuticals, several techniques apart from SSNMR spectroscopy are utilized, such as PXRD, FTIR spectroscopy, Raman spectroscopy, DSC, optical and electron microscopies, and TGA. Usually, a combined application of many of these techniques is required, depending on the aim and the nature of the system under study. However, in this chapter, the focus is on SSNMR, where we want to highlight the advantages and limitations of this technique and its application in characterization of ASDs.

It is important to mention that SSNMR is a non-destructive, non-invasive, flexible, quantitative, multinuclear technique that allows a variety of experiments to be performed to examine the physical and chemical states of both API and the excipients.⁵ Moreover, with the development of NMR crystallography, crystal structures may be solved through the combined use of X-ray diffraction and SSNMR.⁶ Furthermore,

SSNMR has the capability to selectively investigate individual component of ASDs and does not usually require any previous treatment of the sample.⁷ For all these aspects, SSNMR analysis can provide crucial and relevant information on pharmaceutical solids.

Unfortunately, there are a few limitations associated with this technique, which arise from its complexity, long experimental times and high operation costs.⁸ However, with recent advancements in SSNMR hardware and software these disadvantages may be overcome. There are many excellent reviews on the pharmaceutical applications of SSNMR available in the literature.^{2,9-11}

2.2 NMR-General Introduction

2.2.1 NMR Theory

The NMR phenomenon is based on the Zeeman interaction between the magnetic moment of the nucleus (μ) and the external magnetic field (B_0). The nuclear magnetic moment is described by the following equation:

$$\mu = \frac{\gamma I h}{2\pi} \quad (2.1)$$

where I is nuclear spin quantum number, γ is the magnetogyric ratio and h is Planck's constant. The Zeeman interaction takes place with nuclei having a non zero spin quantum number (I). When nuclei having a magnetic moment are placed into a static magnetic field, they start to precess around their z -axis. The frequency of this movement is termed Larmor frequency ω_0 and is proportional to the strength of B_0 and the magnitude of γ . For instance, ^1H in the magnetic field of 7.05 T will possess a Larmor

precession frequency of ~300 MHz, while ^{13}C in the same static magnetic field will have a Larmor frequency of ~75 MHz.

In the absence of external magnetic field, the nuclear magnetic moment is quantized into $2I + 1$ possible orientations or energy levels. Here, the discussion is limited to nuclei having spin $I = 1/2$ such as ^1H and ^{13}C . In this case, the nuclei can line up either parallel or antiparallel to B_0 . The low energy state is labeled α (+1/2) with magnetic moment aligned with the magnetic field, whereas the high energy state is labeled β (-1/2) with magnetic moment aligned opposite to the magnetic field (Figure 2.1). The transition between these states give rise to observable NMR signal and the population difference between these states is governed by the Boltzmann distribution:

$$\frac{N_\beta}{N_\alpha} = e^{-\Delta E/kT} \quad (2.2)$$

where N is the number of nuclei present in each spin state, $\Delta E = \gamma h B_0 / 2\pi$, k is the Boltzmann constant, and T is the absolute temperature. It can be seen from this relation that higher magnetic field spectrometers lead to a larger population difference and hence a stronger signal, and signal-to-noise ratio (S/N).

The respective energy is provided by applying a radio frequency pulse (rf), B_1 , with a frequency of about ω_0 along a direction perpendicular to B_0 . This causes the net magnetization to precess in the x - y plane of the laboratory frame at an angle governed by the intensity and duration of the rf pulse. This nuclear precession generates an alternating current in a coil surrounding the sample, whose evolution with time represents the NMR signal. The signal or free induction decay (FID) is collected in the time domain and then subjected to Fourier transformation to give rise to the NMR spectrum.

2.2.2 The Chemical Shift

The nucleus is surrounded by electrons that generate a small local field and shield the local magnetic field experienced (B_{loc}) by the nucleus (Figure 2.2). The strength of the B_{loc} depends on the specific electron density and this shielding give rise to the phenomenon of chemical shift. Therefore, chemically non-equivalent nuclei experience different magnetic fields causing them to precess at different frequencies and in the NMR spectrum they are revealed as well separated peaks. In the NMR spectrum, the x -axis is commonly expressed in terms of chemical shift (δ) having the units in parts per million (ppm). This scale is considered useful because it is independent of the strength of B_0 and the location on the scale is relative to the location of a reference substance whose δ is conventionally taken to be zero. In the case of ^{13}C and ^1H , tetramethylsilane (TMS) is used as a reference.¹²

Generally, B_{loc} is the product of B_0 and $(1 - \sigma)$, where σ is the element of the shielding tensor. In a molecule, electrons are distributed anisotropically and that makes the value of σ dependent upon the molecular orientation with respect to B_0 . For molecules in liquid state, where fast and isotropic Brownian molecular tumbling exists, the anisotropy averages to zero. However, in solids where molecular tumbling is absent and consequently the resonance frequency for each nucleus is slightly different. This implies that for a “powder” sample, where all possible molecular orientations occur, the different δ values result in a very broad resonance lines and subsequent loss of resolution.

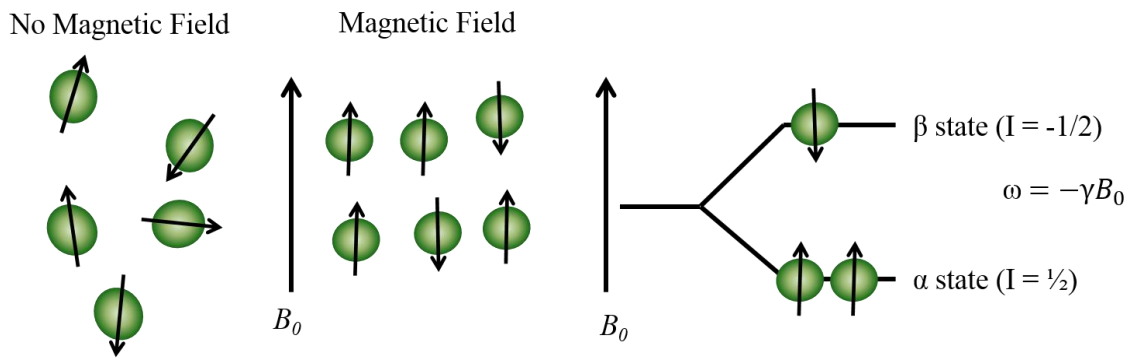


Figure 2.1. Schematic depicting the response of nuclear spins in the presence of the external magnetic field. The splitting of nuclear spin states is also shown.

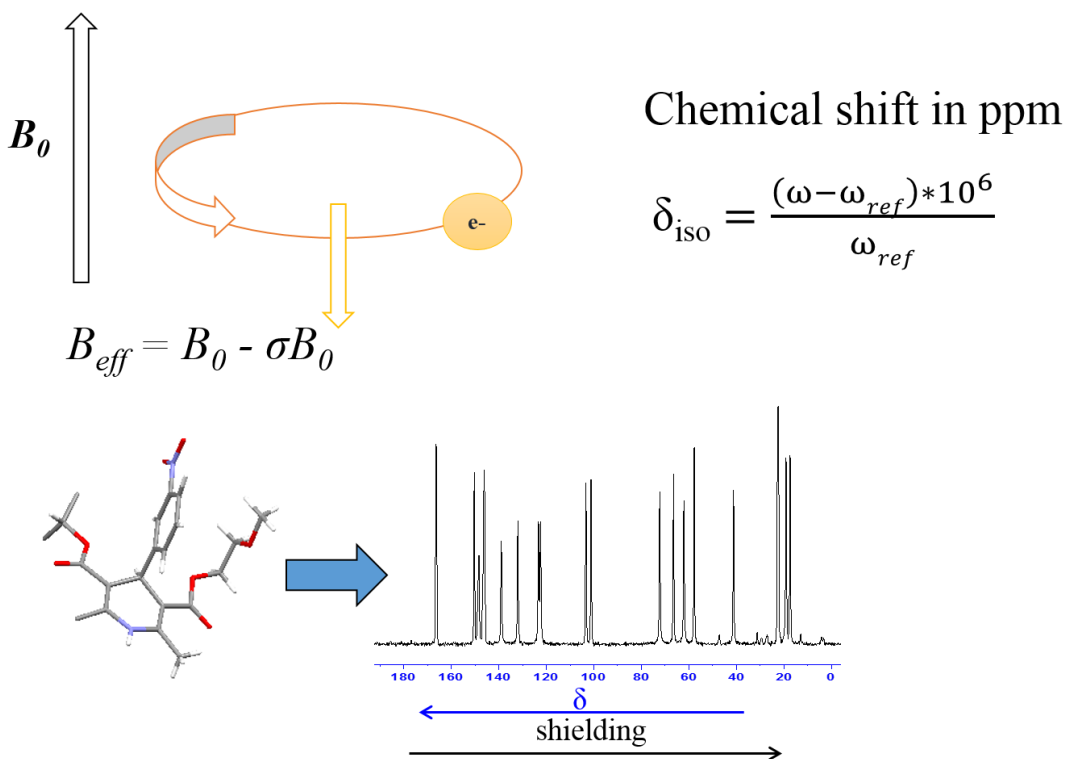


Figure 2.2. Illustration of the magnetic shielding of a nucleus by surrounding electrons and the effective magnetic field experienced by the nucleus.

2.3 SSNMR Principles and Techniques

In the early 1950s, NMR spectroscopy was essentially used as a solution based technique, where unlike solids a high-resolution spectra could be acquired. Through the 1950s and 1960s, researchers were devoted to advancing the field of SSNMR. As discussed in the previous section, the spectrum obtained for a solid sample showed line broadening, and that limited the application of SSNMR. It was not until the late 1970s that Schaefer et al. were able to demonstrate the utility of ^{13}C SSNMR for solid polymer samples with the help of cross polarization (CP) and magic angle spinning (MAS).^{13,14} In this section, we will review the basic principles involving a SSNMR experiment and some other useful techniques, especially those used in ASDs research.

2.3.1 Dipolar Coupling and High-Power Proton Decoupling

On a molecular level, the magnetic dipoles of neighboring nuclei perturb the magnetic field experienced by surrounding nuclei. This result in the direct magnetic coupling of two nuclei directly thorough space and can occur on a heteronuclear and homonuclear base. It is important to note that the extent of this depends upon the magnetic moments of nuclei, the distance r between them, and their orientation with respect to B_0 . Thus, this interaction is significant for spin $\frac{1}{2}$ nuclei with large magnetic moments such as ^1H and ^{19}F . In the pharmaceutical domain, samples are abundant in carbon and proton nuclei, and that makes heteronuclear ^{13}C - ^1H coupling a significant contributor to line broadening (based on their natural abundance, Table 2.1). In fact, heteronuclear ^{13}C - ^1H and homonuclear ^1H - ^1H coupling in the solid state are generally in the order of 50 kHz and 100 kHz, respectively. The heteronuclear ^{13}C - ^1H coupling can be suppressed by applying high decoupling fields at the ^1H Larmor frequency, which cause

^1H spins to flip between the α (+1/2) and β (-1/2) spin states so that the dipolar interactions are averaged to zero.⁹ Even after eliminating heteronuclear dipolar interactions ^{13}C - ^1H , the broad lines are still seen in SSNMR spectrum primarily due to chemical shift anisotropy (CSA).

2.3.2 Chemical Shift Anisotropy and Magic Angle Spinning

As mentioned previously, the molecules in the solid state exist at fixed orientations relative to B_0 and which results in distribution of chemical shifts termed as chemical shift anisotropy (CSA). The concept of magic angle spinning (MAS) was originally proposed by Andrew et al. in 1958 to remove line broadening for solid samples.¹⁵ The idea can be understood by taking into account the nature of shielding tensor, σ , which can be divided into two components- an isotropic component and an anisotropic component as described by the following equation:

$$\sigma_{obs} = \sigma_{iso} + (3 \cos^2 \theta - 1) \sigma_{aniso} \quad (2.3)$$

where θ is the angle made between the internuclear vector and B_0 . By spinning the sample at “magic angle” of 54.74° or $54^\circ 44'$ causes the anisotropic term to reduce to zero and only the isotropic chemical shift is retained. Thus, spinning the sample at an angle equal to the magic angle at sufficient high speed (sample rotation greater than the magnitude of CSA) will average the orientation dependent interactions (Figure 2.3).

If the sample spinning rate is less than the width of CSA, spinning side bands (SSB) are generally observed at intervals equal to the spinning speed. These SSB contain intensity from the parent peak and can potentially overlap with the other signals, which complicate the spectral interpretation. Generally, they are easily identified by changing

the spinning rate and observing which signals change in frequency. Moreover, specific pulse sequences like total suppression of spinning sideband (TOSS) can be incorporated to minimize their occurrence.¹⁶

Table 2.1. NMR frequency listing for a few common nuclei found in the pharmaceutical samples.

<i>Nucleotide</i>	<i>Spin</i>	<i>Natural Abundance</i>	<i>NMR frequency (MHz) at a field (T) of</i>	
			<i>5.87</i>	<i>11.74</i>
¹ H	1/2	99.98	250.00	500.00
¹³ C	1/2	1.10	38.38	76.75
¹⁵ N	1/2	0.37	25.33	50.66
¹⁹ F	1/2	100	235.19	470.39
³¹ P	1/2	100	101.20	202.40
¹⁴ N	1	99.63	18.06	36.12
¹⁷ O	5/2	3.7*10 ⁻²	33.89	67.78

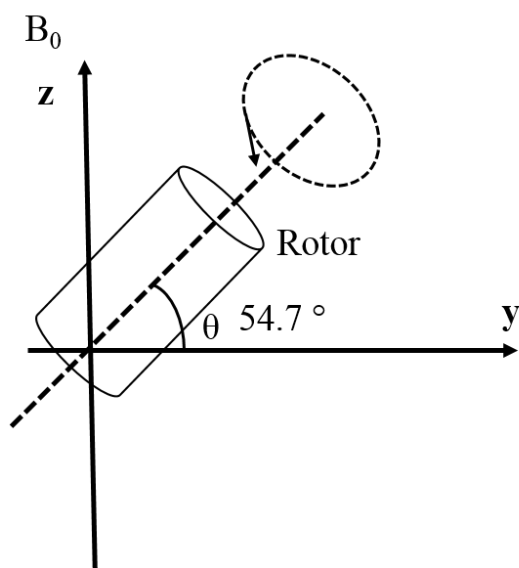


Figure 2.3. A schematic of magic-angle spinning.

2.3.3 Cross Polarization

In general, SSNMR experiments lack sensitivity because of a nearly equal population distribution of the two spin states for spin 1/2 nuclei. Moreover, for solid samples, the sensitivity is decreased further due to the low natural abundance of the ^{13}C nuclei (~1%), which constitute the majority of the sample chemically. In a SSNMR experiment, owing to the long T_1 time of rare spin nuclei (^{13}C or ^{15}N), very long acquisition times may be needed for a reasonable S/N ratio. In order to overcome this issue, the technique of cross polarization (CP) was first implemented by Pines et al.^{17,18} The basic idea of this technique is that bulk magnetization is transferred from the abundant spin system having short T_1 (^1H) to the rare spin system (^{13}C or ^{15}N) with long T_1 .

As per the principles of quantum mechanics, any polarization transfer between the two spin systems can take place only when ΔE between the energy levels of the two participating spin systems be of equal magnitude. This is the case when the Hartmann-Hahn condition is satisfied.

$$\Delta E_H = \gamma_H B_{1H} = \gamma_X B_{1X} = \Delta E_X \quad (2.4)$$

where, γ_H is the gyromagnetic ratio of ^1H and B_{1H} is the ^1H - rf -field while B_{1X} and γ_X are the respective parameters for X-spin system. The CP pulse sequence consists of simultaneous irradiation of the ^1H and X spin systems by variable magnetic fields through a locked rf -pulse during contact time, t_c (Figure 2.4). The magnitude of the spin locking fields B_{1H} and B_{1X} is chosen correctly to satisfy the Hartmann-Hahn condition. Once this condition is fulfilled, the dilute X spin system takes the magnetization from the

abundant ^1H spins. As a last step in the sequence, the NMR signal of the X spins is then measured during the acquisition time under ^1H high-power decoupling.

The advantage from the CP pulse sequence is two fold: first, signal enhancement of X spins, which is determined by the gyromagnetic ratios of participating spin systems ($\sim 4x$ in ^{13}C experiments); and second, reduction of the delay time between pulse sequences, since only the ^1H spin-lattice relaxation remains relevant, which corresponds to a greater number of scans translating to higher S/N.⁹

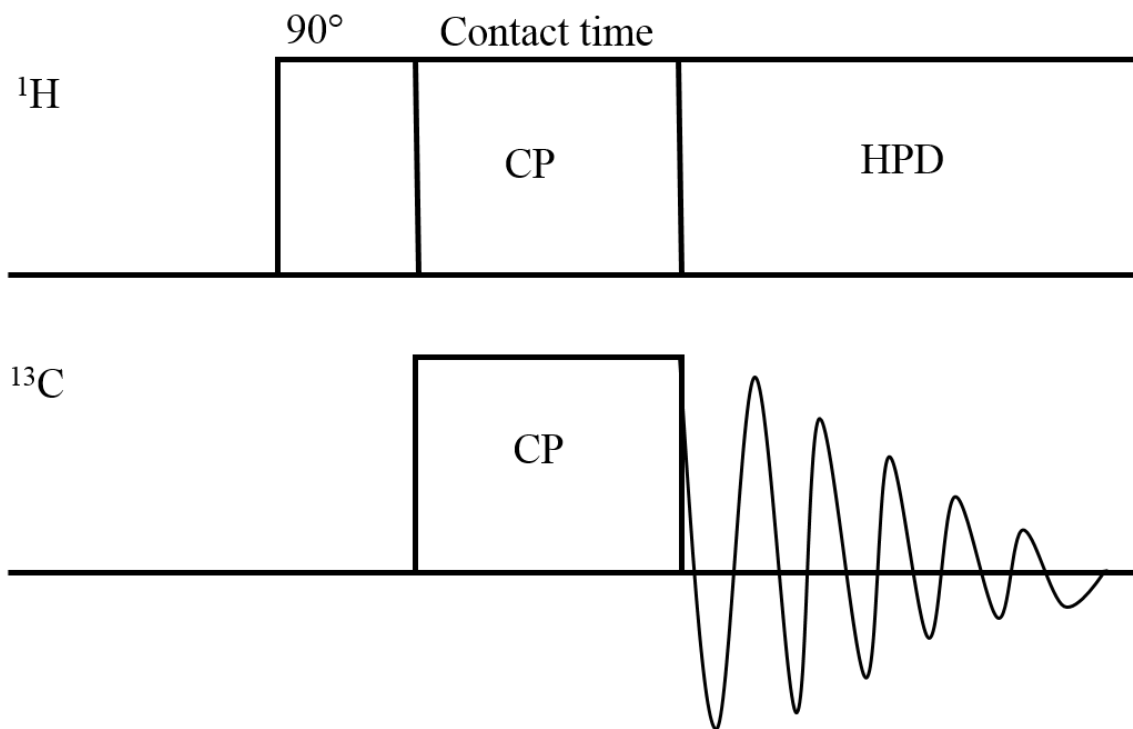


Figure 2.4. A scheme of cross polarization pulses sequence. The rectangles represent *rf* pulses, while the oscillating curve represents the FID.

2.3.4 Relaxation

After the termination of *rf* pulse the net magnetization of the ensemble of spins begins to relax back to their equilibrium values. The process of returning to equilibrium

is termed as *relaxation*.¹⁰ Broadly speaking, there are three important relaxation processes briefly described below:

1. *Spin-lattice relaxation* (also known as longitudinal relaxation) – This is defined as the amount of time taken to regain equilibrium of the z component of M following a perturbation. The term “lattice” denotes the surroundings, which receive the energy in the process to re-establish the equilibrium. The process is generally described by an exponential relationship with a relaxation time constant, T_1 , given by the following equation:

$$M_z(t) - M_0 = [M_z(0) - M_0] \exp\left(-\frac{t}{T_1}\right) \quad (2.5)$$

where $M_z(0)$ is the magnetization in the z direction after the perturbation. The time T_1 is the inverse of a first-order rate constant for the relaxation process. For multipulse experiments, the optimum recycle delay of $5 \times T_1$ is suggested in order to observe the fully relaxed signal after each pulse.¹⁹

2. *Spin-spin relaxation* (also known as transverse relaxation) – This is related to the xy component of M and describes its decay to zero. It is given by the time constant, T_2 and in general for solids $T_1 \gg T_2$, but although in liquids they are often of the same order of magnitude. For example, for protons T_2 is typically in the range of 10-100 μs whereas T_1 is typically in the range 0.1-100 s.¹⁰
3. *Spin-lattice relaxation in the rotating frame* – This is described as the return to equilibrium of transverse magnetization kept aligned to a given direction by a “spin-lock” pulse. It is denoted by $T_{1\rho}$.

2.4 Applications - Amorphous solid dispersions

In the previous sections, we discussed the fundamentals of SSNMR and other key concepts related to the experiments. This section is devoted to the applications of SSNMR in the field of ASDs. In this regard, SSNMR stands out among currently available techniques in probing the structural and dynamic behavior of individual components, as well as the intermolecular interactions and the phase mixing on a molecular level.⁵ With the advancements in the area, it is possible to investigate various subtle but important features pertaining to ASDs in terms of the state of the amorphous API, quantification of hydrogen bonding, distance of hydrogen bonds, and homogeneity on the nanometric scale.^{12,20-22} In the following sections, we will discuss and highlight various SSNMR methodologies utilized in exploring drug-polymer homogeneity and molecular interactions for complex systems like ASDs.

2.4.1 Proton Relaxation Times and Spin Diffusion

SSNMR provides very useful tools for measuring the degree of mixing among each component in systems like ASDs via proton relaxation times. The proton relaxation times: spin-lattice relaxation time ($^1\text{H } T_1$) and spin-lattice relaxation time in the rotating frame ($^1\text{H } T_{1\rho}$) are commonly used to provide valuable information about the heterogeneity of the sample. These relaxation times are affected by the process of spin diffusion.¹⁹ Basically, spin diffusion is an outcome of dipolar coupling and in a network of dipolar-coupled spins, the spatial diffusion of nuclear magnetization occurs from a locally excited site to distant sites. In case of two components close together spatially, proton magnetization within them is averaged by spin diffusion. Thus, for a homogeneous sample the proton relaxation times tend to average to a common value,

whereas a non-uniform relaxation behavior is detected for each component for a heterogeneous sample. The proton relaxation times are usually measured using a high-resolution CP method and are conveniently detected via ^{13}C nucleus to achieve spectral resolution of various components. The pulse sequences used to record $^1\text{H } T_1$ and $^1\text{H } T_{1\rho}$ are listed in Table 2.2. For methods employed to obtain $^1\text{H } T_1$ times, the saturation recovery sequence was employed for the experiments described in this thesis work. In a typical saturation recovery experiment, the recovery of nuclear magnetization to the equilibrium after perturbation via a train of $\pi/2$ pulses is observed. In order to follow the build up of magnetization in the direction of external magnetic field B_0 , M_z is determined after various delay times t by applying $\pi/2$ pulses to flip the instantaneous magnetization $M_z(t)$ in the xy plane and observe the subsequent signal. The signal recovery is fitted to the following function:

$$M_z(t) = M_0(1 - e^{-\frac{t}{T_1}}) \quad (2.6)$$

where, M_0 is the equilibrium magnetization and T_1 is the spin-lattice relaxation time constant. In the case of $^1\text{H } T_{1\rho}$ pulse sequence, spectra are recorded as function of the spin-lock time and the signal decay is fitted to the following function:

$$M_z(t) = M_0 e^{-\frac{t}{T_{1\rho}}} \quad (2.7)$$

where, M_0 is the equilibrium magnetization and $T_{1\rho}$ is the spin-lattice relaxation in rotating frame time constant. The pulse sequences for measuring $^1\text{H } T_1$ and $^1\text{H } T_{1\rho}$ are shown in Figure 2.5 and 2.6.

Table 2.2. List of pulse sequences used for measuring relaxation times.

<i>Pulse Sequence</i>	<i>Relaxation Time</i>	<i>Nucleus</i>
Inversion recovery	T_1	H or X
Saturation recovery	T_1	H or X
Inversion recovery with CP	T_1	H
“Torchia” method	T_1	X
Variable spin-lock	$T_{1\rho}$	H or X
Delayed contact	$T_{1\rho}$	H
Variable spin-lock with CP	$T_{1\rho}$	X

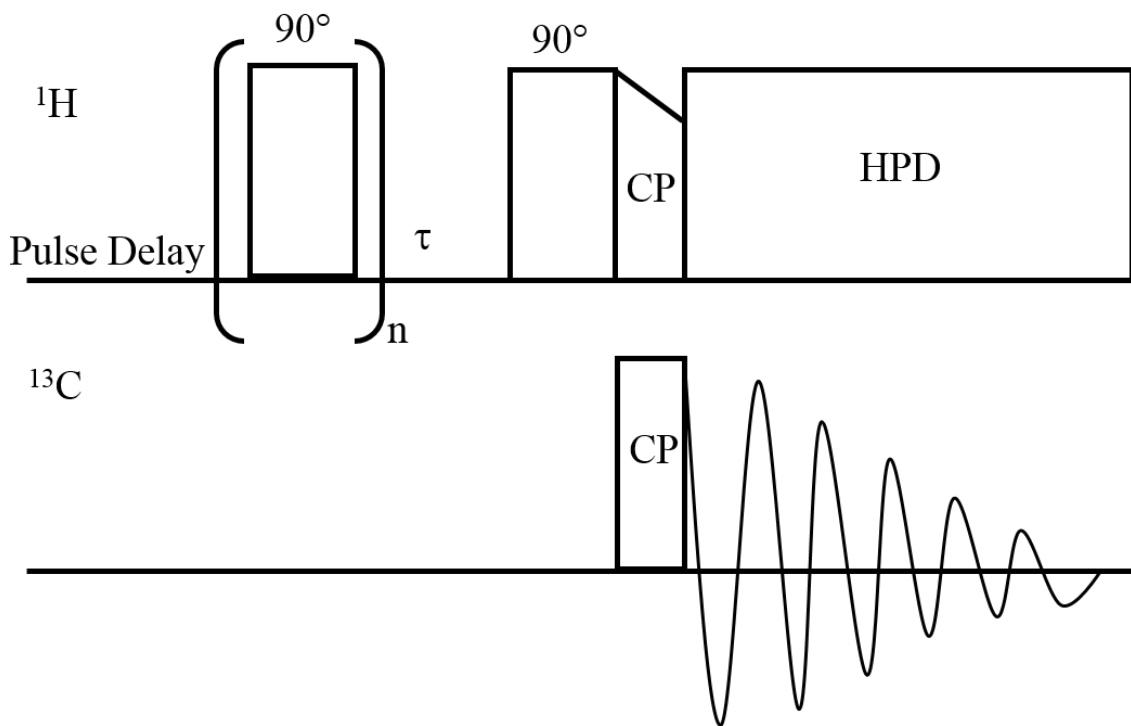


Figure 2.5. A scheme of pulse sequence for ^1H T_1 using saturation recovery.

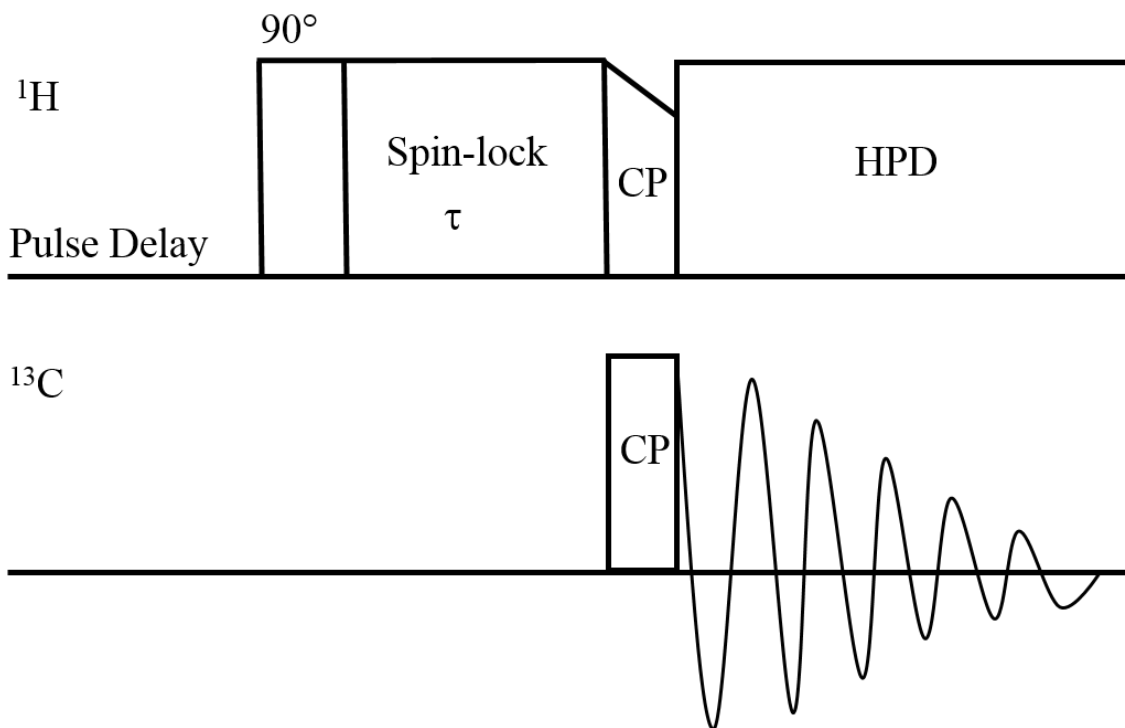


Figure 2.6. A scheme for pulse sequence for measuring ^1H $T_{1\rho}$.

A useful semiquantitative estimation of domain sizes can be obtained from the average diffusive path length L :

$$L = (6DT)^{1/2} \quad (2.8)$$

where, D is the spin diffusion coefficient and T is the time ^1H T_1 or ^1H $T_{1\rho}$. In this relationship, D is dependent upon the average proton-proton distance and the strength of the dipolar interaction. In the current work, the value of D was taken to be 10^{-12} cm^2/s .²³ If the diffusive path length is smaller than the domains in the sample, protons for each component will decay independently of one another and different values of relaxation time are measured for each component. Conversely, if the diffusive path length is larger than the size of domains in the sample, a single relaxation is obtained for each component. The main difference between ^1H T_1 and ^1H $T_{1\rho}$ is that they probe molecular

motion of different timescales. In general, $^1\text{H } T_1$ relaxation time is sensitive to motions occurring on MHz scale, whereas $^1\text{H } T_{1\rho}$ is sensitive to motions occurring on kHz scale.¹⁰ Thus, $^1\text{H } T_{1\rho} \ll ^1\text{H } T_1$ so spin diffusion has an influence over smaller distances than it does for $^1\text{H } T_1$.

Since $^1\text{H } T_1$ is typically of the order of 5 s and $^1\text{H } T_{1\rho}$ of the order of 50 ms, the maximum diffusive path lengths are about 50 nm and 5 nm respectively.²⁴ Based on these typical values and assuming that component relaxation times are sufficiently different, there exist three possibilities for phase homogeneity in ASDs:

- (1) An ASD is classified as “homogenous” when common values for $^1\text{H } T_1$ and $^1\text{H } T_{1\rho}$ are observed and any domains must be smaller than 5 nm.
- (2) An ASD is classified as “partially homogenous” when a common $^1\text{H } T_1$ but multiple $^1\text{H } T_{1\rho}$ values are obtained and for such a system the average domain size is between 5 and 50 nm.
- (3) An ASD is classified as “non-homogenous” when multiple $^1\text{H } T_1$ and $^1\text{H } T_{1\rho}$ values are measured for each component and the average domain size is larger than 50 nm.

The main advantages of using SSNMR to characterize phase homogeneity in ASDs are listed below:

- (1) The domain size accessible to SSNMR can go below 30 nm²⁵, which is below DSC limit of detection. Hence, it is well-suited for investigating nano-phase separation in ASDs beyond the limits of thermal analysis.
- (2) The information obtained is usually very detailed and an accurate estimation of domains can be easily made.

- (3) Using CP, it is easier to distinguish the relaxation behaviour of each component and can be resolved without decomposing the proton relaxation curves.

2.4.2 Molecular Interactions

In the study of ASDs, another important area for applications of SSNMR is molecular interactions. Very often, molecular interactions play a significant role in physical stabilization of ASDs and hence their detailed characterization is usually required. For complex systems like ASDs, SSNMR analysis can reveal the presence of interactions either directly through the changes in the high-resolution ^{13}C spectra or indirectly via detecting the changes in parameters sensitive to the dynamics of the system. Usually changes in ^{13}C CP/MAS spectra can reveal the presence of specific interactions such as hydrogen bonding between the groups when compared with neat drug and polymer or physical mixtures. In systems where hydrogen bonding exists, deshielding is observed in 1D ^{13}C spectra as a result of change in local environment with isotropic chemical shift moving toward higher values.²⁶ In pharmaceutical systems, typical hydrogen bonding involve groups such as $-\text{OH}$, $-\text{NH}$ and $-\text{SH}$, where the labile protons attached to the heteroatoms act as donors. For such cases, X CP/MAS experiments can serve as a special probe to study drug-polymer H-bonding. The nucleus like ^{19}F offers several advantages like 100% natural abundance, short acquisition times, high sensitivity and no interference from excipients.²⁷ This makes ^{19}F MAS experiments highly desirable for fluorinated APIs. In this thesis work, we acquired ^{15}N CPMAS spectra for ketoconazole dispersions, where changes in the local environment of nitrogen were monitored in the presence of polyacrylic acid. The drawbacks that come with ^{15}N SSNMR experiments are long acquisition times and low sensitivity.²⁸ This issue may be

solved by isotopic enrichment. The other potential option is to utilize quadrupolar nuclei like ^{14}N to circumvent the need of isotopic labelling.²⁹ Recently, quadrupolar nuclei (spin $> 1/2$) such as ^{14}N , ^{35}Cl , ^{17}O have been used to study the change in hydrogen bond geometry in ASDs.^{30,31} In a study done by Vogt et al., a computational method involving the comparison of isotropic ^1H chemical shift of a single molecule with that of its crystal structure was used to assess the relative strength of hydrogen bonding interactions in ASD of diflunisal.³¹

The advancements in high resolution two-dimensional SSNMR involving 2D correlation experiments allow excellent opportunities to investigate spatial proximities between chemically distinguished nuclei. In these experiments, homonuclear and heteronuclear dipolar decoupling pulse sequences are used in order to obtain a much-improved resolution in comparison to standard one-dimensional experiments. Homonuclear decoupling sequences such as frequency switched Lee-Goldburg (FSLG) or phase-modulated Lee-Goldburg (PMLG) are incorporated with MAS in CRAMPS (combined rotation and multiple pulse sequence) to obtain high resolution two dimensional spectra. Pham et al. demonstrated the applicability of HETCOR experiments in conjunction with TOSS for exploring miscibility and molecular interactions for multiple model systems involving binary and ternary ASDs.¹²

2.4.3 Detection and Quantitation of Amorphous Phases

One criterion to confirm the presence of amorphous phase is through broader resonances as shown in the Figure 2.7. In amorphous samples, molecules can exist in multiple conformations resulting in broad distribution of isotropic chemical shift values for each chemically inequivalent nuclear site. In addition, comparing line widths with the

crystalline phase may be useful evidence of amorphization. For the cases where crystalline and amorphous phase coexist within the same sample, the detection of amorphous phase may be difficult due to likely overlap with crystalline peaks and the weak intensity of the amorphous phase peaks. In such a situation, one potential strategy is to decrease the recycle delay between two consecutive transients in a regular CP/MAS experiment. Decreasing the recycle delay results in a partial suppression of crystalline signals, and subsequently favoring the amorphous signals.

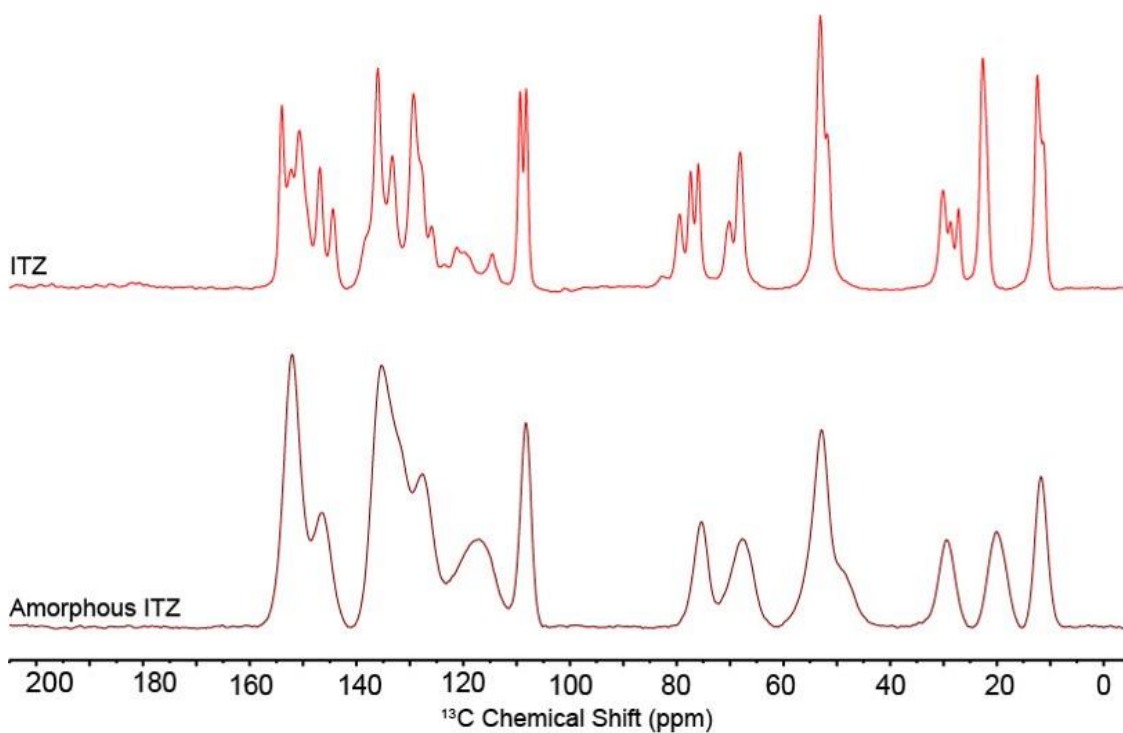


Figure 2.7. A comparison of ¹³C CP/MAS spectra of crystalline and amorphous itraconazole (ITZ).

Once the presence of the amorphous phase is confirmed, it is important to quantify it as well from a pharmaceutical standpoint. There are several case studies published in the literature where SSNMR has been used for the quantification of amorphous systems.³²⁻³⁴ The NMR signal is proportional to the number of nuclei,

provided that the spectrum is suitably recorded. Generally, it is assumed that CP/MAS spectra are not quantitative, as the transfer of magnetization does not occur uniformly for each carbon during the CP step.³² In order to obtain quantitative information from ¹³C CP/MAS spectra, it is important to carefully select the contact time for the CP pulse sequence. The intensity of the signal strongly depends on the contact time, which is usually specific to each chemically inequivalent nucleus, and can also change depending on the phase. Offerdahl et al. successfully quantified different forms of the artificial sweetener neotame.³² In the Figure 2.8, the experimental CP dynamics of the crystalline and the amorphous form of neotame is shown.

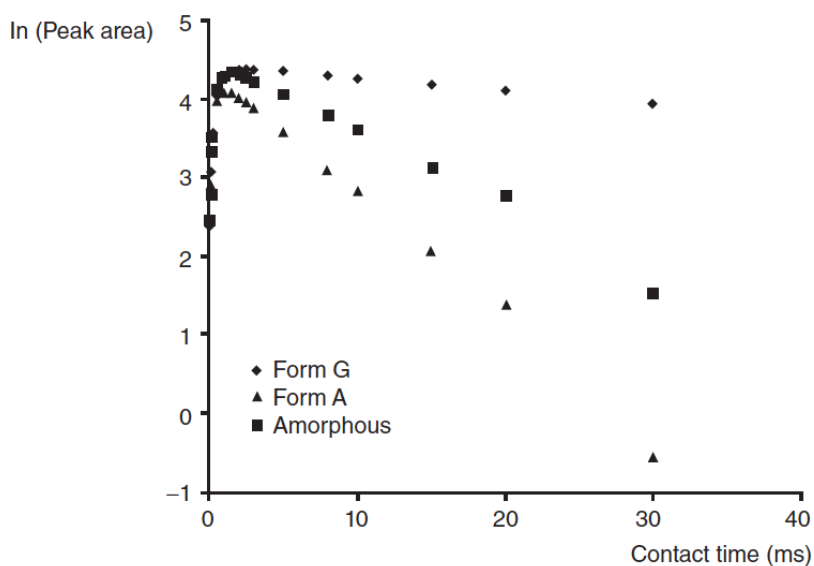


Figure 2.8. ¹³C cross polarization dynamic curves for various forms of neotame, taken from reference.³²

In general, CP dynamics depend on the two rate constants, T_{CH} and $T_{1\rho H}$ as shown in the equation. This equation can be applied when $T_{1\rho C} \gg T_{CH}$.

$$M(t) = \frac{M_0 \left[\exp\left(-\frac{t}{T_{1\rho H}}\right) - \exp\left(-\frac{t}{T_{CH}}\right) \right]}{1 - \left(\frac{T_{CH}}{T_{1\rho H}}\right)} \quad (2.9)$$

where $M(t)$ is the magnetization and t is the contact time. $T_{1\rho H}$ is the spin-lattice relaxation times in the rotating frame for proton. T_{CH} is the cross polarization time constant, which depends on the strength of the dipolar coupling between ^{13}C and ^1H . T_{CH} time determines the rate of increase of ^{13}C magnetization, whereas $T_{1\rho H}$ dictates the decay of magnetization. By fitting the CP dynamics curve to the equation, it is possible to obtain the information on parameters $T_{1\rho H}$, T_{CH} and M_0 is the thermal equilibrium value of ^{13}C magnetization.

2.5 Conclusions

In this chapter, a comprehensive overview of the basics of SSNMR was presented. The main focus of this chapter was to introduce some key concepts and experimental features pertaining to the use of SSNMR for pharmaceutical samples. In addition, some important applications of SSNMR with respect to the amorphous systems were highlighted. Special emphasis was given to the applications of proton relaxation time measurements for evaluating phase homogeneity in ASDs.

CHAPTER 3. PHASE BEHAVIOR OF AMORPHOUS SOLID DISPERSIONS OF FELODIPINE: HOMOGENEITY AND DRUG-POLYMER INTERACTIONS

3.1 Introduction

Over the past few decades, amorphous solid dispersions (ASDs) have been of great interest to pharmaceutical scientists to address the oral bioavailability issues associated with poorly water-soluble drugs.¹⁻⁴ ASDs consist of an active pharmaceutical ingredient (API) that is typically dispersed in an inert polymeric matrix.^{5, 6} Despite promising advantages, a major concern that has resulted in limited marketed formulations is the physical instability of these complex formulations.⁷ Physical instability is often manifested as the API crystallizing in the formulation, which is often predicated on phase separation, where the drug and carrier migrate and generate distinct phases. Thus, phase separation can be a prelude to recrystallization.⁸ It is therefore important to understand phase homogeneity in ASDs to enable rational formulation design.

One important factor that dictates the physical stability of ASDs is the spatial distribution of the API in the polymeric matrix.⁹ Three possibilities exist: (1) a homogenous system with a single phase where API is uniformly distributed throughout the polymeric matrix, (2) a non-homogeneous system where API and polymer are totally phase separated, and (3) a partially homogeneous system with drug rich and polymer rich phases. From a pharmaceutical viewpoint, an intimately mixed ASD is usually preferred, as it is likely to have better physical stability and product efficacy.¹⁰ In addition to phase homogeneity, other factors to potentially impact physical stability include storage conditions, hygroscopicity of the polymer, solubility of the drug in polymer, and the glass transition temperature (T_g) of the system.¹¹⁻¹³ Regardless of the mechanism, it is generally

agreed that intimate mixing of the drug and the polymer is desired to achieve maximum stabilization¹⁴. Therefore, understanding the factors controlling phase behavior and nano-domain structure of ASDs is crucial to rational formulation design.

There are many analytical tools that have been used for determining drug-polymer miscibility in ASDs. Differential scanning calorimetry (DSC) is one of the standard techniques for characterizing phase homogeneity in ASDs if the minimum size of phase separated domains is 30 nm or higher.^{15, 16} A single T_g , intermediate to those of an API and polymer is considered as a sign of a homogenous system. In contrast, multiple T_g values indicate a phase separated system but this criterion is not reliable. In several instances, it has been demonstrated that it is possible to observe a single T_g for a phase separated system, and vice versa.^{17, 18} Furthermore, detection of sub 30 nm domains may be challenging to characterize via DSC. Other analytical tools include Raman mapping, which has shown to be able to detect phase separation in systems where T_g is undetected by DSC.¹⁹ Conventional high-resolution imaging techniques such as scanning electron microscopy (SEM), transmission electron microscopy (TEM), and atomic force microscopy (AFM) have also been employed to study miscibility.²⁰⁻²² However, these traditional characterization methods often have low spatial resolution with respect to the distribution of the components of ASD, and are unable to identify the chemical compositions of different microstructures. The lack of analytical methodology that can detect phase heterogeneity on the order of a few nanometers often leads to the difficulties in elucidation of phase behavior of ASDs at that level of resolution.

Solid-state nuclear magnetic resonance (SSNMR) spectroscopy has recently emerged as a technique to investigate phase behavior of ASDs with atomic level

specificity and selectivity.²³ SSNMR can provide valuable information on the heterogeneity of the sample at the nanometer level.²⁴⁻²⁸ It is especially useful for ASDs where nano heterogeneities can exist beyond the resolution limits of thermal analyses. Specifically, proton spin-lattice relaxation times (^1H T_1 and $T_{1\rho}$) are measured to determine and understand phase homogeneity.^{29, 30} An intimately-mixed ASD is reflected in identical values of ^1H T_1 and $T_{1\rho}$ for the API and the polymer components. On the contrary, a detectable difference between the relaxation times for the API and the polymer provides the evidence for a heterogeneous or phase separated system.^{31, 32} In recent years, SSNMR has attracted increased attention in the field of ASDs to study phase homogeneity.^{24, 33-35} Policianova et al., probed homogeneity of acetylsalicylic acid dispersions on the scale of ca. 10-500 nm.³⁶ In a study by Yuan et al., compositional dependent homogeneity was studied for nifedipine-PVP ASDs prepared by different methods. ^1H $T_{1\rho}$ measurements indicated that 95:5 and 90:10 nifedipine-PVP ASDs prepared by melt-quenching were non-homogeneous on the molecular level.²⁷ Most recently, Yang et al. demonstrated that at extrusion temperature higher than 160 °C better miscibility was achieved for the drug and polymer with length scale of mixing of 20-80 nm for nifedipine-copovidone dispersions prepared via hot melt extrusion.³³ In spite of these previous studies, little SSNMR work has been reported on the systematic study of the factors affecting the compositional homogeneity in ASDs.

The domains are affected by the composition of the drug-polymer mixture and the underlying molecular interactions. The level of mixing between API and the polymer is maximized when the individual components are involved in intermolecular interactions such as hydrogen bonding (H-bonding).³⁷⁻³⁹ There are several examples in the literature

where pharmaceutical polymers containing H-bond donor/acceptors have shown to form H-bond with drug molecules containing acceptor/donor groups. The formation drug-polymer interactions can lead to better physical stability and dissolution properties.^{40, 41} Routinely, H-bonding interactions between the drug and polymer are studied by fourier transform infrared (FT-IR) spectroscopy. There are numerous examples in literature where presence of H-bonding has been shown by FT-IR measurements.⁴²⁻⁴⁷ Even though widespread, FT-IR technique has its drawbacks. It is possible to achieve unreliable results due to broad and overlapping absorption bands. SSNMR can offer better resolution between the components of ASDs and reveal the nature of interactions between H-bond donors and acceptors quantitatively. Yuan et al., demonstrated the use of high resolution ¹³C SSNMR measurements to monitor H-bonding interactions in amorphous indomethacin and its ASDs.³⁵

For the current study, we hypothesize that the systems with stronger and more extensive drug-polymer H-bonding interactions will exhibit better compositional homogeneity than the systems with weaker and less extensive drug-polymer interactions. We used a BCS class II API felodipine (FEL) as our model drug and three different polymers poly(vinylpyrrolidone) (PVP), poly(vinylpyrrolidone)/vinyl acetate (PVP/VA), and poly(vinylacetate) (PVAc). FEL is a dihydropyridine derivative with one H-bond donor and several acceptors in its structure. The polymers have only H-bond acceptors in their backbone thereby offering different possibilities for H-bonding interactions with FEL, thus helping us establish our hypothesis. In H-bonded systems, the phase behavior of resulting dispersions is determined by the extent and strength of H-bonds between the donor and acceptor groups. We are aware of no previous SSNMR studies regarding the

role of H-bonding on compositional homogeneity. The chemical structure of all the compounds along with the physicochemical properties is shown in Table 3.1. The first part of this article is devoted to investigate the phase behavior of FEL dispersions using DSC. In the second part of this article, SSNMR is used to elucidate the extent of H-bonding and correlate that to phase homogeneity. We show that SSNMR methods can be used to study comprehensively the phase behavior and speciation in ASDs, which cannot be achieved using conventional analytical tools.

3.2 Experimental Section

3.2.1 Materials

Felodipine (FEL; purum 99%) was purchased from BOC Sciences (Shirley, NY). PVP K25 (Kollidon 25, $M_w = 28\text{-}34$ kg/mol) and PVP/VA (Kollidon VA 64, $M_w = 45\text{-}70$ kg/mol) were kindly donated by BASF Corp. (Edison, NJ). PVP and PVP/VA were dried at 70 °C under vacuum to remove residual moisture before use. PVAc (average $M_w = 100$ kg/mol) was purchased from Sigma-Aldrich (St. Louis, MO). Polymer samples were stored over Drierite at all the times.

3.2.2 Preparation of Amorphous Materials

Preparation of Amorphous Felodipine. Amorphous felodipine was prepared by *in situ* melt quenching inside the spinning NMR rotor. Sample was packed into 7.5 mm zirconia rotors with Teflon or Kel-F end caps (Revolution NMR, LLC., Fort Collins, CO). The rotor was heated in the NMR probe equipped with a variable-temperature accessory stack (Varian, Palo Alto, CA) at 155 °C for approximately 10 min while

spinning at 4 kHz. The rotor was then rapidly cooled to room temperature to generate glassy felodipine.

Preparation of Felodipine Amorphous Solid Dispersions. Amorphous solid dispersions of felodipine with PVP, PVP/VA, and PVAc were prepared by melt quenching in the lab setting. To prepare dispersions via this approach, one gram samples at various drug:polymer weight ratios ranging from 50:50 to 90:10 (on weight basis) were cryomilled at 10 Hz (SPEX SamplePrep 6770 Freezer/Mill, SPEX SamplePrep LLC., Metuchen, NJ) for five cycles, each comprising 2 min of milling and 2 min of cooling. Liquid nitrogen was employed as a coolant. The cryomilling procedure was used to ensure optimally mixed drug-polymer mixtures before melting. The cryo-milled mixtures were then transferred into a Teflon beaker and heated in an oil bath at 160 °C for 10 min or until completely melted. The melted mixtures were then quenched-cooled using liquid nitrogen to generate dispersions. The resulting dispersions were vacuum-dried at room temperature overnight to remove any residual moisture. All dispersions samples were confirmed amorphous by powder X-ray (Figure 3.5). All amorphous samples were stored in glass vials over Drierite in the freezer when not analyzed.

3.2.3 Differential Scanning Calorimetry (DSC)

DSC analyses were performed using a Q2000 (TA Instruments, New Castle, DE) equipped with a RCS90 refrigerated cooling system (TA Instruments; New Castle, DE). The instrument was calibrated for temperature and heat flow using indium as a standard. Approximately 5-7 mg of sample was hermetically sealed in an aluminum pan with one pinhole in the lid. All the dispersion samples were analyzed via heat-cool-heat cycle under nitrogen purge (50 mL/min). A typical thermal cycle consisted of following stages:

1) heating from 20 °C to 165 °C (first heating); 2) isothermal for 10 min followed by cooling to -10 °C (cooling stage); 3) reheating to 165 °C (second heating). For the heating cycles, an underlying heating rate of 2 °C/min was used with modulation amplitude of ± 0.21 °C applied every 40 s. For each sample, measurements were conducted in duplicate. The data were analyzed by Universal Analysis software (Version 4.7, TA Instruments, New Castle, DE). The value of T_g reported was the half height of the transition in the reversing heat flow signal.

3.2.4 Solid-State NMR Spectroscopy

^{13}C SSNMR spectra were acquired using a Tecmag Redstone spectrometer (Tecmag Inc., Houston, TX) operating at approximately 300 MHz for ^1H and 75 MHz for ^{13}C . Samples were packed into 7.5 mm zirconia rotors and sealed with Teflon or Kel-F end-caps (Revolution NMR LLC., Fort Collins, CO). One dimensional ^{13}C spectra were acquired using cross polarization magic angle spinning (CP/MAS) at 4 kHz, using total sideband suppression (TOSS)⁴⁸ and SPINAL64⁴⁹ decoupling. The ^1H 90° pulse width was set to 4.0 μs and the contact time of 1.5 ms was used in all the measurements. The ^{13}C chemical shift scale was referenced with the methyl peak of 3-methylglutaric acid, which was set to 18.84 ppm.⁵⁰

The proton relaxation times were detected via ^{13}C nucleus to resolve the resonances for respective components. The chemical shift regions unique to FEL and the polymers were integrated to obtain the proton relaxation times (details in Results and Discussion). Proton spin-lattice relaxation time in the laboratory frame (^1H T_1) was measured using a ^{13}C -detected saturation recovery pulse sequence with TOSS. ^1H T_1 obtained by fitting intensity-recovery time data by the following equation:

$$M(t) = M_0(1 - e^{-\frac{t}{T_1}}) \quad (3.1)$$

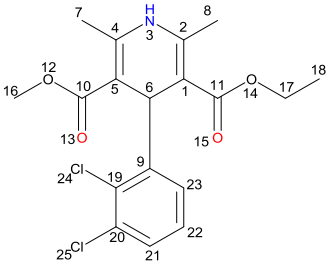
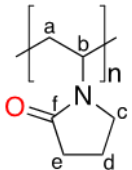
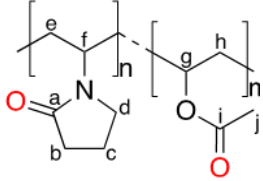
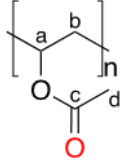
where $M(t)$ is the integrated signal intensity at delay time t , M_0 is an amplitude parameter from the fit, and T_1 is the obtained spin-lattice relaxation time. Proton relaxation time in the rotating frame ($^1H T_{1\rho}$) was measured by varying the spin lock duration time after a 90° pulse. The $T_{1\rho}$ decay times were obtained by analyzing the integrated carbon signal intensity according to the following equation:

$$M(t) = M_0 e^{-\frac{t}{T_{1\rho}}} \quad (3.2)$$

where $M(t)$ is the integrated peak intensity and t is the spin-lock duration time. M_0 is an amplitude parameter from the fit, and $T_{1\rho}$ is the fitted spin-lattice relaxation time in the rotating frame. All data fitting was done using GraphPad Prism (GraphPad Software, Inc., La Jolla, CA).

The NMR spectra of amorphous FEL and the dispersions samples were deconvoluted using MNOVA software (MestreLab Research, Version 10.0, Santiago de Compostela, Spain) in the carbonyl region. For the dispersion samples, the spectra were fitted with three or four peaks depending on the system. The parameters like the peak width and the Gaussian/Lorentzian ratio were kept fixed across samples in the same system. The area percentages for the various species were calculated from the total area of the deconvoluted peaks and the area for FEL peaks were then normalized to the total area of its carbonyl peaks.

Table 3.1. Chemical Structures showing H-bond donors (in blue) and acceptors (in red) of model compounds along with their physicochemical properties.

Compound	Structure	T _m (°C)	T _g (°C)	H-Bond Donors/Acceptors
Felodipine		144.4	46.2	Donor and Acceptors
PVP K25		--	170.0	Acceptor
PVP/VA		--	109.0	Acceptors
PVAc		--	44.4	Acceptor

3.2.5 Theoretical Calculations

Gas-phase calculations were completed with the Gaussian09 software package,⁵¹ utilizing the B3PW91⁵² density functional and the 6-311G(2d2p)⁵³ basis set for structural optimizations. This particular theory was chosen based upon its performance as reported

by Chen *et. al.*,⁵⁴ and its performance on the systems studied herein. All gas-phase calculations used molecular structures extracted from the single crystal X-ray data retrieved from the CCDC as starting points. All geometry optimizations allowed the molecules to fully relax with no symmetry restrictions, while the single-point energy calculations held the molecules in rigid conformations. The default total energy convergence criteria for was used ($\Delta E < 10^{-6}$ hartree) for geometry optimizations. The DFT grid was set to program option “ultrafine” for all simulations. The NMR chemical shifts were predicted using HF/6-31G(d)^{55, 56} level of theory and the GIAO command in Gaussian09.

3.3 Results and Discussion

The most common approach to analyze homogeneity at the molecular level is DSC. The presence of a T_g in a dispersion of drug and polymer has been suggested to indicate that the sample is homogeneous at a molecular domain size of ≥ 30 nm. When studying homogeneity at smaller domain sizes, more advanced techniques such as SSNMR are needed that can probe down the 2-5 nm range. For this reason, the samples were initially analyzed using DSC to probe whether any differences in homogeneity could be observed based upon multiple T_g values or deviations from the predicted values.

3.3.1 DSC Results

3.3.1.1 DSC Heating Cycles

As noted in the above paragraph, thermal analysis is one of the most convenient approaches to assess the homogeneity and thermal behavior of dispersions.⁵⁷ Inhomogeneity is often marked by two T_g values, corresponding to the T_g values of the

individual components.⁵⁸ The DSC analysis of the neat polymers showed a T_g of 170 °C for PVP, 109 °C for PVP/VA and 44.4 °C for PVAc (Table 3.1). Amorphous FEL showed a T_g of 46.2 °C, accompanied by an exothermic crystallization, and followed by melting with an endothermic peak at 144 °C, which is consistent with previously-reported results.⁴³ It is worth noting that PVAc has slightly lower T_g than the amorphous FEL.

The DSC thermograms from the first heating cycle for FEL:Polymer dispersions with various compositions are shown in Figure 3.1. For each set of ASDs, a single composition-dependent T_g was observed in the reversing heat flow traces, which implies that the FEL and polymers were homogeneous over the composition range. Melting endotherms were observed for certain compositions (samples containing less than or equal 20% PVP, 20% PVP/VA and 40% PVAc) in each system. The presence of a melting endotherm can be attributed to either the presence of residual crystallinity in the sample, or to crystallization taking place at temperatures above T_g . Because a crystallization exotherm was observed in the non-reversing heat flow (*vide infra*), the latter explanation is more likely. This suggests that there is some degree of nano heterogeneity and the amorphous drug-rich domains can rearrange into crystalline phases due to increased mobility of the system above T_g . This phenomenon of crystallization above T_g is polymer dependent and the details will be discussed in the later section. In order to further investigate this phenomenon, a second DSC scan was performed on these samples to see if the crystallization exotherm/melting endotherm was observed for samples when the thermal history was removed as a variable.

The characteristics seen in first heating cycle represent the state of the samples as they were prepared, which was by melt quenching. After the first heating scan, both the thermal history of the samples and any residual moisture content are removed from the samples, and this can result in the samples being more homogenous for accurate measurement of T_g of a homogeneous system. The DSC thermograms of the second heating scans were slightly different than the first heating scan, with sharper T_g step changes and the absence of any melting endotherms. The absence of melting endotherms signifies that quench cooling in the DSC pan after the first heating scan was sufficient to eliminate the crystal formation during the cooling cycle. As it can be seen from Figure 3.2, only one T_g was detected in each set of dispersions for the composition range studied, with the T_g value being a function of the drug to polymer ratio. In order to understand the impact of this crystallization appearing in the first heating scan but not the second, the data was analyzed first to see if there was any drug-polymer interactions that might be observed in the DSC data, specifically in the form of a change in the T_g values. A change in the T_g from the first to second scan could indicate a change in the homogeneity of the samples, where the second scan may result in a more homogeneous sample, and therefore less susceptible to crystallization.

The DSC thermograms (first and second) had similar mean T_g values from both the cycles. Even though these dispersions appear to be homogeneous, since they exhibited a single T_g for both the heating runs that was very close in value, this does not necessarily ensure that they are homogenous below the 30 nm scale as noted above for DSC homogeneity measurements.

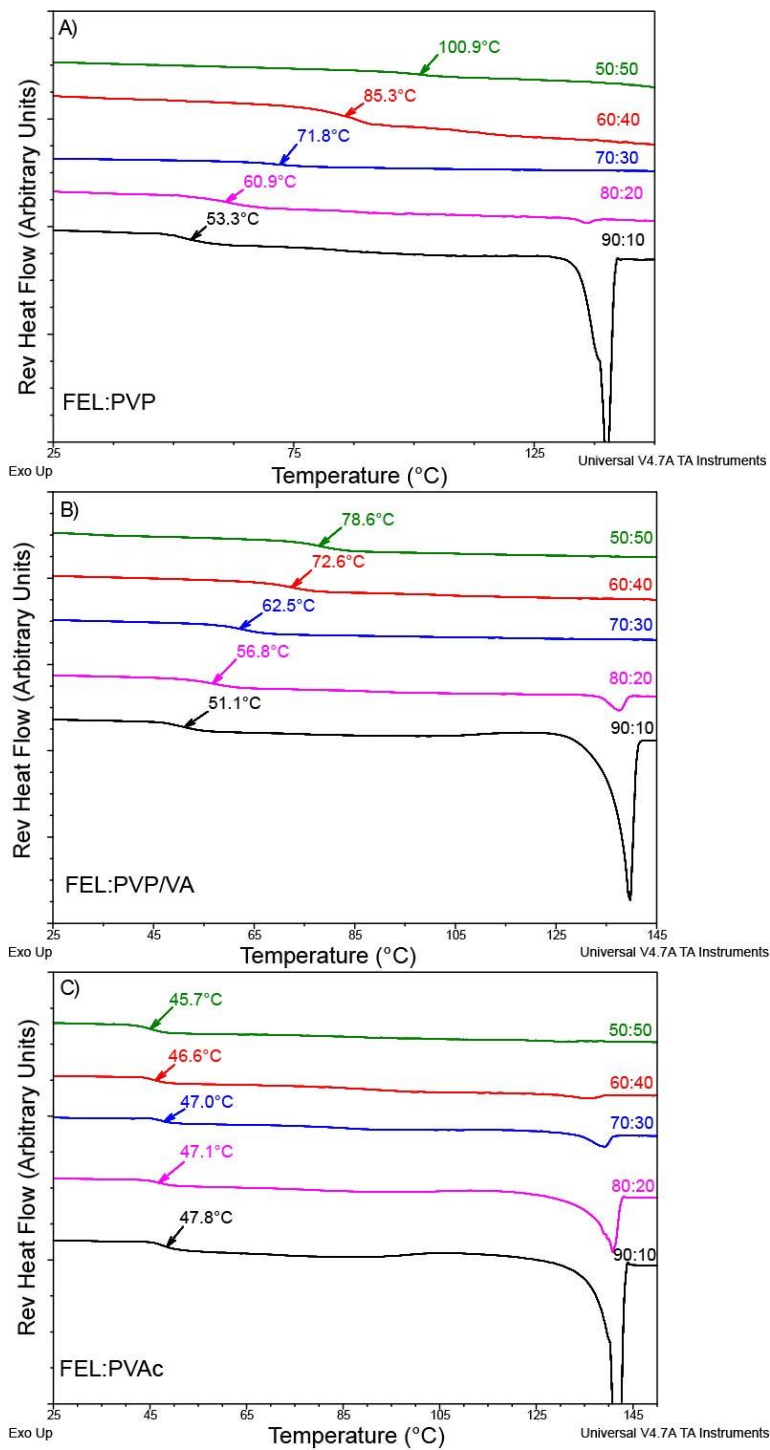


Figure 3.1. DSC thermograms from first heating scan for FEL:Polymer dispersions A) FEL:PVP B) FEL:PVP/VA and C) FEL:PVAc. The values reported here are the mean glass transition temperatures.

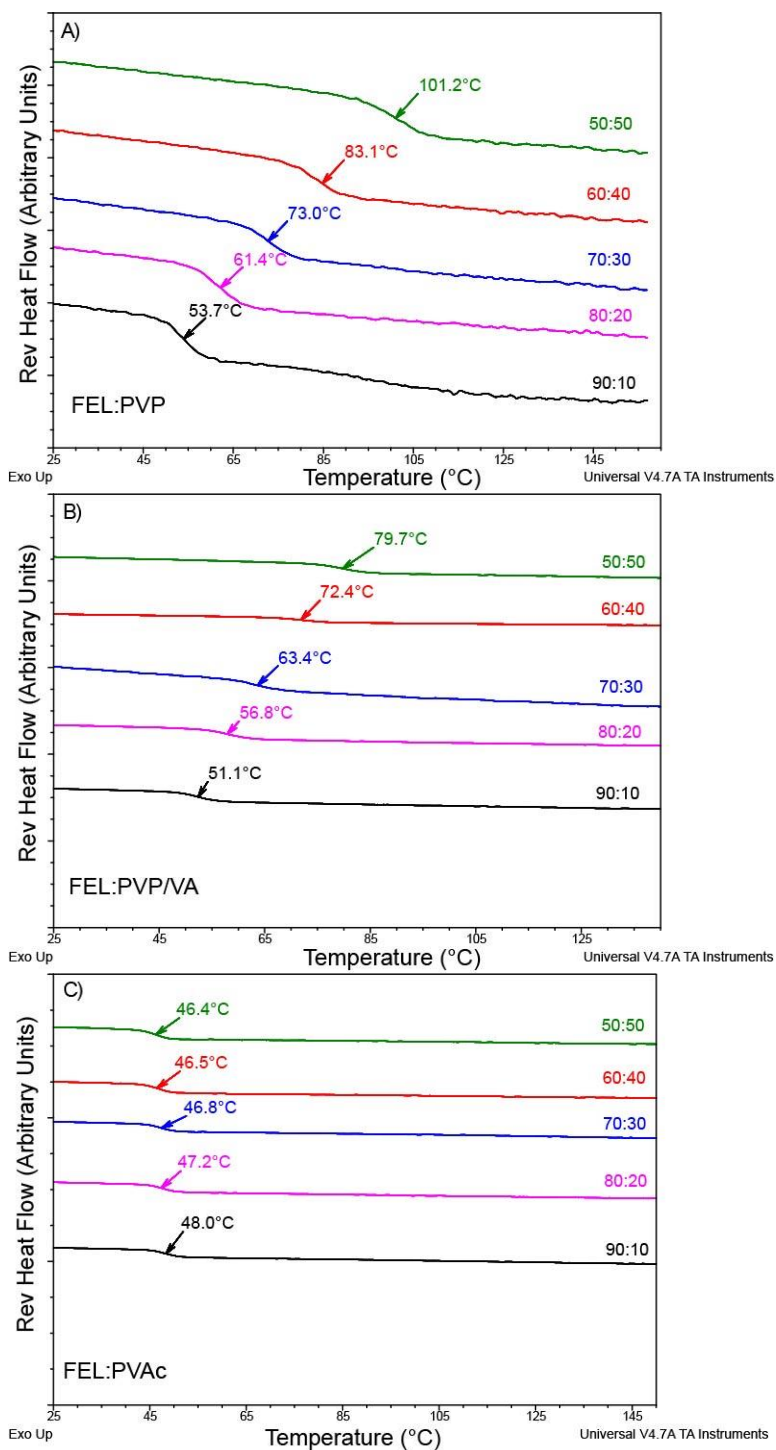


Figure 3.2. DSC thermograms from second heating scan for FEL:Polymer dispersions A) FEL:PVP B) FEL:PVP/VA and C) FEL:PVAc. The values reported here are the mean glass transition temperatures.

3.3.1.2 Fitting DSC Data to Gordon-Taylor Equation

DSC data can be plotted as a function of composition to determine if there are potential interactions between the drug and the polymer, where deviations from linearity suggest that there may be drug/polymer interactions. A number of empirical models have been proposed to study the T_g composition dependence of dispersions. Among the equations proposed, the Gordon-Taylor equation is widely used.⁵⁹ It is described as follows:

$$T_g = \frac{[(w_1 T_{g1}) + (k T_{g2})]}{[w_1 + (k w_2)]} \quad (3.3)$$

where T_g is the glass transition of the dispersion, T_{g1} and T_{g2} are those of pure components, w_1 and w_2 are the weight fractions of each component, and the constant k is an adjustable fitting constant. The mean T_g values from the second heating scans were used for the Gordon-Taylor equation. For fitting the data it is convenient to linearize and rewrite the original Gordon-Taylor equation as:

$$T_g - T_{g1} = k * (T_{g2} - T_g) * \left(\frac{w_2}{w_1}\right) \quad (3.4)$$

A plot of $T_g - T_{g1}$ versus $(T_{g2} - T_g) * (w_2/w_1)$ will yield k via linear regression. Using this approach, we get k values of 0.81, 1.18, 0.91 for FEL:PVP, FEL:PVP/VA, and FEL:PVAc dispersions respectively.

Figure 3.3 shows the plot of T_g values obtained after the second heating scan vs. the weight fraction of polymer for the three polymer systems. The broken lines in Figure 3.3 were obtained by inserting the resulting values of k into equation (3) and plotting the corresponding T_g values. A slight negative deviation is seen for FEL:PVP and

FEL:PVP/VA dispersions, which likely reflects the presence of weak specific interactions. Compared to FEL:PVP and FEL:PV/VA dispersions, FEL:PVAc system had no deviations from the predicted Gordon-Taylor curve. This ideal behavior could be due to negligible presence of any specific intermolecular interactions, or that the intermolecular FEL-FEL interactions were replaced with the similar strength of intermolecular FEL:PVP/VA interactions. It is worth mentioning that the T_g of amorphous FEL and PVAc were almost similar, which caused T_g values of resulting dispersions to change very slightly for the composition range studied.

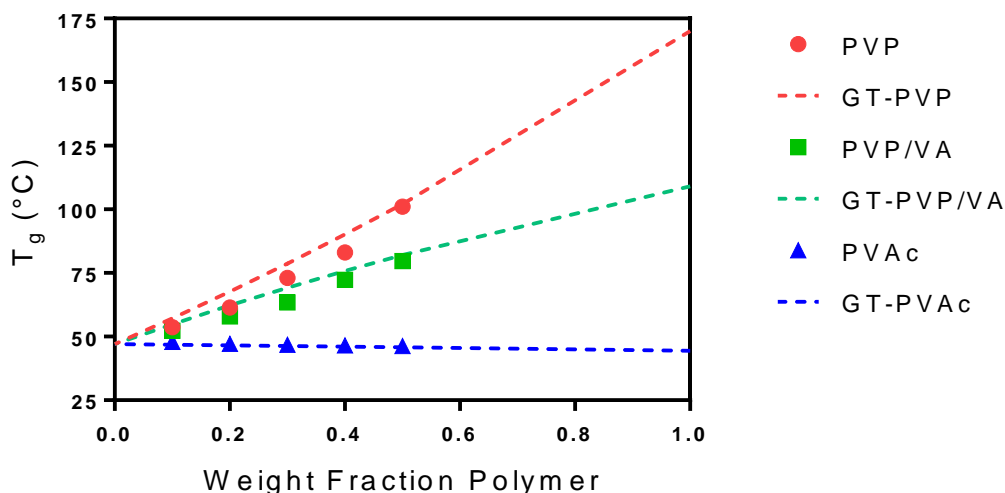


Figure 3.3. T_g -composition relationship for FEL:Polymer dispersions. Mean experimental T_g values are denoted by symbols (red circle for FEL:PVP, green square for FEL:PVP/VA, and blue triangle for FEL:PVAc). The respective Gordon-Taylor curves are shown in colored broken lines.

3.3.1.3 Drug Crystallization-First Heating Scan

Figure 3.1 showed that for samples containing less than or equal to 20 % polymer for FEL:PVP and FEL:PVP/VA ASDs, FEL crystallized upon heating. For FEL:PVAc

ASDs, samples containing less than 50% polymer showed signs of FEL crystallizing upon heating. To support the idea that the crystallinity was produced during heating and was not present prior to analysis via DSC, PXRD (Figure 3.5) and ^{13}C CP/MAS (*vide infra*) clearly pointed to the absence of any crystallinity present within their detection limit.

The reversible heat flow data shown in Figure 3.1 is useful for determining the T_g values, but the non-reversible heat flow events can provide insight into events such as crystallization occurring in the samples. Figure 3.4 shows DSC thermograms for the non-reversing heat flow for the 90:10 (Plot 3.4 A) and 80:20 (Plot 3.4 B) compositions. Amorphous FEL exhibited a crystallization exotherm at 80.9 $^{\circ}\text{C}$. The crystallization temperature of amorphous FEL increased with polymer loading for all three polymers. In addition, it can be seen that the crystallization temperature was the highest with PVP for both of the polymer loadings. Overall, the stabilization potential of a polymer is rank ordered as PVP>PVP/VA>PVAc. In fact, the rank ordering correlates well with the results reported by Bhugra et.al.⁶⁰ The authors showed that crystallization temperature could be an indicator of the strength of drug-polymer interaction. For their case study with nifedipine, a similar trend was seen and the authors concluded that PVP had the most potential to retard crystallization in comparison with other polymers studied. This is also consistent with the study performed by Yuan et.al, where the authors showed that PVP systems had a stronger interaction with indomethacin as compared to systems with PVP/VA³⁵.

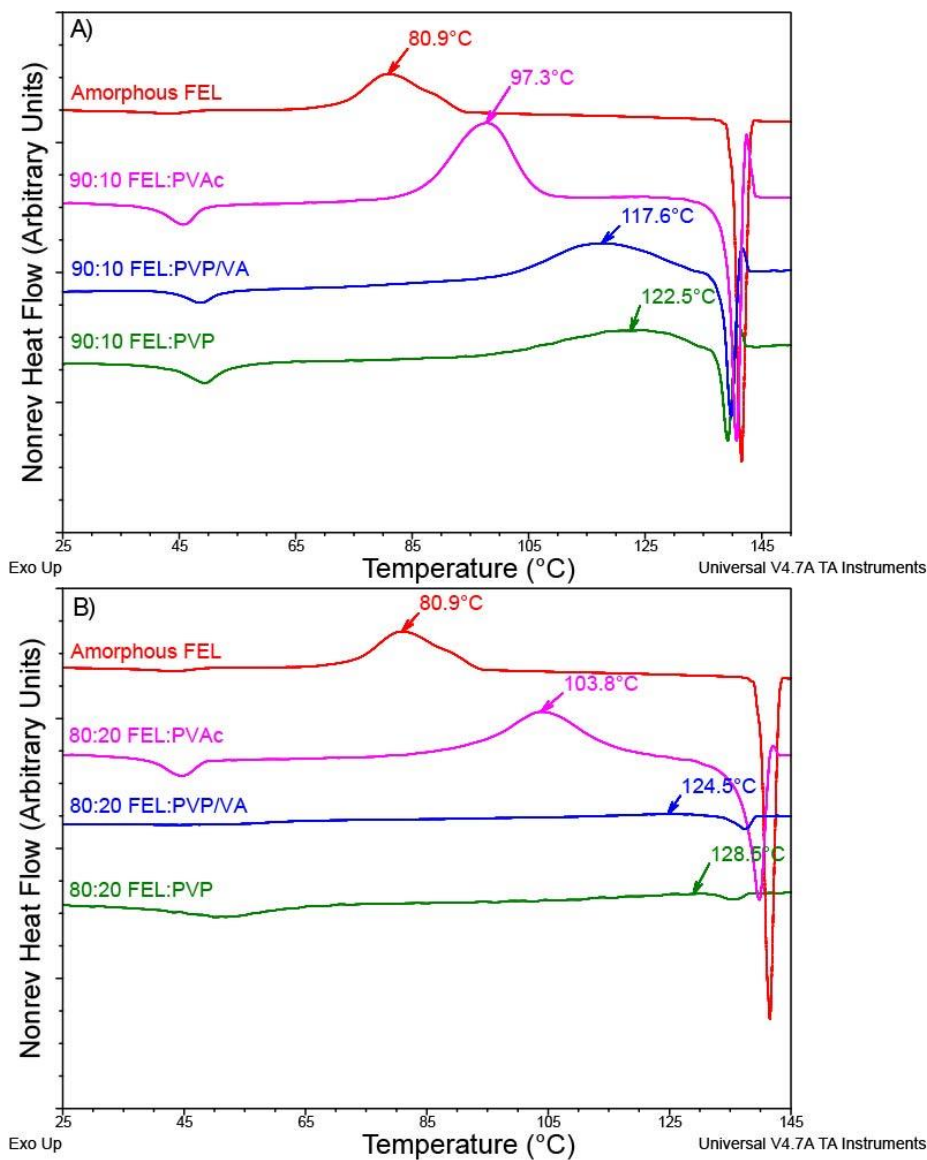


Figure 3.4. DSC thermograms showing non reversing heat flow versus temperature as a function of polymer loading: A) 10% polymer B) 20% polymer.

3.3.1.4 Summary – DSC Results

The DSC data in the previous sections highlighted several trends. First, there were differences between the first and second heating cycles in the DSC thermograms, suggesting that the samples as initially prepared were different than the samples that were heated above the melting point of the drug, cooled, and then reheated. The most

likely explanation we have pointed out is that there was some degree of phase heterogeneity present when the samples were initially prepared. However, the most definitive evidence for that could be the observation of two glass transition temperatures in the DSC thermograms, or even a change in the T_g of the samples from the first and second heating curves, which was not observed. There was no direct evidence for phase heterogeneity from the DSC results. Second, the strength of drug-polymer interactions was consistent with PVP having the strongest H-bonding interaction with FEL, followed by PVP/VA and PVAc in that order. However, the relative strength of this interaction was not quantified, except by the change in the crystallization temperature.

To answer these questions, SSNMR was used to study the homogeneity of the samples as a function of polymer composition, and for a select sample, the equivalent of a second heating scan was done *in situ* in the SSNMR rotor. In addition, SSNMR was employed to investigate the structural changes in the drug as a function of polymer loading to better understand the strength and extent of the drug-polymer H-bonding interactions.

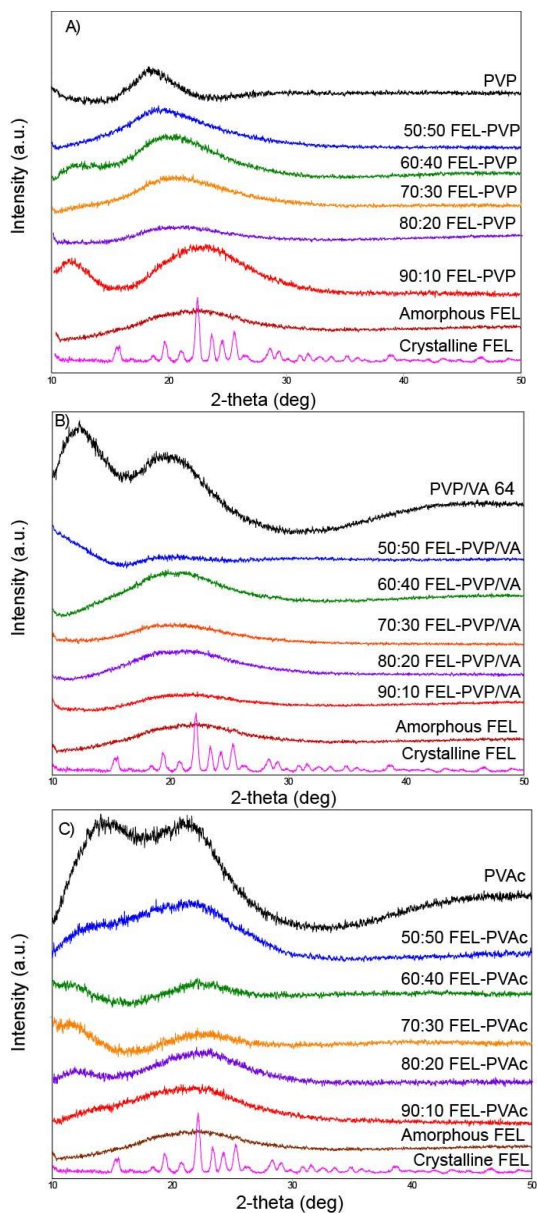


Figure 3.5. X-ray powder diffraction patterns of FEL:Polymer dispersions for A) FEL:PVP, B) FEL:PVP/VA and C) FEL:PVAc.

3.3.2 ^{13}C CP/MAS Solid-State NMR Results – Miscibility

3.3.2.1 SSNMR Spectra and Interpretation

The ^{13}C CP/MAS spectra of as-received FEL and amorphous FEL are shown in Figure 3.6. The assignments of resonances as given in Table 3.1 for various carbons of

as-received FEL were done based on previous literature reports.⁶¹ In the recorded ¹³C CP/MAS spectrum, the crystalline material could be easily be identified and distinguished from the amorphous state based on its narrow and well resolved resonances in contrast to broad NMR signals seen for the amorphous FEL. The ¹³C CP/MAS spectra for the polymers are displayed in Figure 3.6. All the three polymers depicted amorphous characteristics as exhibited by their broad resonances. For pure PVP, four distinct peaks were observed although it has six carbons in its structure. This is owing to the overlaps observed in the carbon resonances. The resonance at 175 ppm corresponded to the carbonyl group (C=O) of PVP pyrrolidone backbone. Similarly for neat PVP/VA, only eight resonances could be resolved in the spectrum. The carbonyl region of the spectrum of PVP/VA consisted of resonances at 175 ppm and 170.9 ppm, which arose from two carbonyl carbons one from the pyrrolidone moiety and other from the acetate functionality. In the PVAc spectrum, four resonances were seen with no overlap in the resonances. Peaks at 40 ppm and 66 ppm corresponded to the polymer backbone. Meanwhile, the other resonance at 170.2 ppm came from the carbonyl group.

The ¹³C CP/MAS spectra of FEL dispersions with various polymers are shown in Figure 3.7 (Plots A, B and C). The spectra confirmed the amorphous nature of the dispersions formulated via melt quenching. For the spectra of dispersions, it was noted that there were some non-overlapping resonances for the drug and polymers. The carbon signals around 146 ppm, 128 ppm and 104 ppm were selective for FEL (red dashed boxes in Figure 3.7). Meanwhile, the carbon signals around 175 ppm served as non-overlapping peak for PVP and the carbon resonance around 68 ppm was selective for

both PVP/VA and PVAc (blue dashed boxes in Figure 3.7). These specific peaks act as a unique probe to follow the relaxation behavior of FEL and polymers in the dispersions.

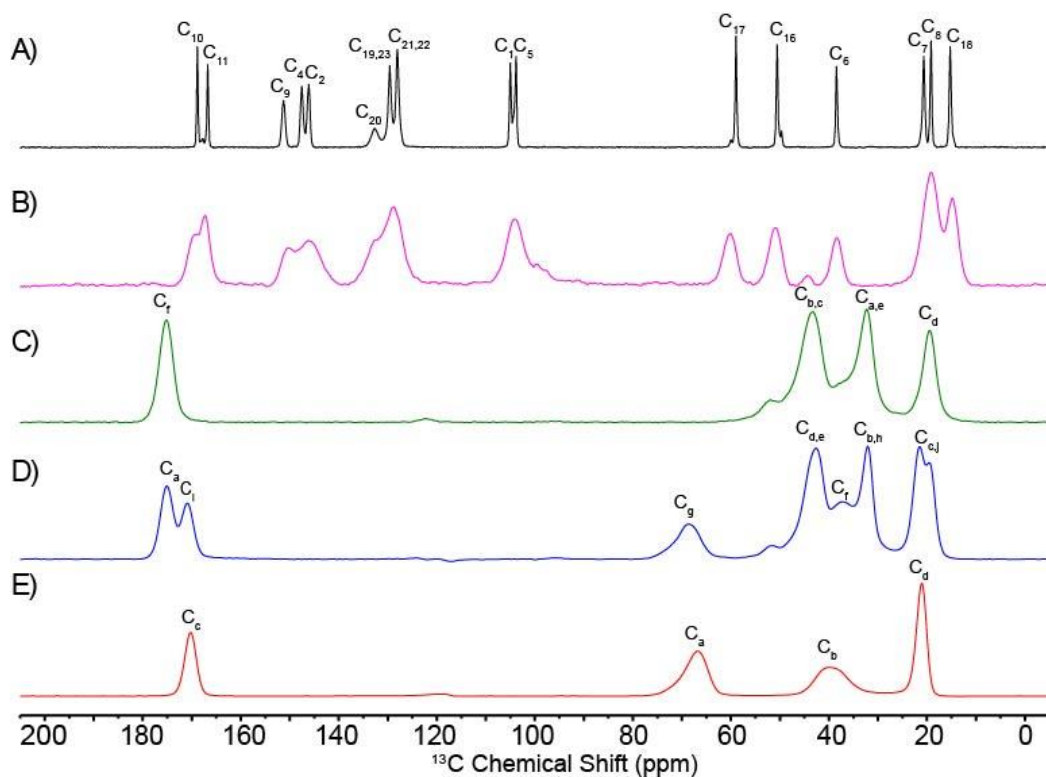


Figure 3.6. Stacked plot of ^{13}C CP/MAS spectra for (A) Felodipine (as received) (B) amorphous felodipine (C) PVP (D) PVP/VA and (E) PVAc. The ^{13}C resonances relate to the numbering scheme presented in Table 3.1.

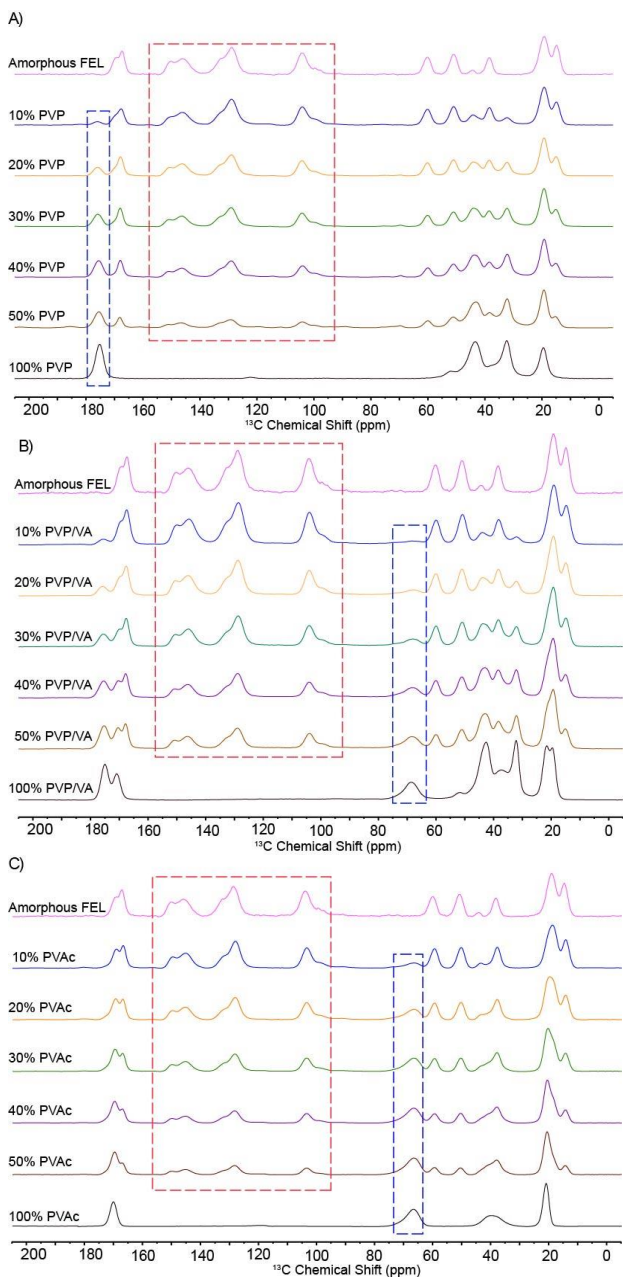


Figure 3.7. ^{13}C CP/MAS spectra of (A) FEL:PVP dispersions (B) FEL:PVP/VA and (C) FEL:PVAc. In each stacked plot the spectra from top to bottom include amorphous FEL, FEL:Polymer dispersions with 50-90% drug load and neat polymer. The central aromatic peaks at 146 ppm, 128 ppm and 104 ppm (indicated by the red box; plot A-C) were attributed to FEL specific resonances while the peaks at 175 ppm (indicated by blue box; plot A), 68 ppm (indicated by blue box; plots B and C) were identified as non-overlapping regions for PVP, PVP/VA and PVAc respectively.

3.3.2.2 SSNMR Relaxation Times - Investigation of Phase Behavior

In order to obtain more detailed information on the compositional homogeneity and phase behavior of dispersions, the proton relaxation experiments were performed, which consisted of measuring the spin-lattice relaxation time in the laboratory frame ($^1\text{H } T_1$), and in the rotating frame ($^1\text{H } T_{1\rho}$) for both the drug and polymer peaks. The measurements are usually performed via ^{13}C resonances to be able to determine the relaxation time values for the drug separately from the polymer. As depicted in Table 3.2, the neat samples of FEL (as-received and amorphous) and polymers were characterized by different $^1\text{H } T_1$ and $T_{1\rho}$ times. An examination of experimental $^1\text{H } T_1$ and $T_{1\rho}$ data for FEL showed that amorphous state has shorter relaxation times than the crystalline FEL, which is characteristic of disordered materials. From Table 3.2, a single proton relaxation value was observed for pure polymers, indicating a single-phase amorphous system. The experimental $^1\text{H } T_1$ and $T_{1\rho}$ values are rank ordered as PVAc>PVP/VA>PVP.

For a system containing multiple components, such as a drug and a polymer, the scale of compositional homogeneity can be estimated from the relaxation behavior of the individual components. Three possibilities exist for the phase behavior classification of dispersions, namely a homogeneous, a partially homogeneous, and a non-homogeneous system, corresponding to a uniformly mixed system, a partially-mixed system, and a phase separated system. In case of a homogeneous system on the molecular scale, the protons of different components spin diffuse and relax at an identical rate. For a phase-separated system, the drug and polymer have different relaxation behavior is observed owing to domain sizes of the drug and polymer being so large that there is incomplete

spin diffusion between the drug and polymer at the largest domain size measured. It should be noted that when a difference in relaxation times is observed, it simply indicates that the entire sample is not fully homogeneous over that domain size, and there could easily be domains that are homogeneous, along with some domains that are only partially or completely phase separated. Since any degree of phase heterogeneity can potentially indicate that there is a propensity for the sample to crystallize, the observation of a lack of homogeneity is more important than determining if the sample is completely phase separated. In most cases, solid-state NMR spectroscopy will indicate a lack of full homogeneity of the sample, rather than total phase separation.

Table 3.2. ^1H T_1 and $T_{1\rho}$ values along with the standard errors associated with the fit for FEL (as-received and amorphous) and Polymers measured via ^{13}C resonances.

Proton Relaxation Time	Felodipine		Polymers		
	As received	Amorphous	PVP	PVP/VA	PVAc
T_1 (s)	61.34±1.56	4.82±0.13	1.73±0.02	2.15±0.04	3.73±0.03
$T_{1\rho}$ (ms)	305.00±6.44	140.70±5.95	23.68±0.13	25.56±0.16	39.86±0.24

The characteristic ^{13}C resonances for FEL and polymers were identified from the ^{13}C CP/MAS spectra (Figure 3.7). It should be noted that the absolute values for ^1H T_1 and $T_{1\rho}$ relaxation times depend on the many factors like water content, particle size, etc.^{62, 63} The absolute relaxation times for the dispersions were intermediate in values when compared to those for the neat components (data not shown). For the current investigation, the differences in the relaxation times between FEL and polymer were

compared for samples in each system. The plots of ^1H T_1 differential between FEL and a given polymer are shown in Figure 3.8. As displayed in Figure 3.8, no apparent trend could be seen in the plot of ^1H T_1 differentials for all the systems. The FEL:PVP system had the same values for ^1H T_1 for FEL and polymer across all the compositions within the error of the measurement. The FEL:PVP/VA also had similar values across all compositions, although the higher drug concentrations (80% and 90%) were slightly different, still within the 95% confidence intervals. Thus, these systems are essentially homogenous on the length scale measured by ^1H T_1 , except potentially the higher drug loading samples. In the case of FEL:PVAc dispersions, no significant differences in ^1H T_1 were observed between FEL and PVAc at PVAc > 10% w/w, confirming phase uniformity at ^1H T_1 length scale of mixing for those compositions.

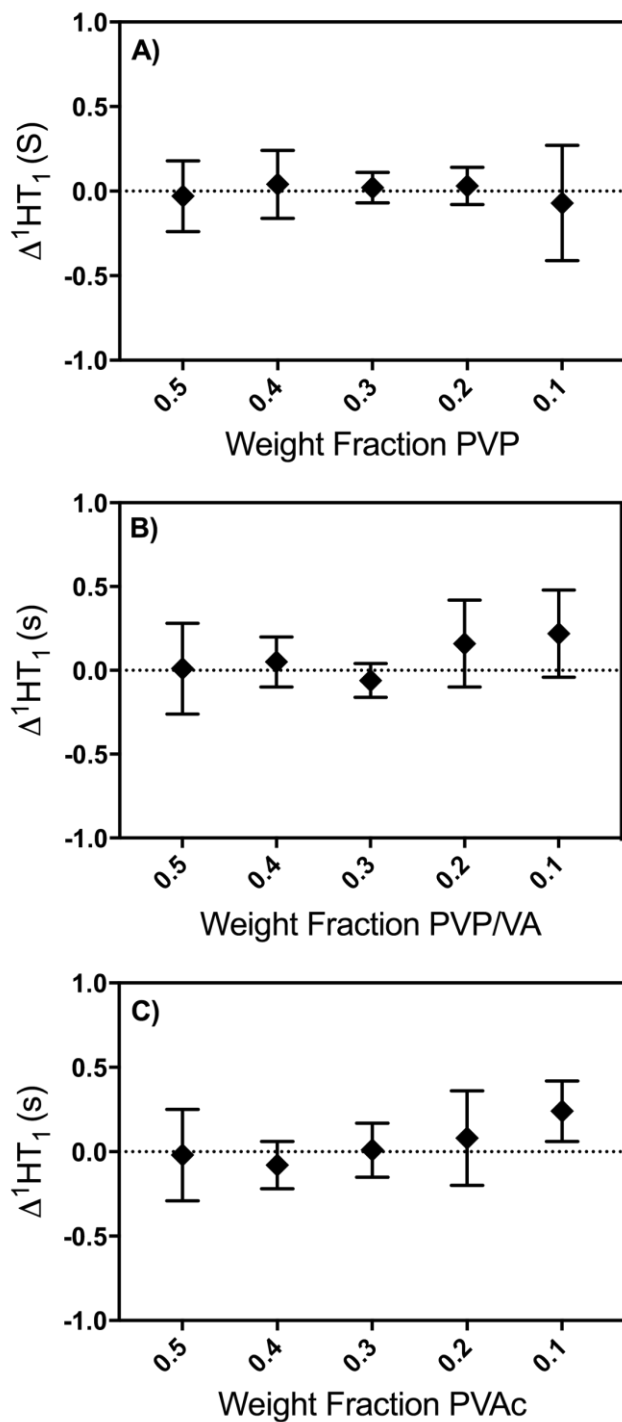


Figure 3.8. $^1\text{HT}_1$ differential between FEL and polymer in dispersions for A) FEL:PVP, B) FEL:PVP/VA and C) FEL:PVAc as a function of weight fraction of polymer. The error bar signifies 95% confidence interval associated with the fit. The dashed line represents the zero.

The relaxation time constant $^1\text{H } T_1$, which is usually a few seconds for ASDs and is usually about two orders of magnitude longer than $^1\text{H } T_{1\rho}$, is averaged out over a large distance (tens of nanometer) while $^1\text{H } T_{1\rho}$ is typically a few tens of milliseconds and is averaged out to over few nanometers.^{64, 65} This makes $^1\text{H } T_{1\rho}$ a way to determine homogeneity over a much smaller domain size compared to $^1\text{H } T_1$ values. The differential $^1\text{H } T_{1\rho}$ plots between FEL and a given polymer are presented in Figure 3.9. For all polymers, there was a change in the $^1\text{H } T_{1\rho}$ values, where the differential values increased with decreasing polymer concentration. It was observed that the FEL:PVP had the lowest differentials, followed by the FEL:PVP/VA and finally the FEL:PVAc. This trend is consistent with the crystallization trends observed in the DSC data. The samples with less than or equal to 10% PVP, 20% PVP/VA and 30% PVAc exhibited non identical $^1\text{H } T_{1\rho}$ times within the error of measurement. This clearly indicates nano-phase separation existing for these compositions on the length scale of $^1\text{H } T_{1\rho}$.

We also investigated whether the molecular weight of the PVP had an impact on phase miscibility as studied by $^1\text{H } T_{1\rho}$. The differential $^1\text{H } T_{1\rho}$ plots between FEL and different grades of PVP polymer for 90% drug loading sample are shown in Figure 3.10. It is apparent from Figure 3.10 that the $^1\text{H } T_{1\rho}$ were different for FEL and PVP grades, suggesting the presence of drug rich nano domains. The extent of phase heterogeneity can be confirmed by the magnitude of the differential. The differential is larger for the higher molecular weight polymers, which is consistent with poorer mixing and less homogeneity due to the lower mobility of polymers for higher molecular weight grades. All of these samples showed a single glass transition, crystallization in the first heating cycle, and no endotherm in the second DSC scan (data not shown).

3.3.2.3 SSNMR Relaxation Times - Determination of Domain Sizes

If the diffusion path length is smaller than the dimensions of the domains in the dispersions, two different relaxation times will be observed, one for the drug and the other for the polymer, or also different relative compositions of drug and polymer, or some combination of these. However, if the diffusion path length is larger than the dimensions of domains in the dispersions, effective spin diffusion causes single average relaxation time for both the components or various domains.⁶⁵ The upper limit of the length scale of mixing can be approximated by the one dimensional Fickian diffusion equation, which is given as:

$$\langle L^2 \rangle \geq (6DT_i) \quad (3.5)$$

where D is the spin diffusion coefficient, which depends on the average proton to proton distance as well as a dipolar interaction. Although the coefficient can vary somewhat, a typical value of 10^{-12} cm²/s is often used for rigid organic solids with a moderate proton spin density.^{32, 66} T_i is the relaxation time, T_1 or $T_{1\rho}$. Using this approach, a reasonable estimation of spatial heterogeneities can be made, which is order of magnitude different than DSC, where it is hard to confirm existence of phase homogeneity based on a single T_g . In addition, the length scale of DSC measurements is usually 10-30 nm,¹⁵ and any heterogeneity which may be present on a smaller scale will go undetected by thermal analysis. From this SSNMR study and the previous DSC study on the dispersions, the scales of domain sizes for the samples are summarized in Table 3.3. It can be clearly seen that FEL:PVP and FEL:PVP/VA dispersions were all homogeneous on a scale below 7 nm for the samples with drug loading less than 90% and 80% respectively. Additionally,

the samples with higher drug loading(s) (90% for FEL:PVP and 80% and 90 % for FEL:PVP/VA) were characterized by larger domains. From the results observed for FEL:PVAc dispersions, we see variation in the homogeneity profile across the compositions studied. The dispersions at PVAc > 30% were found to be intimately mixed on the scale of less than 5 nm. For the compositions with PVAc at 30% and 20%, we observed that domain sizes between 5-40 nm. These findings suggest that these compositions are only partially homogeneous. As to the composition with PVAc at 10%, exhibited non-homogeneous behavior with domains larger than 40 nm.

The data shown here is consistent with the presence of nano-domains being present in the samples prior to the first heating scan, and then being removed by melting in the DSC pan and reheating a second time. Unfortunately, the traditional method of determining phase homogeneity using DSC, i.e. the presence of multiple T_g events, is not useful for these samples, as all showed only a single T_g that was consistent between the first and second heating scans. However, the NMR data so far does not indicate whether the sample becomes homogeneous upon the equivalent of a second heating scan. Figure 3.11 shows the differential ^1H $T_{1\rho}$ plots between a FEL:PVP sample at 90% drug loading before and after heating in the NMR rotor, which is essentially equivalent to a first and second DSC scan. The sample prior to heating had a significant difference in ^1H $T_{1\rho}$ values, whereas the sample after second heating had almost identical ^1H $T_{1\rho}$ values, indicating that the sample was now more homogeneous. This observation is consistent with the first and second heating scans DSC data and supports the presence of nano heterogeneities in as prepared samples.

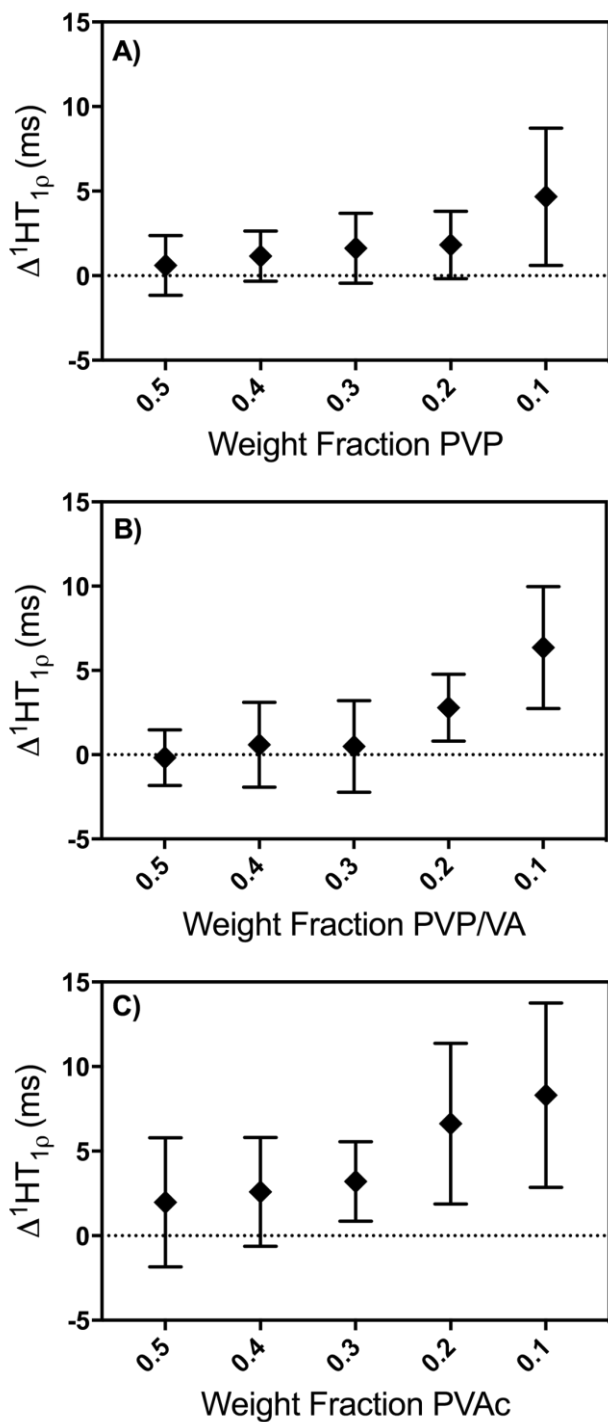


Figure 3.9. $^1\text{HT}_{1p}$ differential between FEL and polymer in dispersions for A) FEL-PVP, B) FEL:PVP/VA and C) FEL:PVAc as a function of weight fraction of polymer. The error bar signifies 95% confidence interval associated with the fit. The dashed line represents the zero.

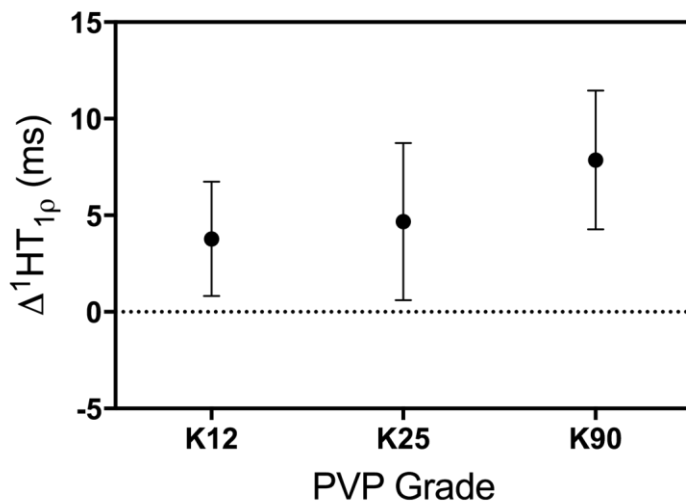


Figure 3.10. $^1\text{HT}_{1\rho}$ differential for 90:10 FEL:PVP ratio as the function of PVP grade. The error bar signifies 95% confidence interval associated with the fit. The dashed line represents the zero.

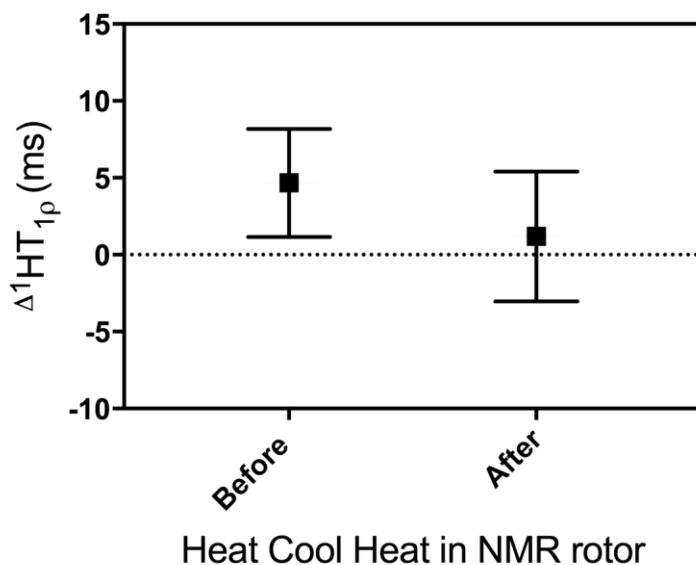


Figure 3.11. $^1\text{HT}_{1\rho}$ differential for 90:10 FEL:PVP before and after heating *in situ* in NMR rotor. The error bar signifies 95% confidence interval associated with the fit. The dashed line represents the zero.

3.3.3 ^{13}C CP/MAS Solid-State NMR Results – Molecular Interactions

In the SSNMR spectra shown in Figure 3.7, the peak intensities for the carbonyl carbons of both FEL and the various polymers change depending upon drug to polymer ratios. In addition, the chemical shifts of the carbonyl carbon (C=O) of PVP and PVP/VA change monotonically with composition (Table 3.4). In general, variation in chemical shifts is seen when the groups are involved in H-bonding.⁶⁷ This is based on the fact that the specific interactions influence the electronic density around a given carbon comprising interacting functionalities, which can induce changes in magnetic shielding due to increase or decrease in its electron density and hence the variation in the chemical shift. For FEL:PVP and FEL:PVP/VA dispersions, the formation of H-bond between the carbonyl group in polymers and an amine group in FEL resulted in a downfield shift in the resonance of the C=O carbon atom of the polymer as the amount of FEL increased in the dispersions. A downfield shift of 1 ppm relative to that of pure PVP was seen for the carbonyl carbon in the 90:10 FEL:PVP dispersion. For the 90:10 FEL:PVP/VA dispersion, a downfield shift of 0.6 ppm relative to that of pure PVP/VA was observed. In the case of FEL:PVAc dispersions, however, no detectable differences in the chemical shift were seen. This result reflects that the acetate group appears to interact very weakly with FEL. Based on the variation in the chemical shift of the carbonyl carbon of polymers, the strength of the H-bonding interactions can be ranked as PVP>PVP/VA>PVAc.

In order to study the extent of FEL-polymer interactions, the ^{13}C CP/MAS spectra were subjected to a deconvolution procedure based on a Gaussian-Lorentzian function to decompose the multiple overlapping peaks emerging from the composition-dependent

FEL:Polymer interactions. In the current investigation, we employed the relative areas of the individual species present in the carbonyl region to estimate the percentage of each component. The deconvoluted spectrum of amorphous FEL in the carbonyl region is illustrated in Figure 3.12. The spectrum revealed a main peak at 167 ppm and a shoulder at 169 ppm. The main peak was attributed to the H-bonded carbonyl group (dimer/bonded) while the shoulder was assigned to the non H-bonded carbonyl group (free/non-bonded) of FEL. These assignments agree well the results from the simulation studies (discussed in later section).

Table 3.3. Domain Sizes in amorphous solid dispersions for FEL:Polymer systems as estimated by SSNMR and DSC. Composition represents felodipine to polymer ratio.

System	Composition	Domain Size (nm)		Classification Type
		SSNMR	DSC	
FEL:PVP	50:50	< 4-5	< 30	Homogeneous
	60:40	< 4-5	< 30	Homogeneous
	70:30	< 4-5	< 30	Homogeneous
	80:20	< 4-5	< 30	Homogeneous
	90:10	5-30	< 30	Partially Homogeneous
FEL:PVP/VA	50:50	< 4-7	< 30	Homogeneous
	60:40	< 4-7	< 30	Homogeneous
	70:30	< 4-7	< 30	Homogeneous
	80:20	4-40	< 30	Partially Homogeneous
	90:10	6-45	<30	Partially Homogeneous
FEL:PVAc	50:50	< 4-5	< 30	Homogeneous
	60:40	< 4-5	< 30	Homogeneous
	70:30	5-40	< 30	Partially Homogeneous
	80:20	5-40	< 30	Partially Homogeneous
	90:10	>40	< 30	Non homogeneous

Table 3.4. ^{13}C chemical shifts (ppm) of carbonyl carbon of polymer in FEL:Polymer dispersions.

System	Resonance C=O group of polymer					
	Composition (Drug:Polymer)					
	0:100	50:50	60:40	70:30	80:20	90:10
FEL:PVP	174.9	175.3	175.4	175.5	175.7	175.9
FEL:PVP/VA	175.2	175.3	175.4	175.5	175.7	175.8
FEL:PVAc	170.2	170.1	170.1	170.2	170.2	170.3

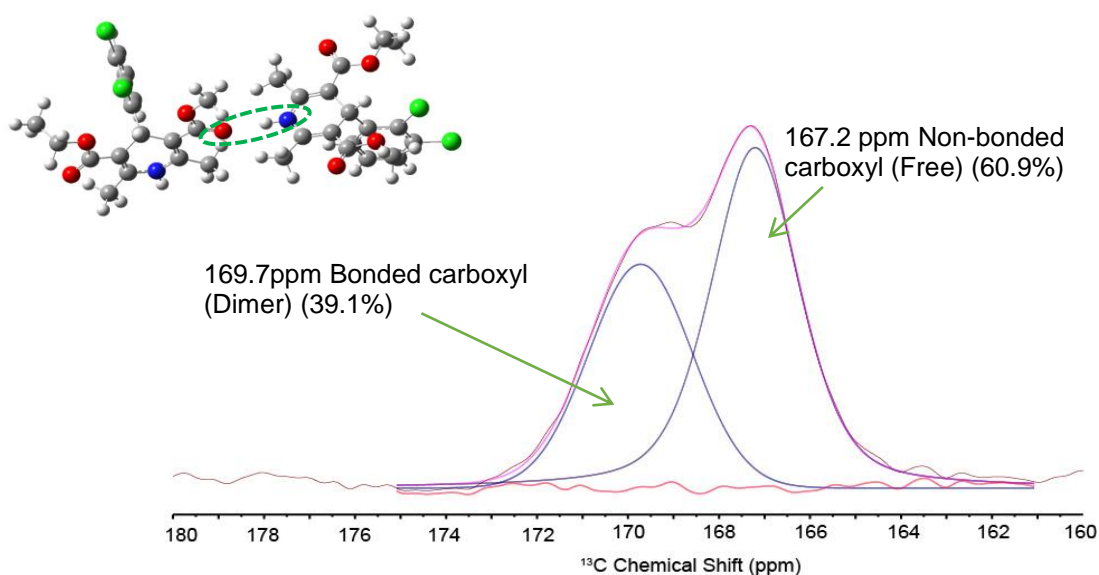


Figure 3.12. Deconvolution of carbonyl region of amorphous FEL. The experimental spectrum is shown in brown; the simulated spectrum is shown in magenta while the residual spectrum is depicted in red. The blue lines represent the fitted individual species used in deconvolution.

Amorphous FEL can exist as dimer by forming self-association via H-bond between the NH group of one molecule with the carbonyl group of the other molecule.⁶⁸ The free C=O fraction comprised 61% while the dimer C=O fraction constituted 39% of the total area. Our experimental results are in good agreement with what Xiang et al. found using molecular dynamic simulations.⁶⁸ Additionally, the carbonyl region of FEL:Polymer dispersion was deconvoluted to explore the molecular interactions of FEL with the polymers for quantitative purpose (Figure 3.13). In this study, the ¹³C carbonyl carbon region was resolved into three (PVP, PVAc) or four (PVP/VA) peaks depending on the polymer type for the systems under study. The intensity of H-bonded (dimer) carbonyl peak of FEL decreased with the increase in the polymer content in the dispersion. It was expected that a large portion of these dimer carbonyl groups of FEL were consumed by formation of the intermolecular H-bonds between FEL and the polymer. This phenomenon revealed that a new distribution of H-bonds was taking place resulting from the competition between dimer and FEL:Polymer H-bonded fractions. By calculating the total area from the contributing components corresponding to the dimer and free carbonyl of FEL, their respective fractions could be obtained. The fraction of dimer and free carbonyl carbon of FEL obtained from peak fitting exercise with the polymers is compared in Figure 3.14. Several observations can be made from the data presented in Figure 3.14. Across this composition range, the dimer fraction of FEL decreased, together with the simultaneous increase in the free fraction. This trend was same for all the three polymers. However, there is a difference in the extent of H-bonding interactions with the three polymers. In the dispersion with 50% polymer load, the dimer fraction was smallest for PVP when compared with PVP/VA and PVAc, suggesting that

the highest number of FEL molecules were bonded with PVP at the same polymer weight percentage. The extent of H-bonding interactions were in decreasing order of PVP>PVP/VA>PVAc. PVP/VA is a copolymer of 60% water-soluble vinyl pyrrolidone and 40% water-insoluble vinyl acetate by weight. Therefore, PVP/VA presents lesser interactions sites for FEL in comparison to PVP for a given weight percent of polymer. PVAc is least effective in breaking the self-association between FEL molecules owing to the fact that the vinyl acetate moiety interacts via relatively weak H-bonding.

FEL has a weak NH donor group.⁶⁹ Using our deconvolution studies, we were able to quantify the extent of H-bonding in weakly bonded systems. Usually, ¹⁵N SSNMR experiments would have been more apt to study the local environment of NH donor group. Song et al. investigated H-bonding interaction in 30% FEL spray dried dispersion with PVP/VA using ¹⁵N solid-state NMR.⁷⁰ For the dispersion sample, the authors found slight change (~ 3 ppm) in ¹⁵N chemical shift with respect to pure drug, which was attributed to the presence of intermolecular H-bonding between FEL and PVP/VA in dispersion. However, the authors mentioned that ¹⁵N chemical shifts were not conclusive because of broad nature of peaks. Furthermore, the authors confirmed H-bonding via ¹H DUMBO NMR experiments. ¹⁵N SSNMR study has its own challenges. ¹⁵N is very low natural abundance with low magnetogyric ratio, and overall low sensitivity. In order to avoid use of ¹⁵N SSNMR experiments, which might not prove to be useful with a compound like FEL, we quantified the extent of H-bonding by monitoring the changes in the ¹³C spectra in the carbonyl region. The polymers were ranked as PVP>PVP/VA>PVAc for their strength and extent of H bonding with FEL. The rank ordering presented here is in agreement with the results obtained by FTIR

spectroscopy for FEL dispersions.⁷¹ This trend could also be understood by taking into consideration basicity of proton acceptor. Wegiel et al. studied the potential of chemically diverse polymers as crystallization inhibitors for resveratrol based on the basicity of proton acceptor as one of the factors. Through their results, it is apparent that PVP carbonyl has the strongest acceptor group (the pK_{BHX} value of 1-methyl-2-pyrrolidone as an acceptor is 2.38) while PVAc has the weakest acceptor group in the polymers studied (the pK_{BHX} value of ethyl acetate as an acceptor is 1.07).⁷² Our SSNMR stimulation results also corroborated these findings (*vide infra*). Through this case study, it is evident that knowledge of phase behavior on a nanometric is needed to explain the presence of heterogeneities in ASDs.

Another interesting aspect to consider here is to understand that the disruption of the dimers is due to the formation of H-bonding interactions between the drug and polymer. In order to test this, we formulated a dispersion of FEL with inert polymer polystyrene with 50% drug loading. Polystyrene (PS) can help us understand this because it lacks any H-bond acceptors in its structure. Therefore, it has almost no capability to interact with FEL via H-bonding. From the data obtained it can be seen, there is very less change seen in the dimer and free fractions when compared to amorphous FEL for the sample with polystyrene whereas a drastic reduction in dimer fraction was observed in the case of polymers PVP, PVP/VA, and PVAc in that order (Figure 3.15). This clearly explains that in the three systems studied, disappearance of dimers is not due to dilution effect rather it can be accounted through H-bond formation.

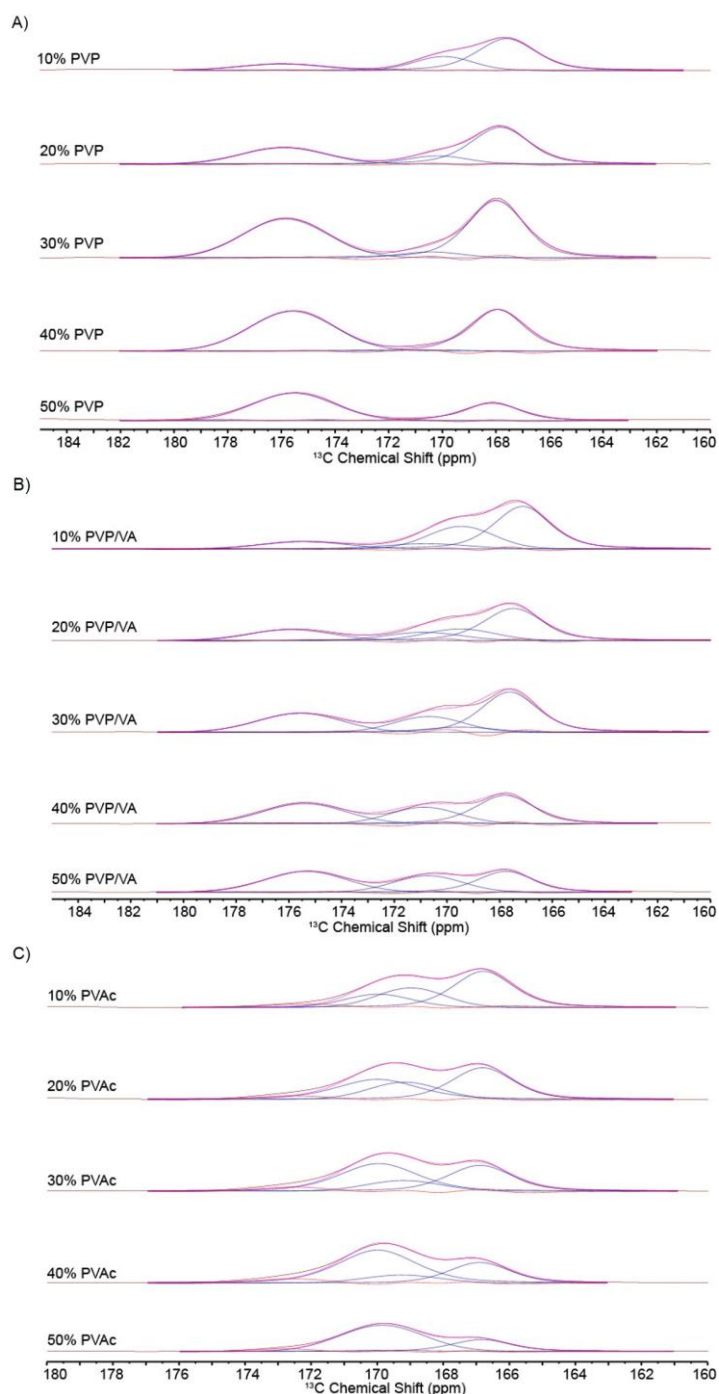


Figure 3.13. ^{13}C SSNMR sub spectra of FEL:Polymer dispersions in the carbonyl region for A) FEL:PVP, B) FEL:PVP/VA and C) FEL:PVAc. The experimental spectrum is shown in brown; the simulated spectrum is shown magenta while the residual spectrum is depicted in red. The blue lines represent the fitted individual species used in deconvolution.

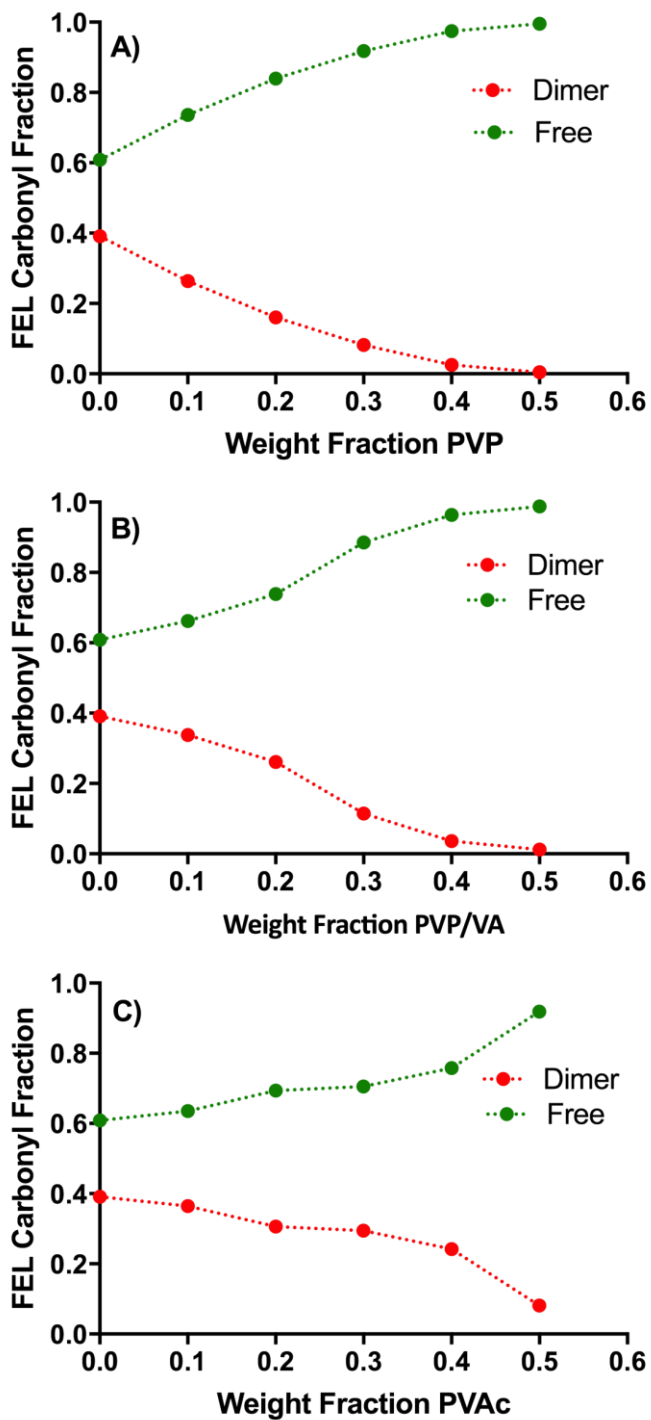


Figure 3.14. The fraction of dimer and free FEL carbonyl carbon for FEL:Polymer dispersions with A) PVP, B) PVP/VA and C) PVAc as a function of polymer weight fraction.

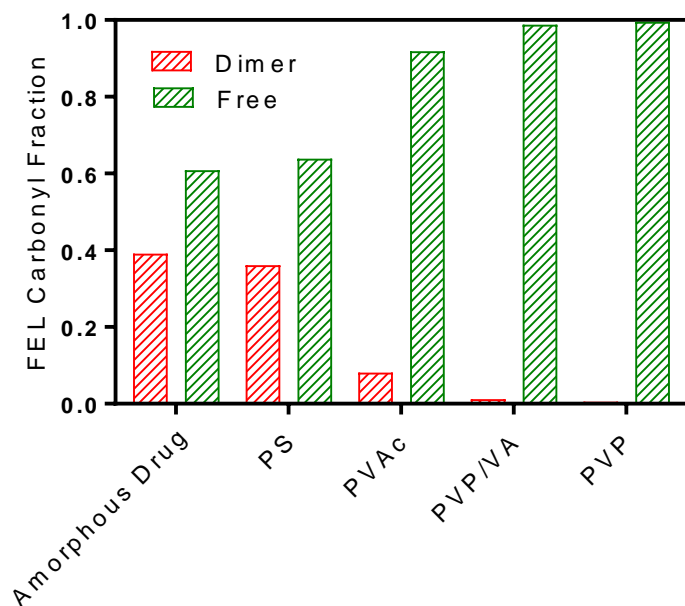


Figure 3.15. The comparison of dimer and free fractions for 50:50 FEL:Polymer samples.

3.3.4 NMR Chemical Shift Calculations for Proposed Species

Several species have been proposed in this paper, including free FEL and dimers of FEL. For this reason, DFT calculations of the proposed species were carried out to ensure that the calculated chemical shifts agreed at least qualitatively with those observed experimentally. Pure FEL was simulated as a single molecule and as dimers, with interactions between the amine and methyl-ester, and the amine and ethyl-ester as separate starting structures. The DFT-calculated chemical shifts were 170 ppm for the H-bonded ester group and 166 ppm for the non H-bonded ester, while the experimental chemical shifts were 169 ppm and 167 ppm, respectively. The results from these simulations helped to confirm the experimental ^{13}C SSNMR spectral assignment of the

pure drug, while also indicating the difference in carbonyl peak location in the presence/absence of H-bonding interactions. While the absolute values obtained from the simulation were not the same as the experimental chemical shifts, the relative positions are the same. Since the calculations of the pure FEL were consistent with the experimentally observed values, an investigation of the FEL-polymer interactions was explored.

In this study, all polymers were created as shortened versions (3-5 monomers) with 3 FEL molecules placed around in favorable positions to allow for completion of the calculations in a timely manner. The calculations illustrated the strength of H-bonding between the FEL and polymer similar to those seen in the experimental data with the theoretical rankings by chemical shift changes being the same: PVP>PVP/VA>PVAc. Although the relative ordering is the same, the absolute values for the chemical shifts are not. The theory tended to over predict the chemical shift change, suggesting stronger hydrogen bond interactions than the experimental data illustrated. This behavior can be explained by the number of H-bonded polymer monomers in the theory vs the experiment. In the calculations, all H-bond acceptor sites in the polymers were forced to H-bond, whereas in the experiment the steric hindrances from having some drug molecules so closely packed would overcome the tendency to H-bond. The ability for the short-chain polymer to bend freely allowed the three monomers to get as far apart, spatially, as they could. In a real-world polymer, the monomers would not all be even spaced out, with parts of the polymer being squeezed or bent based on the solid-state shape.

Another indicator of H-bond strength is the H-bond length (shorter H-bonds usually correlates with stronger H-bonds⁷³), and can be obtained from the optimization output files. The H-bond length (N-O bond) for the FEL-PVP, FEL-PVP/VA, and FEL-PVAc dispersions was 2.980 ± 0.007 , 3.009 ± 0.023 , and 3.077 ± 0.039 , respectively. Using these values and the standard deviations from three H-bond donor-acceptor pairs per calculation, the rank ordering of the polymers by H-bond strength follows the same rank order as found by chemical shift change (PVP>PVP/VA>PVA). According to Jeffrey, the length of H-bond in these three dispersion indicates medium strength, mostly electrostatic interactions (4-14 kcal/mol).⁷³ The distances show similarity between the PVP and PVP/VA dispersion interactions, suggesting the inclusion of vinyl acetate does not inhibit the propensity to H-bond in the PVP/VA even though the number of acceptor sites has decreased. The PVAc does not have as strong of interactions with the FEL as the PVP monomer and the larger standard deviation suggests the location of the monomer on the polymer chain affects the interactions more in the PVAc than the PVP and PVP/VA.

3.4 Conclusions

With a wide variety of analytical tools available to characterize ASDs, a major challenge lies in detecting phase heterogeneity and speciation. From this case study, it was shown how characterization via DSC alone might not be sufficient in order to understand phase heterogeneity on a nanometer level in ASDs. The results from SSNMR were able to explain the existence of nano domains with the matrix more efficiently. However, overall these two approaches agreed in their general trends. Additionally, we demonstrated how SSNMR can be used to quantify drug-polymer H-bonding. We

observed that the strength and extent of FEL:Polymer H-bonding could be ranked order as PVP>PVP/VA>PVAc. Our findings suggest that the phase behavior of ASDs is governed by the nature of H-bonding interactions between the drug and polymer. Moreover, our results from the current exercise have practical value in both understanding and formulating stable ASDs.

CHAPTER 4. UNDERSTANDING DRUG-POLYMER MISCIBILITY IN TWO STRUCTURALLY SIMILAR MOLECULES

4.1 Introduction

Over the last decade, amorphous forms of active pharmaceutical ingredients (APIs) have been used successfully as a platform technology to enhance the oral bioavailability of poorly water soluble drug candidates.¹⁻⁴ However, the amorphous state is inherently unstable and possesses the risk of converting to the more stable crystalline form during storage, manufacturing, and/or dissolution. To overcome this physical instability, a polymer is usually used as a carrier matrix to disperse the API to form an amorphous solid dispersion (ASD).⁵ The physical stabilization achieved through the use of polymers have been attributed to a combination of restricted mobility, increased glass transition temperature (T_g), and intermolecular interactions such as hydrogen bonding, van der Waals forces, and electrostatic interactions.^{6, 7} In order to develop a robust ASD, a homogenous solid dispersion is desired where the drug and polymer are mixed intimately. Since even partial phase separation can be a prelude to recrystallization, a partially mixed or completely phase separated system can potentially negate the advantages obtained from ASDs. Hence, in recent years drug-polymer miscibility has been an area of extensive research.⁸⁻¹⁰ There are two aspects to consider when it comes to drug-polymer miscibility: thermodynamic miscibility and kinetic miscibility. Both are equally important while ensuring the robust development of complex systems like ASDs.

From thermodynamics standpoint, a system is considered miscible when the free energy of mixing (ΔG_{mix}) of the two components is negative, where ΔG_{mix} is given by:

$$\Delta G_{mix} = \Delta H_{mix} - T\Delta S_{mix} \quad (4.1)$$

where ΔH_{mix} is the enthalpy of mixing, ΔS_{mix} is the entropy of mixing and T is the absolute temperature. In contrast, a positive value of ΔG_{mix} signifies unfavorable mixing and potential phase separation. The Flory-Huggins theory, which based on lattice-based solution models, has been used extensively to assess miscibility in drug-polymer blends.^{11, 12} According to this classical approach, ΔG_{mix} can be described as:

$$\Delta G_{mix} = RT(\phi_{drug} \ln \phi_{drug} + \frac{\phi_{polymer}}{m} \ln \phi_{polymer} + \chi_{drug-polymer} \phi_{drug} \phi_{polymer}) \quad (4.2)$$

where R is the gas constant, T is the absolute temperature, ϕ_{drug} and $\phi_{polymer}$ are the volume fraction of drug and polymer respectively, m is the ratio of the volume of a polymer chain to drug molecular volume and $\chi_{drug-polymer}$ is the Flory-Huggins interaction parameter between the drug and polymer. The first two terms on the right hand side defines the entropic contribution, and the last term defines the enthalpic part of the equation to the total free energy of mixing. Given that the entropic contribution is always favorable, the enthalpic contribution will therefore determine the sign of ΔG_{mix} and that makes $\chi_{drug-polymer}$ an important factor. A negative value of $\chi_{drug-polymer}$ favors mixing by making the overall value of ΔG_{mix} negative. The Flory-Huggins interaction parameter can be estimated through several methods.¹³ The most-studied approach is based on melting point depression, which was first used by Marsac et al. for pharmaceutical systems and has been used for several drug-polymer systems.¹⁴⁻¹⁷ In this approach, the depression in melting point of the drug in the presence of polymer is used to predict the interaction parameter using the following relationship:

$$\frac{1}{T_{mix}} - \frac{1}{T_{pure}} = -\frac{R}{\Delta H_{fus}} \left[\ln \phi_{drug} + \left(1 - \frac{1}{m}\right) \phi_{polymer} + \chi_{drug-polymer} \phi_{polymer}^2 \right] \quad (4.3)$$

where T_{mix} and T_{pure} are the melting points of the drug in the binary drug polymer mixture and the pure drug respectively, ΔH_{fus} is the heat of fusion of the pure drug, R is the gas constant, ϕ_{drug} and $\phi_{polymer}$ are the volume fractions of drug and polymer respectively, m is the ratio of the volume of polymer chain to drug molecular volume and $\chi_{drug-polymer}$ is the Flory-Huggins interaction parameter between the drug and polymer. While using this approach for calculating $\chi_{drug-polymer}$, several points are to be considered. Firstly, this method requires the drug and polymer to be stable over the temperature range of interest and that they form a miscible system for the melting point depression to be observed. Secondly, this approach works the best for systems where the polymer T_g is significantly lower than the melting point of the pure drug. In addition, it should be noted that this approach does not provide a universal value of $\chi_{drug-polymer}$ but an estimation close to the melting point of the drug. Although this approach has its own limitations, it has shown to give a reasonable and reliable estimate of $\chi_{drug-polymer}$ in comparison to theoretical approach based on solubility parameters.

The thermodynamic drug-polymer miscibility relates to the phase behavior in the equilibrium state. However, in many real situations the drug molecules in the polymeric matrix may never achieve thermodynamic equilibrium but remain kinetically stable. Hence, it is imperative to assess the kinetic miscibility as well. The kinetic miscibility can be assessed using calorimetric approaches or spectroscopic methods. DSC has been used traditionally to evaluate kinetic miscibility based on the number of T_g events. A

single T_g denotes a miscible system whereas multiple T_g denotes an immiscible system.¹⁸ It has been shown that the rule of a single T_g does not necessarily imply phase homogeneity.¹⁹ Moreover, since the resolution scale for a DSC measurement is generally taken to be > 30 nm, any heterogeneity, which may be present on a smaller scale, may go undetected by DSC analysis. In recent years, spectroscopic techniques like SSNMR has been used to study phase homogeneity on a molecular level based on the proton relaxation time measurements ($^1\text{H } T_1$ and $^1\text{H } T_{1\rho}$).²⁰⁻²² Through these measurements, it is possible to study phase homogeneity on two length scales of mixing. In theory, they can be used to give semi quantitative information on domain sizes and can study phase mixing at domain sizes < 5 nm. In addition, SSNMR can also provide additional information on molecular interactions and mobility.²³ We have earlier shown how in depth analysis can be performed through SSNMR with respect to phase homogeneity and molecular interactions in Chapter 3.

Considering the growing interest in understanding drug-polymer miscibility and how important is to the overall stability of the system, it is useful to evaluate both the aspects miscibility. From this perspective, it would be interesting to use this dual approach to perform a comparative study of two common model BCS class II drugs: nifedipne (NIF) and felodipine (FEL) when formulated as an ASD with Soluplus[®]. Both drugs have similar structural features and properties like T_g ²⁴ and it therefore important to understand the differences if any between them in terms of drug polymer miscibility and interactions. We have previously studied FEL with polymers like PVP, PVP/VA, PVAc and NIF has also been studied in the Munson group before. Thus, we have prior baseline knowledge of these APIs. Recently, Soluplus[®] has been used as a polymeric

matrix and solubilizer for ASDs.^{15, 25} Its low T_g and good thermal stability makes it especially amenable for hot melt extrusion processes and spray drying.²⁶ Chemically, Soluplus[®] is a polyvinyl caprolactam–polyvinylacetate–polyethylene glycol graft copolymer, which was first launched by BASF in 2009.

In this chapter, the melting point depression approach was used to estimate χ value for NIF/FEL-Soluplus systems. Also, Gibb's free energy of mixing was calculated using χ at respective temperatures and phase diagrams were predicted from data obtained from thermal analysis. Moreover, SSNMR was employed to evaluate kinetic miscibility for both systems at different compositions and a comparison of intermolecular interactions was achieved by analyzing ^{13}C SSNMR spectra.

4.2 Experimental

4.2.1 Materials

Nifedipine and felodipine were purchased from TCI America (Portland, OR) and BOC Sciences (Shirley, NY) respectively. Soluplus was a generous gift from BASF (Edison, NJ). Soluplus was stored over Drierite at all times and vacuum dried at 40 °C overnight every time before use. NIF is photo labile and hence was protected from light whenever possible. The chemical structures of raw materials and their physiochemical properties are listed in Table 4.1.

Table 4.1. Physicochemical properties of raw materials.

<i>Compound</i>	<i>Chemical Structure</i>	<i>T_g</i> (°C)	<i>Molecular Weight</i> (g/mol)	<i>Density</i> (g/cm ³)
Felodipine		47.1	384.26	1.28
Nifedipine		46.7	346.34	1.2
Soluplus		77.7	118000	1.2

4.2.2 Solubility Parameter Calculation

The solubility parameters were calculated using the Hoftzer-Van Krevelen group contribution method²⁷, which is expressed as:

$$\delta^2 = \delta_d^2 + \delta_p^2 + \delta_h^2 \quad (4.4)$$

where δ_d , δ_p and δ_h are contribution from dispersive forces, polar forces and hydrogen bonding respectively. These may be individually defined as:

$$\delta_d = \frac{\Sigma F_{di}}{V} \quad (4.5)$$

$$\delta_p = \frac{\sqrt{\Sigma F_{pi}^2}}{V} \quad (4.6)$$

$$\delta_h = \frac{\sqrt{\Sigma E_{hi}}}{V} \quad (4.7)$$

F_{di} is the molar attraction constant due to dispersion component, F_{pi} is the molar attraction constant due to polar component, E_h is the group contribution to hydrogen bonding energy and V is the molar volume.

4.2.3 Preparation of Amorphous Materials

Amorphous FEL and NIF were prepared by melting crystalline as received materials (5 °C above their respective melting points) in a Teflon beaker over an hot oil bath. Once melted, the molten mass was quenched cooled using liquid N₂ to generate the glassy form and was lightly ground in a mortar and pestle. The pure amorphous samples were analyzed immediately to prevent crystallization. The dispersions samples were prepared at various drug loadings from 50% to 90% w/w via melt quenching. To ensure optimum mixing between the drug and polymer, the physical mixtures were first cryomilled (SPEX SamplePrep 6770 Freezer Mill, SPEX SamplePrep, Metuchen, NJ) at 10 Hz for five cycles, each comprising 2 min of milling and 2 min of cooling in a liquid N₂ environment. The cryomilled mixtures were then further treated for melt quenching

with the same procedure as used for the neat amorphous drugs. The dispersion samples thus generated were then vacuum dried at room temperature and stored at -20 °C in desiccators containing Drierite until further analyzed.

4.2.4 Thermal Analysis

DSC experiments were performed using a Q2000 (TA Instruments, New Castle, DE) equipped with a refrigerated cooling accessory (RCS90). Nitrogen gas at a flow rate of 50 mL/min used to maintain the inert atmosphere. The instrument was calibrated using indium and sapphire.

Melting Point Depression Measurement. Mixtures of NIF/FEL with Soluplus were prepared with via cryo milling at 10 Hz for three cycles, each comprising 2 min of milling and 2 min of cooling in a liquid N₂ environment at various weight ratios. These mixtures were then packed in T_{zero} aluminum pans (5-7 mg) and heated at 1 °C/min from 20 to 200 °C. All samples were analyzed in duplicate and the mean values of melting peak was used.

Measurement of T_g. The samples were subjected to modulated DSC experiments with modulation of 0.5 °C every 60 s. To record the T_g values of pure drugs, the amorphous form was generated *in situ* DSC by heating the samples at 10 °C/min from 20 to 180 °C, cooled at a rate of 30 °C/min to -10 °C, and then reheated at 2 °C/min to just above their melting points. For the dispersion samples prepared via melt quenching, the samples (5-7 mg) were packed in T_{zero} aluminum pans and treated with heat-cool-heat cycle. The samples were first heated at the rate of 5 °C/min to 185 °C followed by cooling to -10 °C at a cooling rate of -30 °C/min and reheated at the rate of 5 °C/min to 185 °C. The T_g values were recorded from the second heating cycle and determined by

half height at mid point using the Universal Analysis software (TA Instruments, Newcastle, DE). All samples were run in duplicate and the mean T_g values were reported.

Theoretical prediction of T_g . The T_g values of solid dispersions were predicted using the Gordon Taylor equation²⁸, which is expressed as:

$$T_g = \frac{[(w_1 T_{g1}) + (k T_{g2})]}{[w_1 + (k w_2)]} \quad (4.8)$$

$$k = \frac{T_{g1} * \rho_1}{T_{g2} * \rho_2} \quad (4.9)$$

where T_g is the glass transition of the dispersions, T_{g1} and T_{g2} are those of pure components, w_1 and w_2 are the weight fractions of each component, and $\rho_{1,2}$ are the true densities of each component. The corresponding ρ values were obtained from literature.

4.2.5 ^{13}C Solid-state NMR Spectroscopy

^{13}C SSNMR spectra were acquired using a Tecmag Redstone spectrometer (Tecmag Inc., Houston, TX) operating at approximately 300 MHz for ^1H and 75 MHz for ^{13}C . Samples were packed into 7.5 mm zirconia rotors and sealed with Teflon or Kel-F end-caps (Revolution NMR LLC, Fort Collins, CO). One dimensional ^{13}C spectra were acquired using cross polarization magic angle spinning (CP/MAS) at 4 kHz, using total sideband suppression (TOSS)²⁹ and SPINAL64³⁰ decoupling. The ^1H 90° pulse width was set to 4.0 μs and contact time of 1.5 ms was used in all the measurements. The ^{13}C chemical shift scale was referenced with the methyl peak of 3-methylglutaric acid, which was set to 18.84 ppm.³¹

The NMR spectra of pure amorphous drugs and the dispersion samples were subsequently deconvoluted using MNOVA software (Mestrelab Research, Version 10.0) in the carbonyl region. The parameters for peak width and Gaussian/Lorentzian ratio were kept same while the constraint for peak position was kept at $\pm 5\%$. The area percentages for the various species were calculated from the total area of the peaks deconvoluted and the drug peaks were then normalized to their respective carbonyl peaks.

The proton relaxation times were detected via ^{13}C nucleus to facilitate the identification of regions for respective components. The chemical shift regions specific to FEL/NIF and Soluplus were integrated to obtain the relaxation times. Proton spin-lattice relaxation times in the laboratory frame ($^1\text{H } T_1$) were measured using a ^{13}C -detected saturation recovery pulse sequence with TOSS. $^1\text{H } T_1$ was obtained by fitting integral-recovery time data by the following equation:

$$M(t) = M_0(1 - e^{-\frac{t}{T_1}}) \quad (4.10)$$

where $M(t)$ is the integrated signal intensity at delay time t , M_0 is an amplitude parameter from the fit, and T_1 is the spin-lattice relaxation time in the laboratory frame. Proton relaxation times in the rotating frame ($^1\text{H } T_{1\rho}$) were measured by varying the spin lock duration time after a 90° pulse. The $T_{1\rho}$ decay time was obtained by analyzing the integrated carbon signal intensity according to the following equation:

$$M(t) = M_0 e^{-\frac{t}{T_{1\rho}}} \quad (4.11)$$

where $M(t)$ is the integrated peak intensity and t is the spin-lock duration time. M_0 is an amplitude parameter from the fit, and $T_{1\rho}$ is the fitted spin-lattice relaxation time in the rotating frame. Data was fitted using GraphPad Prism software (GraphPad Software, Inc., La Jolla, CA).

4.3 Results and Discussion

4.3.1 Baseline Characterization

The melt quenched amorphous drugs were observed to be X-ray amorphous (data not shown). The T_g values of model drugs were obtained by generating the amorphous form *in situ* in the DSC pan. The as-prepared dispersion samples were also observed to be X-ray amorphous (data not shown) and the same observation was confirmed by ^{13}C SSNMR spectra (*vide infra*).

4.3.2 Solubility Parameters

In order to understand and predict miscibility between FEL/NIF and Soluplus, theoretical solubility parameters (δ) were calculated via Hoftyzer-Van Krevelen group contribution approach. Solubility parameter values for the materials used in the current study are listed in Table 4.2. The difference of the solubility parameter ($\Delta\delta$) of two materials is suggestive of miscibility or immiscibility. For systems having $\Delta\delta < 7.0 \text{ MPa}^{1/2}$ are likely to be miscible whereas $\Delta\delta > 10.0 \text{ MPa}^{1/2}$ are likely to be immiscible.³² In the present case, the solubility parameters for FEL and NIF were calculated to be 20.53 and 19.43 respectively. Meanwhile, the solubility parameter for Soluplus was reported to be 21.79.³³ The $\Delta\delta$ values for FEL:SOL and NIF:SOL were less than $7.0 \text{ MPa}^{1/2}$.

Table 4.2. Calculation showing solubility parameters of felodipine and nifedipine based on the Hoftyzer-Van Krevelen group contribution method.

Group	Frequency	F_{di} ($J^{1/2} cm^{3/2} mol^{-1}$)	F_{pi}^2 ($J cm^3 mol^{-2}$)	E_{hi} (J/mol)
Felodipine				
CH ₃	4	1680	0	0
CH ₂	1	270	0	0
NH	1	160	44100	3100
Cl	2	900	605000	800
COO	2	780	480200	14000
Phenylene	1	1270	12100	0
C=	4	280	0	0
ring (6)	1	190	0	0
CH	1	80	0	0
Sum	-	5610	1141400	17900
δ = 22.74	-	20.86	3.97	8.16
Nifedipine				
CH ₃	4	1680	0	0
CH ₂	0	0	0	0
NH	1	160	44100	3100
NO ₂	1	500	1144900	1500
COO	2	780	480200	14000
Phenylene	1	1270	12100	0
C=	4	280	0	0
ring (6)	1	190	0	0
CH	1	80	0	0
Sum	-	4940	1681300	18600
δ = 19.43	-	17.12	4.49	8.03

Thus, it can be predicted that both the drugs should exhibit miscibility with Soluplus. This approach has been widely used in literature but comes with several limitations.^{14, 18} For instance, in the case of drug-polymer mixtures expected to form hydrogen bonding or ionic bonding, this method can result in erroneous outcomes. Nonetheless, this approach could be useful as a means for initial miscibility assessment and needs further confirmation from other experimental based methods.

4.3.3 Differential Scanning Calorimetry

4.3.3.1 Estimation of Drug-Polymer Miscibility

The melting point depression approach was used to estimate the Flory-Huggins interaction parameter between FEL/NIF and Soluplus. The depression in melting point of the drug is usually observed in the case of a miscible drug-polymer system and has been used as an indicator of drug-polymer miscibility. This phenomenon results from the negative free energy of mixing linked with the spontaneous mixing of the polymer with the drug and the chemical potential of the drug in the mixture is lowered than the pure drug melt.¹⁴ The extent of melting point depression observed for FEL and NIF systems is used here to distinguish their propensities to mix with Soluplus. From the analysis of the melting point depression data (Figure 4.1) it is shown that melting point of both FEL and NIF decreased with increase in Soluplus content, which is indicative of both the drugs being miscible with Soluplus. However, larger depression in melting point was observed in NIF-SOL system in comparison to FEL-SOL system especially at higher Soluplus concentrations, which potentially resulted from higher miscibility of NIF with Soluplus than FEL. The interaction parameter was estimated from the slopes of $(1/T_{\text{mix}} - 1/T_{\text{pure}}) *$

$(\Delta H_{fus}/-R) - \ln(\phi_{drug}) - (1-1/m)\phi_{polymer}$ plots against the second power of the polymer volume fraction ($\phi_{polymer}^2$) by rearranging the Flory-Huggins equation (Figure 4.2). The linear regression analysis was done for the data points with low Soluplus weight fractions, as at higher concentrations the linearity was lost. Marsac et al. have earlier reported the phenomenon of nonlinear relationship at higher polymer weight fractions.¹⁴ For NIF-SOL and FEL-SOL systems, interaction parameters with a value of -1.413 ($r^2 = 0.991$) and -0.743 ($r^2 = 0.998$) were obtained respectively. The negative value of the interaction parameter for both the systems is suggestive of miscibility and an endothermic heat of mixing. It should be noted that the value obtained with NIF is more negative than FEL, which is reflective of more favorable mixing of Soluplus with the former. In addition, it is also important to mention that the Flory-Huggins interaction parameter is not constant but a function of temperature³⁴, which can be empirically described by:

$$\chi_{drug-polymer} = A + \frac{B}{T} \quad (4.12)$$

where A and B are constants. In order to further understand miscibility between the two components, the melting point depression data was then used to construct a plot $\chi_{drug-polymer}$ versus $1/T_m$ for each system. The plots were used to obtain the values of the entropic (A) and enthalpic (B) contributions to $\chi_{drug-polymer}$ for both the systems. The values of constants “A” and “B” are listed in Table 4.3. Through this analysis, a series of $\chi_{drug-polymer}$ values could be calculated at different temperatures. In addition, this also enabled construction of Gibb’s free energy diagrams as a function of both temperature and composition for each system by combining eqs 4.2 and 4.3 with eq 4.12. The Gibb’s free energy of mixing diagrams for FEL-SOL and NIF-SOL as a function of temperature

and composition are shown in Figure 4.3. It has been pointed out that a negative ΔG_{mix} value is reflective of a miscible system, whereas a positive value signifies a likely partial miscible or immiscible system.¹¹ As shown in Figure 4.3 A, it is apparent that at temperatures ≥ 120 °C the value of $\Delta G_{\text{mix}}/RT$ was negative at all compositions for FEL-SOL system. It is interesting to note that at temperatures ≤ 100 °C all compositions were found to have a positive value of $\Delta G_{\text{mix}}/RT$ and especially at 25 °C larger positive values were obtained. Accordingly, at 25 °C the calculated solubility (% wt) of FEL in Soluplus was found to be extremely low ($\sim 8.29 \times 10^{-9}$). It is clear from Figure 4.3 B that at temperatures ≥ 100 °C resulted in a negative value of $\Delta G_{\text{mix}}/RT$, suggesting miscibility at all compositions in the case of NIF-SOL system. Furthermore, at 25 °C a positive value of $\Delta G_{\text{mix}}/RT$ was observed at all compositions. Consequently, the calculated solubility (% wt) of NIF in Soluplus at 25 °C was estimated to be 8.54×10^{-3} . Overall, it can be predicted that NIF has better miscibility and solubility than FEL in Soluplus. This exercise is useful in selection of the components during ASD formulation development and also help in optimizing process parameters for processes like hot melt extrusion.

Table 4.3. F-H interaction constants A and B as obtained from melting point depression data.

Constant	NIF:SOL	FEL:SOL
A	-11.23	-56.49
B	22499	4270.1

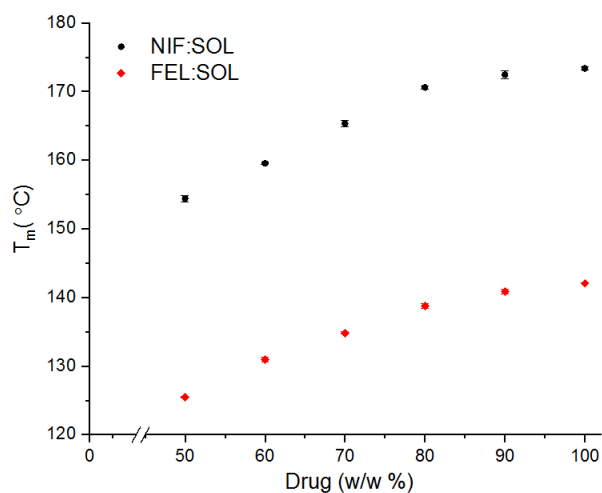


Figure 4.1. Melting temperatures (T_m) of NIF (black circles) and FEL (red diamonds) as a function of drug weight percent. The data points represent the average of two separate runs and errors bars represent the standard deviation.

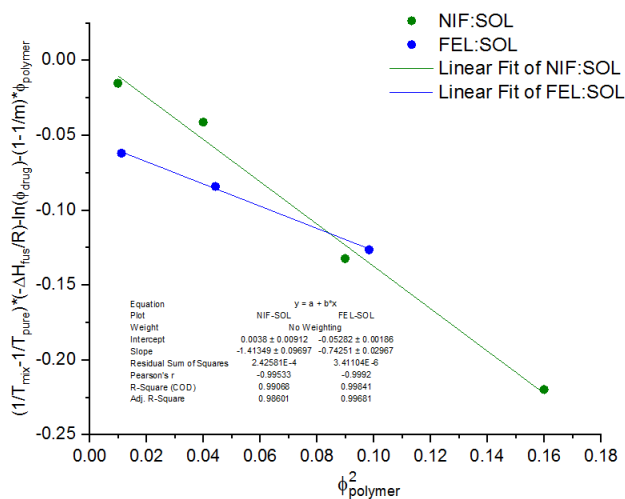


Figure 4.2. Plot used to calculate the Flory-Huggins interaction parameter for NIF:SOL (green circles) and FEL:SOL (blue circles). The slope would represent the value of the Flory-Huggins interaction parameter. The respective values of slope were obtained using linear regression.

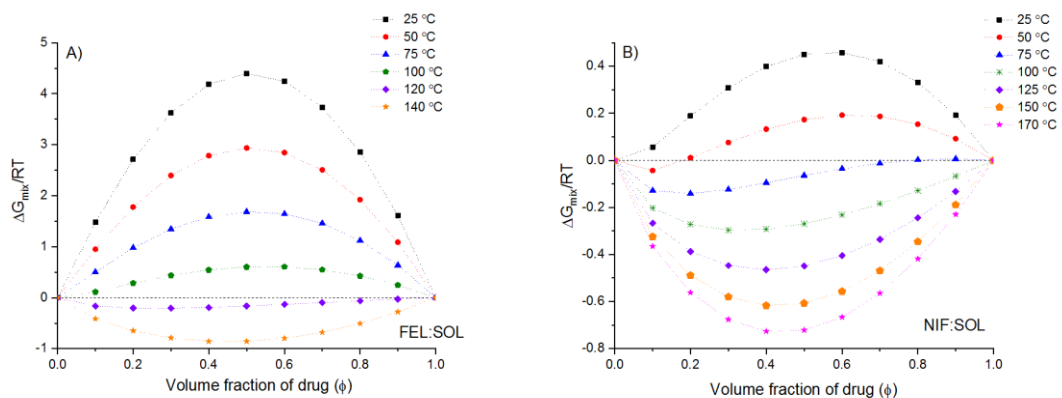


Figure 4.3. A plot of $\Delta G_{\text{mix}}/RT$ as a function of volume fraction of drug (ϕ_{drug}) for (A) FEL:SOL and (B) NIF-SOL.

Another important piece of information that can be further generated here is the temperature-composition phase diagram. In theory, phase diagrams can allow estimation of regions of stability, instability and metastability. Typically, temperature phase diagrams consists of two curves: binodal and spinodal. The binodal curve represents the phase boundary between the stable and metastable region, whereas the spinodal curve represents the phase boundary between the unstable and metastable region. To the right side of spinodal curve, phase separation is expected to occur spontaneously. On the other hand in the metastable region, the system will start to phase separate only after large fluctuation in drug density.³⁵ Moreover, the spinodal phase separation curve can be calculated by equating the second derivative of the free energy to zero as described by:

$$T_s = \frac{2B}{\left(\frac{1}{\phi_{\text{drug}}}\right) + \left(\frac{1}{m\phi_{\text{polymer}}}\right) - 2A} \quad (4.13)$$

The phase diagrams for each system are shown in Figure 4.4. It is evident from Figure 4.4 that both the systems showed temperature dependent solubility and miscibility

but relative to FEL-SOL system, the phase diagram of NIF-SOL shifted towards the higher composition range. Moreover, with NIF-SOL system larger gap was observed between the solubility and miscibility curves. This suggests that NIF has higher solubility and miscibility in Soluplus than FEL. The construction of phase diagrams is a useful exercise since detailed information could be extracted with regards to potential processing conditions, identification of metastable regions, achievable drug loadings and storage temperature.^{12, 35}

4.3.3.2 Glass Transition Temperature (T_g)

The dispersions samples prepared from melt quenching process were subjected to heat cool heat cycle in MDSC experiments. The glass transition temperature event (T_g) from the first cycle was hard to detect due to the nature of very broad and undistinguished signal, a characteristic trait of Soluplus dispersions (data not shown). Hence, the T_g values were recorded from the thermograms of the second heating cycle for each set of dispersions. A single T_g event was observed in the second heating cycle across the composition range studied for both the systems, possibly signifying phase miscibility based on a single T_g rule. As the T_g values of neat amorphous NIF and FEL were close to each other, the experimental T_g values for the dispersions samples from both the systems were found to be similar. The experimental T_g values were compared to the predicted T_g values calculated from the Gordon-Taylor equation in order to understand the nature of deviations as shown in Figure 4.5. The predicted Gordon-Taylor curves were near identical to each other. It is apparent from the Figure 4.5 that both the systems exhibited negative deviation with regard to the predicted curves. In each system, almost identical magnitude of negative deviation was observed except for 10% Soluplus

sample with NIF. The deviation from the ideal behavior is generally considered as indicative of differences in the strength of homointeractions and heterointeractions between the components.¹⁸ A negative deviation could result from the stronger homointeractions leading to an increase in free volume upon mixing and hence a lower T_g value than predicted. A number of other systems have shown a similar behavior.^{36, 37} These empirical models have been used extensively but have their own limitations. Therefore, the results should be interpreted with caution, especially for systems exhibiting deviations. Nonetheless, in the present study Gordon-Taylor equation predicted the presence of specific intermolecular interactions between the components and would be further studied in subsequent sections.

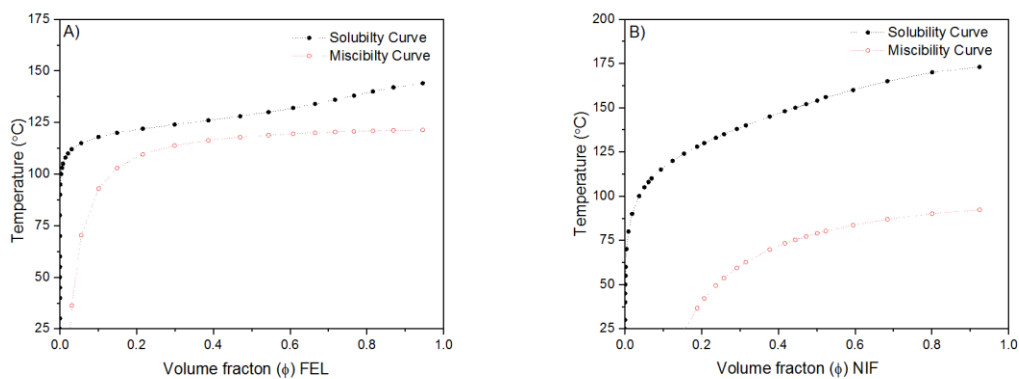


Figure 4.4. Binary phase diagram for (A) FEL:SOL and (B) NIF:SOL.

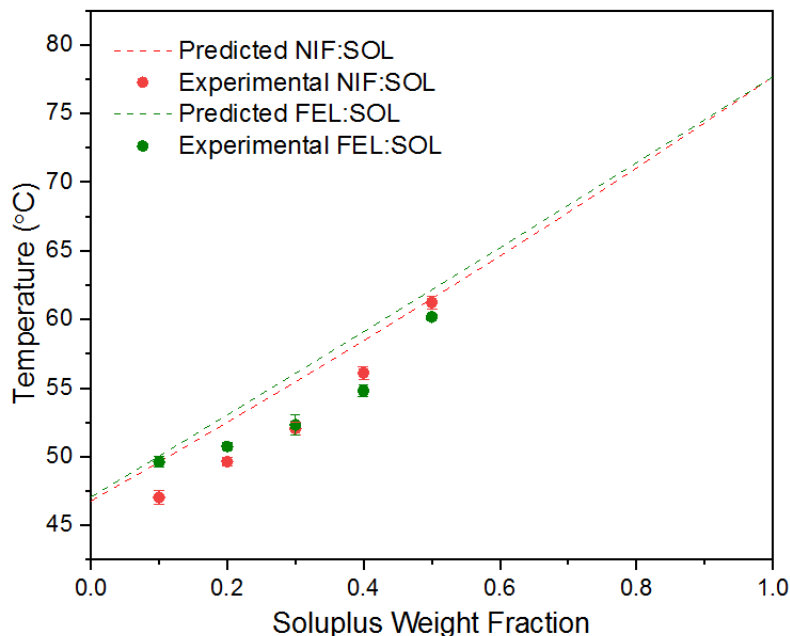


Figure 4.5. A plot showing experimental and predicted T_g as a function of Soluplus weight fraction. The red and green circles represent mean experimental T_g values from DSC second heating cycle for NIF:SOL and FEL:SOL respectively. The error bars denote the standard deviation. The broken lines represent the predicted T_g values from the Gordon-Taylor equation.

To summarize the results discussed in this section, melting point depression data analysis yielded the Flory-Huggins interaction parameter and predicted the thermodynamic miscibility and solubility for both systems. Our results indicated that the interaction potential with Soluplus was higher with NIF and same for the solubility and miscibility. Despite several limitations associated with the melting point depression approach, a reasonable comparison could be drawn for both the systems. We ensured sufficient mixing between the drug and polymer via cryo-ground mixtures, giving each component a better chance for optimum interaction. In addition, the melting point temperature of both the drugs was higher than the T_g of Soluplus, allowing Soluplus to

exist in the supercooled liquid state and thereby ensuring better mixing and interaction. The thermodynamic miscibility between FEL/NIF and Soluplus is an important parameter to study but an equally important aspect to consider here is the kinetic mixing between them. The state of mixing between FEL/NIF and Soluplus will be investigated in the later section from SSNMR. The predictions derived from Gordon-Taylor equation were consistent in both the systems and possibly pointed to the presence of specific intermolecular interactions.

4.3.4 FTIR Spectroscopy

In order to understand the nature of underlying interactions between the drug and polymer, FTIR spectra were recorded for ASDs and compared with the pure components. Both FEL and NIF have hydrogen bond donor and acceptor groups in their structures. It has been shown in the literature that the amine group in the structure of FEL and NIF can participate in hydrogen bonding. Soluplus has potential sites in its structure to interact through hydrogen bonding as well. Hence, any changes in the peak position and shape in the FTIR spectrum relative to the pure components would provide evidence for any specific interactions such as hydrogen bonding. FTIR spectra of FEL:SOL and NIF:SOL system are presented in Figure 4.6. For amorphous FEL (Plot A), two peaks marked the NH stretching region: a main peak at 3331 cm^{-1} and a shoulder peak at 3415 cm^{-1} . These were assigned to a NH group bonded to the carbonyl group of adjacent molecule of FEL, and to a non-hydrogen bonded NH group, respectively. The FTIR spectrum of amorphous NIF in the NH stretching region was characterized by similar peak positions (Plot B).³⁸ With increasing SOL content, the hydrogen bonded NH peak became broader and a shoulder started to develop around 3290 cm^{-1} in the case of

FEL:SOL system. The shoulder peak increased in intensity with increase in SOL concentration and can be attributed to FEL-SOL hydrogen bonding interaction, wherein the amine group of FEL acts as a donor. In the case of NIF:SOL, similar trend was observed with increasing SOL weight %. In the carbonyl region (Plots C and D), the spectrum of pure Soluplus displayed two peaks assigned to ester carbonyl (1732 cm^{-1}) and tertiary amide carbonyl (1632 cm^{-1}).²⁵ For hydrogen bonding to take place between FEL/NIF and Soluplus, either or both of these carbonyl groups can act as a proton acceptor leading to change in the peak positions in the carbonyl region. However, no direct evidence of any change for these peaks could be obtained because of heavy overlap from FEL and NIF absorbance peaks (Plots C and D). From FTIR analysis, it is clear that both FEL and NIF interacted in a similar fashion with Soluplus and formed possibly drug-polymer hydrogen bonds interactions.

4.3.5 Solid-state NMR Spectroscopy

In recent years, SSNMR has been used to analyze molecular interactions, homogeneity and phase behavior in ASDs on a molecular level.²³ We utilized SSNMR to further elucidate the intermolecular interactions between FEL/NIF and Soluplus. The ^{13}C CP/MAS spectra of the as received materials are displayed in Figure 4.7. The assignments of the resonances for crystalline FEL were reported previously in chapter 4, whereas for crystalline NIF the peaks were assigned based on previous literature reports.²¹ The spectrum of Soluplus consisted of resonances at 175.7 ppm from the carbonyl group of vinylcaprolactam ring, at 170.6 ppm due to carbonyl group of acetate and in the range of 22 to 72 ppm ascribed to aliphatic carbons. The comparison of ^{13}C spectra of dispersions with the pure amorphous components is shown in Figure 4.8. It is

clear from the spectra of dispersions that melt quenching rendered samples amorphous as evident by broad resonances in contrast to sharp resonances seen for crystalline drugs. In the spectra of dispersion samples for both FEL:SOL and NIF:SOL, the intensity of Soluplus peaks decreased with decrease in Soluplus concentration and vice versa. In addition, the same trend was observed for drug peaks as its concentration varied. In general, the spectra of dispersion samples were superposition of the spectra of the pure amorphous components except in the carbonyl region, where some differences were observed. In the carbonyl region (160-180 ppm), some apparent differences in chemical shifts were seen. The carbonyl peak of Soluplus at 175.7 ppm showed a downward shift in the dispersion samples for both systems with decrease in Soluplus content. At 10% Soluplus loading, the peak resonated further downfield around 177.2 ppm for both the systems. This variation in chemical shift may indicate formation of hydrogen bonding between FEL/NIF and Soluplus. The carbonyl peak of 170.6 ppm from acetate functional group did not seem to shift to this extent and no apparent movement could be detected for this peak. In this case, the carbonyl group from vinylcaprolactam is a stronger proton acceptor than acetate group and hence participates in hydrogen bond formation. The strength of this interaction seems to be similar in both the systems as evident by near identical downfield shift behavior. The results seen here are in agreement with previous study conducted in Chapter 3, wherein acetate group interacted to a lesser extent in comparison to the pyrrolidone group. In addition, it is interesting to note here that a larger downfield shift was seen with Soluplus than PVP, which may signify that the acceptor strength of the carbonyl group of vinylcaprolactam moiety is stronger than the carbonyl group of pyrrolidone ring.

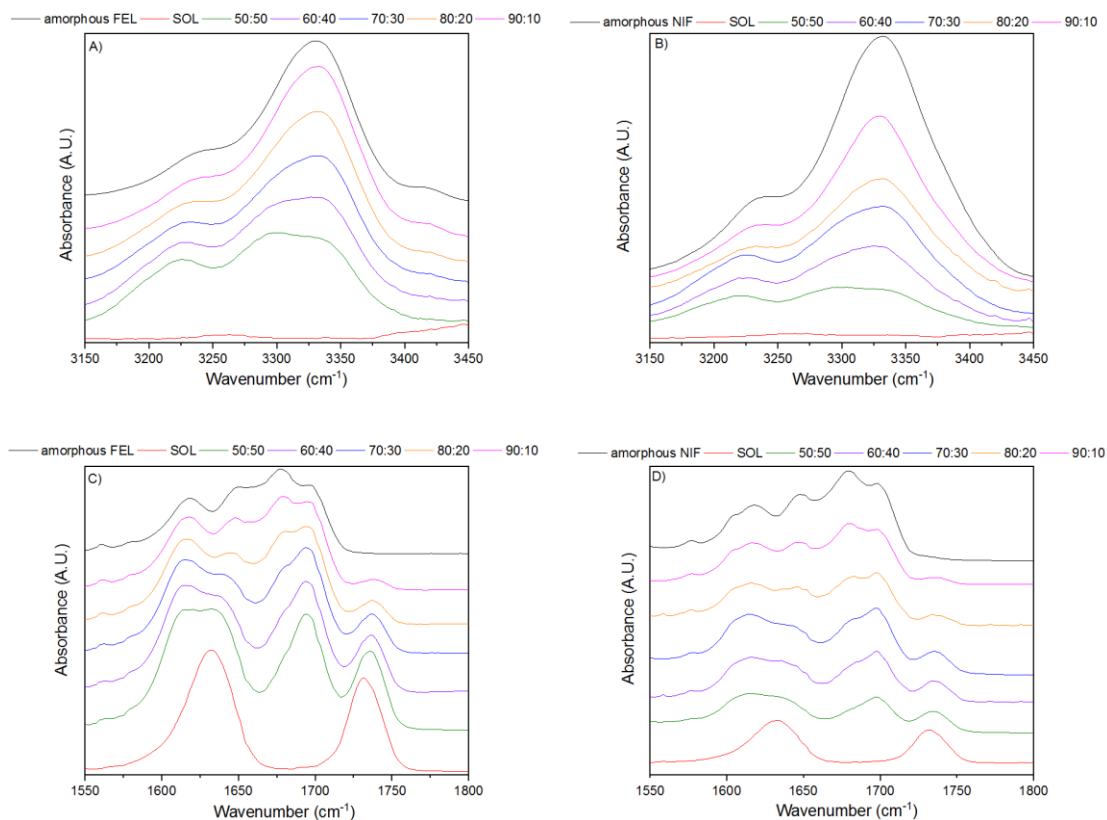


Figure 4.6. FTIR spectra for FEL:SOL (plots A, C) and NIF:SOL (plots B, D) samples. The NH stretching region (3150-3450 cm⁻¹) and the carbonyl stretching region (1550-1800 cm⁻¹) are shown in plots (A, B) and (C, D) respectively.

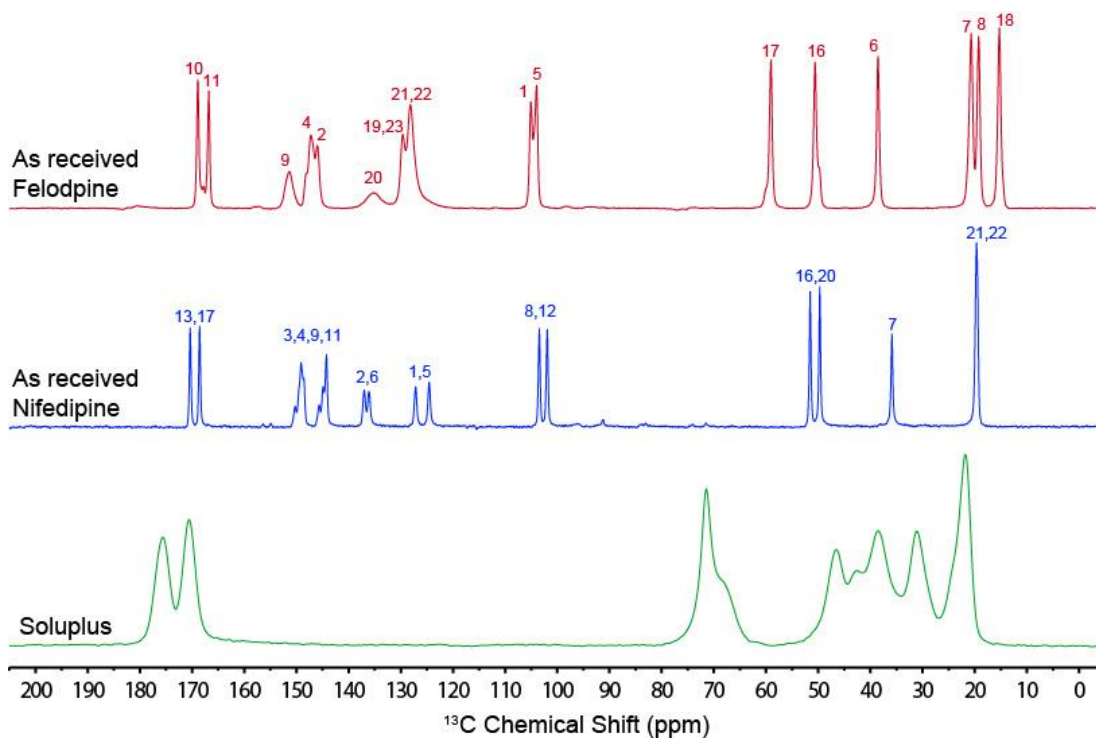


Figure 4.7. Stacked plot for ^{13}C CP/MAS Spectra of as received felodipine (top), as received nifedipine (middle) and Soluplus (bottom). Resonance assignments are done in reference to the numbering scheme used in Table 4.1.

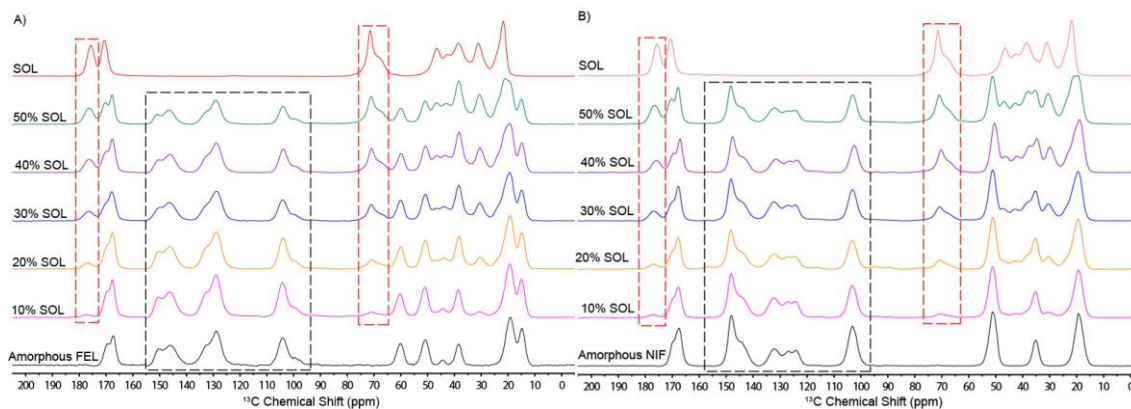


Figure 4.8. Stacked ^{13}C CP/MAS spectra for dispersions samples (A) FEL-SOL system and (B) NIF-SOL system.

We have earlier seen in Chapter 3 that it was possible to quantify the hydrogen bonding interactions in the case of felodipine with polymers such as PVP, PVP/VP and PVAc. The same approach was adopted here with the goal of understanding how FEL and NIF interacted with Soluplus. From our previous study, it was shown that in amorphous FEL approximately 40% of molecules existed in hydrogen bonded (dimer) state and remaining 60% were non-hydrogen bonded (free). Similar analysis of the carbonyl region of amorphous NIF was performed in order to quantify the different states. Upon deconvolution, amorphous NIF carbonyl region was found to exhibit two populations: (i) hydrogen bonded (dimer) at 169.9 ppm and (ii) non-hydrogen bonded (free) at 167.5 ppm, constituting 29% and 71% respectively. Thus, a lesser degree of self-association was seen in amorphous NIF in comparison to amorphous FEL. The deconvolution exercise was also performed on dispersion samples to elucidate the changes in these two fractions. In the presence of Soluplus, drug-polymer hydrogen bonding is expected and that could change the ratio of “dimer” and “free” fractions in both systems. The carbonyl region was deconvoluted to obtain the underlying peaks areas. In the present study, we focused on the two peaks attributed to FEL/NIF, which represented the two states in which FEL/NIF carbonyl region existed. Hence, the percentage for the two populations were reported based on total FEL/NIF carbonyl peak areas. The results from this exercise are summarized in Figure 4.9 and a few common trends could be seen. With increase in Soluplus concentration, the percentage of “dimer” population decreases with concurrent increase in the percentage of “free” population for both the systems. This clearly suggest that FEL/NIF self-association gets disrupted in the presence of Soluplus and more free FEL/NIF becomes available to form drug-polymer

hydrogen bond. For both the systems, the “dimer” fraction declined gradually with increase in Soluplus concentration. The trends seen here suggested a similar interaction pattern existed in both the systems with some slight differences. Very interestingly, at any given Soluplus weight percent “free” NIF fraction was higher than the corresponding FEL fraction. One potential explanation is that NIF has a lower molecular weight than FEL, resulting in NIF hydrogen bonding with Soluplus to a greater extent than FEL. Thus, NIF presents higher ratio of donor to acceptor group relative to FEL on the molar basis. Furthermore, it was shown in Chapter 3 that the extent of hydrogen bonding in felodipine-polymer dispersions could be rank ordered as PVP>PVP/VA>PVAc. However, in the present study with Soluplus somewhat different behavior was seen where Soluplus was found to be less effective in terms of the extent of hydrogen bonding in comparison with those three polymers. For instance, at 50% PVP weight percent dimer fraction disappeared almost completely whereas in the case of Soluplus there was still a reasonable percentage detected. From the structure of Soluplus, it can be seen that it contains fewer R-C(O)-N-R₂ (6.6 mmol/g) groups than PVP (9 mmol/g). In addition, steric considerations may also affect the availability of Soluplus donor groups to hydrogen bond with FEL. Considering these factors, Soluplus does not hydrogen bond with drugs like FEL or NIF as efficiently.

The length scale of mixing in ASDs could also be studied using proton relaxation measurements detected through the ¹³C nucleus. By determining the proton relaxation times of individual components in an ASD in comparison to the proton relaxation times of neat components, it may be used to establish an upper limit of length scale of mixing. These experiments are based on spin diffusion phenomenon, which tend to average the

proton relaxation times to a single value in an intimately mixed system. In contrast in a non homogenous system, spin diffusion process is not as efficient, and therefore different protons relax independently of one another, giving rise to different relaxation profiles. Furthermore, the domains sizes ranging from a few angstroms to a few tens of nanometers can be estimated through these experiments, depending on the use of relaxation times of either $^1\text{H } T_1$ or $^1\text{H } T_{1\rho}$. The main difference between $^1\text{H } T_1$ and $^1\text{H } T_{1\rho}$ is that they are sensitive to motions on different time scales (MHz vs kHz).³⁹ Therefore, $^1\text{H } T_1$ with a longer time scale provides information about domains over larger length scales than $^1\text{H } T_{1\rho}$. Using this analysis, it is possible to study and characterize nano-heterogenous structures on two domain sizes, which is very useful for systems like ASDs. Moreover, it is very important to use complementary techniques like DSC, which has been a tool to assess homogeneity in ASDs based on a single T_g rule, to help detect phase heterogeneity on a smaller scale. The detection of nanophases in ASDs is crucial for understanding the propensity to crystallize, and techniques like SSNMR can permit analysis of nano heterogeneities beyond the resolution limits of traditional techniques.

The plots of $^1\text{H } T_1$ and $^1\text{H } T_{1\rho}$ for FEL:SOL system as a function Soluplus weight % are shown in Figure 4.10. For compositions $\geq 30\%$ Soluplus loading, common $^1\text{H } T_1$ values for each component were obtained that were within the experimental error (Plot A). This implies that domain sizes for these compositions are smaller than the diffusion path length within the time $^1\text{H } T_1$. For the compositions $< 30\%$ Soluplus loading, different $^1\text{H } T_1$ values were recorded for each component within the error of measurement, which indicates an non-homogeneous system on the scale of the spin diffusion path length within the $^1\text{H } T_1$ measurement size for these compositions. It is

evident from Figure 4.10 (Plot B) that different relaxation behavior was observed for both components for the ^1H $T_{1\rho}$ measurements for all compositions, which strongly suggest at least some degree of non-homogeneity on ^1H $T_{1\rho}$ length scale of mixing, although at higher Soluplus loadings, these heterogeneities get very small. Thus, heterogeneity was detected for these compositions on a smaller scale based on ^1H $T_{1\rho}$ measurements. It is interesting to note that same trends are seen for NIF:SOL system, as evident from the plots in Figure 4.11. An examination of the experimental ^1H T_1 data showed similar relaxation behavior for compositions $\geq 30\%$ Soluplus, whereas clear differences existed for samples with $< 30\%$ Soluplus loading (Plot A). As to the ^1H $T_{1\rho}$ data in Figure 4.11 (Plot B), non-identical $^1\text{H}T_{1\rho}$ relaxation times within experimental error were measured for both components across the composition range. This clearly indicates nano-heterogeneities existing for these compositions on the length scale of the ^1H $T_{1\rho}$ measurement.

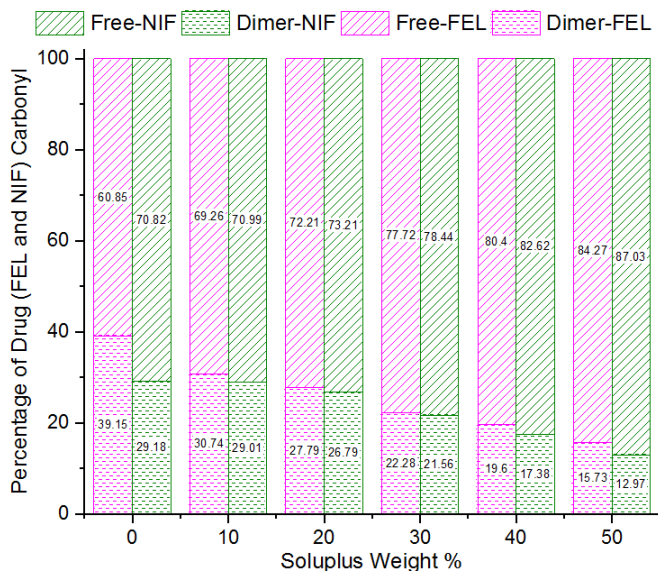


Figure 4.9. Bar graphs depicting the differences in “free” and “dimer” fractions for NIF:SOL system (green bars) and FEL:SOL system (pink bars).

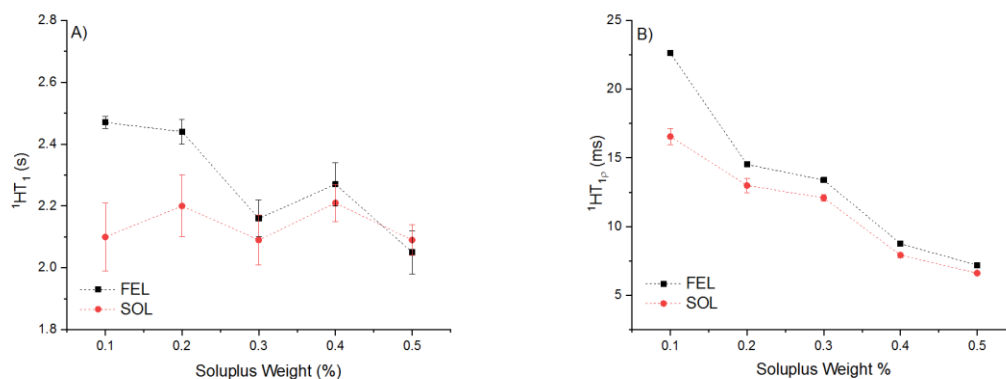


Figure 4.10. $^1\text{HT}_1$ (black squares) and $^1\text{HT}_{1\rho}$ (red circles) plots for FEL:SOL system as a function of Soluplus weight percent.

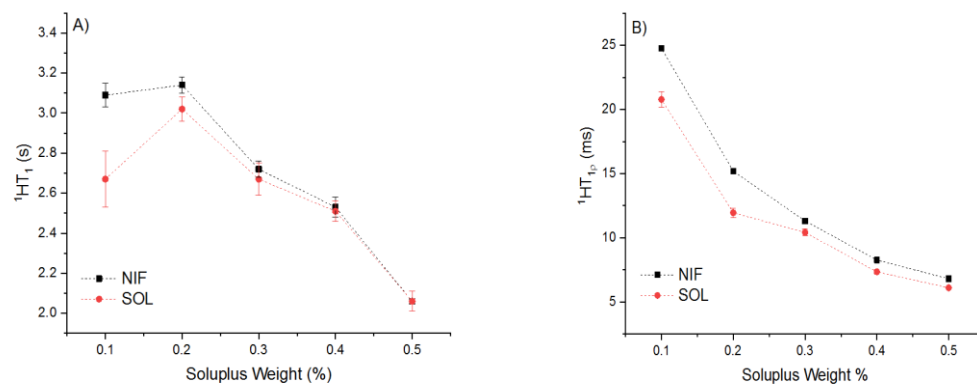


Figure 4.11. $^1\text{HT}_1$ (black squares) and $^1\text{HT}_{1\rho}$ (red circles) plots for NIF:SOL system as a function of Soluplus weight percent.

The phase behavior of both the systems on a nanometric scale revealed some similarities as discussed in the paragraph above. Nonetheless, some small differences could be seen especially in the $^1\text{H T}_{1\rho}$ data. The degree of phase heterogeneity for both systems was more or less same based on the $^1\text{H T}_1$ data, but larger degree of phase heterogeneity was estimated in the case of FEL:SOL system especially for the composition with 10% Soluplus loading. In our opinion, this can result from the

differences seen earlier for the extent of hydrogen bonding. We have shown in previous sections that NIF:SOL system was more extensively hydrogen bonded to Soluplus in comparison to FEL:SOL system, and this could influence the nature of nano-heterogeneous domains with the matrix to some extent especially on a smaller scale. In addition, a useful approximate estimation of the upper limit of the domain size can be calculated based on the following equation:

$$\langle L \rangle \cong (6D^1HT_i)^{\frac{1}{2}} \quad (4.14)$$

where $\langle L \rangle$ is the average diffusive path length for the effective spin diffusion, D is the spin diffusion coefficient and $^1H T_i$ is the characteristic time over which spin diffusion takes place. Typically, value of D is assumed to be 10^{-12} cm²/s. Equating $^1H T_i$ with either $^1H T_1$ or $^1H T_{1\rho}$ provides a reasonable estimation of domain sizes of nano heterogeneities. The results for domain sizes for ASDs of both the systems are listed in Table 4.4. The results from the Table 4.4 indicate that the domain sizes in both the systems were near identical for the compositions studied. It should be noted here that the calculation of domain sizes is based on the relaxation times of individual components. Hence, the extent of phase heterogeneity, which is based on the difference in the relaxation times of drug and polymer, does not always reflect in domain sizes.

Table 4.4. Domain sizes (nm) as calculated from SSNMR analysis.

Composition (Drug:Polymer)	NIF:SOL	FEL:SOL
50:50	2-35	2-35
60:40	2-39	2-37
70:30	2-40	2-37
80:20	>40	>37
90:10	>40	>37

4.4 Conclusions

In this chapter, the miscibility of two structurally similar molecules, felodipine and nifedipine, with Soluplus was studied in depth. The melting point depression approach was employed to study the thermodynamic miscibility for both the systems. The results from the melting point depression study indicated better miscibility of NIF with Soluplus in comparison to FEL. In addition, phase diagrams of temperature-composition were successfully constructed for both the systems. The experimental T_g values for the compositions studied were compared to those predicted from the Gordon-Taylor equation. It was found that both the system showed a similar pattern in terms of the deviations observed. The hydrogen bonding patterns were studied via FTIR and SSNMR analyses. It was revealed that both the drugs interacted with Soluplus via hydrogen bonding, and the preferred interaction site was the vinylcaprolactam moiety in Soluplus backbone. Furthermore, it was shown that NIF hydrogen bonded more extensively with Soluplus in comparison to FEL. The proton relaxation time measurements revealed the presence of heterogeneous domains in both the systems and

the upper limit of the domain sizes were also estimated. The analysis of the proton relaxation measurements indicated that higher extent of phase heterogeneity in FEL:SOL system. Overall, this study is important to understand the drug-polymer miscibility to rationally design ASDs formulations.

CHAPTER 5. MOLECULAR INTERACTIONS AND PHASE BEHAVIOR OF BINARY AND TERNARY AMORPHOUS SOLID DISPERSIONS OF KETOCONAZOLE

5.1 Introduction

In recent years amorphous solid dispersions (ASDs) have gained widespread attention to address the issue of poor bioavailability for poorly-water soluble drugs.¹ This formulation strategy is a viable approach for BCS Class II and IV compounds but the inherent propensity of amorphous form to convert to the crystalline form poses a serious challenge to the bioavailability advantage that comes with it.²⁻⁴ Consequently, the role of polymers in overall stabilization of the system has been studied in great depth.⁵⁻⁷ It is now well recognized that polymers stabilize via two mechanisms: (a) increasing glass transition temperature (T_g) of the system, and (b) forming intermolecular drug-polymer interactions.⁸ Typically, ASDs have been formulated using one polymer in the matrix. In recent years, a new class of ternary ASDs has emerged, which can contain a mixture of two polymers.⁹⁻¹⁴

In order to better understand the physicochemical properties of ternary ASDs, it is important to elucidate the phase behavior and molecular interactions present within the system. In contrast to a simple system like binary ASDs, presence of two polymers in ternary ASDs may strongly influence the overall phase mixing of the different components, and with it the physical stability of the system. Moreover, characterizing these intermolecular interactions is equally important because the interplay of various intermolecular species can impact phase homogeneity and hence the resultant stability of ternary ASDs. However, in depth details of intermolecular interactions and phase behavior are still not clear in ternary ASDs due to the limited amount of research done on

them. Based on the preceding discussion, it is apparent that there is a need to fully understand these complex systems on a molecular level.

In the present study, we evaluated the physical stability of ketoconazole (KET), a BCS class II antifungal compound, in presence of different polymers for spray dried binary and ternary ASDs. Hydroxypropyl methylcellulose (HPMC) and polyacrylic acid (PAA) were chosen as polymeric carriers for this study. HPMC and PAA present different possibilities for drug-polymer interactions individually based on their chemical structures. Both the polymers have been previously studied as carriers for ASDs formulations.^{15,16} Mistry et al. studied the role of drug-polymer interactions on the molecular mobility of KET ASDs with polymers like PAA, poly (2-hydroxyethyl methacrylate) (PHEMA) and PVP. The authors demonstrated reduced mobility and a decrease extent of crystallization for ASDs containing PAA, which was attributed to the fact PAA interacted strongly with KET.¹⁷ Chen et al. correlated drug polymer-interaction and phase mixing with initial drug dissolution for KET ASDs with PVP, PVP/VA, HPMC or HPMCAS.¹⁸ Although both PAA and HPMC have used individually for KET ASDs, the combined use of these polymers has not been studied so far. This work presents a detailed solid-state characterization for KET ternary ASDs in comparison to individual binary ASDs. The specific goal of the current research is to investigate the impact of addition of a second polymer on the phase mixing and solid-state interaction patterns for KET in ternary ASDs at a molecular level. A detailed solid-state characterization approach was employed using several analytical techniques such as DSC, FT-IR spectroscopy and solid-state NMR spectroscopy. Finally, the physical stability of binary and ternary ASDs was evaluated by PXRD at two different conditions.

The findings of this comprehensive study can provide useful mechanistic insights into these systems and serve as a precedent for understanding the role of a second polymer on phase mixing and drug-polymer interactions, which is critical for the rational design of novel ternary ASDs.

5.2 Experimental

5.2.1 Materials

Ketoconazole (KET; 99%) was purchased from BOC Sciences (Shirley, NY). HPMC (Pharmacoat 606) was a kind gift from Shin-Etsu Chemical Co., Ltd. (Tokyo, Japan). PAA ($M_w \sim 1800$) was purchased from Aldrich (St. Louis, USA). Polymer samples were stored in a vacuum desiccator over Drierite at room temperature.

5.2.2 Preparation of Amorphous Materials

Preparation of Amorphous Ketoconazole. Amorphous ketoconazole was prepared by melt quenching. The as-received sample was transferred to a Teflon beaker and heated in an oil bath at 160 °C until completely melted. The sample was then quench-cooled using liquid nitrogen, and the resulting glass was powdered using a mortar and pestle. Amorphous state was confirmed by PXRD, and all other characterizations were performed immediately.

Preparation of KET:PAA Amorphous Solid Dispersions. ASDs of KET with PAA were prepared via spray drying with ProCept 4M8-Trix spray dryer (ProCept, Zelzate, Belgium) with N₂ closed loop recirculation unit. A solution of drug and polymer were dissolved in 95:05 (v/v) mixture of methanol and water (5% w/v solids). Spray dryer conditions were as follows: N₂ gas, medium cyclone, atomization pressure 0.35

bar, liquid flow rate 85 rpm, 0.8 mm bifluid nozzle, process gas flow 7.4 L/min, inlet temperature 85 °C. The resulting dispersions were dried in a vacuum desiccator over Drierite at room temperature overnight to remove any residual moisture. All dispersions samples confirmed amorphous by PXRD, and were stored in 20 mL glass scintillation vials in the freezer until analysed.

Preparation of KET:HPMC and KET:PAA:HPMC Amorphous Solid Dispersions. Binary dispersions of KET with HPMC and ternary dispersions of KET, HPMC and PAA were prepared via spray drying with ProCept 4M8-Trix spray dryer (ProCept, Zelzate, Belgium) with N₂ closed loop recirculation unit. A solution of drug and polymer were dissolved in a 75:25 mixture of ethanol and water (5% w/v solids). Spray dryer conditions were as follows: N₂ gas, medium cyclone, atomization pressure 0.35 bar, liquid flow rate 85 rpm, 0.8 mm bifluid nozzle, process gas flow 7.4 L/min, inlet temperature 105 °C. The resulting dispersions were dried in a vacuum desiccator over Drierite at room temperature overnight to remove any residual moisture. All dispersions samples confirmed amorphous by PXRD and were stored in 20 mL glass scintillation vials in the freezer until analysed.

5.2.3 Differential Scanning Calorimetry

DSC analyses were performed using a Q2000 (TA Instruments, New Castle, DE) equipped with a RCS90 refrigerated cooling system (TA Instruments; New Castle, DE). The instrument was calibrated for temperature and heat flow with an indium standard. 5-7 mg of sample was loaded into an aluminum DSC pan with a hermetically sealed lid with one pinhole. All the dispersion samples were analyzed via heat-cool-heat cycle under nitrogen purge (50 mL/min). A typical thermal cycle consisted of following stages:

1) heating from 20 °C to 180 °C at 5 °C/min (primary heating); 2) isothermal for 5 min followed by cooling to -10 °C at 30 °C/min (cooling stage); 3) heating to 200 °C at 5 °C/min (secondary heating). For the heating cycles, a modulation amplitude of ± 0.5 °C was applied every 60 s to discern reversible thermal events. The first heating cycle was used to erase any thermal history of the sample and to get rid of any residual solvent. For each sample, measurements were done in duplicate. The data was analyzed by TA Universal Analysis software (version 4.7, TA Instruments, New Castle, DE). The value of T_g reported was the half height of the transition in the reversing heat flow signal.

Theoretical T_g of the mixture was calculated using the Gordon-Taylor equation (eq. 5.1) in conjunction with the Simha-Boyer rule (eq. 5.2).

$$T_g = \frac{w_1 T_{g1} + k w_2 T_{g2}}{w_1 + k w_2} \quad (5.1)$$

where w_1 and w_2 are the weight fractions and T_{g1} and T_{g2} are the glass transition temperatures (°C) of each component. k is found by using eq. 5.2.

$$k = \frac{\rho_1 T_{g1}}{\rho_2 T_{g2}} \quad (5.2)$$

where ρ_1 and ρ_2 are the densities of each component.

5.2.4 Fourier Transform Infrared Spectroscopy

A Thermo Fisher Scientific Nicolet iS50 FT-IR (Thermo Fisher Scientific, Waltham, MA) with an attenuated total reflectance (ATR) attachment was used to collect FTIR spectra from 400 cm^{-1} to 4000 cm^{-1} . Data were collected in 64 scans with a resolution of 4 cm^{-1} and a data spacing of 0.482 cm^{-1} . Spectra were normalized and base

line corrected using Omnic software (Version 9.5, Thermo Fisher Scientific, Waltham, MA).

5.2.5 Solid-state Nuclear Magnetic Resonance Spectroscopy

^{13}C SSNMR spectra were acquired using a Tecmag Redstone spectrometer (Tecmag Inc., Houston, TX) operating at approximately 300 MHz for ^1H and 75 MHz for ^{13}C . Samples were packed into 7.5 mm zirconia rotors and sealed with Teflon or Kel-F end-caps (Revolution NMR LLC, Fort Collins, CO). One dimensional ^{13}C spectra were acquired using cross polarization magic angle spinning (CP/MAS) at 4 kHz, using total sideband suppression (TOSS)¹⁹ and SPINAL64²⁰. The ^1H 90° pulse width was set to 4.5 μs and contact time of 1.5 ms was used in all the measurements. The pulse delay for 1D experiments was 4 s and a total of 4096 scans were collected. The ^{13}C chemical shift scale was referenced with the methyl peak of 3-methylglutaric acid, which was set to 18.84 ppm.²¹ The relaxation times were detected via ^{13}C nucleus, which facilitates identification of regions for respective components. Proton spin-lattice relaxation time in the laboratory frame (^1H T_1) were measured using a ^{13}C -detected saturation recovery pulse sequence with TOSS. ^1H T_1 were obtained by fitting integral-recovery time data by the following equation:

$$M(t) = M_0(1 - e^{-\frac{t}{T_1}}) \quad (5.3)$$

where $M(t)$ is the peak intensity at delay time t , M_0 is an amplitude parameter from the fit, and T_1 is the obtained spin-lattice relaxation time in the laboratory frame. Proton relaxation times in the rotating frame (^1H $T_{1\rho}$) were measured by varying the spin lock

duration time after a 90° pulse. ¹H T_{1ρ} decay times were obtained by analyzing the integrated carbon signal exponentially according to the following equation:

$$M(t) = M_0 e^{-\frac{t}{T_{1\rho}}} \quad (5.4)$$

where $M(t)$ is the peak intensity and t is the spin-lock duration time. M_0 is an amplitude parameter from the fit, and $T_{1\rho}$ is the fitted spin-lattice relaxation time in the rotating frame. All data fitting was done using GraphPad Prism (GraphPad Software, Inc., La Jolla, CA). The regions selective for drug and polymers were used to get the integrals. The region from 111-159 ppm was selective for KET, the regions 177-190 and 27-33 ppm were non-overlapping for PAA, and the regions 57-65 and 99-105 ppm were unique for HPMC. These resolved areas are shown in highlighted boxes in Figure 5.7 (*vide infra*).

5.2.6 Powder X-ray Diffraction

PXRD patterns were collected on the Rigaku Miniflex 600 benchtop diffractometer (Rigaku Corporation, Tokyo, Japan), with Cu K α radiation (40 kV x 15 mA). The experiments were conducted at room temperature, between 2° to 50° 2 θ at a scan speed of 2.0°/min and a step size of 0.02° 2 θ under continuous mode.

5.2.7 Physical Stability

The physical stability of the binary and ternary dispersions was studied for 70% drug loading at two different stress conditions: 40 °C/75% RH and RT/94% RH. This drug loading was chosen to observe crystallization in samples in real time. The samples

were analyzed by PXRD at different time points (time 0, 1 week, 2 weeks, 1 month, 2 months, 3 months, and 6 months).

5.3 Results and Discussion

5.3.1 Chemical Structures

The chemical structures of compounds are shown in Figure 5.1. The model lipophilic drug, KET, belongs to the class of antifungal compounds. It is a weak base with two pK_a values; the imidazole ring ($pK_a = 6.51$) and the piperazine ring ($pK_a = 2.94$).²² Its structure presents potential sites for intermolecular interactions such as acid-base or hydrogen bonding interactions. PAA is a strong donor and medium acceptor, and has a carboxylic acid as its monomer with pK_a of 4.75.²³ HPMC is a neutral cellulosic polymer, which has been extensively used as a polymeric matrix for ASDs.²⁴ HPMC has many hydroxyl groups in its structure with capability of acting both as donor and acceptor. HPMC is devoid of any carbonyl groups and hence will act an excellent system with no interference in the carbonyl regions both for FTIR and SSNMR analyses.

5.3.2 DSC Results

For an accurate measurement of the T_g , amorphous KET was generated *in situ* inside DSC pan by heating the crystalline drug above its melting point, followed by quench cooling. Amorphous KET had a T_g of 47.0 °C, which is consistent with the previous reports.²⁵ The polymers were amorphous in nature and displayed an average T_g of 99.9 °C and 145.5 °C for PAA and HPMC respectively. It is clear from the T_g values of neat materials that they are different from each other. This wider gap is desired when DSC is used to study phase homogeneity in ASDs. It is generally recommended that T_g

of individual components must be at least 10 °C apart in order to determine phase homogeneity via DSC.²⁶

T_g is an important index for assessing the physical stability and mobility of ASDs.²⁷ We also evaluated the T_g values of binary and ternary ASDs as a function of composition by mDSC exposing the samples to a heat cool heat protocol. The results from the first heating cycle are shown in Figure 5.2. The binary systems of KET:PAA and KET:HPMC displayed a single T_g between the T_g s of individual components for all compositions, implying phase homogeneity. Similar trend was seen in the ternary samples. The T_g values obtained for KET:PAA were higher than for the KET:HPMC system. Thus, the rank ordering of the polymers based on effectiveness of the polymers to increase the T_g of KET is PAA>HPMC. Furthermore, 90:10 sample in all the systems displayed a melting endotherm, which possibly signifies the existence of drug-rich amorphous domains within the matrix. In the DSC analysis, it has been shown that the presence of a single T_g does not always indicate phase homogeneity.²⁸ Therefore, solid-state NMR was used to confirm phase homogeneity for these samples (*vide infra*).

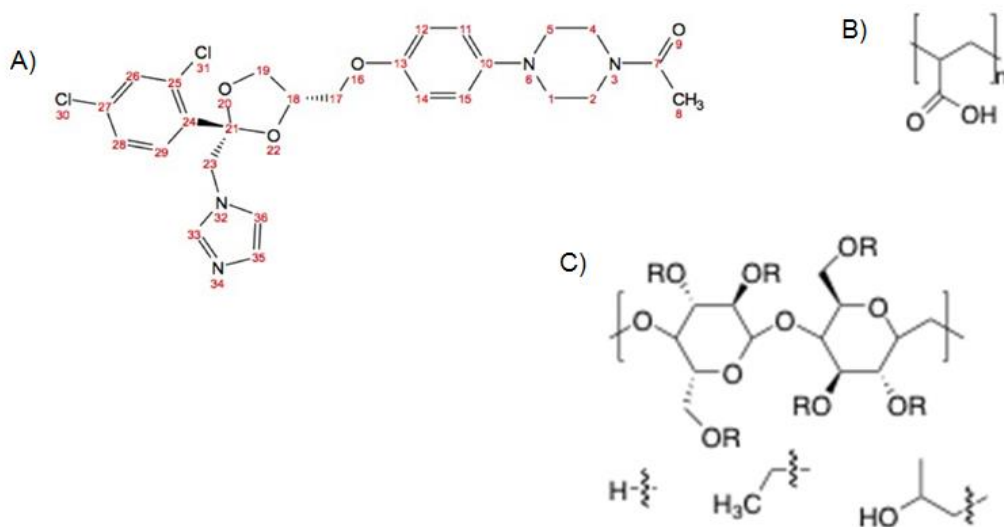


Figure 5.1. Chemical structures of (A) ketoconazole (KET) (B) PAA and (C) HPMC.

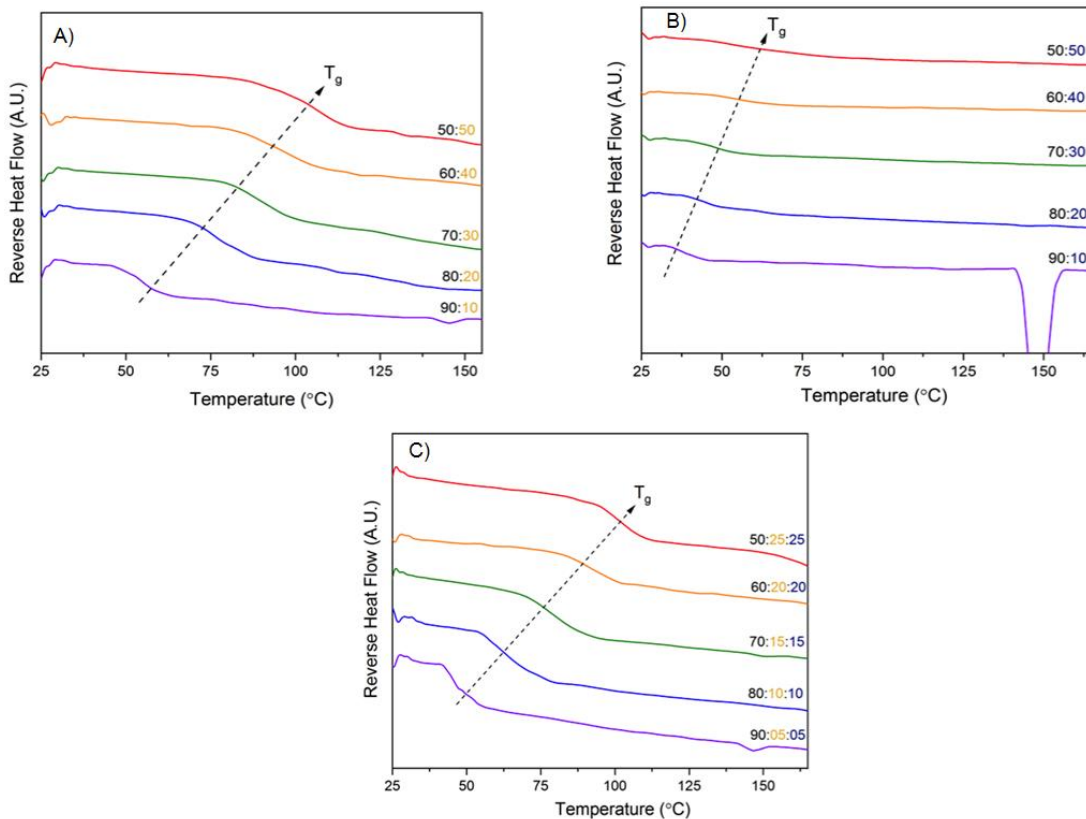


Figure 5.2. DSC thermograms from first heating cycle for (A) KET:PAA binary system (B) KET:HPMC binary system and (C) KET:PAA:HPMC ternary system. The composition of the samples is indicated by drug:polymer ratio on a weight basis: black for KET, gold for PAA and blue for HPMC.

The thermal history of the sample generally affects the T_g of the system. In order to erase the thermal history of the sample, it is generally agreed to expose the sample to heat cool heat cycle in DSC. The T_g values from the second heating cycle yield more accurate values with sharper step change (shorter T_g widths). This is clearly depicted in the thermograms obtained from the second heating cycle in Figure 5.3. The T_g values thus obtained were slightly higher than the first heating cycle. This trend was most pronounced in KET:HPMC binary system. The change in the T_g values from the second heating cycle reflects the behavior of spray-dried samples in the DSC, where the samples

lose residual solvent following heating, and thus showing higher T_g values without any melting endotherms, in part due to better mixing.

A number of equations are reported in the literature for predicting theoretical T_g values for drug-polymer mixtures.²⁷ In the Figure 5.4, the Gordon-Taylor equation was used to generate the theoretical T_g curve lines, and the experimental values were drawn from the mean T_g values from the second heating cycle. Typically, the deviation positive or negative is suggestive of non-ideal mixing behavior between the drug and polymer, and has often been used to indicate the presence of specific intermolecular interactions. In addition, the direction and magnitude of deviation in these plots have been used to determine if homo or hetero interactions are dominating.²⁹ The experimental T_g values for the samples with less than 50% drug loading could only be generated for binary KET:PAA system by preparing *in situ* dispersions inside the DSC pan from the respective physical mixtures. For systems containing HPMC, both binary and ternary, this approach could not be adopted, and therefore the experimental curves do not cover the entire composition range.

In the binary KET:PAA system, a pronounced positive deviation was observed for the composition range from 10-90% drug loading. It is interesting to observe that the highest T_g value was noted for the composition 30:70 (105.5 °C), and the largest deviation between the experimental and theoretical T_g values was seen for the composition 50:50 ($\Delta T_g = 32.7$ °C). Similar positive deviations of experimental T_g values have been reported for the other drug-polymer systems like indomethacin-eugragit and loperamide-PAA.^{30,31} This strong positive deviation shows that the drug-polymer heterointeractions are stronger than drug-drug or polymer-polymer

homointeractions. Based on the basic nature of KET and the acidic nature of PAA, there is a possibility of ionic interaction. For salt formation to take place between acids and bases, it is generally accepted that the $\Delta pK_a > 2$.³² If we compare the ΔpK_a between KET (imidazole ring) and PAA, we get a value of 1.76. This value of ΔpK_a does not satisfy the rule of thumb completely, but the strong positive deviation between the experimental and theoretical T_g values does point to partial proton transfer taking place in this scenario. Another potential interaction site is the carbonyl group of KET, which can take part in hydrogen bonding. It has been reported in literature that a specific interaction like strong hydrogen bonding can also result in positive deviation for systems like IMC-PVA.³³ In this case, it is difficult to ascertain using T_g data which interaction is responsible for this behavior, if we also take hydrogen bonding in account as a contributing interaction.

In contrast to the KET-PAA binary system, the KET-HPMC binary system showed a negative deviation between the experimental and theoretical T_g values, as seen in Figure 5.4. The negative deviation could result from dominating drug-drug and/or polymer-polymer homo-interactions or to an increase in free volume upon mixing. Similar to the KET:PAA binary system, the largest deviation in T_g was observed for a 50:50 composition ($\Delta T_g = -28.2$ °C). Other systems like curcumin-HPMC and felodipine-HPMC have also shown similar behavior.^{34,35}

It is interesting to note in the Figure 5.4 that the ternary system of KET-PAA-HPMC showed positive deviation between the experimental and theoretical T_g values, similar to what was seen in the binary KET:PAA system. Again, the 50:50 composition resulted in the maximum deviation between the experimental and theoretical T_g values

($\Delta T_g = 16.0$ °C), and more importantly, this value is almost half of what was seen in the binary KET:PAA system. Additionally, the overall deviation for ternary system was influenced by the positive deviation and the negative deviations effects of KET:PAA and KET:HPMC binary systems respectively, resulting in the experimental T_g values to lie in between the two curves. Although in ternary systems the amount of PAA is reduced to half on weight basis, a strong positive deviation was observed, especially for compositions $< 80\%$ KET, suggesting a similar interaction pattern existed, and probably interactions between KET-PAA outweighed the others. It is possible to observe negative deviations for ternary ASDs. Albadarin et al. observed negative deviation from the theoretical values in ternary dispersions of itraconazole with Soluplus and HPMCP.³⁶

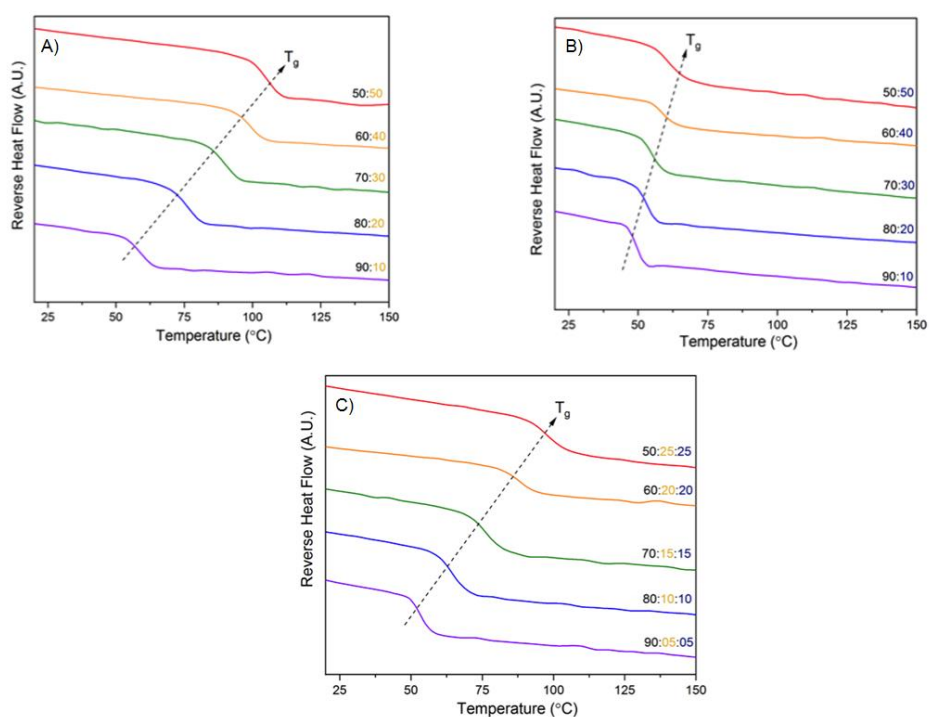


Figure 5.3. DSC thermograms from second heating cycle for (A) KET:PAA binary system (B) KET:HPMC binary system and (C) KET:PAA:HPMC ternary system. The composition of the samples is indicated by drug:polymer ratio on a weight basis: black for KET, gold for PAA and blue for HPMC.

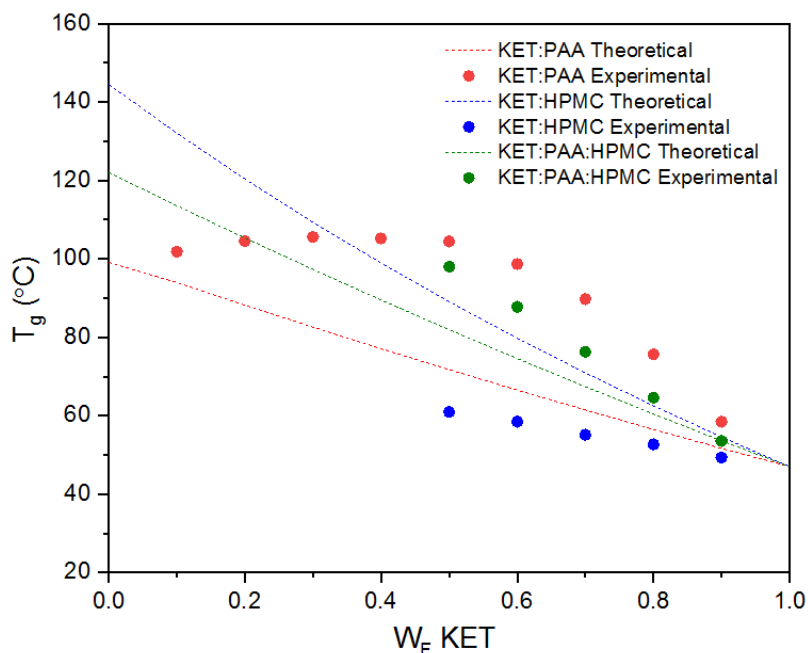


Figure 5.4. Mean experimental and theoretical T_g plotted as a function of weight fraction of KET for KET: PAA dispersions (red color), KET:HPMC dispersions (blue color) and KET:PAA:HPMC dispersions (green color). The dotted lines represent theoretical T_g values obtained from the Gordon-Taylor equation.

5.3.3 FTIR Spectroscopy

FTIR spectroscopy was used to study the intermolecular interactions between KET and each polymer in binary and ternary ASDs. FTIR plots for each system are depicted in Figure 5.5. The carbonyl region of the KET:PAA in the binary dispersions is shown in Figure 5.5 A. It has been already shown in the literature that pure PAA can self associate through hydrogen bonding, and exists in two forms: free and dimer.³⁷ Therefore, the spectrum of pure PAA is characterized by vibrations at 1737 cm^{-1} and 1695 cm^{-1} , attributed to free (non-hydrogen bonded) and dimer (hydrogen bonded), respectively. It has been suggested that KET is likely to interact with PAA via ionic interactions.¹⁷ In the present study, this is supported by the appearance of one new

specific peak at 1544 cm^{-1} , assigned to asymmetric stretching vibration of the carboxylate group. This new peak becomes more pronounced in samples with greater than or equal to 30% PAA. The formation of the carboxylate ion should also reveal a peak around 1400 cm^{-1} arising from symmetric stretching vibration of the carboxylate group. This peak was hard to discern in the spectra due to strong absorption peaks of both KET and PAA. This is in good agreement with the spectrum of the sodium salt of PAA, which shows two prominent peaks corresponding to the carboxylate asymmetric stretching at 1549 cm^{-1} and carboxylate symmetric stretching at 1399 cm^{-1} (Figure 5.6). Nie et al. have reported similar results for carboxylate group formation resulting from ionic interaction between HPMCP and clofazimine.³⁸ Additional evidence for proton transfer can be found in the region of $2200\text{-}3400\text{ cm}^{-1}$ (Figure 5.5 B). Pure PAA displays a characteristic broad absorption band at 3040 cm^{-1} for O-H stretching. A broad shoulder peak around 2530 cm^{-1} appeared in KET:PAA dispersions samples assigned to $^+\text{N-H}$ stretch formed upon the protonation of the imidazole group in KET. Furthermore, a hypsochromic shift of dimer peak of PAA from 1695 cm^{-1} to 1716 cm^{-1} was observed in the dispersions indicating disruption of dimers giving rise to new fraction of free carboxylic acid.

Another interesting finding can be seen in the $1300\text{-}1800\text{ cm}^{-1}$ region (Figure 5.5 A). The amorphous KET showed C=O stretching band at 1640 cm^{-1} . In the presence of PAA, a shoulder around 1607 cm^{-1} appeared in the dispersion samples with greater than or equal to 20% PAA. The intensity of this extra vibration band at 1607 cm^{-1} increased with increase in polymer loading. This phenomenon may be an indication of presence of a new species of KET carbonyl group. Generally, hydrogen bonding results in a shift to lower wave numbers. This shift to lower wavenumbers from 1640 cm^{-1} to 1607 cm^{-1} is

possibly pointing to the formation of a hydrogen bond, where the carbonyl group of KET can act as an acceptor and the carboxylic acid group of PAA as a donor. No changes could be seen in the O-H stretching region of PAA due to overlapping bands. At this stage, it is logical to hypothesize that the hydrogen bonding could also be a possible mode of interaction between KET and PAA and more evidence is needed to support this hypothesis.

In the case of KET: HPMC binary dispersions, no evidence of any interaction could be derived from FTIR spectra. As shown in the Figure 5.5 C, HPMC caused no change in the peak corresponding to the carbonyl group of KET in the region of 1550-1800 cm^{-1} . Additionally, the O-H stretch region in KET:HPMC samples was difficult to discern due to the presence of multiple overlapping absorption bands (Figure 5.5 D). Basically, the FTIR spectra of this binary system were linear addition of the pure amorphous components weighted by each component amount. This observation is consistent with the findings from Chen et al.¹⁸ The authors pointed out that KET is poorly miscible with HPMC based on the weak Flory-Huggins interaction parameter (positive χ value), which collectively indicate the absence of any specific interactions between KET and HPMC.

The results for FTIR spectra of ternary ASDs of KET:PAA:HPMC are shown in Figure 5.5 (plots E and F). The ternary ASDs retain spectral features from binary KET:PAA ASDs except for some minor differences. The dimer peak of PAA shifted to higher wavenumbers similar to binary KET:PAA ASDs. The carboxylate peak around 1544 cm^{-1} became less intense in comparison to KET:PAA samples likely because of less amount of PAA present in ternary samples. It is noteworthy to mention that the peak

intensity of hydrogen bonded carbonyl group of KET (1607 cm^{-1}) decreased in the ternary ASDs. Likewise, the $^+\text{N-H}$ stretch peak around 2530 cm^{-1} became less pronounced for ternary ASDs. In the case of ternary dispersions, the possibility of two polymers interacting with each other needs to be taken into the account. In order to explore this scenario, polymer blends with different weight ratios of PAA and HPMC were studied via FTIR. From the Figure 5.7, it is clearly evident that in the presence of HPMC there is loss of PAA dimers. At 80% HPMC weight ratio, the dimer peak intensity is drastically reduced. The disruption of PAA dimer fraction could be a result of intermolecular interactions between HPMC and PAA or simply due to a dilution effect. If these two species were to interact on a molecular level via hydrogen bonding, a shift to a lower wavenumbers is anticipated. The FTIR spectra of these polymer blends do not seem to suggest such an occurrence. In fact, the dimer peak of PAA (1695 cm^{-1}) moved to higher wavenumbers as the weight fraction of HPMC is increased. For polymer blends it is likely that PAA and HPMC are not involved in strong interactions, and therefore in ternary ASDs there are no other competing interaction present. The interaction pattern in the ternary ASDs seems to suggest that interaction between KET and PAA is still favored in the presence of HPMC.

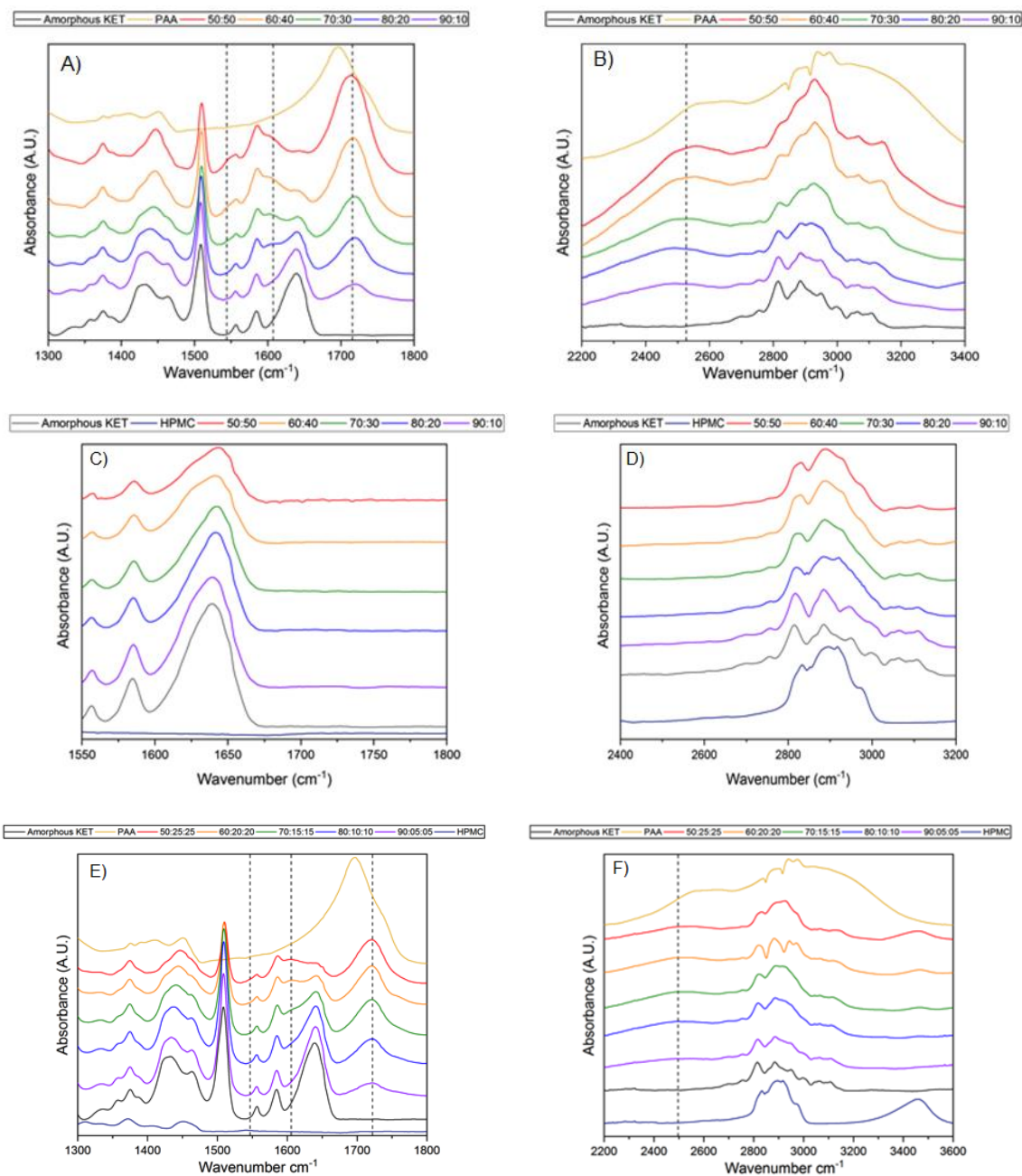


Figure 5.5. FTIR spectra of pure KET, pure PAA and dispersions showing the carbonyl stretching region and the single bond region for KET:PAA binary system (plots A and B), KET:HPMC binary system (plots C and D) and KET:PAA:HPMC ternary system (plots E and F).

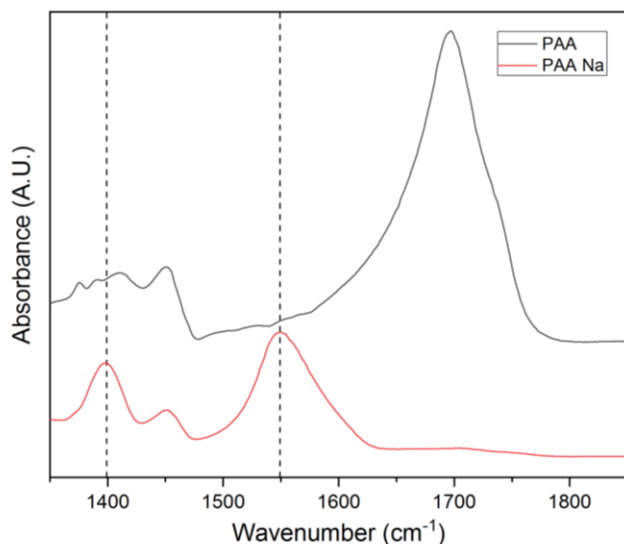


Figure 5.6. FTIR spectrum of PAA and its sodium salt. The peaks $\sim 1549 \text{ cm}^{-1}$ and 1399 cm^{-1} found in sodium salt of PAA are attributed to asymmetric and symmetric stretching vibration of the carboxylate group respectively.

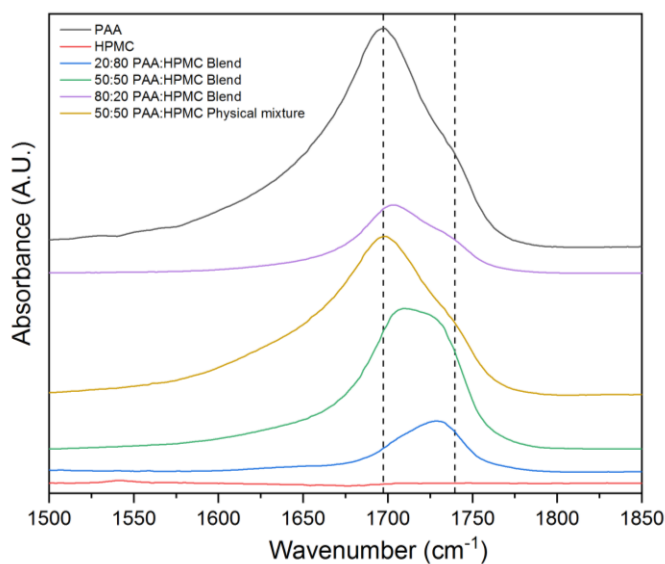


Figure 5.7. Comparison of FTIR spectra of PAA, HPMC and their spray dried blends. In presence of HPMC, the intensity of dimer peak ($\sim 1695 \text{ cm}^{-1}$) decreases and moves to higher wavenumbers as the weight fraction of HPMC increases. Spectrum of 50:50 physical mixture of PAA and HPMC is shown as a reference.

5.3.4 Solid-state NMR spectroscopy

5.3.4.1 ^{13}C CP/MAS Experimental Results

In recent years, SSNMR has been used as a part of analysis for ASDs for its unique capability to provide atomic level information on intermolecular interactions and phase homogeneity.³⁹⁻⁴¹ In order to understand holistically the system under study and to complement routine analysis techniques, SSNMR experiments utilizing CP/MAS and spin diffusion were included. Figure 5.8 shows ^{13}C SSNMR spectra of the raw materials. The spectrum of crystalline KET consisted of sharp resonances typical of crystalline materials. The peaks were assigned according to the numbering scheme used in the structure. There is one molecule in each asymmetric unit in the crystal structure based on one peak for each carbon atom found in the spectrum. In contrast, amorphous KET displayed broader peaks suggestive of a disordered state. The carbonyl carbon centered around 169 ppm is of interest to probe any possible interactions with polymers for hydrogen bonding. In addition, other potential sites of interest are the carbon signals in the imidazole ring, which appear in the aromatic region (110-150 ppm), to investigate any ionic interactions. The polymers exhibited amorphous nature as confirmed by relatively broad signals in Figure 5.8. Pure HPMC does not have any carbonyl signal. It is useful to note that the carbonyl region of PAA consisted of two peaks; one main peak of 182.6 ppm and the shoulder peak at 177.2 ppm. These two peaks corresponded to dimer and free fractions. Upon deconvolution of the region, the respective contribution of the peaks in terms of percentage was quantified. It was estimated that dimer and free fractions were 44% and 56% respectively.

It is important to compare the molar ratio of donor to acceptor groups with respect to acidic and basic groups in both binary KET:PAA and ternary KET:PAA:HPMC systems for the drug loadings under study. The molecular weights of KET (531.43 g/mol) and monomer unit of PAA (72.06 g/mol) were used in Figure 5.9. For the composition range between 50-80% drug loadings, the ratio of donor/acceptor functionalities exceeded 1. Also, the theoretical composition of 1:1 molar ratio was calculated to be 88.11% KET on weight basis. In comparison to binary system, the molar ratios for ternary system were half in values for each composition, considering PAA amount reduced to half and there were no acidic groups in HPMC. The 78.71% weight fraction of KET corresponded to 1:1 molar stoichiometry of KET:PAA in ternary compositions. Thus, in theory below 88.11% and 78.71% weight of KET all imidazole groups should be protonated in binary and ternary ASDs respectively, if there is no steric hindrance.

¹³C CPMAS spectra of the binary KET-PAA dispersions at various drug loadings are shown in Figure 5.10 A. The spectra displayed broader Gaussian resonances, which confirmed their amorphous character. No significant changes were observed in the spectra except in the carbonyl region. On analysis of the carbonyl region (160-190 ppm) some interesting spectral features were noted. Firstly, there is a change in the intensity of the dimer peak across the range of drug loadings as evident in Figure 5.11 A. This suggests that there is loss of PAA dimers resulting from an interaction with KET. As pointed by the FTIR analysis, KET and PAA can form ionic bonds, resulting in the formation of carboxylate ion. In the carbonyl sub spectra given here, no apparent peaks were observed which could be attributed to carboxylate ion formation. In order to confirm the peak position of the carboxylate group, we compared the ¹³C spectrum of

sodium salt of PAA with pure PAA in Figure 5.12. It was shown that carboxylate ion resonated further downfield around 186 ppm. Since this region in our samples did not reveal any direct changes, an ionic interaction is likely to be hidden there. Very interestingly, there is a new peak around 172 ppm, which is more resolved in dispersions from 50 to 70 % and shifted further upfield as KET loading increased to 90% as seen in Figure 5.11 A. This peak was found to be absent in the spectrum of 50:50 physical mixture of amorphous KET and PAA (Figure 5.13). We hypothesize that this peak is due to the hydrogen bonding of the carbonyl group of KET with PAA. From the molar ratio calculations we know that there is an excess of PAA present for compositions $\leq 88.11\%$, which most likely makes this hydrogen bond a possibility. In addition, this also supports our earlier hypothesis for the 1607 cm^{-1} peak in FTIR analysis. It is clear from the analysis of the carbonyl region that there are possibly two different fractions contributing to the KET carbonyl intensities: hydrogen-bonded (H-bonded) and non-hydrogen bonded (Non H-bonded) species.

^{13}C CP/MAS spectra of the binary KET:HPMC dispersions are displayed in Figure 5.10 B. No change in chemical shift was observed in any region for the dispersions samples in comparison with the pure components, and no evidence of any interaction could be found. There was no spectral inference from HPMC in the carbonyl region, and the respective peaks of KET and HPMC increased/decreased depending on the composition. This is also in good agreement with the findings of FTIR analysis.

The possibility of PAA interacting with HPMC was again explored with SSNMR as presented in Figure 5.14. The differences could be seen in the carbonyl region for PAA:HPMC spray blends at various weight ratios. In presence of HPMC, the dimer

fraction goes down and correspondingly the free fraction increases. For the 80:20 HPMC:PAA blend, the dimer fraction decreased to 7 % from 44% in pure PAA while the free fraction increased from 56% to 93%. No change in the chemical shift was observed. These changes confirm the absence of any strong interaction between PAA and HPMC. This is consistent with the FTIR results reported earlier, and confirms that in the ternary system these two polymers most likely do not interact.

From the spectra of ternary KET:PAA:HPMC dispersions, the following spectral features were noted from Figures 5.10 C and 5.11 B. As shown in Figure 5.10 C, similar trends were seen in ternary samples as with the binary KET:PAA system, and only the carbonyl region revealed some changes. Again, as depicted in Figure 5.11 B, the peak attributed to hydrogen-bonded KET (~172 ppm) clearly existed and PAA dimer peak (~182 ppm) intensity decreased with increasing drug load, implying the disappearance of dimers due to the disruption of self-association of PAA. Meanwhile, the peak associated with the free fraction of KET (~169 ppm) became more resolved in spectra with higher drug loads. It was difficult to compare the carbonyl regions of binary KET:PAA and ternary KET:PAA:HPMC systems in terms of quantification of various species that existed because of an extensive peak overlap.

In order to understand the carbonyl region of binary KET:PAA and ternary KET:PAA:HPMC systems, a detailed deconvolution exercise was performed. In the present study, we fitted the respective sub spectra (160-190 ppm) with five peaks using an iterative least-square peak fitting method with Gaussian-Lorentzian function (Figure 5.15). The five peaks criteria satisfied the existence of various species in KET and PAA. The three out of five peaks belonged to PAA carbonyl portion: carboxylate (~186 ppm),

dimer (~182 ppm) and free (~177 ppm) while the other two constituted the two carbonyl species of KET: H-bonded (~172 ppm) and non H-bonded (~169 ppm). For the fitting procedure, the chemical shift and line width were kept locked for all the samples. By dividing the corresponding areas with the total area and multiplying with 100, we obtained the respective area percentage of each species. The progression of the area percentages from the various species for binary KET:PAA and ternary KET:PAA:HPPMC samples as the function of KET weight % is illustrated Figures 5.16. We will first focus on the changes observed for PAA species for the both systems. It is clear from Figure 5.16 that the area percentage of the PAA peaks decreased with increasing drug load for both the systems. Also, the area percentages of all PAA peaks in the binary samples (Plot A) were higher than those in the ternary samples (Plot B) for the same KET weight percentage. This is expected because there is less PAA present in the ternary samples. The decrease in the free PAA fraction was more gradual in the binary system in comparison to the ternary system, where at 90% KET content the area reduced to more than 50%. Interestingly, the dimer fraction reduced to almost the same percentage in both the systems at the 90% drug load, even though the binary 50:50 composition had almost twice the amount present. Furthermore, the carboxylate peak did not contribute significantly to the total area, which is suggestive of the fact that, for these compositions, hydrogen bonding is the dominating interaction.

On the other hand, some interesting trends were observed for the area percentages of the KET peaks as shown in Figure 5.16. First, the higher amount of non H-bonded peak was found in the ternary systems for each composition (Plot B). Second, the area percentages of non-H bonded peak increased when moving from 50 to 90 % KET content

for both the systems. For the H-bonded peak in the binary system (Plot A), there was an increase in the peak area when moving from 50 to 70% KET, reaching the maximum value, after which it decreased. In contrast, in the ternary samples (Plot B) the area percentage decreased gradually for compositions up to 80% KET content before an abrupt reduction at 90% KET composition. The plots in Figure 5.16 compare the area percentages obtained from the deconvolution procedure, but in order to make comparison for the interaction patterns between the binary and ternary systems, it is necessary to further treat the area percentages and normalize them based on the total area of either groups: KET carbonyl group and PAA carbonyl group.

Figure 5.17 compares the percentages of the various species of PAA and KET for both binary and ternary systems as computed on the basis of total KET/PAA carbonyl area. These plots summarize the deconvolution exercise in a clearer fashion and a few conclusions could be drawn. For total PAA carbonyl fraction (Plot A), contribution of each species was in the given order: Free>Dimer>Carboxylate for both the systems. Overall, higher percentages were seen for carboxylate and dimer fractions in the binary system than in the ternary system. Meanwhile, more free PAA was present in the ternary system. The ratio of free to dimer fractions increased with KET percent content in both the systems. On the other hand, for total KET carbonyl fraction (Plot B), the higher percentage of KET was H-bonded in binary system than in ternary system for each composition. The ratio of non-H bonded to H-bonded fractions increased for both the systems with increasing drug content, and a steeper increase was seen for the ternary system. In summary, it can be concluded that the binary samples had more ionic and hydrogen bonding interactions vs. ternary samples. Nevertheless, the ternary samples still

had a similar interaction pattern with only half the amount of PAA present. This analysis is also consistent with the results seen in the FTIR section. The low intensity of carboxylate peak in the FTIR spectra could now be attributed to the less amount being present. In addition, the peak attributed to H-bonded carbonyl of KET was more pronounced for samples with lower drug loads, which is due to a higher fraction of KET carbonyl being H-bonded for those compositions. We are not aware of any similar studies being conducted earlier where comparison could be established between the molecular interaction pattern for binary and ternary ASDs.

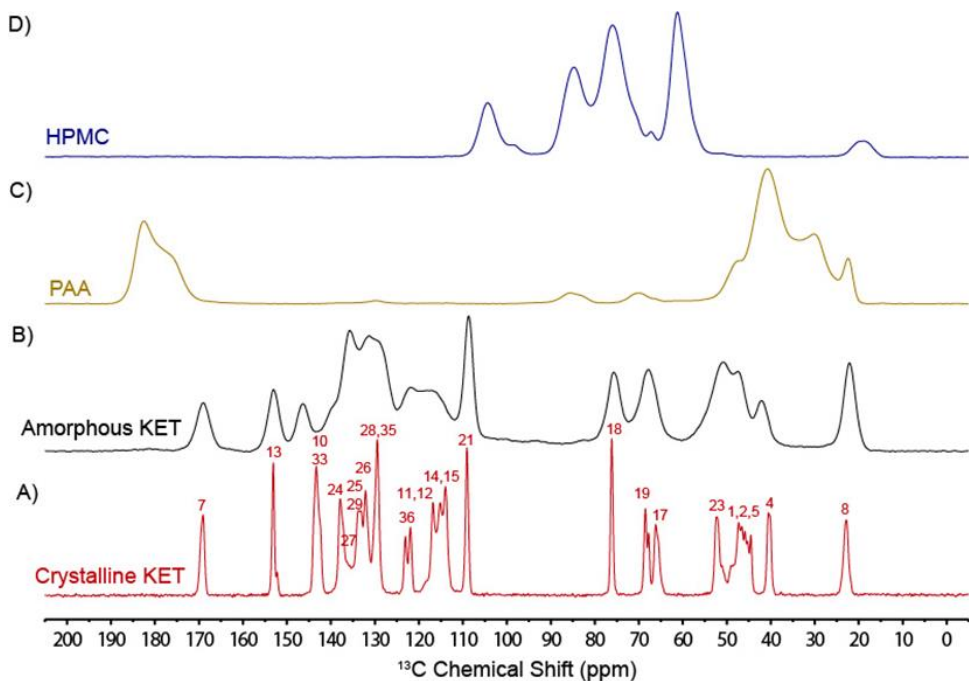


Figure 5.8. Comparison of ^{13}C CP/MAS spectra of (A) crystalline KET (B) amorphous KET (C) PAA and (D) HPMC.

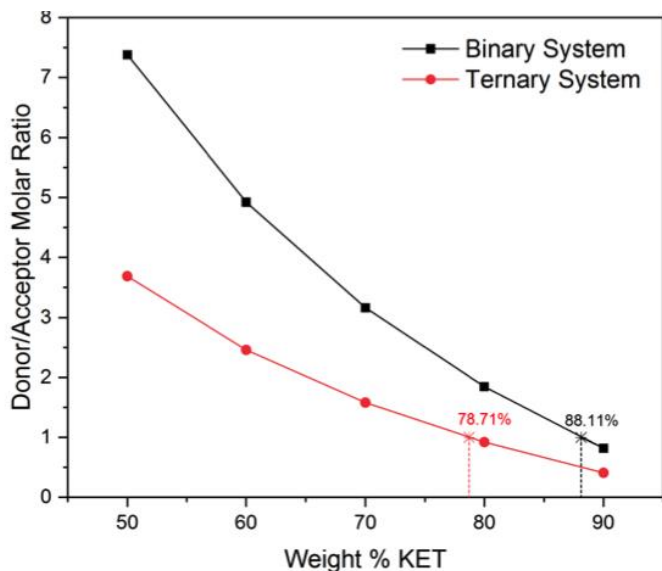


Figure 5.9. Donor to acceptor molar ratio calculated for binary KET:PAA and ternary KET:PAA:HPMC as a function of weight percent of KET. The cross point on the curve represent the theoretical 1:1 molar ratio in each case.

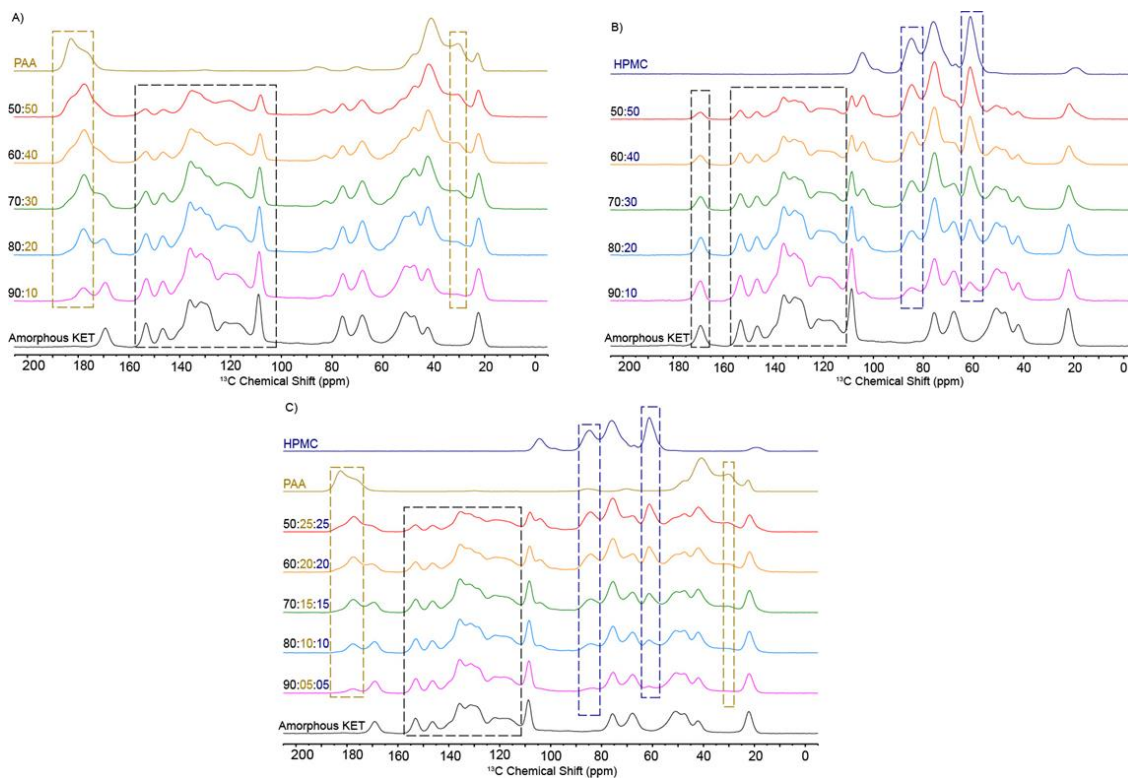


Figure 5.10. Comparison of ^{13}C CP/MAS spectra of (A) crystalline KET (B) amorphous KET (C) PAA and (D) HPMC.

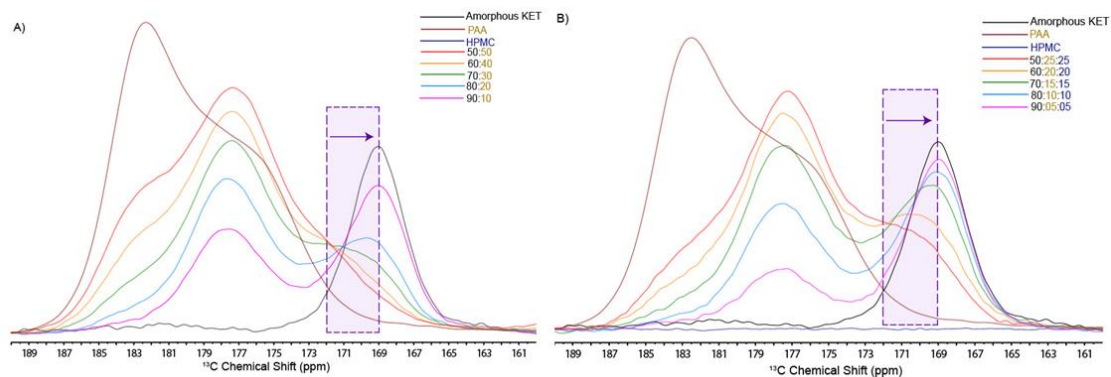


Figure 5.11. ^{13}C CP/MAS sub spectra in the carbonyl region (160-190 ppm) for (A) KET:PAA binary dispersions and (B) KET:PAA:HPMC ternary dispersions. The shaded box shows how peak around 172 ppm shifts upfield with increase in drug loading.

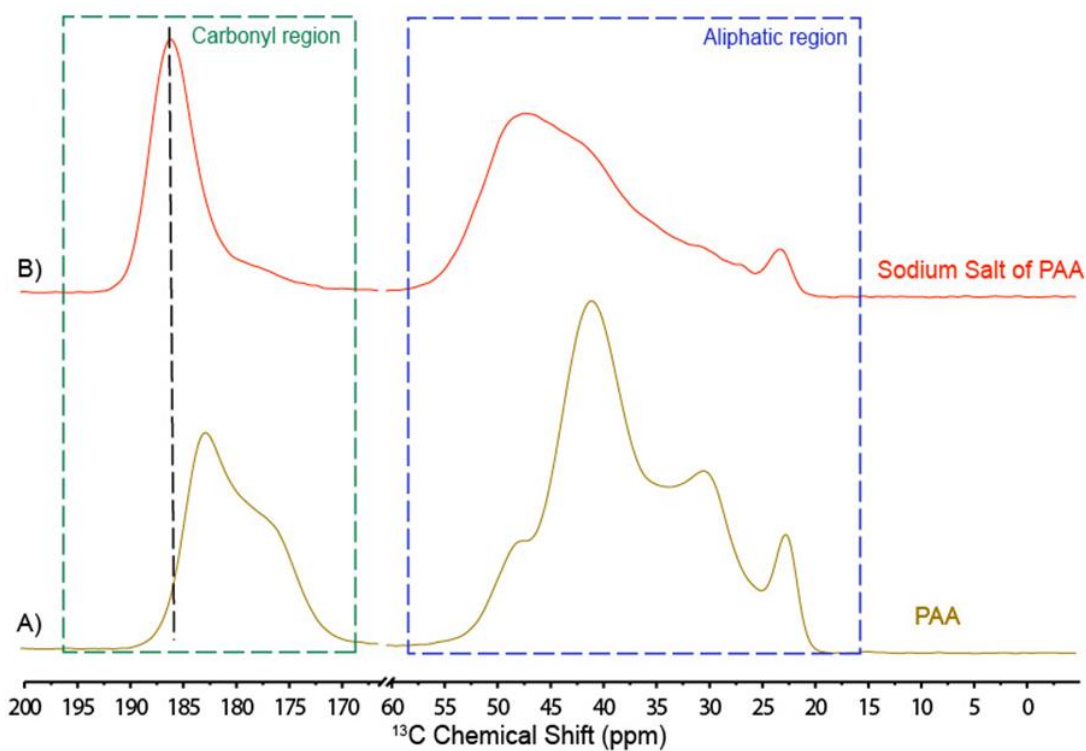


Figure 5.12. ^{13}C CP/MAS SSNMR spectra of PAA and sodium salt of PAA. The main peak in the carbonyl region of sodium salt resonated around ~ 186 ppm.

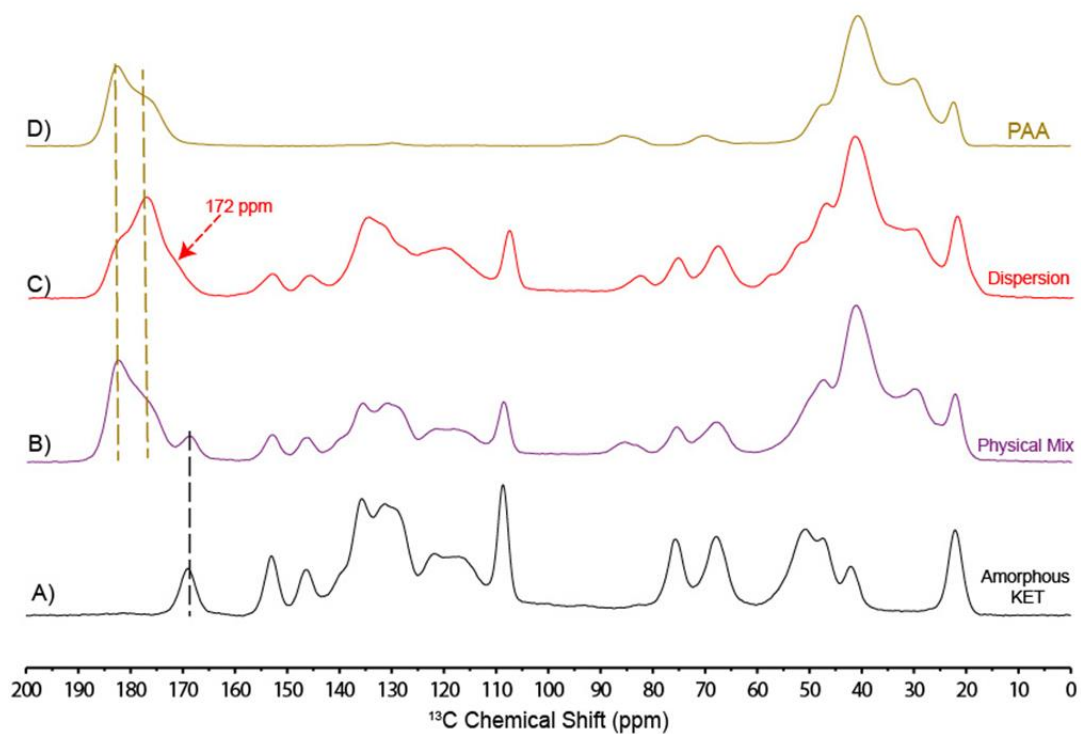


Figure 5.13. ^{13}C CP/MAS spectra of 50:50 KET:PAA binary dispersion (red) and 50:50 KET:PAA physical mixture (purple). The shoulder peak around 172 ppm is visible in dispersion sample but absent in physical mixture. Spectra of PAA and amorphous KET is included as a reference.

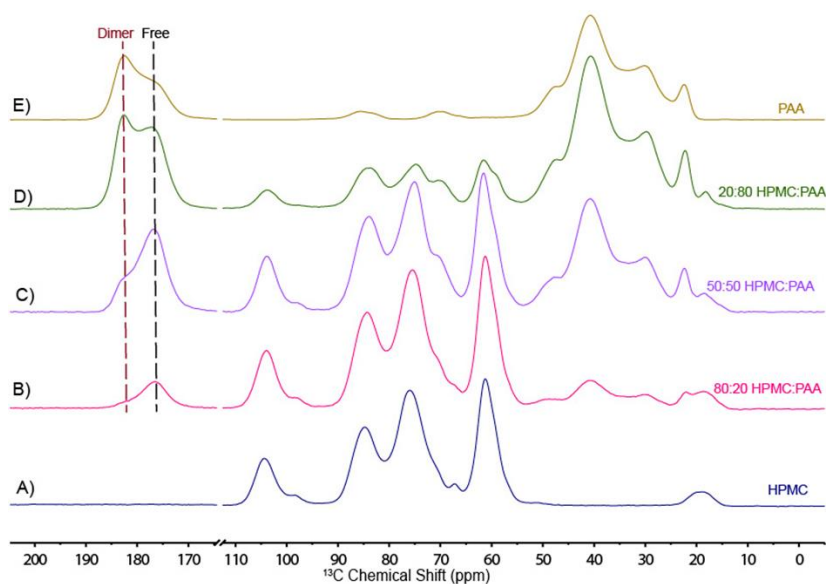


Figure 5.14. ^{13}C CP/MAS spectra of spray dried blends of PAA and HPMC at various ratios.

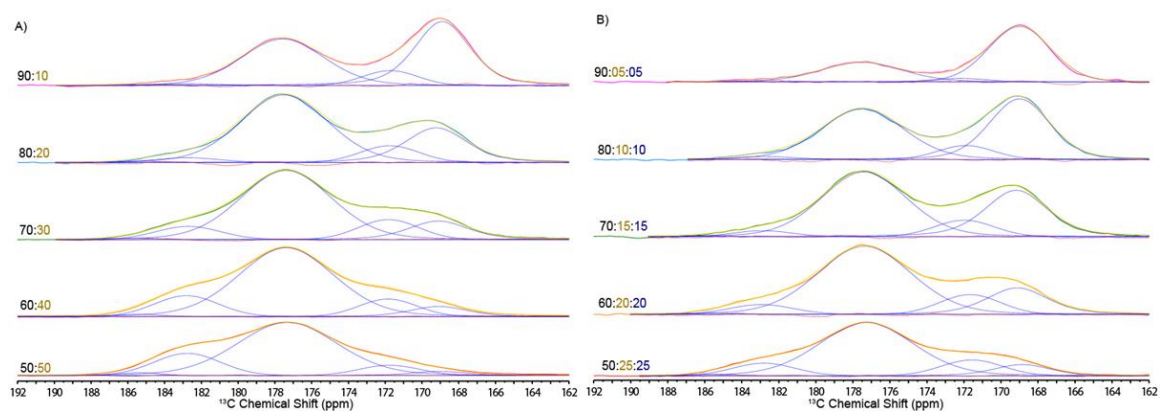


Figure 5.15. Deconvolution of the carbonyl region of (A) binary KET:PAA samples and (B) ternary KET:PAA:HPMC samples. The fitted peaks are shown in blue; the sum of the fit is shown in yellow; the residual is shown in red.

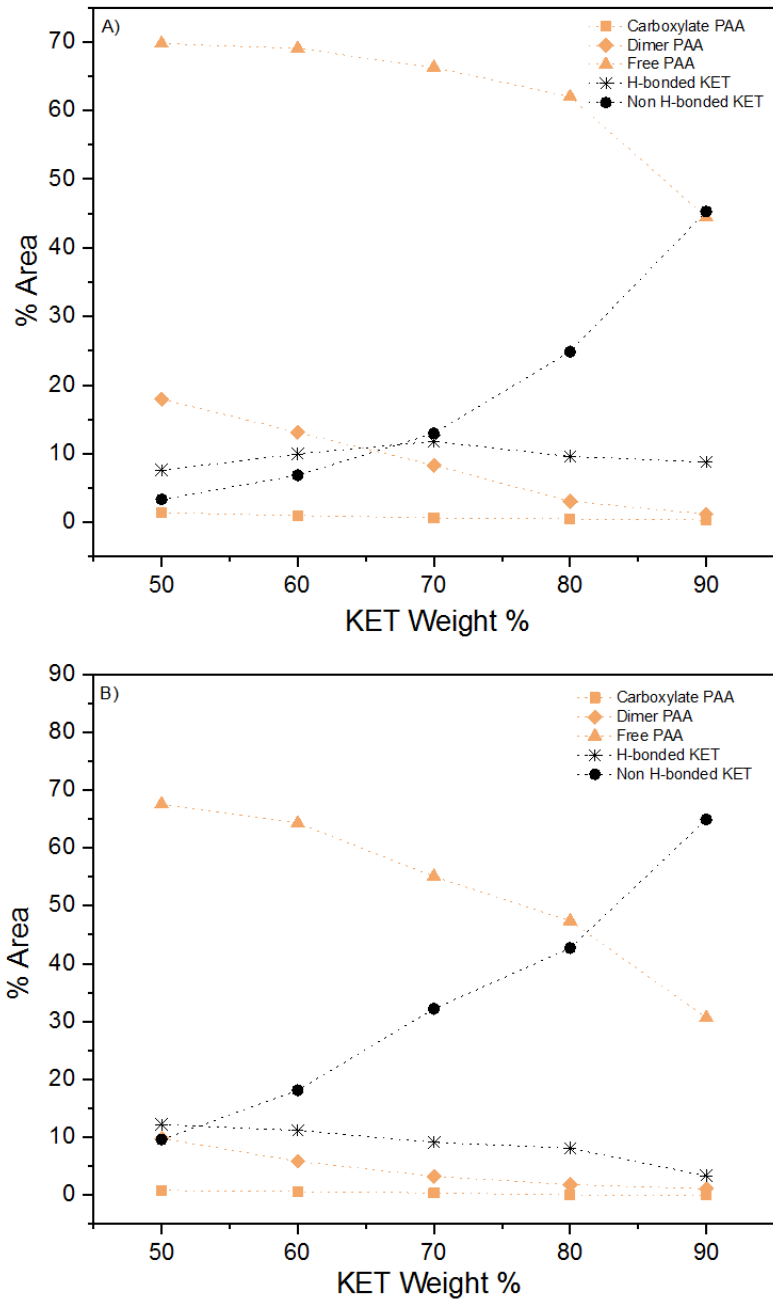


Figure 5.16. Plots of % peak area for various species as a function of KET weight % obtained from deconvolution of the carbonyl region from SSNMR spectra for (A) KET:PAA binary system and (B) KET:PAA:HPMC ternary system. The black and gold curves belong to KET and PAA species respectively.

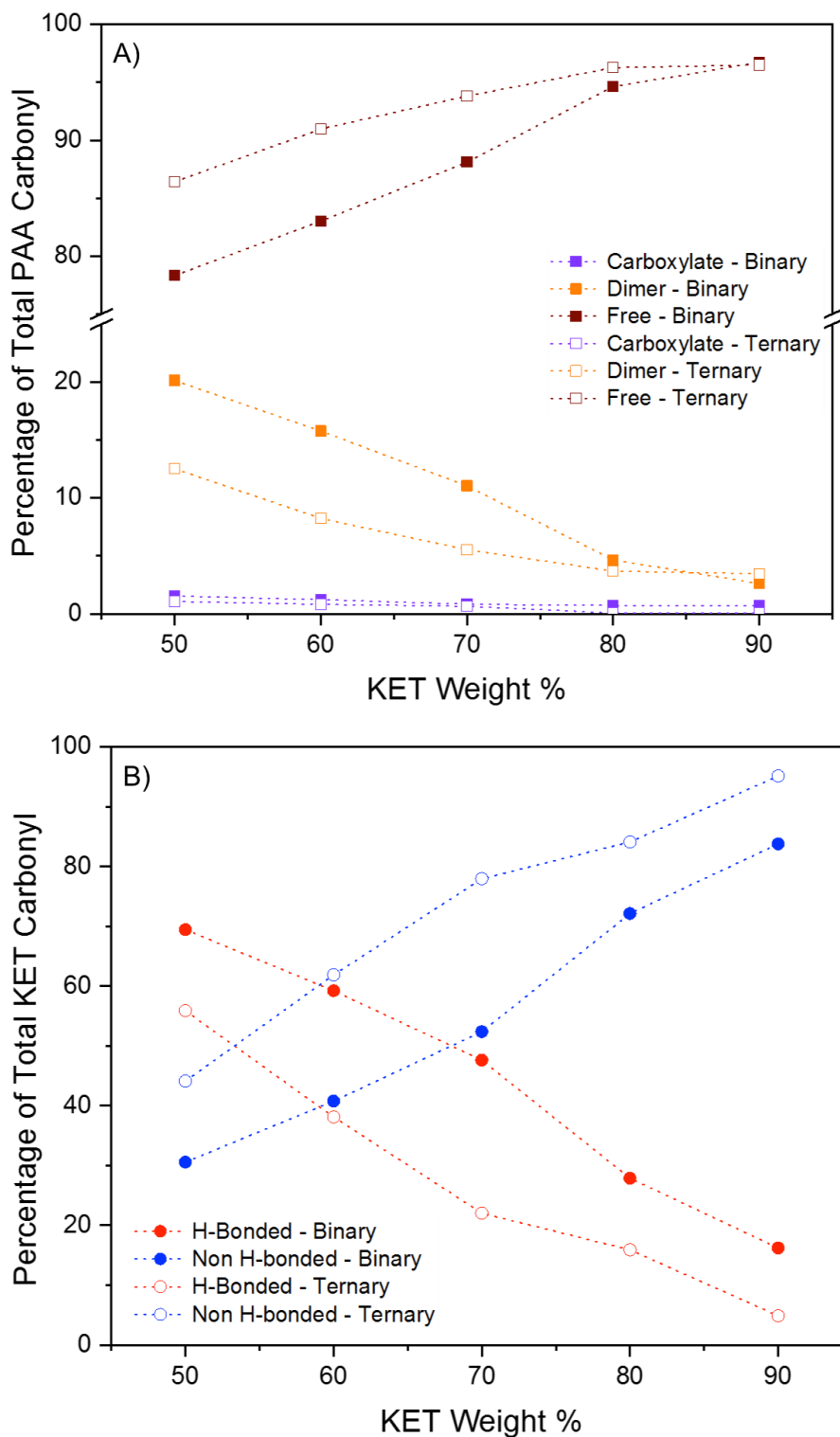


Figure 5.17. Plots depicting comparison of various species in binary and ternary systems calculated for total (A) PAA carbonyl fraction and (B) KET carbonyl fraction as a function of KET weight%.

5.3.4.2 ^{15}N CP/MAS Spectra Analysis

^{15}N SSNMR experiments were performed in order to further understand the acid-base interactions between KET and PAA. ^{15}N is known to have both a very low magnetogyric ratio and natural abundance, which makes it very less sensitive and therefore time consuming to analyze. Another challenge that comes with ^{15}N spectra of amorphous materials is the presence of broader resonances, which makes detection more complicated, and this becomes more aggravated in the presence of excipients, which can further reduce the signal intensity due to dilution. However, even with these challenges, ^{15}N data collected in our study did reveal some important features regarding the local nitrogen environment of KET. The ^{15}N spectra of samples are compared in Figure 5.18. Given the time it took to acquire each spectrum (~3-4 days), only one composition close to the 1:1 molar ratio was selected (80:20 composition on weight basis for both the systems). In the spectrum of amorphous KET, four resonances could be detected. The peak at 259 ppm was attributed to the imidazole N34 nitrogen in KET. In the dispersion samples, no variation in chemical shifts of other resonances was observed except for nitrogen N34. The nitrogen N34 peak shifted upfield ~16 ppm and ~ 19 ppm in binary and ternary samples, respectively, and this change in chemical shift is suggestive of proton transfer or salt formation. Similar results have been reported by Lubach et al. for indomethacin and eudragit system, where ~16 ppm shift relative to polymer was noted for a 70% dispersion sample.⁴² In another study, similar change in chemical shift of amorphous lapatinib was observed when formulated with HPMCP, resulting from tization of drug.⁴³ This exercise supports the results obtained from FTIR and ^{13}C

SSNMR experiments and further provides evidence for the presence of ionic interaction between KET and PAA.

5.3.4.3 Investigation of Phase Homogeneity by SSNMR

In order to further understand the homogeneity of dispersions at a nanometric level, ^{13}C -detected proton relaxation experiments were performed. Two different kinds of proton relaxation measurements were included: spin-lattice relaxation time in the laboratory frame ($^1\text{H } T_1$), and in the rotating frame ($^1\text{H } T_{1\rho}$). The relaxation parameter $^1\text{H } T_1$ studies homogeneity on larger domain sizes than $^1\text{H } T_{1\rho}$, since for solids $^1\text{H } T_1 \gg ^1\text{H } T_{1\rho}$. Typically, for an intimately-mixed system, identical relaxation behavior is seen for individual components due to spin diffusion. If not, different relaxation values are seen for each component. A common $^1\text{H } T_1$ value signifies mixing to a scale of about 20-50 nm, whereas a common $^1\text{H } T_{1\rho}$ value denotes mixing to a scale of about 2-5 nm. For reference, the proton relaxation times for the individual components are given in Table 5.1. The relaxation times for the KET:PAA binary system are shown in Figure 5.19 (plots A and D). Each composition showed a single relaxation $^1\text{H } T_1$ and $T_{1\rho}$ value within the error of measurement, suggesting that dispersions are homogenous to a calculated domain size of <2 nm. The plots of relaxation times for KET:HPMC binary system are shown in Figure 5.19 (plots B and E). It can be found that near identical relaxation values are obtained for $^1\text{H } T_1$ and $T_{1\rho}$ for composition up to 80% drug load, indicating phase homogeneity on a scale less than 3 nm. Whereas sample with 90% drug started to show signs of nano heterogeneity as confirmed by slight differences seen for $^1\text{H } T_1$ and $T_{1\rho}$ relaxation times, with an estimated domain size of > 40 nm. The relaxation times for ternary KET:PAA:HPMC system are shown in Figure 5.19 (plots C and F). A similar

relaxation behavior was observed in the case of ^1H T_1 and $T_{1\rho}$ for all three components up to 80% drug load, but some phase heterogeneity detected at 90% drug load with PAA. Therefore, for ternary samples, a homogeneous domain size of < 3 nm and > 40 nm was estimated for samples up to 80% drug load and 90% drug load respectively. To summarize these results, no drastic differences were observed between the ternary and binary systems in terms of phase homogeneity. In addition, the results provide further insight into molecular level mixing on a smaller scale of resolution than DSC.

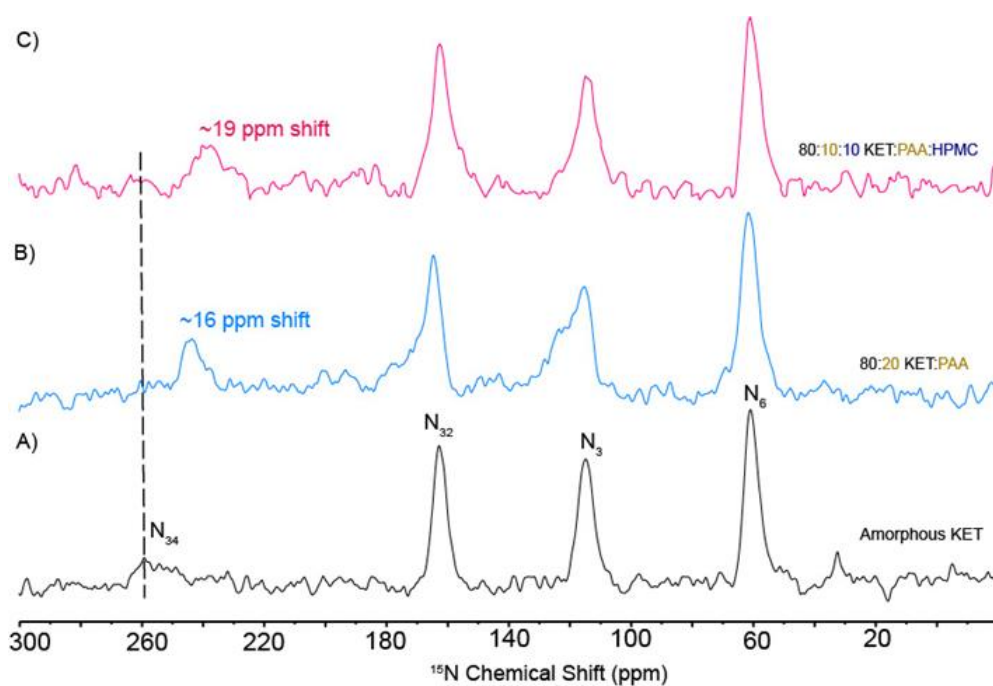


Figure 5.18. ^{15}N CPMAS SSNMR spectra of (A) amorphous KET, (B) 80:20 KET:PAA binary dispersion and (C) 80:10:10 KET:PAA:HPMC ternary dispersion.

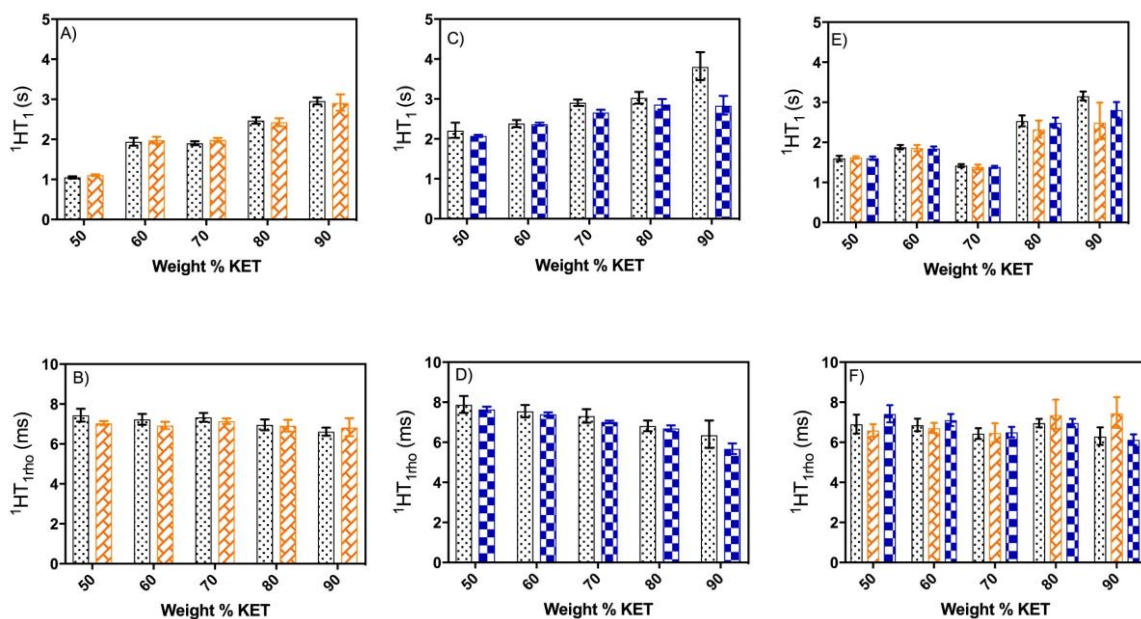


Figure 5.19. Comparison of $^1\text{HT}_1$ (plots A, C, E) and $^1\text{HT}_{1p}$ (plots B, D and F) for drug and polymer(s) components. The relaxation times for KET, PAA, HPMC are shown in black, orange and blue bars respectively. Plots A, C and E belong to $^1\text{HT}_1$ relaxation times for binary KET:PAA system, binary KET:HPMC system and ternary KET:PAA:HPMC system respectively. Plots B, D and F belong to $^1\text{HT}_{1p}$ relaxation times for binary KET:PAA system, binary KET:HPMC system and ternary KET:PAA:HPMC system respectively.

Table 5.1. Proton relaxation times of as received and amorphous KET along with polymers PAA and HPMC.

Proton Relaxation Time	Ketoconazole		Polymers	
	As received	Amorphous	PAA	HPMC
T_1 (s)	13.88±0.11	5.32±0.24	1.45±0.04	1.35±0.02
T_{1p} (ms)	52.71±0.76	4.30±0.07	8.58±0.07	12.53±0.10

5.3.5 Physical Stability

Physical stability of the 70:30 composition from each system was evaluated at two different conditions, RT/94% RH and 40 °C/75% RH for up to six months. PXRD was used to determine the point of initial crystallization. PXRD patterns of the binary and ternary ASDs stored at RT/94% RH are shown in Figure 5.20 (plots A, B and C) for a period of 6 months. The binary system with HPMC crystallized the fastest, displaying signs of crystallization at the 1 week time point. In contrast, the binary system with PAA remained physically stable at RT/94% RH over a period of 6 months with no signs of crystallization. However, the composition of ternary system was shown to perform robustly at these conditions for up to 2 months, when it started to show early signs of crystallization, and crystallized thereafter.

The plots of PXRD data for binary and ternary ASDs at 40 °C/75% RH are illustrated in Figure 5.20 (plots D, E and F). At 40 °C/75% RH, the binary dispersion with HPMC again crystallized the fastest with crystallization being detected from 1 week onwards. Very interestingly, the binary dispersion with PAA and the ternary dispersion retained their amorphous state throughout the period of 6 months, with no diffraction peaks being visible at this condition. This finding suggested that replacing 50% of HPMC with PAA in the binary composition could significantly improve the physical stability.

From the stability analysis, it was revealed that HPMC did not alone inhibit crystallization at both conditions. This could be explained by lack of any specific interactions within the system, which made this binary system the most susceptible to crystallization. Also, we found that HPMC was not as effective as PAA in increasing the

T_g of the ASDs, which also contributed towards poor stability of this binary system at both conditions. As compared with the HPMC binary system, the PAA binary system did outperform in terms of rendering the system physically stable at both conditions. This behavior of PAA is consistent with the ability of PAA to form stronger interactions with KET and higher enhancement in the T_g . Even though PAA is more hygroscopic than HPMC, that did not result in crystallization. Similarly, Weuts et al. found that PAA could maintain loperamide in the amorphous state and give a stable dissolution profile at different storage conditions.³¹ In the case of ternary dispersions samples, adding HPMC did not disrupt KET:PAA interactions drastically nor cause any significant reduction in T_g as revealed from the DSC study. Our detailed SSNMR comparison of binary PAA system and ternary system did reveal that there are some differences in how these two systems interact on a molecular level. It is clear that the 70:30 ternary dispersion had less ionic and H-bonding interactions than the counterpart binary system, and this explains the somewhat poor performance, particularly at RT/94% RH. Otherwise, those disparities still translated to better physical stability in comparison with binary HPMC system.

Our results are very encouraging in a way that they provide support for the use of binary polymer combinations to optimize the performance of ASDs. We have now shown using HPMC alone as a matrix could result in poor physical stability but using a binary combination of PAA and HPMC could help achieve a desired level of physical stability. From dissolution point of view, we have seen from reports in literature that by incorporating a cellulosic polymer in the system could help prolong supersaturation.⁴⁴ Hence, this combination of PAA and HPMC could potentially give a balanced dissolution

profile with better physical stability. This aspect is something that we are currently exploring. We also have to keep in mind that the approach of combining polymers might not always work as shown by Meng et al.⁴⁵ The authors reported that the ternary dispersion of itraconazole with carbopol and povidone demonstrated poor physical stability and drug release behavior when compared to individual polymer based binary dispersions. Nonetheless, ternary ASDs require a detailed solid-state characterization from a molecular perspective to select polymer combinations rationally in order to optimize the overall performance.

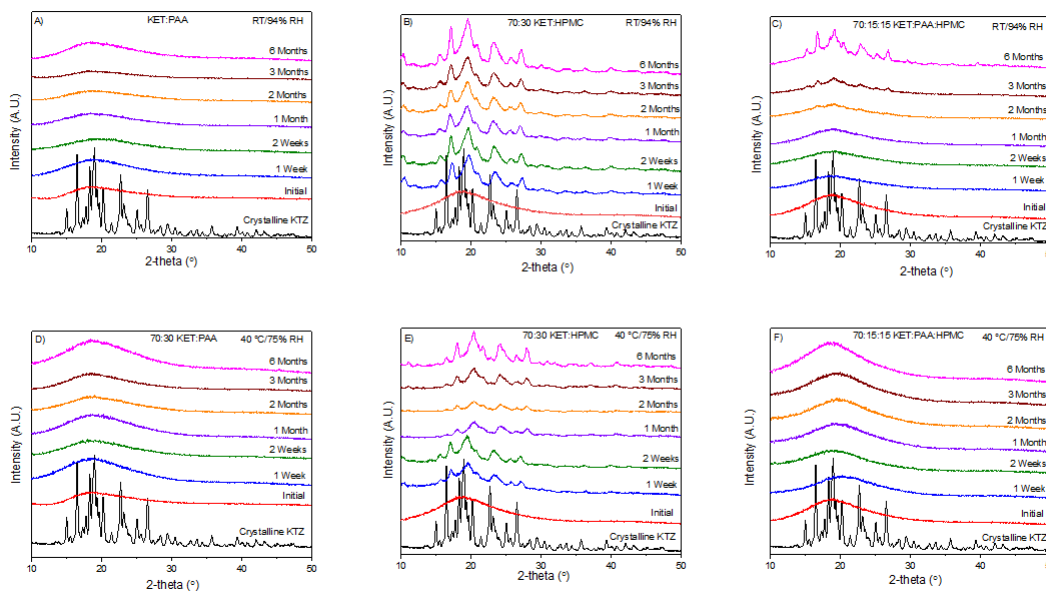


Figure 5.20. PXRD patterns of stability binary and ternary dispersions for (A) KET:PAA (B) KET:HPMC and (C) KET:PAA:HPMC stored at RT/94% RH. The plots of stability samples stored at 40 °C/75% RH are shown in (D) KET:PAA (E) KET:HPMC and (F) KET:PAA:HPMC. Crystalline KET is included as a reference.

5.4 Conclusions

In current study, we have evaluated the molecular interaction patterns in binary and ternary ASDs of KET using various solid-state characterization techniques. From DSC analysis, a large positive deviation was observed for KET:PAA binary and KET:PAA:HPMC ternary systems, whereas KET:HPMC binary system showed negative deviation. Our spectroscopic data from FTIR and ^{13}C SSNMR showed that PAA interacted with KET via ionic and hydrogen bonding interactions both in binary and ternary ASDs. Moreover, spectral evidence can be found for lack of any specific interactions between KET and HPMC. The results from ^{15}N SSNMR analysis further provided evidence for an ionic interaction between KET and PAA. Through a detailed ^{13}C SSNMR deconvolution study, it was established that the binary KET:PAA system had a higher prevalence of ionic and hydrogen bonds than the ternary KET:PAA:HPMC system. This serves as one successful example of establishing a comparison between the binary and ternary ASDs from a molecular perspective. ASDs were found to be homogenous on a nanometric level using proton relaxation measurements for both the binary and ternary systems. A stronger interaction in binary KET:PAA and ternary KET:PAA:HPMC systems translated to better stability at different storage conditions. In summary, this study also established a proof of concept for the approach of combining a second interacting polymer to a non-interacting drug-polymer matrix to achieve better physical stability. We believe our results are valuable contribution to the growing field of ternary ASDs, and provide a better understanding of how to design ternary ASDs with optimum performance.

CHAPTER 6. IMPACT OF HPMCAS GRADE ON PHASE BEHAVIOR OF ITRACONAZOLE SOLID DISPERSIONS: EFFECT OF PREPARATION METHOD

6.1 Introduction

In this chapter, we will discuss the role of different grades of hydroxypropyl methylcellulose acetate succinate (HPMCAS) on the phase behavior of itraconazole (ITZ) dispersions. In recent years, HPMCAS has been identified as one of the most effective cellulose based polymers especially for manufacturing spray dried dispersions (SDDs).^{1,2} HPMCAS has some unique characteristics that makes it amenable for spray drying process.³ They are listed below:

- (1) It possesses a high T_g in its unionized state. The high T_g reduces the drug mobility and results in excellent physical stability of HPMCAS based dispersions.
- (2) It has good solubility in volatile organic solvents like acetone and methanol, thereby permitting economical and controllable processing for manufacturing SDDs.
- (3) At any pH above 5, the polymer becomes at least partially ionized, which causes the charge to develop and minimizes the formation of large polymer aggregates and stabilizes the drug-polymer colloids.
- (4) Its amphiphilic nature permits poorly water-soluble drugs to interact with the hydrophobic regions while the hydrophilic region allows these structures to remain as stable colloids in aqueous medium.

Commercially, HPMCAS is available in three grades, designated as -L, -M, and -H as listed in Table 6.1. These grades have different percentages of substituents: methoxy, hydroxypropoxyl, acetate and succinate. Spray drying is a conventional

method for the preparation of amorphous solid dispersions, but from a practical standpoint, it is best to have techniques that can be used to predict the properties of the spray-dried dispersion prior to the actual spray drying process.⁴ Recently, cast films have been explored to anticipate the feasibility of samples prepared using methods such as spray drying and hot melt extrusion.^{5,6} For instance, Durante et al. employed a predictive model to estimate the miscibility of ITZ with different polymers for cast films and SDDs.⁷ In this study, the authors could rank order the polymers (Eudragit EPO<<PVP/VA< HPMCAS-MG) in terms of miscibility and their results reflected the same trends between films and SDDs. In this study, the utility of films have been investigated for a model system consisting of ITZ and different grades of HPMCAS in order to anticipate the viability of large-scale processes such as spray drying. This study was a collaborative effort between the Munson group and Prof. Polli's group at University of Maryland. The film and spray dried samples were prepared at University of Maryland, whereas detailed solid-state characterization was performed at University of Kentucky, with a special focus on SSNMR spectroscopy.

The first objective of this chapter was to assess the impact of different grades of HPMCAS on the phase behavior of ITZ dispersions. Secondly, the role of preparation method on the phase mixing of the drug with polymer was also evaluated. In addition, long-term accelerated stability studies (40 °C/75 % RH) were conducted to evaluate the physical stability of film and spray dried samples. Only the results gathered at University of Kentucky are presented here. Chemical structures are shown in Figure 6.1.

6.2 Experimental

6.2.1 Preparation Method

Preparation of Amorphous Itraconazole. Amorphous ITZ was prepared by *in situ* by melt quenching inside the spinning NMR rotor. Sample was packed into 7.5 mm zirconia rotors with Teflon or Kel-F end caps (Revolution NMR, LLC., Fort Collins, CO). The rotor was heated in the NMR probe equipped with a variable-temperature accessory stack (Varian, Palo Alto, CA) at 175 °C for approximately 10 min while spinning at 4 kHz. The rotor was then rapidly cooled to room temperature to generate amorphous ITZ.

Preparation of film samples. HPMCAS films were cast by dissolving each of the three grades of HPMCAS in a 2:1 (w/w) mixture of dichloromethane and methanol. ITZ was then added to the solutions to constitute 10, 20 and 30% (w/w) of the total solid content in the solution. The total solid concentration in the final solutions was kept at 10% (w/w). Solutions were then poured into round 50 mL aluminum pans (121 mm diameter x 5 mm height) at 50 g per pan and evaporated for 45 min. The pans were transferred to a drying oven and dried at 40 °C for over 12 hr. The film samples were then stored in a desiccating cabinet (RH < 5%) and subsequently milled into flakes by trituration.

Preparation of Spray dried samples. Spray drying was performed using a Buchi B-290 spray dryer (Buchi Corporation; New Castle, DE) in the closed-loop mode. Solutions identical to those used for film casting were pumped into the atomizer at a rate of 16 g/min. The inlet and outlet temperatures were 100 °C and 56 °C, respectively. Spray drying process parameters (i.e. inlet temperature, percent solids, pump rate,

atomizing gas pressure) had been previously examined to yield above methods. The spray dried powder (i.e. SDDs) were collected and dried for an additional 12 hr at 40 °C and stored in a desiccating cabinet (RH < 5%).

6.2.2 Solid-State NMR Spectroscopy

¹³C SSNMR spectra were acquired using a Tecmag Redstone spectrometer (Tecmag Inc., Houston, TX) operating at approximately 300 MHz for ¹H and 75 MHz for ¹³C. Samples were packed into 7.5 mm zirconia rotors and sealed with Teflon or Kel-F end-caps (Revolution NMR LLC, Fort Collins, CO). One dimensional ¹³C spectra were acquired using cross polarization magic angle spinning (CP/MAS) at 4 kHz, using total sideband suppression (TOSS)⁸ and SPINAL64⁹ decoupling. The ¹H 90° pulse width was set to 4.5 μs and contact time of 1.5 ms was used in all the measurements. The pulse delay for 1D experiments was 4 s and a total of 4096 scans were collected. The ¹³C chemical shift scale was referenced with the methyl peak of 3-methylglutaric acid, which was set to 18.84 ppm.¹⁰

The maximum peak intensity for the chemical shift regions selective to ITZ and HPMCAS resonances were used to obtain relaxation times (details in Results and Discussion section). The relaxation times were detected via ¹³C nucleus, which facilitates identification of regions for respective components. Proton spin-lattice relaxation time in the laboratory frame (¹H T₁) were measured using a ¹³C-detected saturation recovery pulse sequence with TOSS. Relaxation times were obtained by fitting intensity-recovery time data by the following equation:

$$M(t) = M_0(1 - e^{-\frac{t}{T_1}}) \quad (6.1)$$

where $M(t)$ is the peak intensity at delay time t , M_0 is an amplitude parameter from the fit, and T_1 is the obtained spin-lattice relaxation time. Proton relaxation times in the rotating frame ($^1\text{H } T_{1\rho}$) were measured by varying the spin lock duration time after a 90° pulse. The $T_{1\rho}$ decay times were obtained by analyzing the integrated carbon signal intensity exponentially according to the following equation:

$$M(t) = M_0 e^{-\frac{t}{T_{1\rho}}} \quad (6.2)$$

where $M(t)$ is the peak intensity and t is the spin-lock duration time. M_0 is an amplitude parameter from the fit, and $T_{1\rho}$ is the fitted spin-lattice relaxation time in the rotating frame. All data fitting was done using GraphPad Prism (GraphPad Software, Inc., La Jolla, CA).

6.2.3 Powder X-ray Diffraction

PXRD patterns were collected on the Rigaku Miniflex 600 benchtop diffractometer (Rigaku Corporation, Tokyo, Japan), with Cu $K\alpha$ radiation (40 kV x 15 mA). The experiments were conducted at room temperature, between 2° to 50° 2θ at a scan speed of $2.0^\circ/\text{min}$ and a step size of 0.02° 2θ under continuous mode.

6.2.4 Vapor Sorption

Moisture sorption isotherms of pure components and dispersions were measured by an automated water sorption analyser (Q5000SA, TA instruments, New Castle, DE). The neat samples were initially dried at 0% relative humidity (RH) at 25°C for 180 min with equilibrium criterion of $< 0.001\%$ w/w change for 15 min. The samples were then exposed to different RH conditions from 10 to 90% at 25°C with 10% step increase. The

maximum dwell time of 180 min was used with the same equilibrium criterion. The dispersion samples were subjected to constant RH of 75% at 40 °C until equilibrated after initial drying at 0% RH with a dm/dt window of weight change % < 0.001 over 15 min.

6.3 Results and Discussion

6.3.1 ¹³C CP/MAS Solid-state NMR Spectra

The ¹³C CP/MAS spectra of as-received ITZ and amorphous ITZ are shown in Figure 6.2. The crystalline ITZ could be easily distinguished from amorphous ITZ based on sharp and narrow resonances seen in the ¹³C spectra. The amorphous form is characterized by broader signals characteristic of disordered state. The peak at 152 ppm corresponds to the carbonyl group (C=O) in the amorphous ITZ. The ¹³C CP/MAS spectra for the polymers are displayed in Figure 6.2. All the three grades of HPMCAS were found to be amorphous. The HPMCAS grades were devoid of aromatic resonances as shown in Figure 6.2. It is interesting to note the differences in peak shapes for different grades of HPMCAS in the carbonyl region (160-180 ppm). Upon deconvolution of the region, the area could be resolved into two peaks (~173 ppm and ~170 ppm). These two peaks correspond to succinate and acetate ester functionalities, respectively, although it should be noted that the succinate moiety has an equal contribution to succinate and acetate peak, due to its partial ester structure. The analysis also yielded respective percentages of these moieties as displayed in Figure 6.3. L grade has the highest succinate to acetate ratio among three grades, which explains why the carbonyl peak is apparently the most downfield in L grade. The other aliphatic resonances were

measured to be similar in ppm in all the three grades, although the peak at ~28 ppm is due to the succinate component, and its intensity changes with succinate concentration.

The dispersions samples were prepared via two approaches: rotary evaporation and spray drying. The samples obtained from rotary evaporation were termed “film” samples. The ^{13}C CP/MAS spectra of film samples formulated with HPMCAS grades are shown in Figure 6.4. For the spectra of dispersions with HPMCAS, samples up to 20% drug loading were amorphous in nature whereas the samples with 30% ITZ showed the presence of some amount of residual crystallinity. The degree of crystallinity could be quantified for different grades of HPMCAS. The region between 90-115 ppm was deconvoluted and the peak at 109 ppm was attributed to the crystalline ITZ fraction. The degree of crystallinity was calculated using following equation:

$$\phi_{ITZ} = 100 * \frac{P_{109}}{P'_{109}} \quad (6.3)$$

where P_{109} is the peak intensity for 109 ppm signal in the sample and P'_{109} is the peak intensity of 109 ppm signal of pure crystalline ITZ. The degree of crystallinity was rank ordered as H>M>L (Table 6.3; initial condition). Thus, the highest crystallinity was associated with H grade. And, the same trend was seen from DSC analysis (data not shown). In the case of the spray-dried samples, it was evident from Figure 6.5 that samples were completely amorphous for all the drug loadings. The spray-dried dispersions were better than the film samples in this regard, as they were devoid of any residual crystallinity. The spray drying process is generally regarded as more efficient in rendering the samples amorphous than the rotary evaporation as it ensures better mixing of the drug and polymer.

Three regions between resonances 9-14 ppm, 45-55 ppm and 111-159 ppm were selective for ITZ (shown in pink shaded boxes in Figures 6.4 and 6.5), while two regions between peaks 80-90 ppm and 160-180 ppm served as non-overlapping areas for HPMCAS (shown in green shaded boxes in Figures 6.4 and 6.5). These selective regions were used in proton relaxation measurements to follow the relaxation behavior of ITZ and HPMCAS in the samples (*vide infra*). In addition, any variation in chemical shift for any peak in the spectra was also noted. HPMCAS has proton donors and acceptors in its structure whereas ITZ has proton acceptors (Figure 6.1). Therefore, there is a likelihood of hydrogen bond formation between the respective donors and acceptor functionalities in the drug and polymer. It has been observed that any change in chemical shifts could potentially result from H-bonding.¹¹ The carbonyl region of HPMCAS did not show any significant changes for both film and spray dried samples. In addition, any variation in the carbonyl peak (~152 ppm) of ITZ was difficult to detect due to presence of multiple peaks in the same region. Therefore, no direct evidence of hydrogen bonding or any specific interaction could be obtained from the ¹³C CP/MAS spectra.

Table 6.1. Composition of different grades of HPMCAS (wt %).

Substituent	HPMCAS		
	L Grade	M Grade	H Grade
Methoxyl Content	20-24	21-25	22-26
Hydroxypropoxyl Content	5-9	5-9	6-10
Acetyl Content	5-9	7-11	10-14
Succinoyl Content	14-18	10-14	4-8

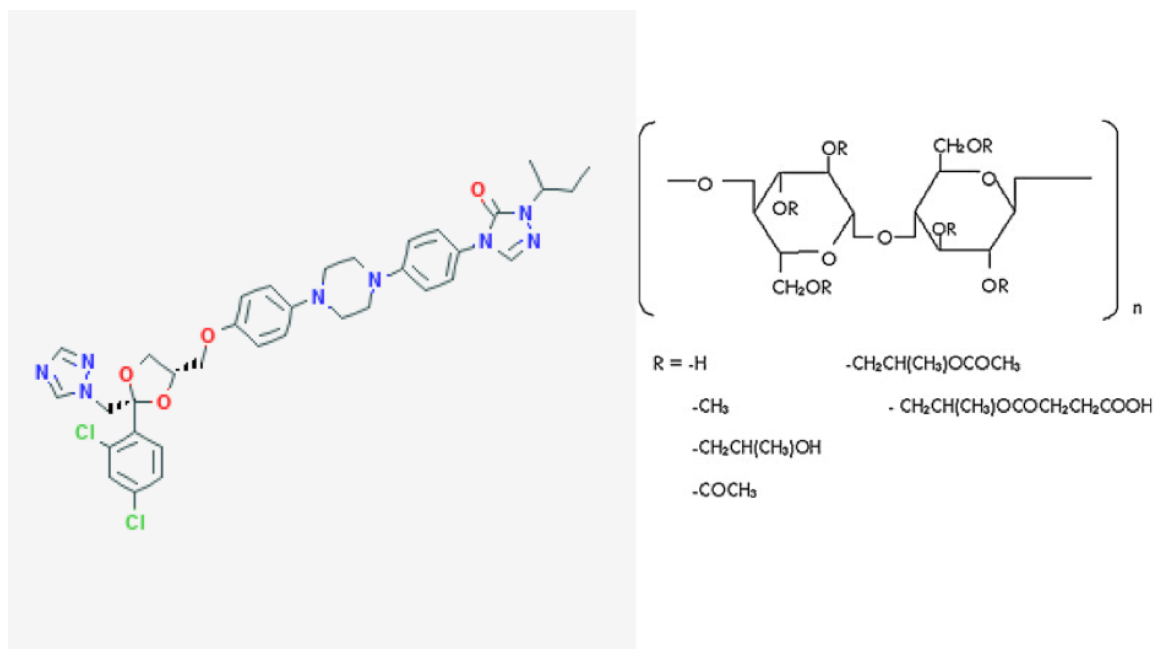


Figure 6.1. Chemical structures of itraconazole (left) and HPMCAS (right).

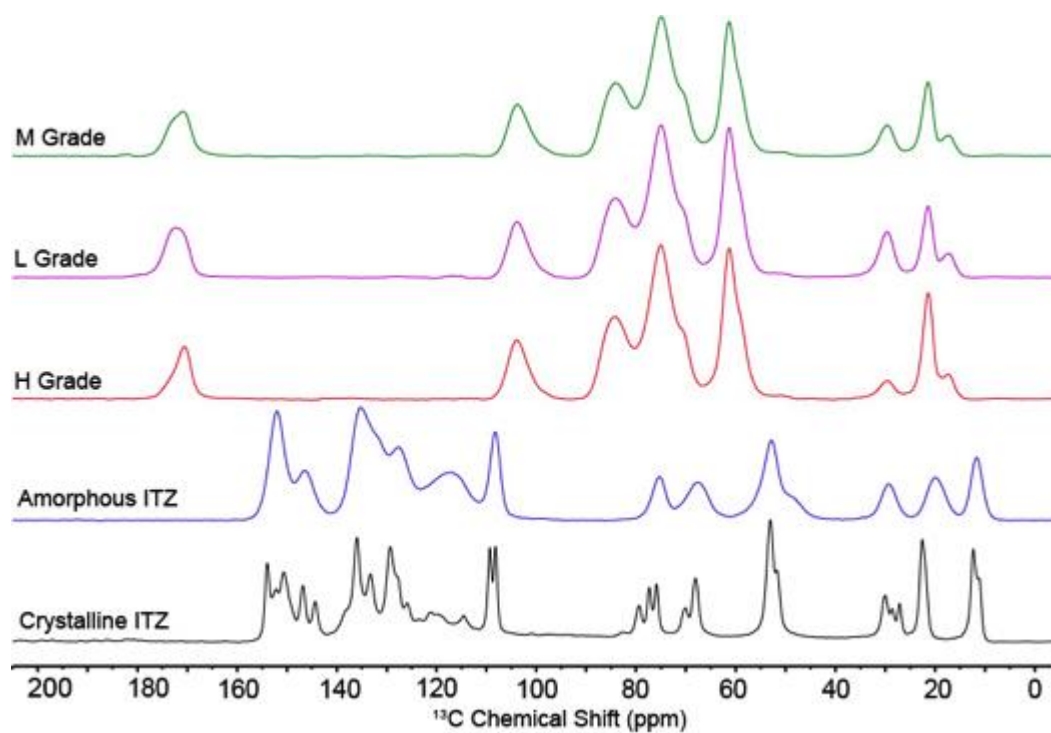


Figure 6.2. SSNMR spectra from bottom to top include crystalline ITZ, amorphous ITZ and HPMCAS grades-H, L and M.

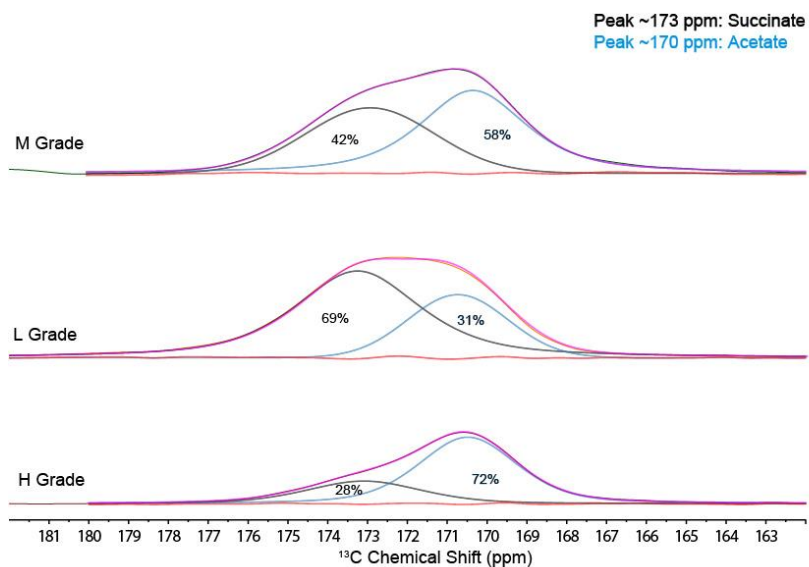


Figure 6.3. Deconvolution of the carbonyl region (160-180 ppm) in SSNMR spectra for HPMCAS grades. The fitting of succinate and acetate peaks is shown in black and blue respectively; the sum of the species is shown in magenta; the residual difference between the experimental and fitted peaks is shown in orange.

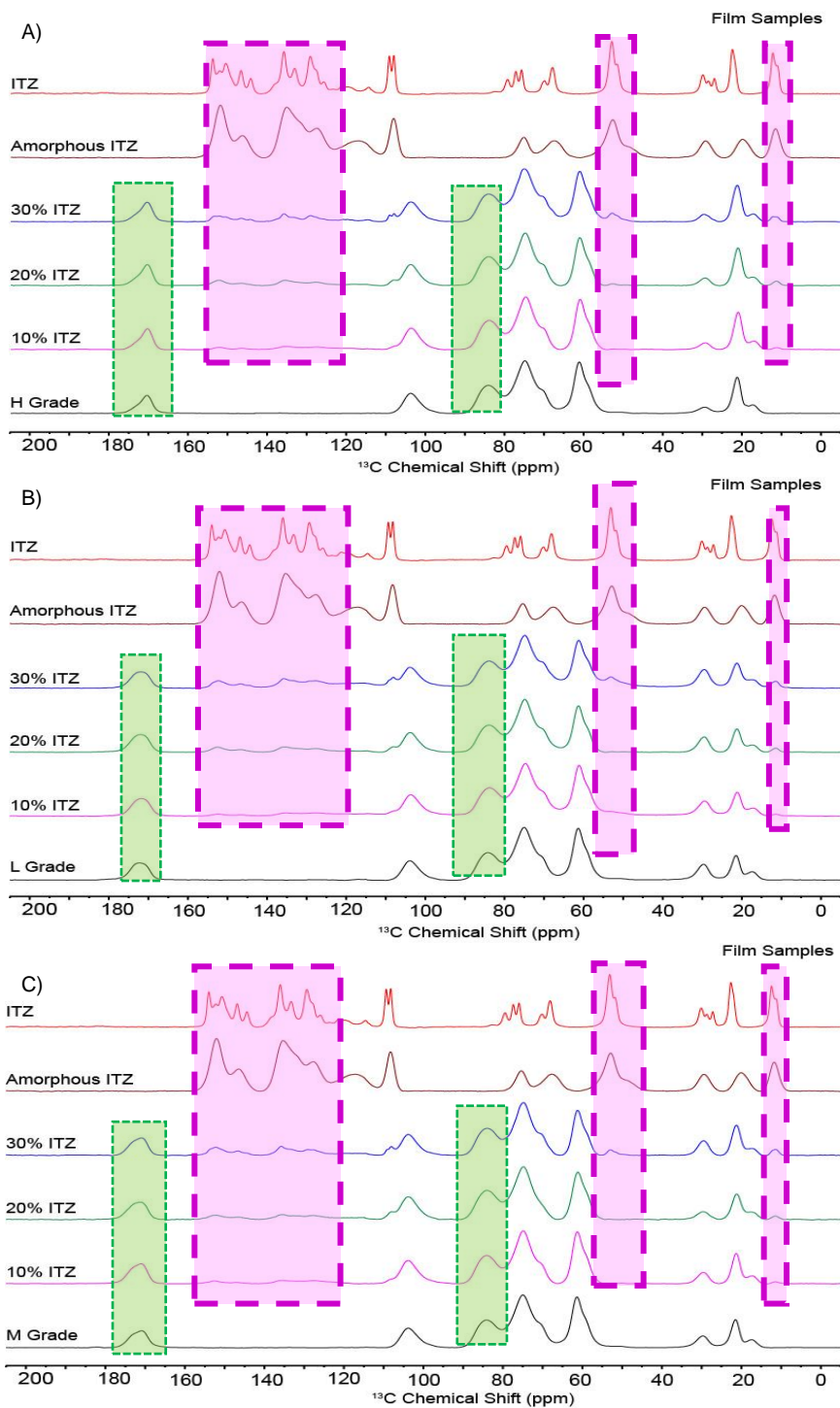


Figure 6.4. Stacked ^{13}C CP/MAS spectra for ITZ film samples formulated with (A) HPMCAS H grade, (B) HPMCAS L grade and (C) HPMCAS M grade. Green and pink shaded boxes represent HPMCAS and ITZ specific regions respectively.

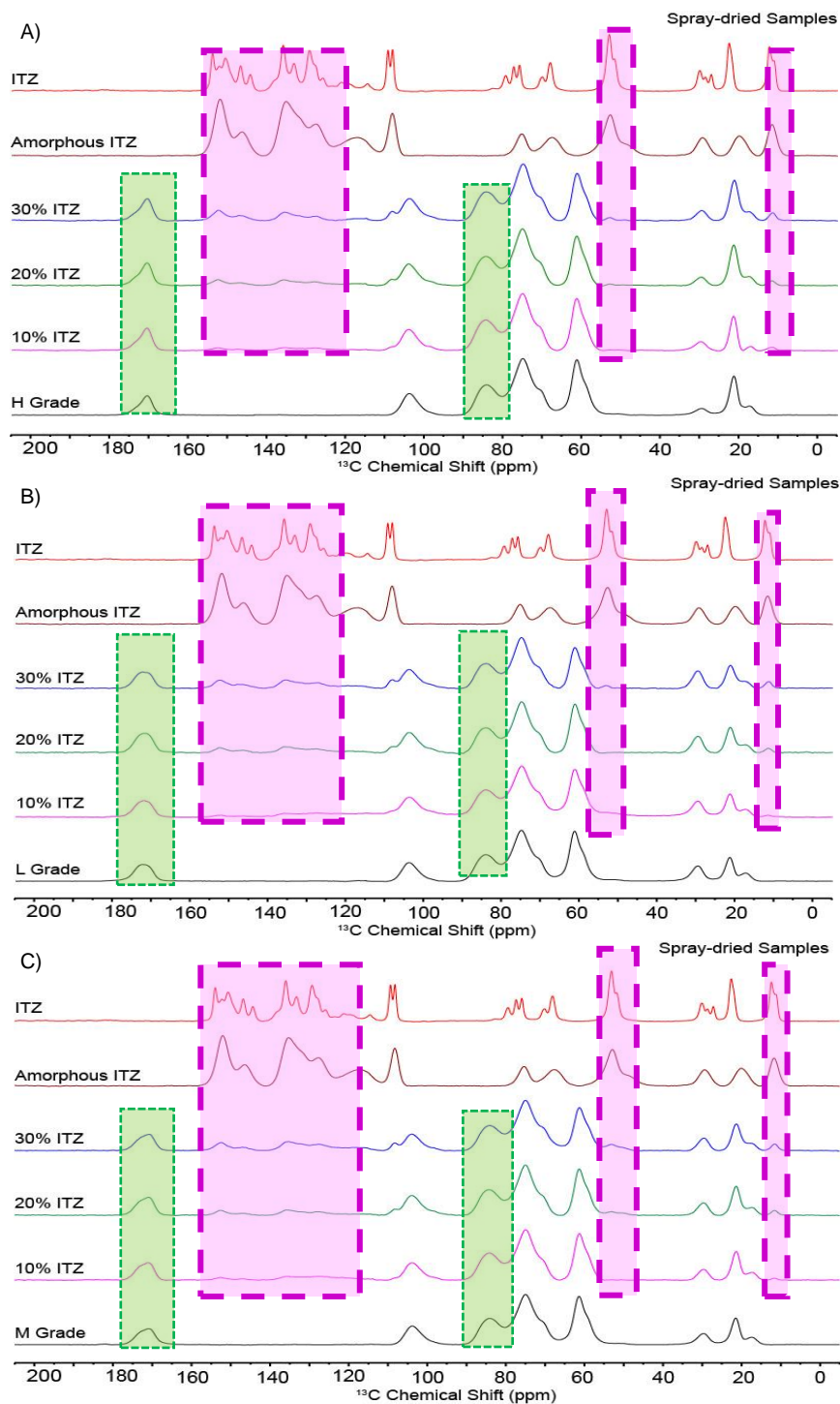


Figure 6.5. Stacked ^{13}C CP/MAS spectra for ITZ spray dried dispersion samples formulated with (A) HPMCAS H grade, (B) HPMCAS L grade and (C) HPMCAS M grade. Green and pink shaded boxes represent HPMCAS and ITZ specific regions respectively.

6.3.2 Phase Homogeneity Using Proton Relaxation Measurements

In order to understand phase mixing on a nanometric scale, proton relaxation measurements were employed, which consisted of measuring spin-lattice relaxation times in the laboratory frame $^1\text{H } T_1$, and in the rotating frame $^1\text{H } T_{1\rho}$. The relaxation behavior of ITZ and HPMCAS was resolved via ^{13}C resonances. These parameters can provide valuable insights regarding the phase mixing between the drug and the polymer on two different length scales of mixing. The relaxation time constants $^1\text{H } T_1$ and $^1\text{H } T_{1\rho}$ are sensitive to motions in MHz range and kHz range, respectively. Because the $^1\text{H } T_1$ times are 2-3 orders of magnitude longer than $^1\text{H } T_{1\rho}$ times, $^1\text{H } T_1$ is averaged out to larger distances (20-50 nm) than $^1\text{H } T_{1\rho}$ (2-5 nm). The relaxation times of pure materials are shown in Table 6.2. Generally, amorphous materials show shorter $^1\text{H } T_1$ and $^1\text{H } T_{1\rho}$ relaxation times in comparison to their crystalline counterparts owing to greater mobility. In the case of ITZ, the amorphous sample is characterized by shorter $^1\text{H } T_1$ time whereas the opposite behavior is seen for $^1\text{H } T_{1\rho}$. For HPMCAS grades, $^1\text{H } T_1$ times were measured to be less than 2 s. It is interesting to note that $^1\text{H } T_{1\rho}$ time was measured longest for the H grade. Meanwhile, both L and M grade showed almost identical $^1\text{H } T_{1\rho}$ times. Greater differences were observed in $^1\text{H } T_{1\rho}$ times between amorphous ITZ and HPMCAS.

Dispersion samples showed differences in relaxation time of ITZ and HPMCAS, corresponding to some degree of phase heterogeneity between the drug and the polymer. For a perfectly homogenous system, drug and polymer would show identical relaxation times. Therefore, any differences observed in the relaxation behavior of the drug and polymer would result from phase heterogeneity or non-uniform distribution of drug and

polymer in the matrix. The plots of ^1H T_1 differential between ITZ and different grades of HPMCAS are shown in Figure 6.6 for the film and spray dried samples. It is evident from the Figure 6.6 (Plot A) that no significant differences were seen up to 20% ITZ loading, whereas the sample with 30% loading started to show some differences, resulting in a larger differential value for the film samples. The extent of phase heterogeneity on ^1H T_1 scale of mixing could be ranked ordered as $\text{H}>\text{M}>\text{L}$. However, for the spray-dried samples no such trend could be seen for any drug loading, and all the samples were found to be homogenous on ^1H T_1 scale of mixing (Plot B). The plots of ^1H $T_{1\rho}$ differential between ITZ and different grades of HPMCAS are displayed in Figure 6.7 for film and spray dried samples. On smaller domains (Plot A), the film samples were clearly phase non homogeneous at 30% drug loading, and same extent of phase separation was observed ($\text{H}>\text{M}>\text{L}$). In contrast, the spray dried samples (Plot B) were completely phase mixed showing no differences in differential values within 95% confidence intervals.

In summary, the film samples were homogenous up to 20% drug loading, whereas 30% sample showed signs of phase heterogeneity on both the domains. In the case of 30% ITZ sample, the extent of phase heterogeneity was found to be different for different grades of HPMCAS (L grade being best). This is also supported from the residual crystallinity analysis. It was shown that better mixing between ITZ and HPMCAS could be established through spray drying. And, all the three grades exhibited similar performance for spray dried samples and no phase heterogeneity was seen.

6.3.3 Determination of Domain Sizes

Proton relaxation measurements can also be used to estimate the upper limit of the length scale of mixing because these processes are governed by spin diffusion. The equation used to obtain semi quantitative information about domain size is given by:

$$L^2 = 6DT_i \quad (6.4)$$

where D is the spin diffusion coefficient, which depends on the average proton to proton distance as well as a dipolar interaction. It has a typical value of 10^{-12} cm²/s.^{12,13} T_i is the relaxation time, T_1 or $T_{1\rho}$. Using this approach, the domains sizes were estimated to be < 3 nm for all the samples except 30% ITZ film samples. In the case of 30% ITZ film samples, domain sizes were estimated be >30 nm, 2-30 nm and >30 nm for H, L and M grades respectively. These samples were known to show some degree of phase heterogeneity and hence their larger domain sizes.

Table 6.2. ¹H T_1 and $T_{1\rho}$ values along with the standard errors associated with fit for ITZ (as-received and amorphous) and HPMCAS grades measured via ¹³C resonances.

Proton Relaxation Time	Itraconazole		Polymers		
	As received	Amorphous	H Grade	L Grade	M Grade
¹ H T_1 (s)	3.34±0.08	1.57±0.02	1.76±0.07	1.93±0.05	1.80±0.04
¹ H $T_{1\rho}$ (ms)	2.88±0.07	3.65±0.05	7.63±0.19	5.99±0.10	5.97±0.25

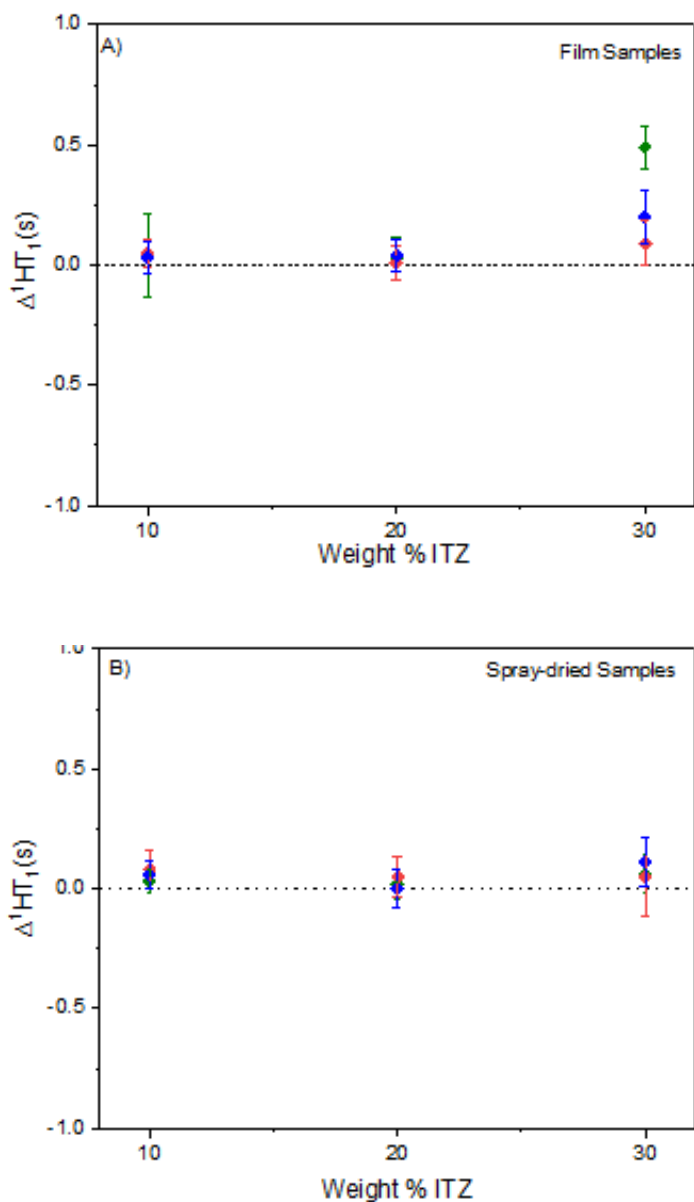


Figure 6.6. Absolute difference in ^1H T_1 values between ITZ and HPMCAS grades for A) film and B) spray dried samples as a function of ITZ weight percent. The error bars represent the 95% confidence interval associated with the fit. The dashed line signifies the zero difference line. The green, red and blue diamond symbols represent HPMCAS H, L and M grades respectively.

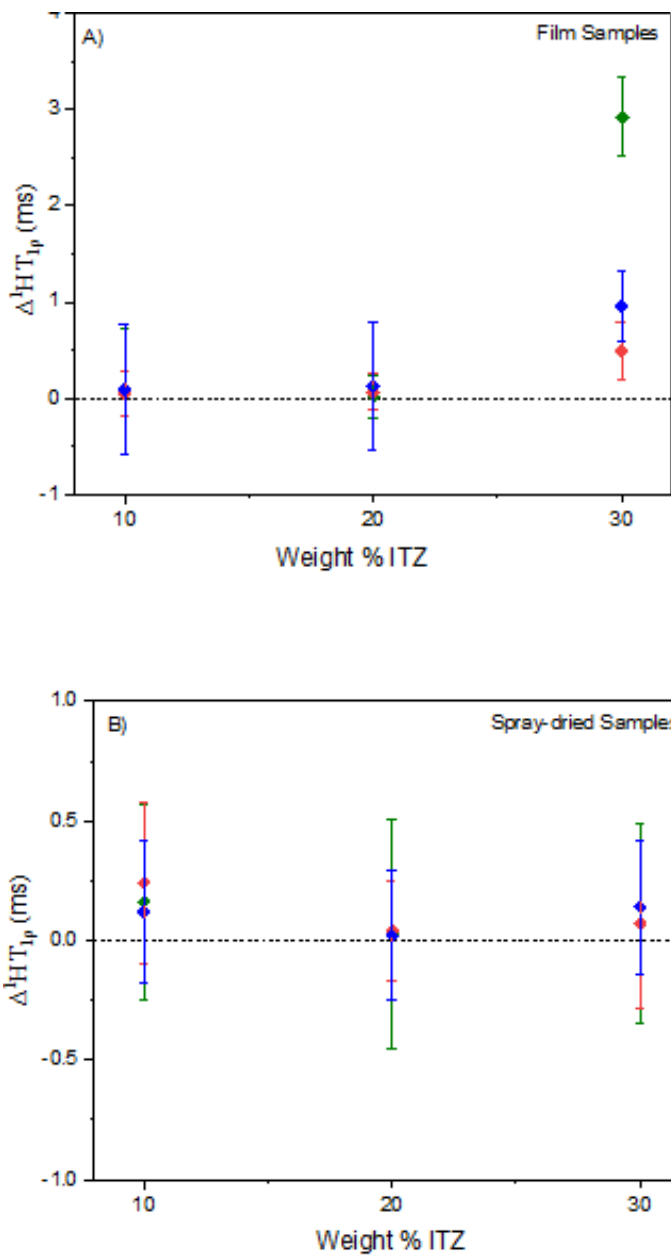


Figure 6.7. Absolute difference in ^1H $T_{1\rho}$ values between ITZ and HPMCAS grades for A) film and B) spray dried samples as a function of ITZ weight percent. The error bars represent the 95% confidence interval associated with the fit. The dashed line signifies the zero difference line. The green, red and blue diamond symbols represent HPMCAS H, L and M grades respectively.

6.3.4 Physical Stability

The physical stability of amorphous materials is very important because of their propensity to crystallize. It is therefore common to study the behavior of ASDs at accelerated stability conditions wherein the role of humidity and elevated temperature is evaluated. The stability study was carried out for the 30% ITZ loading (film and spray dried samples) at 40 °C/75% RH in open vials for a period of 6 months, and the samples were examined via SSNMR and PXRD. PXRD data showed no change in spray-dried samples over time (Figure 6.8). The spray-dried samples remained amorphous up to 6 months, with no detection of crystallinity for all of the grades of HPMCAS. It is also noteworthy to point that SSNMR analysis of spray-dried samples revealed the same trend. No changes were observed in the ^{13}C CPMAS spectra of the spray-dried samples (Figure 6.9). The ^1H T_1 and ^1H $T_{1\rho}$ relaxation data indicated that stability spray-dried samples did not phase separate over time at these conditions, and there was no significant change in the differential values of the relaxation times (Figure 6.10). In the case of film stability samples, no further crystallization was observed by qualitative analysis from PXRD (Figure 6.11). Also, ^{13}C CP/MAS spectra of stability samples did not reveal any new crystalline peaks except for the previously reported peak at ~109 ppm (Figure 6.12). In addition, it is surprising to observe that there was reduction in measured apparent crystallinity over time for these samples as calculated by SSNMR (Table 6.3). This kind of behavior is counterintuitive, as it is known that moisture can promote phase separation and/or crystallization in amorphous materials.¹⁴ At this point, we can speculate that this trend can result from changes induced by RH equilibrated samples in SSNMR spectra. Nonetheless, this needs further investigation to ascertain if this behavior is real or not.

The relaxation data also suggest no further phase separation took place and the differential values for both $^1\text{H } T_1$ and $^1\text{H } T_{1\rho}$ did not change drastically over a period of 6 months (Figure 6.13). Both the systems were found to be robust at these conditions.

From the isothermal moisture sorption experiments, it can be seen that pure HPMCAS grades did not absorb a significant amount of moisture, and maximum % weight again was under 10% at the highest RH (Figure 6.14). The polymers could be rank ordered for hygroscopicity from highest to lowest moisture being $L > M > H$. H grade has highest acetate/succinate ratio, which makes it the most hydrophobic in the series. In addition, amorphous ITZ was very hydrophobic, with less than 2% water absorbed at 90% RH. The moisture uptake by stability samples was under 3% from TGA analysis for all the time points (data not shown). HPMCAS has a high T_g under dry conditions. The T_g values of as prepared samples with 30% drug loading were measured to be above 100 °C (data not shown). When exposed to higher RH conditions, there is smaller decrease in T_g of HPMCAS when compared to typical water-soluble polymers owing to its hydrophobic nature and therefore less moisture uptake. As a result, the stability samples still had T_g values well above the storage temperature of 40 °C (data not shown). Overall, drug mobility remains low, which in part explains why the samples exhibited long-term kinetic physical stability under standard accelerated stability conditions. Similar results were observed in a study done by Chakravarty et al.¹⁵ Their results pointed out that the long-term physical stability could be achieved using HPMCAS as the polymeric matrix for spray dried dispersions.

6.4 Conclusions

In this study, a detailed SSNMR characterization was conducted on ITZ film and spray dried samples. SSNMR analysis revealed that spray drying resulted in intimate mixing between ITZ and HPMCAS. The film samples were found to contain residual crystallinity at 30% drug load. In addition, the extent of phase heterogeneity was found to be HPMCAS grade dependent (H>M>L). The stability data suggested that the components of both sets of dispersions remain phase mixed as studied by proton relaxation times. Overall, this characterization study is important in understanding the performance of different grades of HPMCAS and how the method of preparation can dictate kinetic mixing between the components for rational development of ASDs.

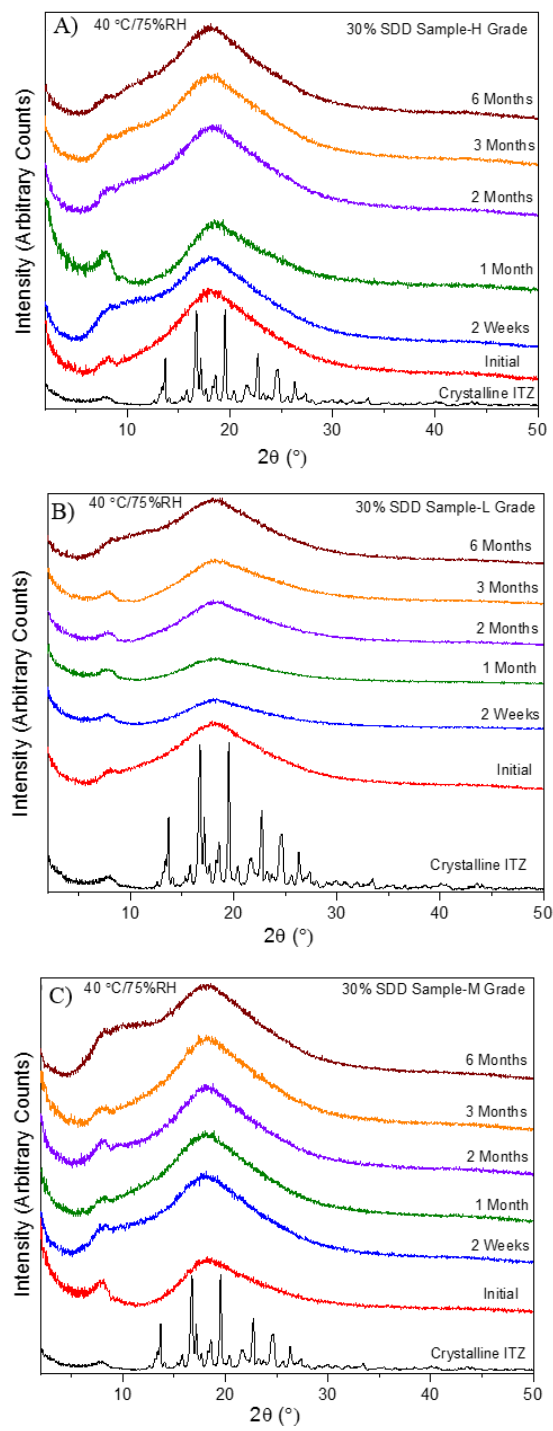


Figure 6.8. PXRD patterns of stability spray dried samples at 40 °C/75% RH for (A) H Grade (B) L Grade and (C) M Grade.

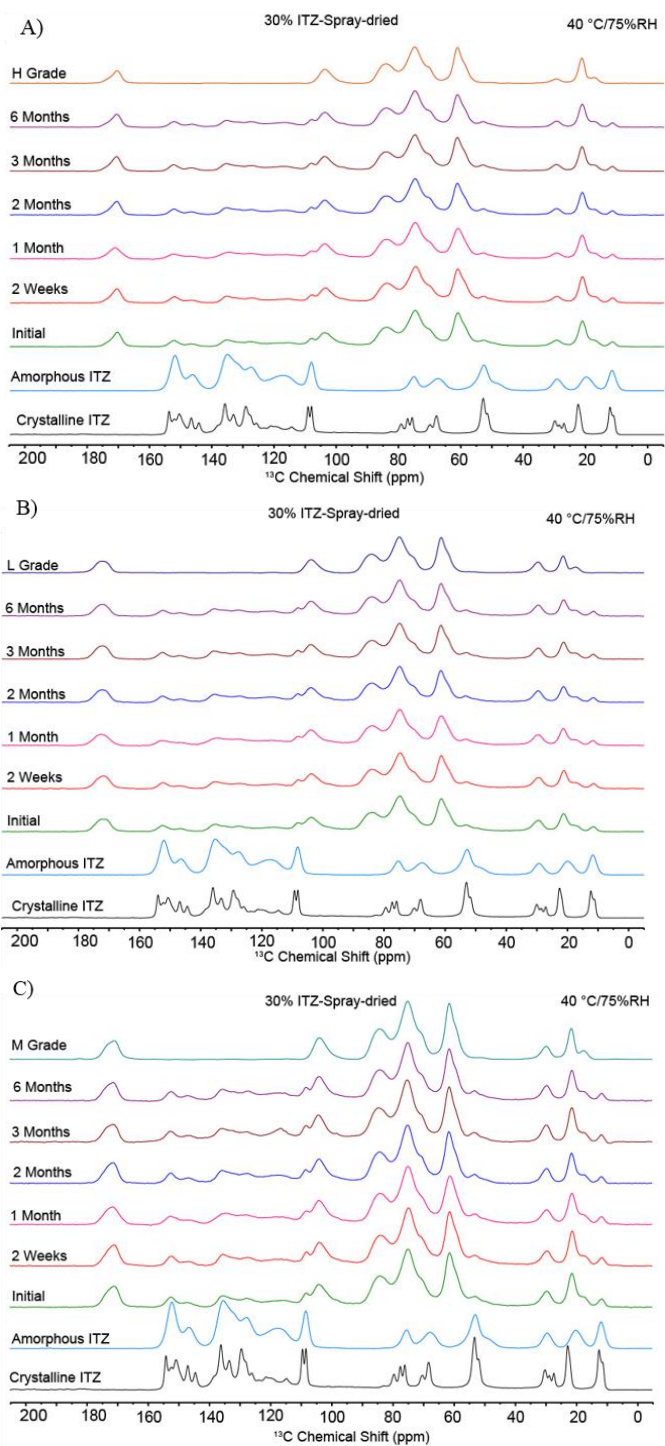


Figure 6.9. Stacked plots for SSNMR spectra of crystalline ITZ, amorphous ITZ and spray dried stability samples at 40 °C/75 % RH for (A) H grade (B) L grade and (C) M grade.

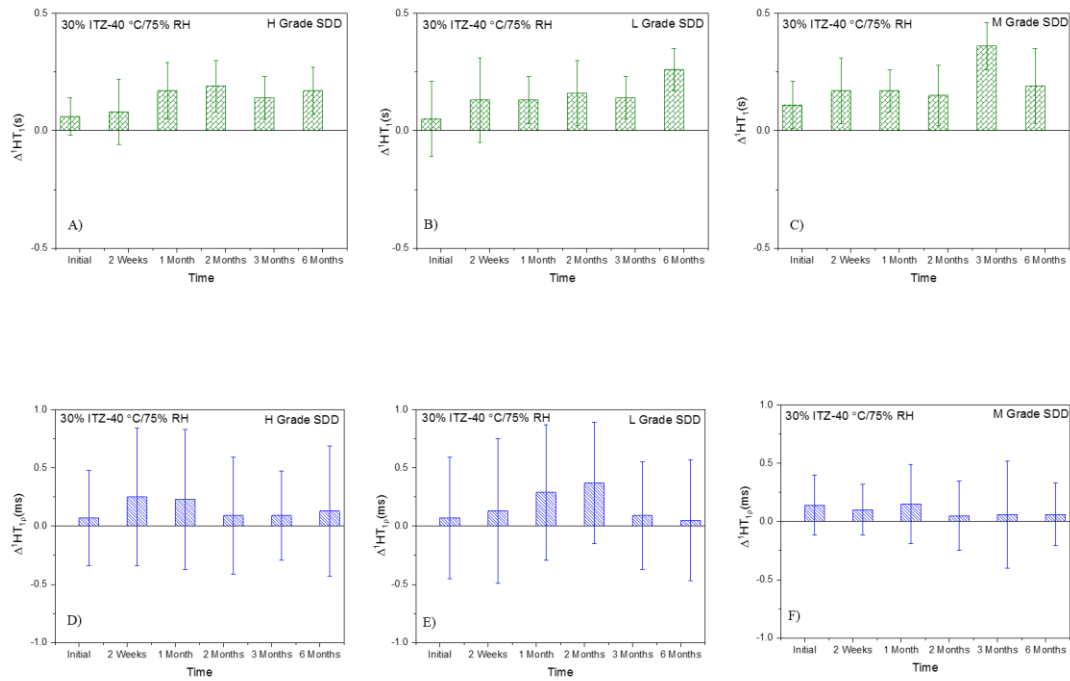


Figure 6.10. Absolute differences in $^1\text{H } T_1$ (plots (A-C); green bars) and $^1\text{H } T_{1\rho}$ (plots (D-E); blue bars) values between ITZ and HPMCAS spray dried stability samples (40 °C/75 % RH) for a period of 6 months. The error bars represent the 95% confidence interval associated with the fit.

Table 6.3. Comparison of percent crystallinity for different time periods for 30% ITZ film stability sample (40 °C/75 %RH) as measured by SSNMR.

Time	H Grade	M Grade	L Grade
Initial	22.7	15.4	12.0
3 Months	15.1	11.2	9.2
6 Months	16.0	11.0	7.7

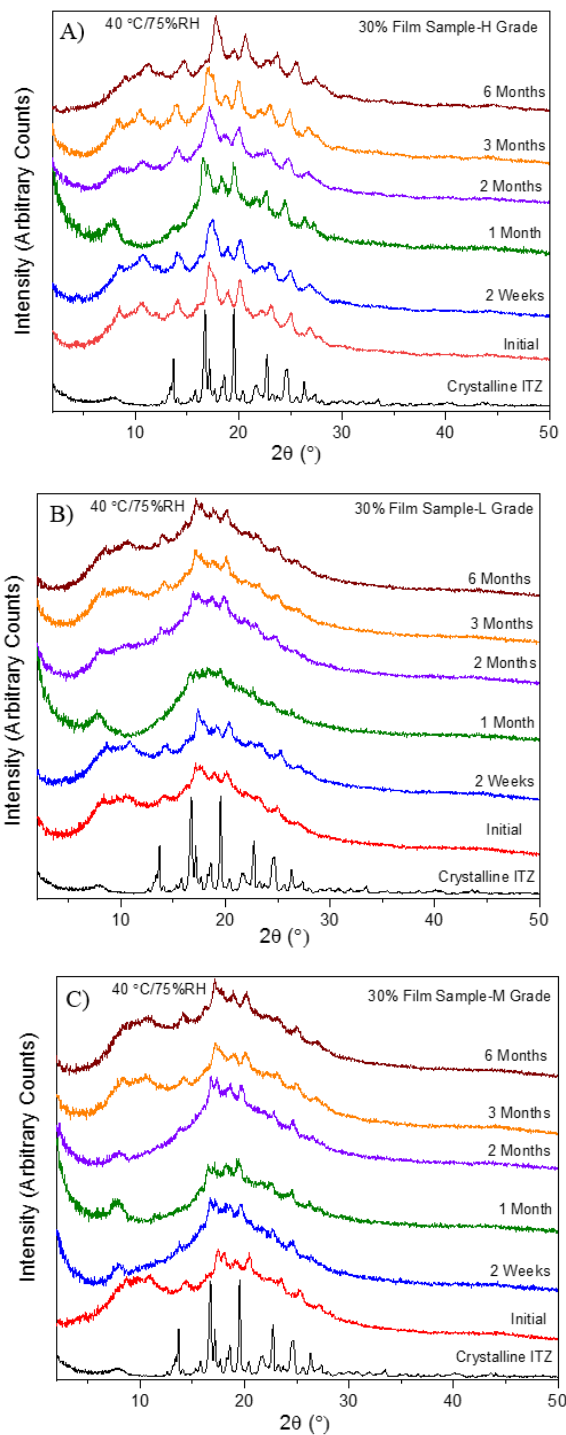


Figure 6.11. PXRD patterns of stability film samples at 40 °C/75% RH for (A) H Grade (B) L Grade and (C) M Grade.

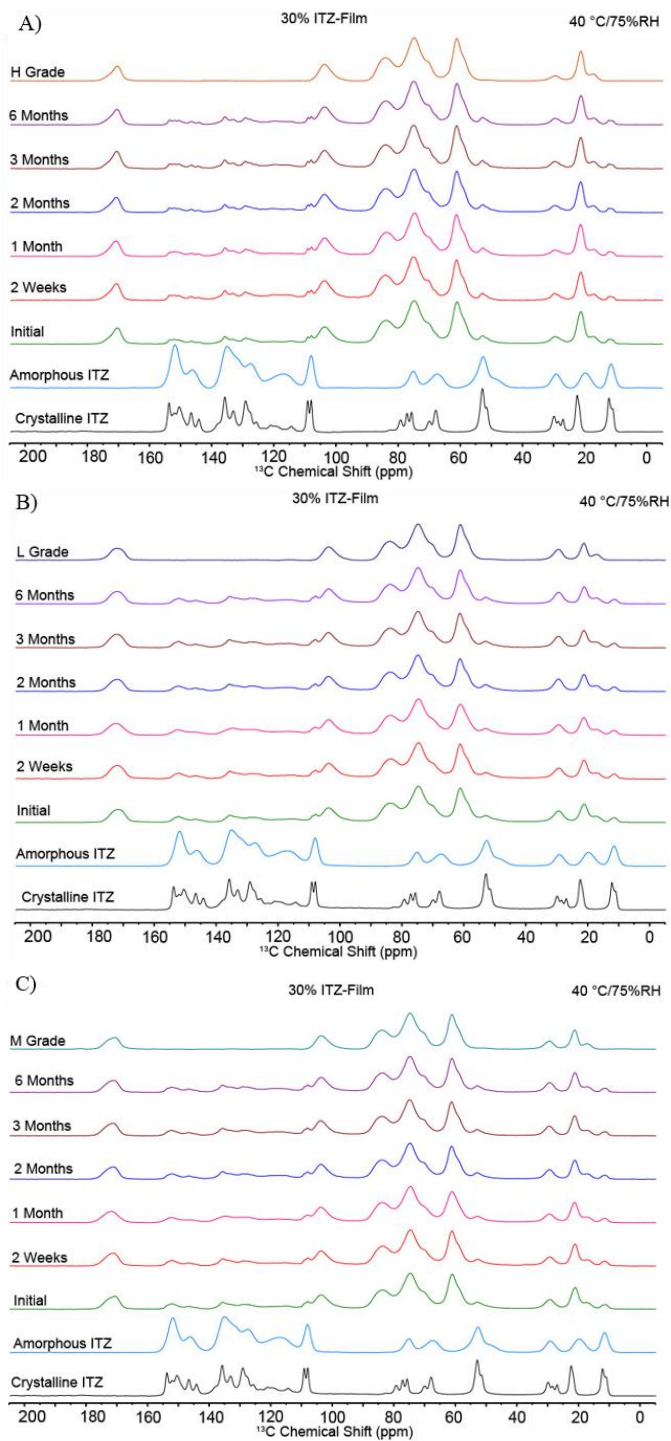


Figure 6.12. Stacked plots for SSNMR spectra of crystalline ITZ, amorphous ITZ and film samples at 40 °C/75 % RH for (A) H grade (B) L grade and (C) M grade.

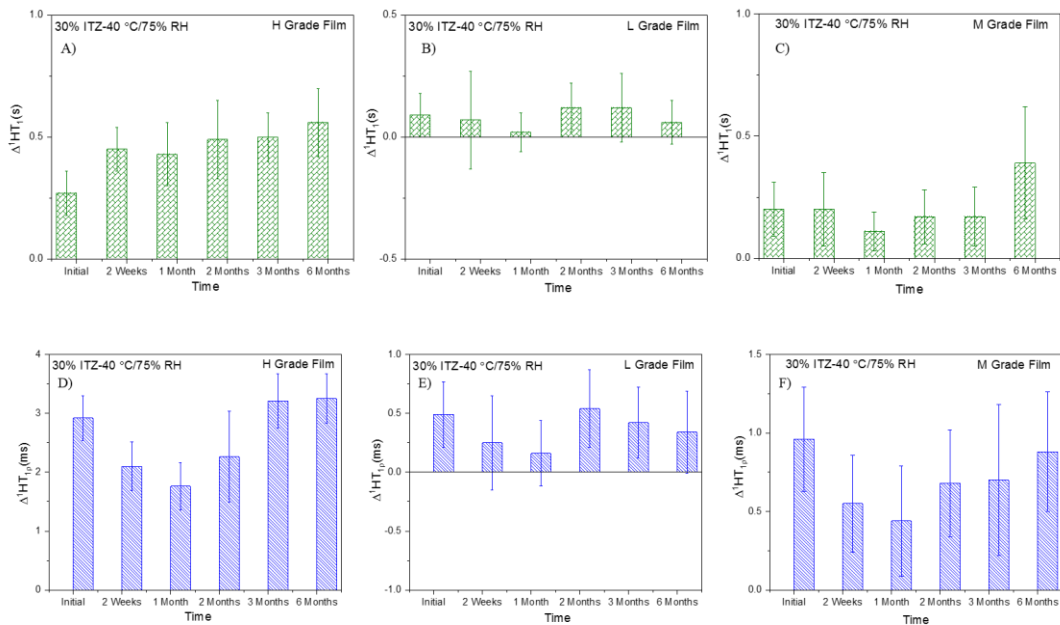


Figure 6.13. Absolute difference in $^1\text{H } T_1$ (plots (A-C); green bars) and $^1\text{H } T_{1p}$ (plots (D-E); blue bars) values between ITZ and HPMCAS film stability samples (40 °C/75 % RH) for a period of 6 months. The error bars represent the 95% confidence interval associated with the fit.

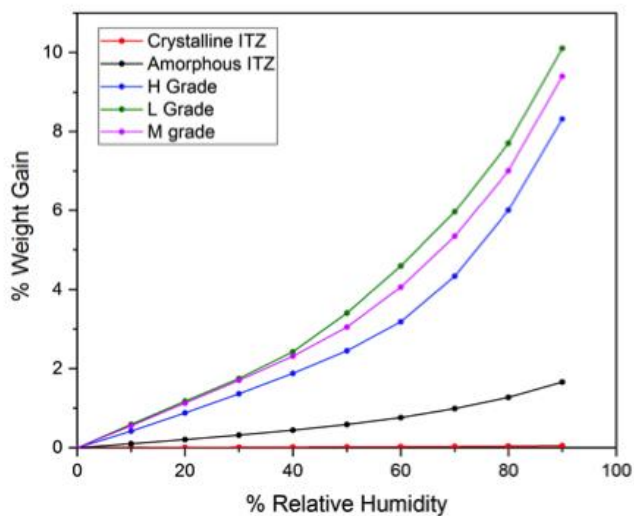


Figure 6.14. Moisture sorption isotherms of ITZ, amorphous ITZ and HPMCAS grades.

CHAPTER 7. SUMMARY AND FUTURE DIRECTIONS

7.1 Summary

The central theme of this thesis research revolves around understanding the phase homogeneity in ASDs. Throughout this thesis work, phase homogeneity and drug-polymer interactions were studied using SSNMR spectroscopy and other analytical techniques. Various model systems were evaluated to gain molecular level understanding of the factors controlling phase homogeneity and the physical stability of ASDs. As a first step in Chapter 1, we provided the literature survey on the classification of ASDs, the preparation methods, the solid-state characterization techniques, and the factors affecting physical stability. Chapter 2 was aimed at providing the basic understanding of SSNMR principles along with its advantages and limitations. Various experimental features like cross polarization (CP), magic angle spinning (MAS) and high power proton decoupling were presented. Special attention was given to the applications of SSNMR spectroscopy in the field of ASDs. The applicability of proton relaxation times ($^1\text{H } T_1$ and $^1\text{H } T_{1\rho}$) in evaluating sub nanometric phase homogeneity and their advantages over thermal analysis were highlighted. In addition, the usefulness of SSNMR for understanding the type, extent and strength of intermolecular drug-polymer interactions was discussed.

Chapter 3 presented a case study on the role of hydrogen bonding on the phase homogeneity of felodipine melt quenched dispersions with three different polymers, PVP, PVP/VA and PVAc. In the first part of the study, a comparative assessment of phase homogeneity involving DSC and SSNMR analyses was conducted on the model systems. In the second part of the study, the strength and extent hydrogen bonding

interactions were quantified using SSNMR ^{13}C CP/MAS spectra. Using a new approach, it was possible to quantify various species present in amorphous felodipine and its dispersions without the need of doing ^{15}N SSNMR based experiments. More precisely, in amorphous felodipine 40% and 60% of molecules were categorized as “dimer” and “free” respectively. It was shown that polymers capable of forming hydrogen bonding interactions disrupted the existing drug-drug interactions resulting in drug-polymer hydrogen bonding interactions. The strength and extent of hydrogen bonding interactions were rank ordered as PVP>PVP/VA>PVAc. Our results suggested that the phase homogeneity was governed by the strength and extent of hydrogen bonding between the drug-polymer. Moreover, it was demonstrated how SSNMR was useful in understanding and characterizing the presence of nano heterogeneities.

It is crucial to understand the thermodynamic miscibility between the drug and polymer to formulate a stable ASD system. We therefore thoroughly investigated and compared the relationship between thermodynamic miscibility and phase homogeneity in two structurally similar molecules, felodipine and nifedipine in Chapter 4. Soluplus was selected as a model polymer. The melting point depression approach was used to estimate the Flory-Huggins interaction parameter for the two systems under study. Our analysis revealed that nifedipine had higher miscibility with Soluplus, when compared to felodipine. A similar analysis of hydrogen bonding interactions was performed on both the systems, where tendencies of felodipine and nifedipine to interact with Soluplus were compared. It was found that nifedipine was more extensively hydrogen bonded to Soluplus than felodipine, while both the drugs had a similar strength of hydrogen bonding interaction. Following the insight into the phase homogeneity of both the

systems, it was shown that nano domains existed within both the systems with felodipine dispersions slightly more heterogeneous.

Conventionally, ASDs have been formulated as a binary matrix but in recent years a new class of ASDs have emerged, where generally a second polymer is added to the formulation. Having the presence of a second polymer necessitates a comprehensive solid-state characterization in order to study the intermolecular interactions and phase behavior on a molecular level. With this goal in mind, ketoconazole was selected as a model drug and hydroxypropyl methyl cellulose (HPMC) and polyacrylic acid (PAA) were chosen as polymeric carriers. Binary ketoconazole dispersions with HPMC lacked any specific interactions, whereas binary ketoconazole PAA dispersions and ternary ketoconazole PAA and HPMC showed spectroscopic evidence for ionic and hydrogen bonding interactions. The ^{13}C SSNMR deconvolution study established a comparison for molecular interactions between the binary and ternary dispersions, with the binary ketoconazole PAA system showing higher prevalence of ionic and hydrogen bonds than the ternary ketoconazole HPMC PAA system. Moreover, binary and ternary ASDs were found to be homogenous on a nanometric level, implying the presence of a second polymer did not impact the phase homogeneity. In addition, a stronger interaction in binary ketoconazole PAA and ternary ketoconazole HPMC PAA system translated to better physical stability at different storage conditions. Overall, this study provided a detailed molecular level characterization of binary and ternary ASDs in order to design ASDs formulation with optimum performance.

In Chapter 6, the impact of grade of hydroxypropyl methyl cellulose acetate succinate (HPMCAS) on the phase behavior of itraconazole dispersions was

investigated. The samples were prepared via different approaches: film casting versus spray drying. SSNMR analysis revealed substantial differences in the phase behavior of dispersions prepared by these two methods. For “film” samples, residual crystallinity was detected at drug loadings of > 20 % and found to be dependent on the HPMCAS grade, with H grade showing the highest crystallinity. Additionally, it was evident from the proton relaxation measurements that “film” samples were homogenous up to 20% itraconazole loading, whereas the sample with 30% itraconazole concentration started to show the presence of phase heterogeneity and its extent could be rank ordered as H>M>L. In contrast, the spray dried samples were amorphous and measured to be homogenous for all the drug loadings. Both “film” and spray dried samples were observed to be robust at accelerated stability conditions and did not show any further changes in phase homogeneity, implying that HPMCAS was efficient in decreasing drug mobility and keeping the drug kinetically stable. It was an important study to elucidate the phase behavior of different grades of HPMCAS along with the effect of preparation methods.

7.2 Future Directions

Throughout this dissertation, the proton relaxation measurements have been employed to study the phase homogeneity of ASDs on different model systems. Though such measurements have been proven to be quite useful, a detailed understanding and appreciation of the differences seen for different model compounds and carriers is much desired. Based on our experience working with different model systems, future studies should involve studying the various factors, which can potentially influence such measurements. It is worth giving a thought why do different APIs and polymers have

such different proton relaxation times? Besides, is it possible to relate the differences with some molecular properties? The proton relaxation measurements give a good estimation of upper limit of domain sizes. In Chapter 3, we have seen how domain sizes vary with the composition and polymer type. It was agreed that the extent of phase homogeneity is governed on the nature of hydrogen bonding between the drug and polymer. As a next logical step, it would be interesting to see some sort of correlation between the domain sizes and the onset of crystallization. Moreover, the impact of moisture on domain sizes could potentially be explored to predict the relative physical stability of ASDs. Usually, the domain sizes are reported to indicate the extent of phase homogeneity. Another relevant question is what is the real physical meaning of “domains” and how do they impact the overall phase behavior of ASDs. Moreover, the impact of moisture on domain sizes could potentially be explored to predict the relative physical stability of ASDs.

Specific interactions like hydrogen bonding have been studied in depth through ^{13}C CP/MAS experiments in this thesis work. Some model systems showed the variation in chemical shifts as a response to the changes induced by hydrogen bonding (Chapter 3 and 4), whereas systems involving HPMCAS didn't directly reveal the presence of hydrogen bonding as seen in Chapter 7. In order to collect more evidence for specific interactions, two-dimensional experiments such as ^1H -X CP/MAS HETCOR should also be explored. As a next step for the quantification hydrogen bonding in ASDs systems, it would be interesting to incorporate models like “Painter Coleman association model” and compare the SSNMR data to FTIR and Raman spectroscopy. Additionally, as an extension to the studies done in this thesis work, where compositions ranging from 50 %

to 90 % w/w drug were studied, it would be helpful to explore the other compositions as well.

Ternary ASDs are new emerging field in ASDs research, where more scientific understanding is needed. Interestingly, we were able to present a detailed solid-state characterization and compared the physical stability of binary and ternary ASDs. However, the influence of a second polymer on dissolution characteristics needs further exploration. Moreover, it would also be interesting to develop any correlation between the phase homogeneity and dissolution characteristics. Finally, the study on ternary ASDs could be extended on other model drugs and polymer combinations. Along those lines, studying surfactants as a part of ternary ASDs could possibly open new avenues for research.

REFERENCES

Chapter 1

- (1) Buckley, S. T.; Fischer, S. M.; Fricker, G.; Brandl, M. *Eur. J. Pharm. Sci.* **2012**, *45*, 235.
- (2) Bosselmann, S.; Williams III, R. O. *Formulating Poorly Water Soluble Drugs*, Springer: 2012.
- (3) Amidon, G. L.; Lennernäs, H.; Shah, V. P.; Crison, J. R. *Pharm. Res.* **1995**, *12*, 413.
- (4) Food; Administration, D. *Food and Drug Administration*, **2000**.
- (5) Smithey, D.; Gao, P.; Taylor, L. *AAPS News Magazine* **2013**, *16*, 11.
- (6) Stegemann, S.; Leveiller, F.; Franchi, D.; De Jong, H.; Lindén, H. *Eur. J. Pharm. Sci.* **2007**, *31*, 249.
- (7) Di, L.; Fish, P. V.; Mano, T. *Drug Discovery Today* **2012**, *17*, 486.
- (8) Ali, S.; Kolter, K. *Am. Pharm. Rev., dec* **2012**.
- (9) Griffin, B. *Am. Pharm. Rev* **2012**, *15*.
- (10) Di, L.; Kerns, E. H.; Carter, G. T. *Curr. Pharm. Des.* **2009**, *15*, 2184.
- (11) Hörter, D.; Dressman, J. *Adv. Drug. Delivery Rev.* **2001**, *46*, 75.
- (12) Kawabata, Y.; Wada, K.; Nakatani, M.; Yamada, S.; Onoue, S. *Int. J. Pharm.* **2011**, *420*, 1.
- (13) Kaushal, A. M.; Gupta, P.; Bansal, A. K. *Crit. Rev. Ther. Drug Carrier Syst.* **2004**, *21*.
- (14) Van den Mooter, G. *Drug Discovery Today: Technol.* **2012**, *9*, e79.
- (15) Hancock, B. C.; Parks, M. *Pharm. Res.* **2000**, *17*, 397.
- (16) Huang, L.-F.; Tong, W.-Q. T. *Adv. Drug. Delivery Rev.* **2004**, *56*, 321.
- (17) Laitinen, R.; Löbmann, K.; Strachan, C. J.; Grohgan, H.; Rades, T. *Int. J. Pharm.* **2013**, *453*, 65.
- (18) Serajuddin, A. T. M. *J. Pharm. Sci.* **1999**, *88*, 1058.
- (19) Vasconcelos, T.; Sarmiento, B.; Costa, P. *Drug Discovery Today* **2007**, *12*, 1068.
- (20) Al-Obaidi, H.; Buckton, G. *AAPS PharmSciTech* **2009**, *10*, 1172.
- (21) Ito, A.; Watanabe, T.; Yada, S.; Hamaura, T.; Nakagami, H.; Higashi, K.; Moribe, K.; Yamamoto, K. *Int. J. Pharm.* **2010**, *383*, 18.
- (22) Hancock, B. C.; Zografi, G. *J. Pharm. Sci* **1997**, *86*, 1.

- (23) W.Y. Lee, T.; A. Boersen, N.; Hui, H. W.; Chow, S. F.; Wan, K. Y.; H.L. Chow, A. *Curr. Pharm. Des.* **2014**, *20*, 303.
- (24) Bhattacharya, S.; Suryanarayanan, R. *J. Pharm. Sci.* **2009**, *98*, 2935.
- (25) Chiou, W. L.; Riegelman, S. *J. Pharm. Sci.* **1971**, *60*, 1281.
- (26) Sekiguchi, K.; Obi, N. *Chem. Pharm. Bull.* **1961**, *9*, 866.
- (27) Vo, C. L.-N.; Park, C.; Lee, B.-J. *Eur. J. Pharm. Biopharm.* **2013**, *85*, 799.
- (28) Patil, H.; Tiwari, R. V.; Repka, M. A. *AAPS PharmSciTech* **2016**, *17*, 20.
- (29) Crowley, M. M.; Zhang, F.; Repka, M. A.; Thumma, S.; Upadhye, S. B.; Kumar Battu, S.; McGinity, J. W.; Martin, C. *Drug Dev. Ind. Pharm.* **2007**, *33*, 909.
- (30) Brough, C.; Williams, R. *Int. J. Pharm.* **2013**, *453*, 157.
- (31) Ellenberger, D. J.; Miller, D. A.; Williams, R. O. *AAPS PharmSciTech* **2018**, *19*, 1933.
- (32) Janssens, S.; De Zeure, A.; Paudel, A.; Van Humbeeck, J.; Rombaut, P.; Van den Mooter, G. *Pharm. Res.* **2010**, *27*, 775.
- (33) Paudel, A.; Worku, Z. A.; Meeus, J.; Guns, S.; Van den Mooter, G. *Int. J. Pharm.* **2013**, *453*, 253.
- (34) Srinarong, P.; de Waard, H.; Frijlink, H. W.; Hinrichs, W. L. J. *Expert. Opin. Drug Delivery* **2011**, *8*, 1121.
- (35) Serajuddin, A. T. *J. Pharm. Sci.* **1999**, *88*, 1058.
- (36) Baird, J. A.; Taylor, L. S. *Adv. Drug Delivery Rev.* **2012**, *64*, 396.
- (37) Coleman, N. J.; Craig, D. Q. M. *Int. J. Pharm.* **1996**, *135*, 13.
- (38) Reading, M.; Luget, A.; Wilson, R. *Thermochim. Acta* **1994**, *238*, 295.
- (39) Knopp, M. M.; Löbmann, K.; Elder, D. P.; Rades, T.; Holm, R. *Eur. J. Pharm. Sci.* **2016**, *87*, 164.
- (40) Newman, A.; Engers, D.; Bates, S.; Ivanisevic, I.; Kelly, R. C.; Zografi, G. *J. Pharm. Sci.* **2008**, *97*, 4840.
- (41) Schneider, H. A. *Makromol. Chem.* **1988**, *189*, 1941.
- (42) Ford, J. L.; Mann, T. E. *Adv. Drug. Delivery Rev.* **2012**, *64*, 422.
- (43) Stodghill, S. P. *Am. Pharm. Rev.* **2010**, *13*, 29.
- (44) Bates, S.; Zografi, G.; Engers, D.; Morris, K.; Crowley, K.; Newman, A. *Pharm. Res.* **2006**, *23*, 2333.
- (45) Bøtker, J. P.; Karmwar, P.; Strachan, C. J.; Cornett, C.; Tian, F.; Zujovic, Z.; Rantanen, J.; Rades, T. *Int. J. Pharm.* **2011**, *417*, 112.

- (46) Chauhan, A.; Chauhan, P. *J. Anal. Bioanal. Tech.* **2014**, *5*, 1.
- (47) Colthup, N.; Daly, L.; Wiberley, S.; *Introduction to Infrared and Raman Spectroscopy*, Academic Press: San Diego, 1990.
- (48) Jeffrey, G. A.; Jeffrey, G. A. *An Introduction to Hydrogen Bonding*, Oxford University Press: New York, 1997.
- (49) Lin, S.-Y.; Lin, H.-L.; Chi, Y.-T.; Huang, Y.-T.; Kao, C.-Y.; Hsieh, W.-H. *Int. J. Pharm.* **2015**, *496*, 457.
- (50) Weuts, I.; Van Dycke, F.; Voorspoels, J.; De Cort, S.; Stokbroekx, S.; Leemans, R.; Brewster, M. E.; Xu, D.; Segmuller, B.; Turner, Y. Z. A.; Roberts, C. J.; Davies, M. C.; Qi, S.; Craig, D. Q. M.; Reading, M. *J. Pharm. Sci.* **2011**, *100*, 260.
- (51) Coates, J.; Rintoul, L.; Fredericks, P. In *Analytical Instrumentation Handbook*, 3rd ed; CRC Press, 2004.
- (52) Févotte, G.; Calas, J.; Puel, F.; Hoff, C. *Int. J. Pharm.* **2004**, *273*, 159.
- (53) Vogt, F. G.; Williams, G. R. *Pharm. Res.* **2012**, *29*, 1866.
- (54) Padilla, A. M.; Chou, S. G.; Luthra, S.; Pikal, M. J. *J. Pharm. Sci.* **2011**, *100*, 1362.
- (55) Brouwers, J.; Brewster, M. E.; Augustijns, P. *J. Pharm. Sci.* **2009**, *98*, 2549.
- (56) Ruckenstein, E.; Djikaev, Y. S. *Adv. Colloid Interface Sci.* **2005**, *118*, 51.
- (57) Jungblut, S.; Dellago, C. *Eur. Phys. J. E* **2016**, *39*, 77.
- (58) Hoffman, J. D. *J. Chem. Phys.* **1958**, *29*, 1192.
- (59) Gerges, J.; Affouard, F. *J. Phys. Chem. B* **2015**, *119*, 10768.
- (60) Mullin, J.; *Crystallization*, Elsevier Science, 2001.
- (61) Schmelzer, J. W. P. *J. Non-Cryst. Solids* **2008**, *354*, 269.
- (62) Shah, N.; Sandhu, H.; Choi, D. S.; Chokshi, H.; Malick, A. W. *Amorphous Solid Dispersions. Theory and Practice*, Springer, 2014.
- (63) Janssens, S.; Van den Mooter, G. *J. Pharm. Pharmacol.* **2009**, *61*, 1571.
- (64) Yu, L. *Adv. Drug. Delivery Rev.* **2001**, *48*, 27.
- (65) Gordon, M.; Taylor, J. S. *J. Appl. Chem.* **1952**, *2*, 493.
- (66) Simha, R.; Boyer, R. *J. Chem. Phys.* **1962**, *37*, 1003.
- (67) Couchman, P.; Karasz, F. *Macromolecules* **1978**, *11*, 117.
- (68) Fox, T. G. *Bull. Am. Phys. Soc.* **1956**, *1*, 123.
- (69) Hancock, B. C.; Zografi, G. *Pharm. Res.* **1994**, *11*, 471.
- (70) Yang, Z.; Han, C. D. *Macromolecules* **2008**, *41*, 2104.

- (71) Marsac, P. J.; Konno, H.; Taylor, L. S. *Pharm. Res.* **2006**, *23*, 2306.
- (72) Taylor, L. S.; Zografi, G. *Pharm. Res.* **1997**, *14*, 1691.
- (73) Gupta, P.; Thilagavathi, R.; Chakraborti, A. K.; Bansal, A. K. *Mol. Pharmaceutics* **2005**, *2*, 384.
- (74) Matsumoto, T.; Zografi, G. *Pharm. Res.* **1999**, *16*, 1722.
- (75) Song, Y.; Zemlyanov, D.; Chen, X.; Nie, H.; Su, Z.; Fang, K.; Yang, X.; Smith, D.; Byrn, S.; Lubach, J. W. *Mol. Pharmaceutics* **2015**, *13*, 483.
- (76) Kestur, U. S.; Van Eerdenbrugh, B.; Taylor, L. S. *CrystEngComm* **2011**, *13*, 6712.
- (77) Rumondor, A. C. F.; Marsac, P. J.; Stanford, L. A.; Taylor, L. S. *Mol. Pharmaceutics* **2009**, *6*, 1492.
- (78) Marsac, P. J.; Shamblin, S. L.; Taylor, L. S. *Pharm. Res.* **2006**, *23*, 2417.
- (79) Flory, P. J. *Principles of polymer chemistry* **1953**, 495.
- (80) Lin, D.; Huang, Y. *Int. J. Pharm.* **2010**, *399*, 109.
- (81) Tian, Y.; Booth, J.; Meehan, E.; Jones, D. S.; Li, S.; Andrews, G. P. *Mol. Pharmaceutics* **2013**, *10*, 236.
- (82) Newman, A. *Pharmaceutical Amorphous Solid Dispersions*, John Wiley & Sons, 2015.

Chapter 2

- (1) Mirau, P. A. *J. Magn. Reson.* **1992**, *96*, 480.
- (2) Tishmack, P. A.; Bugay, D. E.; Byrn, S. R. *J. Pharm. Sci* **2003**, *92*, 441.
- (3) Stoven, V.; Lallemand, J. Y.; Abergel, D.; Bouaziz, S.; Delsuc, M. A.; Ekondzi, A.; Guittet, E.; Laplante, S.; Le Goas, R.; Malliavin, T.; Mikou, A.; Reisdorf, C.; Robin, M.; van Heijenoort, C.; Yang, Y. *Biochimie* **1990**, *72*, 531.
- (4) Kaplan, O.; Cohen, J. S. *Trends. Pharmacol. Sci.* **1990**, *11*, 398.
- (5) Geppi, M.; Mollica, G.; Borsacchi, S.; Veracini, C. A. *Appl. Spectrosc. Rev.* **2008**, *43*, 202.
- (6) Harris, R. K. *J. Pharm. Pharmacol.* **2007**, *59*, 225.
- (7) Harris, R. K.; Hodgkinson, P.; Larsson, T.; Muruganatham, A. *J. Pharm. Biomed. Anal.* **2005**, *38*, 858.
- (8) Monti, G. A.; Chattah, A. K.; Linck, Y. G. *Annual Reports on NMR Spectroscopy*, Academic Press, 2014.
- (9) Bugay, D. E. *Pharm. Res.* **1993**, *10*, 317.
- (10) Paudel, A.; Geppi, M.; Van den Mooter, G. *J. Pharm. Sci* **2014**, *103*, 2635.

- (11) Berendt, R. T.; Sperger, D. M.; Munson, E. J.; Isbester, P. K. *Trends Anal. Chem.* **2006**, *25*, 977.
- (12) Pham, T. N.; Watson, S. A.; Edwards, A. J.; Chavda, M.; Clawson, J. S.; Strohmeier, M.; Vogt, F. G. *Mol. Pharmaceutics* **2010**, *7*, 1667.
- (13) Schaefer, J.; Stejskal, E. O.; Buchdahl, R. *Macromolecules* **1975**, *8*, 291.
- (14) Schaefer, J.; Stejskal, E. O.; Buchdahl, R. *Macromolecules* **1977**, *10*, 384.
- (15) Andrew, E. R.; Bradbury, A.; Eades, R. G. *Nature* **1959**, *183*, 1802.
- (16) Dixon, W. T.; Schaefer, J.; Sefcik, M. D.; Stejskal, E. O.; McKay, R. A. *J. Magn. Reson.*(1969) **1982**, *49*, 341.
- (17) Pines, A.; Gibby, M. G.; Waugh, J. S. *Chem. Phys. Lett.* **1972**, *15*, 373.
- (18) Pines, A. *J. Chem. Phys.* **1973**, *59*, 569.
- (19) Knicker, H. *Org. Geochem.* **2011**, *42*, 867.
- (20) Yuan, X.; Xiang, T.-X.; Anderson, B. D.; Munson, E. J. *Mol. Pharmaceutics* **2015**, *12*, 4518.
- (21) Urbanova, M.; Sturcova, A.; Kredatusova, J.; Brus, J. *Int. J. Pharm.* **2015**, *478*, 464.
- (22) Policianova, O.; Brus, J.; Hruby, M.; Urbanova, M.; Zhigunov, A.; Kredatusova, J.; Kobera, L. *Mol. Pharmaceutics* **2014**, *11*, 516.
- (23) Bovey, F. A.; Mirau, P. A. *NMR of Polymers*, Academic Press, 1996.
- (24) Yuan, X.; Sperger, D.; Munson, E. J. *Mol. Pharmaceutics* **2013**, *11*, 329.
- (25) Newman, A.; Engers, D.; Bates, S.; Ivanisevic, I.; Kelly, R. C.; Zografi, G. *J. Pharm. Sci* **2008**, *97*, 4840.
- (26) Tongyin, Y.; Mingming, G. *Prog. Polym. Sci.* **1990**, *15*, (6), 825-908.
- (27) Aso, Y.; Yoshioka, S.; Miyazaki, T.; Kawanishi, T. *Chem. Pharm. Bull.* **2009**, *57*, 61.
- (28) Song, Y.; Yang, X.; Chen, X.; Nie, H.; Byrn, S.; Lubach, J. W. *Mol. Pharmaceutics* **2015**, *12*, 857.
- (29) Tatton, A. S.; Pham, T. N.; Vogt, F. G.; Iuga, D.; Edwards, A. J.; Brown, S. P. *CrystEngComm* **2012**, *14*, 2654.
- (30) Tatton, A. S.; Pham, T. N.; Vogt, F. G.; Iuga, D.; Edwards, A. J.; Brown, S. P. *Mol. Pharmaceutics* **2013**, *10*, 999.
- (31) Vogt, F. G.; Yin, H.; Forcino, R. G.; Wu, L. *Mol. Pharmaceutics* **2013**, *10*, 3433.
- (32) Offerdahl, T. J.; Salsbury, J. S.; Dong, Z.; Grant, D. J. W.; Schroeder, S. A.; Prakash, I.; Gorman, E. M.; Barich, D. H.; Munson, E. J. *J. Pharm. Sci.* **2005**, *94*, 2591.

(33) Tan, I.; Flanagan, B. M.; Halley, P. J.; Whittaker, A. K.; Gidley, M. J. *Biomacromolecules* **2007**, *8*, 885.

(34) Lefort, R.; De Gusseme, A.; Willart, J. F.; Danède, F.; Descamps, M. *Int. J. Pharm.* **2004**, *280*, 209.

Chapter 3

(1) He, Y.; Ho, C. *J. Pharm. Sci* **2015**.

(2) Laitinen, R.; Löbmann, K.; Strachan, C. J.; Grohgan, H.; Rades, T. *Int. J. Pharm.* **2013**, *453*, (1), 65-79.

(3) Brough, C.; Williams, R. *Int. J. Pharm.* **2013**, *453*, (1), 157-166.

(4) Van den Mooter, G. *Drug Discovery Today: Technol.* **2012**, *9*, (2), e79-e85.

(5) Yu, L. *Adv. Drug. Delivery Rev.* **2001**, *48*, (1), 27-42.

(6) Chiou, W. L.; Riegelman, S. *J. Pharm. Sci* **1971**, *60*, (9), 1281-1302.

(7) Vo, C. L.-N.; Park, C.; Lee, B.-J. *Eur. J. Pharm. Biopharm.* **2013**, *85*, (3), 799-813.

(8) Qi, S.; Moffat, J. G.; Yang, Z. *Mol. Pharmaceutics* **2013**, *10*, (3), 918-930.

(9) Qian, F.; Huang, J.; Hussain, M. A. *J. Pharm. Sci* **2010**, *99*, (7), 2941-2947.

(10) Baird, J. A.; Taylor, L. S. *Adv. Drug. Delivery Rev.* **2012**, *64*, (5), 396-421.

(11) Konno, H.; Taylor, L. S. *J. Pharm. Sci.* **2006**, *95*, (12), 2692.

(12) Karavas, E.; Ktistis, G.; Xenakis, A.; Georgarakis, E. *Drug Dev. Ind. Pharm.* **2005**, *31*, (6), 473-489.

(13) Ahlneck, C.; Zografi, G. *Int. J. Pharm.* **1990**, *62*, (2), 87-95.

(14) Newman, A.; Nagapudi, K.; Wenslow, R. *Ther. Delivery* **2015**, *6*, (2), 247.

(15) Newman, A.; Engers, D.; Bates, S.; Ivanisevic, I.; Kelly, R. C.; Zografi, G. *J. Pharm. Sci.* **2008**, *97*, (11), 4840-4856.

(16) Bikiaris, D.; Papageorgiou, G. Z.; Stergiou, A.; Pavlidou, E.; Karavas, E.; Kanaze, F.; Georgarakis, M. *Thermochim. Acta* **2005**, *439*, (1), 58-67.

(17) Qian, F.; Huang, J.; Zhu, Q.; Haddadin, R.; Gawel, J.; Garmise, R.; Hussain, M. *Int. J. Pharm.* **2010**, *395*, (1), 232-235.

(18) Lodge, T. P.; Wood, E. R.; Haley, J. C. *J. Polym. Sci. Part B: Polym. Phys.* **2006**, *44*, 756.

(19) Padilla, A. M.; Ivanisevic, I.; Yang, Y.; Engers, D.; Bogner, R. H.; Pikal, M. *J. Pharm. Sci.* **2011**, *100*, (1), 206-222.

(20) Ricarte, R. G.; Lodge, T. P.; Hillmyer, M. A. *Mol. Pharmaceutics* **2015**, *12*, 983.

- (21) Lauer, M. E.; Grassmann, O.; Siam, M.; Tardio, J.; Jacob, L.; Page, S.; Kindt, J. H.; Engel, A.; Alsenz, J. *Pharm. Res.* **2011**, *28*, (3), 572-584.
- (22) Li, N.; Gilpin, C. J.; Taylor, L. S. *Mol. Pharmaceutics* **2017**, *14*, (5), 1691-1705.
- (23) Paudel, A.; Geppi, M.; Van den Mooter, G. *J. Pharm. Sci.* **2014**, *103*, (9), 2635-2662.
- (24) Ueda, K.; Higashi, K.; Moribe, K. *Mol. Pharmaceutics* **2016**, *13*, 852.
- (25) Song, Y.; Yang, X.; Chen, X.; Nie, H.; Byrn, S.; Lubach, J. W. *Mol. Pharmaceutics* **2015**, *12*, (3), 857-866.
- (26) Calahan, J. L.; Azali, S. C.; Munson, E. J.; Nagapudi, K. *Mol. Pharmaceutics* **2015**, *12*, (11), 4115-4123.
- (27) Yuan, X.; Sperger, D.; Munson, E. J. *Mol. Pharmaceutics* **2013**, *11*, (1), 329-337.
- (28) Pham, T. N.; Watson, S. A.; Edwards, A. J.; Chavda, M.; Clawson, J. S.; Strohmeier, M.; Vogt, F. G. *Mol. Pharmaceutics* **2010**, *7*, (5), 1667-1691.
- (29) Schmidt-Rohr, K.; Spiess, H. W., *Multidimensional Solid-State NMR and Polymers*, Elsevier, 2012.
- (30) Clauss, J.; Schmidt-Rohr, K.; Spiess, H. W. *Acta Polym.* **1993**, *44*, (1), 1.
- (31) Litvinov, V. M.; Guns, S.; Adriaensens, P.; Scholtens, B. J. R.; Quaedflieg, M. P.; Carleer, R.; Van den Mooter, G. *Mol. Pharmaceutics* **2012**, *9*, (10), 2924-2932.
- (32) Aso, Y.; Yoshioka, S.; Miyazaki, T.; Kawanishi, T.; Tanaka, K.; Kitamura, S.; Takakura, A.; Hayashi, T.; Muranushi, N. *Chem. Pharm. Bull.* **2007**, *55*, (8), 1227.
- (33) Yang, F.; Su, Y.; Zhang, J.; DiNunzio, J.; Leone, A.; Huang, C.; Brown, C. D. *Mol. Pharmaceutics* **2016**, *13*, (10), 3494-3505.
- (34) Nie, H.; Su, Y.; Zhang, M.; Song, Y.; Leone, A.; Taylor, L. S.; Marsac, P. J.; Li, T.; Byrn, S. R. *Mol. Pharmaceutics* **2016**, *13*, (11), 3964-3975.
- (35) Yuan, X.; Xiang, T.-X.; Anderson, B. D.; Munson, E. J. *Mol. Pharmaceutics* **2015**, *12*, (12), 4518-4528.
- (36) Policianova, O.; Brus, J.; Hruby, M.; Urbanova, M.; Zhigunov, A.; Kredatusova, J.; Kobera, L. *Mol. Pharmaceutics* **2014**, *11*, (2), 516-530.
- (37) Ng, Y. C.; Yang, Z. Y.; McAuley, W. J.; Qi, S. *Eur. J. Pharm. Biopharm.* **2013**.
- (38) Konno, H.; Taylor, L. S. *J. Pharm. Sci.* **2006**, *95*, 2692.
- (39) Gupta, P.; Thilagavathi, R.; Chakraborti, A. K.; Bansal, A. K. *Mol. Pharmaceutics* **2005**, *2*, (5), 384.
- (40) Maniruzzaman, M.; Morgan, D. J.; Mendham, A. P.; Pang, J.; Snowden, M. J.; Douroumis, D. *Int. J. Pharm.* **2013**, *443*, (1-2), 199.
- (41) Zhu, Q.; Taylor, L. S.; Harris, M. T. *Mol. Pharmaceutics* **2010**, *7*, (4), 1291-1300.

- (42) Rumondor, A. C. F.; Marsac, P. J.; Stanford, L. A.; Taylor, L. S. *Mol. Pharmaceutics* **2009**, *6*, (5), 1492.
- (43) Marsac, P. J.; Konno, H.; Taylor, L. S. *Pharm. Res.* **2006**, *23*, 2306.
- (44) Al-Obaidi, H.; Buckton, G. *AAPS PharmSciTech* **2009**, *10*, (4), 1172-1177.
- (45) Sun, M.; Wu, C.; Fu, Q.; Di, D.; Kuang, X.; Wang, C.; He, Z.; Wang, J.; Sun, J. *Int. J. Pharm.* **2016**, *503*, (1), 238-246.
- (46) Lin, S.-Y.; Lin, H.-L.; Chi, Y.-T.; Huang, Y.-T.; Kao, C.-Y.; Hsieh, W.-H. *Int. J. Pharm.* **2015**, *496*, (2), 457-465.
- (47) Paudel, A.; Nies, E.; Van den Mooter, G. *Mol. Pharmaceutics* **2012**, *9*, (11), 3301-3317.
- (48) Dixon, W. T.; Schaefer, J.; Sefcik, M. D.; Stejskal, E. O.; McKay, R. A. *J. Magn. Reson.* **1982**, *49*, (2), 341.
- (49) Fung, B. M.; Khitrin, A. K.; Ermolaev, K. *J. Magn. Reson.* **2000**, *142*, (1), 97.
- (50) Barich, D. H.; Gorman, E. M.; Zell, M. T.; Munson, E. J. *Solid State Nucl. Magn. Reson.* **2006**, *30*, (3-4), 125.
- (51) Frisch, M. J.; Trucks, G. W.; Schlegel, H. B.; Scuseria, G. E.; Robb, M. A.; Cheeseman, J. R.; Scalmani, G.; Barone, V.; Mennucci, B.; Petersson, G. A.; Nakatsuji, H.; Caricato, M.; Li, X.; Hratchian, H. P.; Izmaylov, A. F.; Bloino, J.; Zheng, G.; Sonnenberg, J. L.; Hada, M.; Ehara, M.; Toyota, K.; Fukuda, R.; Hasegawa, J.; Ishida, M.; Nakajima, T.; Honda, Y.; Kitao, O.; Nakai, H.; Vreven, T.; Montgomery Jr., J. A.; Peralta, J. E.; Ogliaro, F.; Bearpark, M.; Heyd, J. J.; Brothers, E.; Kudin, K. N.; Staroverov, V. N.; Kobayashi, R.; Normand, J.; Raghavachari, K.; Rendell, A.; Burant, J. C.; Iyengar, S. S.; Tomasi, J.; Cossi, M.; Rega, N.; Millam, J. M.; Klene, M.; Knox, J. E.; Cross, J. B.; Bakken, V.; Adamo, C.; Jaramillo, J.; Gomperts, R.; Stratmann, R. E.; Yazyev, O.; Austin, A. J.; Cammi, R.; Pomelli, C.; Ochterski, J. W.; Martin, R. L.; Morokuma, K.; Zakrzewski, V. G.; Voth, G. A.; Salvador, P.; Dannenberg, J. J.; Dapprich, S.; Daniels, A. D.; Farkas, Ö.; Foresman, J. B.; Ortiz, J. V.; Cioslowski, J.; Fox, D. J. *Gaussian 09*, Gaussian, Inc: Wallingford, CT, 2009.
- (52) Becke, A. D. *J. Chem. Phys.* **1993**, *98*, (7), 5648-52.
- (53) Krishnan, R.; Binkley, J. S.; Seeger, R.; Pople, J. A. *J. Chem. Phys.* **1980**, *72*, 650-4.
- (54) Chen, H.; Lin, C.; Chen, G.; Lai, G.; Zhao, S. *Huaxue Yanjiu* **2006**, *17*, (4), 6-9.
- (55) Hariharan, P. C.; Pople, J. A. *Theor. Chim. Acta* **1973**, *28*, 213-22.
- (56) Baerends, E. J.; Ellis, D. E.; Ros, P. *Chemical Physics* **1973**, *2*, (1), 41-51.
- (57) Knopp, M. M.; Löbmann, K.; Elder, D. P.; Rades, T.; Holm, R. *Eur. J. Pharm. Sci.* **2016**, *87*, (Supplement C), 164-173.
- (58) W.Y. Lee, T.; A. Boersen, N.; Hui, H. W.; Chow, S. F.; Wan, K. Y.; H.L. Chow, A. *Curr. Pharm. Des.* **2014**, *20*, (3), 303-324.

- (59) Schneider, H. A. *Makromol. Chem.* **1988**, *189*, (8), 1941.
- (60) Bhugra, C.; Telang, C.; Schwabe, R.; Zhong, L. *Mol. Pharmaceutics* **2016**, *13*, (9), 3326-3333.
- (61) Latosińska, J. N. *Chem. Phys. Lett.* **2008**, *463*, (1), 195-200.
- (62) Dempah, K. E.; Lubach, J. W.; Munson, E. J. *Mol. Pharmaceutics* **2017**, *14*, (3), 856-865.
- (63) Sperger, D. M.; Fu, S.; Block, L. H.; Munson, E. J. *J. Pharm. Sci.* **2011**, *100*, (8), 3441-3452.
- (64) Geppi, M.; Mollica, G.; Borsacchi, S.; Veracini, C. A. *Appl. Spectrosc. Rev.* **2008**, *43*, (3), 202-302.
- (65) Guo, M. *Trends Polym. Sci.* **1996**, *4*, (7), 238-244.
- (66) Bovey, F. A.; Mirau, P. A., *NMR of Polymers*, Academic Press, 1996.
- (67) Tongyin, Y.; Mingming, G. *Prog. Polym. Sci.* **1990**, *15*, (6), 825-908.
- (68) Xiang, T.-X.; Anderson, B. D. *J. Pharm. Sci.* **2017**, *106*, (3), 803-816.
- (69) Konno, H.; Taylor, L. S. *J. Pharm. Sci.* **2006**, *95*, (12), 2692-2705.
- (70) Song, Y.; Wang, L.; Yang, P.; Wenslow, R. M.; Tan, B.; Zhang, H.; Deng, Z. *J. Pharm. Sci.* **2013**, *102*, (6), 1915-1923.
- (71) Kestur, U. S.; Taylor, L. S. *CrystEngComm* **2010**, *12*, (8), 2390-2397.
- (72) Wegiel, L. A.; Mauer, L. J.; Edgar, K. J.; Taylor, L. S. *J. Pharm. Sci.* **2013**, *102*, (1), 171-184.
- (73) Jeffrey, G. A.; *An Introduction to Hydrogen Bonding*, Oxford University Press, 1997.

Chapter 4

- (1) Janssens, S.; Van den Mooter, G. *J. Pharm. Pharmacol.* **2009**, *61*, 1571.
- (2) Newman, A.; Engers, D.; Bates, S.; Ivanisevic, I.; Kelly, R. C.; Zografi, G. *J. Pharm. Sci.* **2008**, *97*, (11), 4840-4856.
- (3) Serajuddin, A. T. *J. Pharm. Sci.* **1999**, *88*, (10), 1058.
- (4) Van den Mooter, G. *Drug Discovery Today: Technol.* **2012**, *9*, (2), e79-e85.
- (5) He, Y.; Ho, C. *J. Pharm. Sci.* **2015**.
- (6) Marsac, P. J.; Konno, H.; Taylor, L. S. *Pharm. Res.* **2006**, *23*, 2306.
- (7) W.Y. Lee, T.; A. Boersen, N.; Hui, H. W.; Chow, S. F.; Wan, K. Y.; H.L. Chow, A. *Curr. Pharm. Des.* **2014**, *20*, (3), 303-324.

- (8) Li, N.; Taylor, L. S. *Mol. Pharmaceutics* **2016**, *13*, 1123.
- (9) Higashi, K.; Hayashi, H.; Yamamoto, K.; Moribe, K. *Int. J. Pharm.* **2015**, *494*, (1), 9-16.
- (10) Li, N.; Gilpin, C. J.; Taylor, L. S. *Mol. Pharmaceutics* **2017**, *14*, (5), 1691-1705.
- (11) Tian, Y.; Booth, J.; Meehan, E.; Jones, D. S.; Li, S.; Andrews, G. P. *Mol. Pharmaceutics* **2013**, *10*, 236.
- (12) Zhao, Y.; Inbar, P.; Chokshi, H. P.; Malick, A. W.; Choi, D. S. *J. Pharm. Sci.* **2011**, *100*, (8), 3196.
- (13) Calahan, J. L.; Azali, S. C.; Munson, E. J.; Nagapudi, K. *Mol. Pharmaceutics* **2015**, *12*, (11), 4115-4123.
- (14) Marsac, P. J.; Shamblin, S. L.; Taylor, L. S. *Pharm. Res.* **2006**, *23*, (10), 2417-2426.
- (15) Djuris, J.; Nikolakakis, I.; Ibric, S.; Djuric, Z.; Kachrimanis, K. *Eur. J. Pharm. Biopharm.* **2013**, *84*, (1), 228.
- (16) Dalsania, S.; Sharma, J.; Munjal, B.; Bansal, A. K. *Pharm. Res.* **2018**, *35*, (2), 29.
- (17) Donnelly, C.; Tian, Y.; Potter, C.; Jones, D. S.; Andrews, G. P. *Pharm. Res.* **2015**, *32*, (1), 167-179.
- (18) Baird, J. A.; Taylor, L. S. *Adv. Drug Delivery Rev.* **2012**, *64*, 396.
- (19) Qian, F.; Huang, J.; Zhu, Q.; Haddadin, R.; Gawel, J.; Garmise, R.; Hussain, M. *Int. J. Pharm.* **2010**, *395*, 232.
- (20) Pham, T. N.; Watson, S. A.; Edwards, A. J.; Chavda, M.; Clawson, J. S.; Strohmeier, M.; Vogt, F. G. *Mol. Pharmaceutics* **2010**, *7*, (5), 1667-1691.
- (21) Yang, F.; Su, Y.; Zhang, J.; DiNunzio, J.; Leone, A.; Huang, C.; Brown, C. D. *Mol. Pharmaceutics* **2016**, *13*, (10), 3494-3505.
- (22) Policianova, O.; Brus, J.; Hruby, M.; Urbanova, M.; Zhigunov, A.; Kredatusova, J.; Kobera, L. *Mol. Pharmaceutics* **2014**, *11*, (2), 516-530.
- (23) Paudel, A.; Geppi, M.; Van den Mooter, G. *J. Pharm. Sci.* **2014**, *103*, (9), 2635-2662.
- (24) Gerges, J.; Affouard, F. *J. Phys. Chem. B* **2015**, *119*, (33), 10768-10783.
- (25) Lin, S.-Y.; Lin, H.-L.; Chi, Y.-T.; Huang, Y.-T.; Kao, C.-Y.; Hsieh, W.-H. *Int. J. Pharm.* **2015**, *496*, (2), 457-465.
- (26) Stanković, M.; Frijlink, H. W.; Hinrichs, W. L. *J. Drug Discovery Today* **2015**, *20*, (7), 812-823.
- (27) Krevelen, D. W.; Van Krevelen, D., *Properties of Polymers: Their Correlation with Chemical Structure, their Numerical Estimation and Prediction from Additive Group Contributions*, Elsevier: Amsterdam, 1990.

- (28) Schneider, H. A. The Gordon-Taylor equation. *Makromol. Chem.* **1988**, *189*, (8), 1941.
- (29) Dixon, W. T.; Schaefer, J.; Sefcik, M. D.; Stejskal, E. O.; McKay, R. A. *J. Magn. Reson.* **1982**, *49*, (2), 341.
- (30) Fung, B. M.; Khitrin, A. K.; Ermolaev, K. *J. Magn. Reson.* **2000**, *142*, (1), 97.
- (31) Barich, D. H.; Gorman, E. M.; Zell, M. T.; Munson, E. J. *Solid State Nucl. Magn. Reson.* **2006**, *30*, (3–4), 125.
- (32) Greenhalgh, D. J.; Williams, A. C.; Timmins, P.; York, P. *J. Pharm. Sci.* **1999**, *88*, (11), 1182-1190.
- (33) Lu, J.; Cuellar, K.; Hammer, N. I.; Jo, S.; Gryczke, A.; Kolter, K.; Langley, N.; Repka, M. A. *Drug Dev. Ind. Pharm.* **2016**, *42*, (3), 485-496.
- (34) Qian, F.; Huang, J.; Hussain, M. A. *J. Pharm. Sci.* **2010**, *99*, (7), 2941.
- (35) Lin, D.; Huang, Y. A thermal analysis method to predict the complete phase diagram of drug–polymer solid dispersions. *Int. J. Pharm.* **2010**, *399*, (1–2), 109.
- (36) Konno, H.; Taylor, L. S. *J. Pharm. Sci.* **2006**, *95*, 2692.
- (37) Shamblin, S. L.; Taylor, L. S.; Zografí, G. *J. Pharm. Sci.* **1998**, *87*, (6), 694-701.
- (38) Tang, X. C.; Pikal, M. J.; Taylor, L. S. *Pharm. Res.* **2002**, *19*, (4), 477-483.
- (39) Geppi, M.; Mollica, G.; Borsacchi, S.; Veracini, C. A. *Appl. Spectrosc. Rev.* **2008**, *43*, (3), 202-302.

Chapter 5

- (1) Vasconcelos, T.; Sarmiento, B.; Costa, P. *Drug Discovery Today* **2007**, *12*, 1068.
- (2) Vo, C. L.-N.; Park, C.; Lee, B.-J. *Eur. J. Pharm. Biopharm.* **2013**, *85*, 799.
- (3) Smithey, D.; Gao, P.; Taylor, L. *AAPS News Magazine* **2013**, *16*, 11.
- (4) W.Y. Lee, T.; A. Boersen, N.; Hui, H. W.; Chow, S. F.; Wan, K. Y.; H.L. Chow, A. *Curr. Pharm. Des.* **2014**, *20*, 303.
- (5) Policianova, O.; Brus, J.; Hruby, M.; Urbanova, M.; Zhigunov, A.; Kredatusova, J.; Kobera, L. *Mol. Pharmaceutics* **2014**, *11*, 516.
- (6) Maniruzzaman, M.; Morgan, D. J.; Mendham, A. P.; Pang, J.; Snowden, M. J.; Douroumis, D. *Int. J. Pharm.* **2013**, *443*, 199.
- (7) Calahan, J. L.; Azali, S. C.; Munson, E. J.; Nagapudi, K. *Mol. Pharmaceutics* **2015**, *12*, 4115.
- (8) Janssens, S.; Van den Mooter, G. *J. Pharm. Pharmacol.* **2009**, *61*, 1571.

- (9) Janssens, S.; Nagels, S.; De Armas, H. N.; D'auty, W.; Van Schepdael, A.; Van den Mooter, G. *Eur. J. Pharm. Biopharm.* **2008**, *69*, 158.
- (10) Goddeeris, C.; Willems, T.; Van den Mooter, G. *Eur. J. Pharm. Sci.* **2008**, *34*, 293.
- (11) Al-Obaidi, H.; Buckton, G. *AAPS PharmSciTech* **2009**, *10*, 1172.
- (12) Al-Obaidi, H.; Ke, P.; Brocchini, S.; Buckton, G. *Int. J. Pharm.* **2011**, *419*, 20.
- (13) Ziaee, A.; Albadarin, A. B.; Padrela, L.; Faucher, A.; O'Reilly, E.; Walker, G. *Eur. J. Pharm. Biopharm.* **2017**, *120*, 43.
- (14) Xie, T.; Taylor, L. S. *J Pharm Sci.* **2017**, *106*, 100.
- (15) Rumondor, A. C. F.; Ivanisevic, I.; Bates, S.; Alonzo, D. E.; Taylor, L. S. *Pharm. Res.* **2009**, *26*, 2523.
- (16) Wegiel, L. A.; Mauer, L. J.; Edgar, K. J.; Taylor, L. S. *J. Pharm. Sci.* **2013**, *102*, 171.
- (17) Mistry, P.; Mohapatra, S.; Gopinath, T.; Vogt, F. G.; Suryanarayanan, R. *Mol. Pharmaceutics* **2015**, *12*, 3339.
- (18) Chen, Y.; Wang, S.; Wang, S.; Liu, C.; Su, C.; Hageman, M.; Hussain, M.; Haskell, R.; Stefanski, K.; Qian, F. *Pharm. Res.* **2016**, *33*, 2445.
- (19) Dixon, W. T.; Schaefer, J.; Sefcik, M. D.; Stejskal, E. O.; McKay, R. A. *J. Magn. Reson.* **1982**, *49*, 341.
- (20) Fung, B. M.; Khitrin, A. K.; Ermolaev, K. *J. Magn. Reson.* **2000**, *142*, 97.
- (21) Barich, D. H.; Gorman, E. M.; Zell, M. T.; Munson, E. J. *Solid State Nucl. Magn. Reson.* **2006**, *30*, 125.
- (22) Männistö, P. T.; Mäntylä, R.; Nykänen, S.; Lamminsivu, U.; Ottoila, P. *Antimicrob. Agents Chemother.* **1982**, *21*, 730.
- (23) Lee, J. W.; Kim, S. Y.; Kim, S. S.; Lee, Y. M.; Lee, K. H.; Kim, S. J. *J. Appl. Polym. Sci.* **1999**, *73*, 113.
- (24) Vo, C. L.-N.; Park, C.; Lee, B.-J. *Eur. J. Pharm. Biopharm.* **2013**, *85*, 799.
- (25) Van den Mooter, G.; Wuyts, M.; Blaton, N.; Busson, R.; Grobet, P.; Augustijns, P.; Kinget, R. *Eur. J. Pharm. Sci.* **2001**, *12*, 261.
- (26) Newman, A. W.; Byrn, S. R. *Drug Discovery Today* **2003**, *8*, 898.
- (27) Baird, J. A.; Taylor, L. S. *Adv. Drug. Delivery Rev.* **2012**, *64*, 396.
- (28) Qian, F.; Huang, J.; Zhu, Q.; Haddadin, R.; Gawel, J.; Garmise, R.; Hussain, M. *Int. J. Pharm.* **2010**, *395*, 232.
- (29) Baghel, S.; Cathcart, H.; O'Reilly, N. J. *J. Pharm. Sci.* **2016**, *105*, 2527.

- (30) Liu, H.; Zhang, X.; Suwardie, H.; Wang, P.; Gogos, C. G. *J. Pharm. Sci.* **2012**, *101*, 2204.
- (31) Weuts, I.; Kempen, D.; Verreck, G.; Peeters, J.; Brewster, M.; Blaton, N.; Van den Mooter, G. *Eur. J. Pharm. Sci.* **2005**, *25*, 387.
- (32) Childs, S. L.; Stahly, G. P.; Park, A. *Mol. Pharmaceutics* **2007**, *4*, 323.
- (33) Ueda, H.; Aikawa, S.; Kashima, Y.; Kikuchi, J.; Ida, Y.; Tanino, T.; Kadota, K.; Tozuka, Y. *J. Pharm. Sci.* **2014**, *103*, 2829.
- (34) Konno, H.; Taylor, L. S. *J. Pharm. Sci.* **2006**, *95*, 2692.
- (35) Meng, F.; Trivino, A.; Prasad, D.; Chauhan, H. *Eur. J. Pharm. Sci.* **2015**, *71*, 12.
- (36) Albadarin, A. B.; Potter, C. B.; Davis, M. T.; Iqbal, J.; Korde, S.; Pagire, S.; Paradkar, A.; Walker, G. *Int. J. Pharm.* **2017**, *532*, 603.
- (37) Dong, J.; Ozaki, Y.; Nakashima, K. *Macromolecules* **1997**, *30*, 1111.
- (38) Nie, H.; Su, Y.; Zhang, M.; Song, Y.; Leone, A.; Taylor, L. S.; Marsac, P. J.; Li, T.; Byrn, S. R. *Mol. Pharmaceutics*. **2016**, *13*, 3964.
- (39) Paudel, A.; Geppi, M.; Van den Mooter, G. *J. Pharm. Sci.* **2014**, *103*, 2635.
- (40) Pham, T. N.; Watson, S. A.; Edwards, A. J.; Chavda, M.; Clawson, J. S.; Strohmeier, M.; Vogt, F. G. *Mol. Pharmaceutics* **2010**, *7*, 1667.
- (41) Yuan, X.; Xiang, T.-X.; Anderson, B. D.; Munson, E. J. *Mol. Pharmaceutics* **2015**, *12*, 4518.
- (42) Lubach, J. W.; Hau, J. *Pharm. Res.* **2018**, *35*, 65.
- (43) Song, Y.; Yang, X.; Chen, X.; Nie, H.; Byrn, S.; Lubach, J. W. *Mol. Pharmaceutics* **2015**, *12*, 857.
- (44) Xie, T.; Taylor, L. S. *Pharm. Res.* **2016**, *33*, 739.
- (45) Meng, F.; Meckel, J.; Zhang, F. *Eur. J. Pharm. Sci.* **2017**, *106*, 413.

Chapter 6

- (1) Curatolo, W.; Nightingale, J. A.; Herbig, S. M. *Pharm. Res.* **2009**, *26*, 1419.
- (2) Al-Obaidi, H.; Buckton, G. *AAPS PharmSciTech* **2009**, *10*, 1172.
- (3) Friesen, D. T.; Shanker, R.; Crew, M.; Smithey, D. T.; Curatolo, W. J.; Nightingale, J. A. S. *Mol. Pharmaceutics* **2008**, *5*, 1003.
- (4) Huang, Y.; Dai, W. G. *Acta Pharm. Sin. B* **2014**, *4*, 18.
- (5) Parikh, T.; Gupta, S. S.; Meena, A. K.; Vitez, I.; Mahajan, N.; Serajuddin, A. T. M. *J. Pharm. Sci.* **2015**, *104*, 2142.

- (6) Weuts, I.; Van Dycke, F.; Voorspoels, J.; De Cort, S.; Stokbroekx, S.; Leemans, R.; Brewster, M. E.; Xu, D.; Segmuller, B.; Turner, Y. T. A.; Roberts, C. J.; Davies, M. C.; Qi, S.; Craig, D. Q. M.; Reading, M. *J. Pharm. Sci.* **2011**, *100*, 260.
- (7) Duarte, Í.; Santos, J. L.; Pinto, J. F.; Temtem, M. *Pharm. Res.* **2015**, *32*, 222.
- (8) Dixon, W. T.; Schaefer, J.; Sefcik, M. D.; Stejskal, E. O.; McKay, R. A. *J. Magn. Reson.* **1982**, *49*, 341.
- (9) Fung, B. M.; Khitrin, A. K.; Ermolaev, K. *J. Magn. Reson.* **2000**, *142*, 97.
- (10) Barich, D. H.; Gorman, E. M.; Zell, M. T.; Munson, E. J. *Solid State Nucl. Magn. Reson.* **2006**, *30*, 125.
- (11) Tongyin, Y.; Mingming, G. *Prog. Polym. Sci.* **1990**, *15*, 825.
- (12) Aso, Y.; Yoshioka, S.; Miyazaki, T.; Kawanishi, T.; Tanaka, K.; Kitamura, S.; Takakura, A.; Hayashi, T.; Muranushi, N. *Chem. Pharm. Bull.* **2007**, *55*, 1227.
- (13) Bovey, F. A.; Mirau, P. A. *NMR of Polymers*, Academic Press, 1996.
- (14) Rumondor, A. C. F.; Marsac, P. J.; Stanford, L. A.; Taylor, L. S. *Mol. Pharmaceutics* **2009**, *6*, 1492.
- (15) Chakravarty, P.; Lubach, J. W.; Hau, J.; Nagapudi, K. *Int. J. Pharm.* **2017**, *519*, 44.

VITA

Kanika Sarpal

EDUCATION

2009 – 2011 **M.S. Pharm (Pharmaceutics)**

National Institute of Pharmaceutical Education and Research (N.I.P.E.R),
S.A.S Nagar, India

2005 – 2009 **B. Pharmacy**

University Institute of Pharmaceutical Sciences, Panjab University,
Chandigarh, India

HONORS AND AWARDS

2018 International Pharmaceutical Excipient Council (IPEC) Foundation Graduate Student Award

2018 American Association of Pharmaceutical Sciences (AAPS) Best Poster Abstract Award

2018 AAPS Travelship Award

2018 Small Molecule NMR Conference Scholarship

2018 Pharmaceutical Sciences Excellence in Graduate Achievement Fellowship

2018 **2nd Prize**, Rho Chi Research Day at University of Kentucky

2017 American Association of Indian Pharmaceutical Scientists (AAiPS) Graduate Student Award

2017 Small Molecule NMR Conference Scholarship

2016 **1st Prize**, Poster presentation at Globalization of Pharmaceutics Education Network Conference

2015 **3rd Prize**, Podium talk at Pharmaceutics Graduate Student Research Meeting

PUBLICATIONS

K. Sarpal, Y.B. Pawar and A. K. Bansal. *Self-emulsifying drug delivery systems: A strategy to improve oral bioavailability*. CRIPS. Vol. 11, No. 3, Jul-Sept 2010.

K. Sarpal, S. Delaney, G. Zhang and E. Munson. *Phase Behavior of Amorphous Solid Dispersions of Felodipine: Homogeneity and Drug-Polymer Interactions*. (manuscript submitted).

K. Sarpal, C. Tower and E. Munson. *An Investigation into Molecular Interactions and Phase Behavior of Binary and Ternary Amorphous Solid dispersions of Ketoconazole* (manuscript to be submitted).

M. Honick, **K. Sarpal**, A. Alayoubi, A. Zidan, S. Hoag, R. Hollenbeck, E. Munson, and J. Polli. *Utility of Films to Anticipate Properties of Amorphous Itraconazole Spray Dried Dispersions*. (manuscript submitted).